University of Basel

Swiss Nanoscience Institute

SNI
Swiss Nanoscience Institute
Center of Excellence supported by the University of Basel and the Canton of Aargau

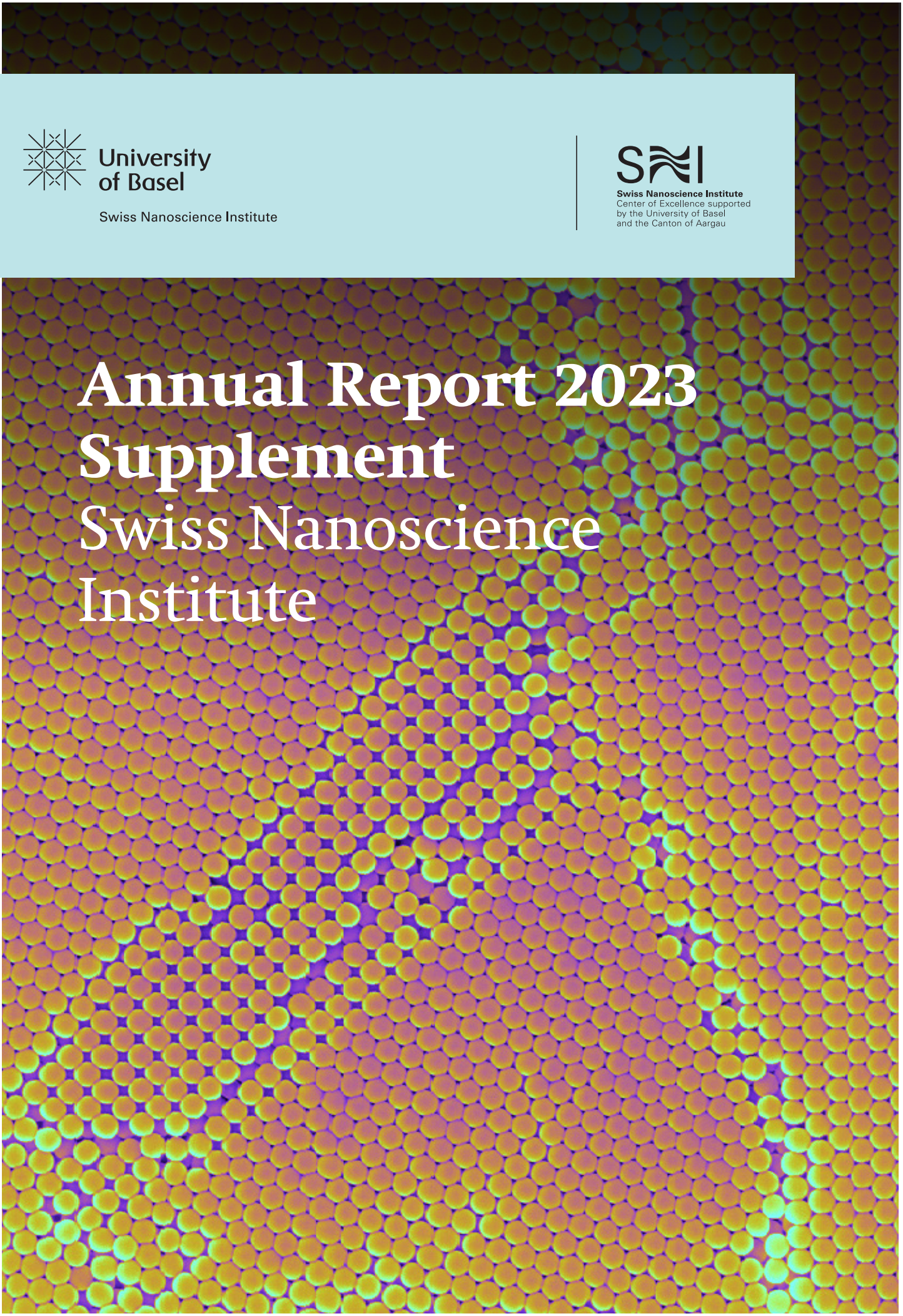

Annual Report 2023 Supplement

Swiss Nanoscience Institute

Cover image:

Microspheres
Microspheres were prepared from styrene via emulsion polymerization by students in the practical training in polymers at FHNW. The spheres are forming hexagonal ordered assemblies when dried on the sample holder. The image was taken with an Electron microscope. The spheres are originally white, the image was colored using Adobe Photoshop. (Image: V. Hollenstein, L. Martinez and S. Saxer, FHNW Muttenz)

Contents

High efficiency preparation of monodisperse plasma membrane derived extracellular vesicles for therapeutic applications

Project P1801: Bioinspired nanoscale drug delivery systems for efficient targeting and safe in vivo application
Project Leader: J. Huwyler and C. Palivan
Collaborator: C. L. Alter (SNI PhD Student)

Introduction

Extracellular vesicles (EVs) hold great potential in bio-pharmaceutical engineering, especially for therapeutic purposes [1]. These vesicles, derived from cells, contain cell specific lipids, proteins such as enzymes and cell adhesion molecules, various nucleic acids including RNA and DNA, along with metabolites, organelles, and sometimes viruses [2,3]. EVs are primarily divided into two categories: exosomes and ectosomes. Exosomes, smaller in size (40 to 150 nm in diameter), arise from the cell's endosomal compartment and are released continuously by both prokaryotic and eukaryotic cells through exocytosis of multivesicular bodies and amphisomes. In contrast, ectosomes are formed by the direct budding or blebbing of the plasma membrane and encompass a broader range of vesicles, including microvesicles, apoptotic bodies (ApoBDs), vesicles (ApoEVs), and large oncosomes, with sizes varying from 50 to over 1000 nm [3]. Therapeutic nucleic acids, proteins, or small molecular weight drugs have been successfully loaded into EVs and delivered to cells both in vitro and in vivo. However, only a few EV technologies have advanced to clinical trials, largely due to challenges in EV production. Standard EV secretion rates vary from 60 to 170 native EVs (especially exosomes) per cell per hour, depending on the cell type [4,5].

To address this challenge, we have developed an innovative alternative to the conventional native EV preparation method, suitable for almost all cell lines and even primary cells. This method involves creating chemically induced giant plasma membrane vesicles (GPMVs), which are then collected and processed into nano-sized plasma membrane vesicles (nPMVs) through size homogenization. Additionally, we have assessed the interaction of nPMVs with in vitro cell cultures and zebrafish embryos (ZFE), comparing their behavior with that of native EVs.

Material and methods

Chemical vesiculation agents (paraformaldehyde and dithiothreitol) were used to induce cellular injury and membrane blebbing in Huh7 and HEK293 cells. The vesiculation started a few minutes after incubation (37°C and 5% CO_2) and the produced GPMVs were harvested from donor cells after 6 h. Then, GPMVs were stained with 1 µM of a lipophilic dye (DiI) and homogenized through filter extrusion in order to produce nPMVs. Native EVs were produced as previously described [6] and labeled with 1 µM DiI. DiI labeled DOPC and DOPC:PS liposomal formulations, serving as negative and positive controls, were produced by thin-film hydration method [7]. Cell viability was assessed using MTS assay (Cell Proliferation, Colorimetric, ab197010). In vitro uptake studies were performed with flow cytometry. ZFE experiments were conducted as previously described [8].

Results and discussion

First, we compared the production rate of our newly developed nPMV preparation protocol with that of an existing native EV preparation protocol, finding production rates of 1100-1400 particles/cell/hour for the nPMV and 5-7 particles/cell/hour for the native EV preparation protocol, respectively. This indicates that our nPMV preparation protocol is at least an order of magnitude more efficient. Furthermore, in the proteome of nPMVs we detected several EV (i.e., CD9, CD81) ectosome (i.e., BSG, SLC3A2), and ApoBD (i.e., Calreticulin) markers 10. These results indicated that nPMVs primarily comprise ApoEVs with little to no significant levels of native EVs. In addition, proteomics showed that nPMVs have around a 40% similar proteome to native EVs, but they also display a distinct proteomic profile. Next, we incubated HEK293/Huh7 nPMVs and native EVs, DOPC:PS, and DOPC liposomes with Huh7 cells for 24 h and analyzed the cell viability. Cell viability was not significantly altered by the nanoparticles (Fig. 1a). The uptake of these nanoparticles was measured by flow cytometry after incubation for 15 min, 1, 4, and 24 h (Fig. 1b).

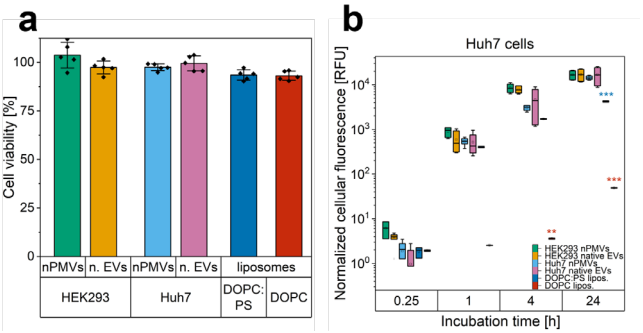

*Fig. 1: Cell viability of Huh7 cells and the interaction of various nanoparticles with Huh7 cells are as follows: a) Huh7 cell viability after 24 hours of incubation with HEK293/Huh7 nPMVs, native EVs, DOPC:PS, and DOPC liposomes, measured by the MTS assay. b) Flow cytometry-based cellular uptake quantification of DiI-labeled HEK293 nPMVs (green), HEK293 native EVs (orange), Huh7 nPMVs (blue), Huh7 native EVs (pink), DOPC:PS (dark blue), and DOPC liposomes (red) by Huh7 cells after the indicated time points. Levels of significance are denoted as follows: *: $p \leq 0.05$, **: $p \leq 0.01$, ***: $p \leq 0.001$.*

We observed a time-dependent uptake (normalized cellular fluorescence) in Huh7 cells for all particles. The uptake was fast in the first 4 h, then started to saturate and reached the highest value after 24 h. Huh7/HEK293 nPMVs and the respective native EVs showed comparable uptake, which was slightly higher than the uptake of DOPC:PS liposomes. Negligible uptake of DOPC liposomes was measured.

We further injected DiI-labeled HEK293/Huh7 nPMVs, native EVs, or DOPC:PS/DOPC liposomes into 48-hour post-fertilization old transgenic (Kdrl:EGFP) ZFE, which express EGFP in their vasculature. 4 and 24 h after injection, we observed that HEK293/Huh7 nPMVs and native EVs were mainly sequestered by scavenger endothelial cells in the caudal vein plexus, possibly through scavenger receptors (e.g. stabilin-11) and dynamin-dependent endocytosis, but also to a lesser extent in tissue resident/patrolling macrophages [10, 11]. A representative image of these nanoparticles is shown in figure 2a. The fast clearance of nPMVs and native EVs was further supported by the low circulation and extravasation factors, which describe the circulation and extravasation behavior of nanoparticles in the zebrafish, as determined by semi-quantitative image analysis [8]. It is interesting to note that identical interactions and observations were previously described for other native EVs [11–13]. Liposomal formulations on the other hand showed significantly higher circulation and extravasation times being indicative for a lower cell interaction behavior (Fig. 2b).

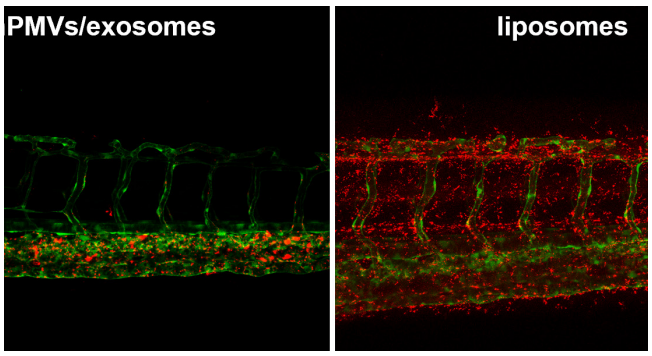

Fig. 2: Biodistribution of nPMVs/native EVs or liposomes (red signal) in the vasculature of transgenic (Kdrl:EGFP) zebrafish embryos (green signal) 24 h after injection. Representative image for the biodistribution of HEK293/Huh7 nPMVs/native EVs (left) and DOPC:PS/DOPC liposomes (right). Scale bar: 100 µm.

Conclusion

We were able to produce high yields of nPMVs from various cell lines with our optimized preparation method, which exceeds the production rate of existing native EV preparation protocols by at least an order of magnitude. Furthermore, we observed a fast and efficient uptake of nPMVs and native EVs in vitro and in vivo. These results suggest that nPVMs can serve as a valuable addition to existing EVs and offer new perspectives for the design of EV based therapeutic systems.

References

[1] D. E. Murphy, O. G. de Jong, M. Brouwer, M. J. Wood, G. Lavieu et al. Extracellular vesicle-based therapeutics: natural versus engineered targeting and trafficking. Exp. Mol. Med. 51, 1–12 (2019)

[2] G. van Niel, G. D'Angelo, G. Raposo, Shedding light on the cell biology of extracellular vesicles. Nat. Rev. Mol. Cell Biol. 19, 213–228 (2018)

[3] E. I. Buzas, The roles of extracellular vesicles in the immune system. Nat. Rev. Immunol. 1–15 (2022)

[4] S. G. Antimisiaris, S. Mourtas, A. Marazioti, Exosomes and Exosome-Inspired Vesicles for Targeted Drug Delivery. Pharmaceutics 10, 218 (2018)

[5] Y.-J. Chiu, W. Cai, Y.-R. V. Shih, I. Lian, Y.-H Lo, A Single-Cell Assay for Time Lapse Studies of Exosome Secretion and Cell Behaviors. Small 12, 3658–3666 (2016)

[6] W. Heusermann, J. Hean, D. Trojer, E. Steib, S. von Bueren, et al. Exosomes surf on filopodia to enter cells at endocytic hot spots, traffic within endosomes, and are targeted to the ER. J. Cell Biol. 213, 173–184 (2016)

[7] H. Zhang, Thin-Film Hydration Followed by Extrusion Method for Liposome Preparation. in Liposomes 17–22 (Humana Press, New York, NY, 2017)

[8] S. Sieber, P. Grossen, P. Detampel, S. Siegfried, D. Witzigmann, J. Huwyler, Zebrafish as an early stage screening tool to study the systemic circulation of nanoparticulate drug delivery systems in vivo. J. Controlled Release 264, 180–191 (2017)

[9] C. L. Alter, P. Detampel, R. B. Schefer, C. Lotter, P. Hauswirth et al. High efficiency preparation of monodisperse plasma membrane derived extracellular vesicles for therapeutic applications, Commun Biol 6, 478 (2023)

[10] G. Arias-Alpizar, B. Koch, N. M. Hamelmann, M. A. Neustrup, J. M. J. Paulusse et al. Stabilin-1 is required for the endothelial clearance of small anionic nanoparticles. Nanomedicine 34, 102395 (2021)

[11] F. J. Verweij, C. Revenu, G. Arras, F. Dingli, D. Loew, et al. Live Tracking of Inter-organ Communication by Endogenous Exosomes In Vivo. Dev. Cell 48, 573-589. e4 (2019)

[12] F. J. Verweij, V. Hyenne, G. V. Niel, J. G. Goetz, Extracellular Vesicles: Catching the Light in Zebrafish. Trends Cell Biol. 29, 770–776 (2019)

[13] V. Hyenne, S. Ghoroghi, M. Collot, J. Bons, G. Follain et al. Studying the Fate of Tumor Extracellular Vesicles at High Spatiotemporal Resolution Using the Zebrafish Embryo. Dev. Cell 48, 554-572.e7 (2019)

Deep learning enhanced directed evolution

Project P1802: From Schrödinger's equation to biology: Unsupervised quantum machine learning for directed evolution of anti-adhesive peptides
Project Leader: M. Nash and A. von Lilienfeld
Collaborator: V. Doffini (SNI PhD Student)

Introduction
The Covid-19 pandemic showed us that our deeply interconnected world is extremely vulnerable to highly contagious pathogens. In this context, viruses are not the only threat we might face in future epidemic scenarios. Specifically, bacteria that show antibiotic resistance characteristics are an enormous hazard to humanity, and this topic has garnered increased interest from across the biomedical research community in recent years. It is crucial to explore new strategies to fight against antibiotic resistant pathogens and develop new pharmacological treatments.

In our project, we focus on a specific class of microbes which use specialized surface proteins called adhesins to bind human tissue and spread the infection inside the host. The detailed structure and mechanism behind many such bacterial binding adhesin domains are known, while for others no structural information is available. Such adhesins typically bind short peptide sequences located on abundant blood or cell-surface proteins of the intended host (Fig. 1). The goal of our project is to identify novel peptide candidates which bind strongly to the bacterial adhesin of the pathogen agent, inhibiting it from attaching to the host's cells.

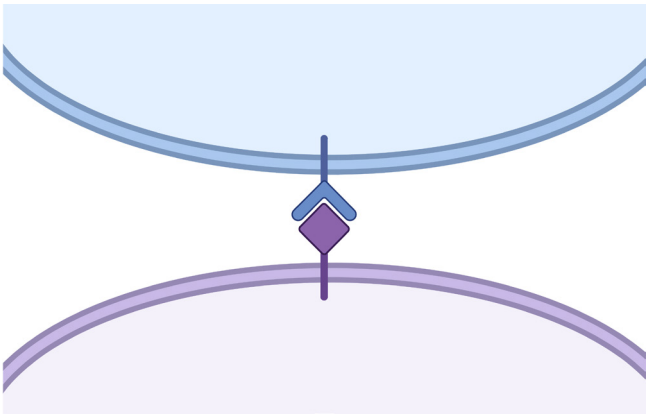

Fig. 1: Schematic representation of the binding between the pathogen (in blue) and the human cell (violet). The binding protein of the microorganism is shown in blue as well, while the attach site of the human cell is the violet square.

By using state of the art technologies like deep mutational scanning and next generation sequencing, it is already possible to generate data for hundreds of thousand different peptide variants in a relative short amount of time. Despite the fact that this might sound like a lot of data, they cover just a minimal fraction of the enormous space of possible amino acid combinations, even for small chains. For example, even for a peptide of a couple dozen amino acids, the number of total possible combinations are many orders of magnitude greater than the stars in the whole universe. Practically, this problem usually leads to a repetitive approach, called directed evolution, where mutations are screened and ranked based on a fitness function. In our case, the fitness function would be a measure of the binding strength between the adhesin protein and the peptide. After this first screening, the best mutations are selected, fixed and millions of new variants are produced changing the amino acids on the other positions. Afterwards, the new variants are screened and ranked again and the procedure is repeated for many iterations until an optimum is reached. Unfortunately, such protocol is not exempt from criticism; firstly, by exploring just single point mutations it is likely to get stuck on a local optimum instead of finding the global one; and secondly, since the presented protocol needs to be repeated multiple times, the burden of experiments needed is still high and it impacts negatively the time, resources and costs involved.

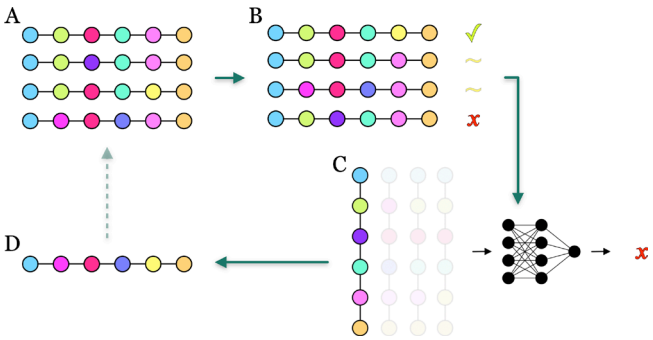

Fig. 2: Schematic representation of deep learning enhanced direct evolution. Starting from upper left, a library containing many mutants is synthesized (A). Then, the different variants are sequenced and sorted by a chosen output (B). After that, a neural network is trained in order to connect the specific sequences to the fitness variable (C). Finally, the model is used to perform in-silico screening of new variants. The best candidates are synthesized in the lab (D) and, eventually, added to the library for a new iteration.

In order to increase the efficiency as well as the accuracy of directed evolution, we propose a deep learning assisted approach (see Fig. 2). Such a methodology is still based on screening and ranking peptides, but in this case a deep neural network is fitted to connect the specific amino acid residues to the corresponding fitness function value. If successful, the deep neural network can be used to screen in-silico many more variants than are available experimentally, giving the possibility to efficiently find a new maximum of the fitness function without the need of many iterations as in the "classical" directed evolution approach. Moreover, since we are not anymore constrained by fixing the single best mutations found in the previous screening, the fitness

maximum we reach using metaheuristic techniques will be theoretically better than the previous one.

Material and methods

During the initial phase of the project, we focused on the synthesis and fluorescent labeling of one of the binding proteins of a pathogenic organism as well as the production of an E. Coli library. This library contains millions of bacteria, where each of the individual cells displays on its surface a specific peptide of defined length. The number of mutations in the library follows a binomial distribution with an 80% wild-type (WT) probability. Such library was cloned via HiFi assembly from fragments produced by Twist Bioscience. It was then screened using the bacterial adhesin labelled with a fluorescent dye molecule (Fig. 3). Peptides that strongly bond the adhesin retained the fluorescent label after washing. The fluorescent intensity was detected by flow cytometry analysis and the cells were sorted.

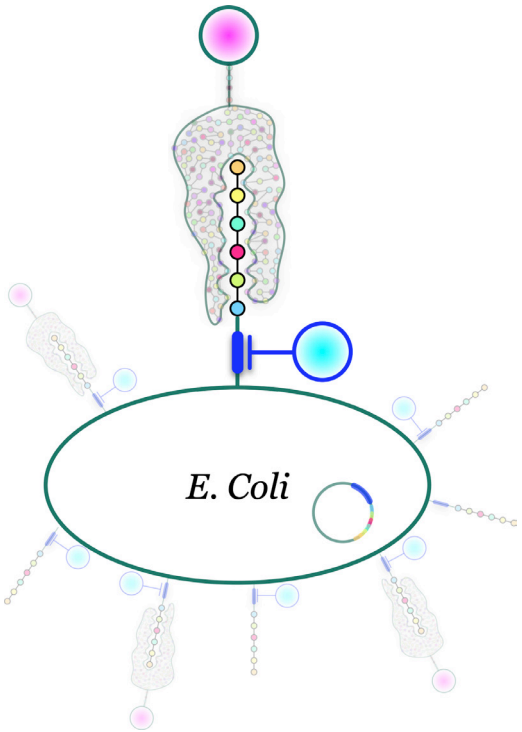

Fig. 3: Schematic representation of the binding between the protein of the pathogenic organism and one of the randomized peptides displayed on the cell surface of an E. Coli. The fluorescent label is shown in pink.

We present here the sorting methodology applied to the peptide library (Fig. 4). A multi-gating strategy was employed to enhance resolution within the fitness landscape. This oblique sorting approach was designed to normalize the quantity of proteins bound to the cells (binding) relative to the number of peptides displayed on the cell surface (expression). The cells, after sorting, were cultivated in individual tubes. The plasmid DNA was then extracted and purified from these cultures. Upon purification, the plasmid DNA samples were dispatched for sequencing analysis.

Results and discussion

The analysis of sequencing data facilitated the identification of mutations exhibiting a stronger affinity for our target compared to the wild type (WT), many of which were previously unreported. Additionally, this dataset served as a foundation for training a machine learning model. This model was subsequently utilized to navigate the fitness landscape in search of mutations with even greater binding strength.

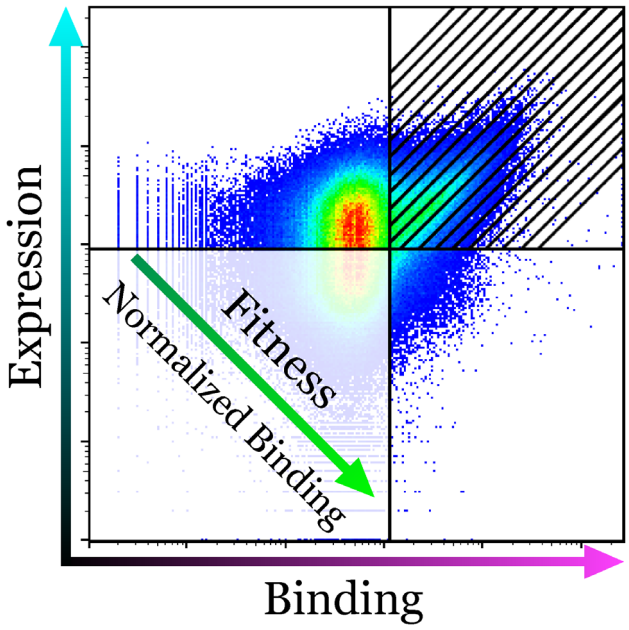

Fig. 4: Scatter plot of the binding between the peptide library and the labelled protein of the pathogenic organism. Each point corresponds to one distinct peptide.

Outlook

In the last phase of the research project, the validation of outcomes will be pursued through the strategic selection of specific mutations identified within the dataset. This validation process will be conducted employing isothermal titration calorimetry (ITC). Concurrently, an examination will also be undertaken on a similar set of mutations, these having been identified by the machine learning model. This dual approach aims to verify the reliability and precision of the results within a meticulously regulated experimental setting.

References

[1] R. Vanella, D. Tien Ta, M. A. Nash, Enzyme-mediated hydrogel encapsulation of single cells for high-throughput screening and directed evolution of oxidoreductases, Biotechnology and Bioengineering, 116(8), 1878–1886 (2019)

[2] K. Yang, Z. Wu and F. Arnold, Machine-learning-guided directed evolution for protein engineering, Nat. Methods 16(8), 687-694 (2019)

Quantifying bacterial responses to antibiotics at the single-cell level

Project P1805: High-throughput multiplexed microfluidics for antimicrobial drug discovery
Project Leader: E. van Nimwegen and V. Guzenko
Collaborator: M.-E. Alaball Pujol (SNI PhD Student)

Introduction

Without effective antimicrobials, the success of modern medicine would be at risk for treating infections including during major surgery and cancer chemotherapy. Misuse and overuse of antimicrobials are key drivers in the development of resistant pathogens; however, it has also become clear in the last decades that sensitivity to treatment varies from cell to cell, even in an isogenic population. In particular, some cells are in physiological states that allow them to survive antibiotic treatment without any resistance mutations [1]. Slow growing cells have been reported to be more tolerant to antibiotics, and this increased tolerance can facilitate the subsequent fixation of resistance mutations [2]. Yet, most in vitro assays that are used to discover and study antimicrobial compounds are based on liquid cultures in which bacterial cells grow exponentially so that slow-growing cells are quickly outgrown, making it impossible to assess the effects of the compounds on slow growing cells. Consequently, the determinants of sensitivity to antibiotics are poorly understood at the single-cell level due to the lack of quantitative data.

In recent years, powerful methods have been developed to quantitatively measure behaviour and responses in single bacterial cells. By combining microfluidics with time-lapse microscopy, it is possible to track growth, gene expression, division, and death within lineages of single cells. An especially attractive microfluidic design is the so-called Mother Machine, where bacteria grow within narrow growth channels that are perpendicularly connected to a main flow channel, which supplies nutrients and washes away cells growing out of the growth channels. In this field, our lab has developed an integrated microfluidic and computational setup to study the response of single bacteria to controlled environmental changes [3]: the dual-input Mother Machine (DIMM). The DIMM allows arbitrary time-varying mixtures of two input media, such that cells can be exposed to a precisely controlled set of varying external conditions. Our image analysis software Mother Machine Analyser (deepMoMA) segments and tracks cell lineages from phase-contrast images with high throughput and accuracy.

In the present project, we use this setup to quantify how the response of individual bacterial cells to treatment with antibiotics depends on their physiological state at the start of the treatment. We focus on treating Escherichia coli (E. coli) with a variety of clinically relevant antibiotics at clinically relevant concentrations. In addition, we aim to develop new microfluidic designs that enable the study of multiple antibiotics and strains in parallel. Our long-term aim is to use this approach to identify compounds that specifically target non-growing subpopulations of pathogenic bacteria.

Designing improved microfluidic devices

Designing microfluidic chips that enable to multiplex the testing of different strains and media requires improving two aspects of current designs: the multiplexing of the media reservoirs and the loading of the cells into the device. For the former, a multiplexed version of the classic DIMM was designed in our lab, with eight inlets and outlets (Fig. 1A). Furthermore, together with the mechanical workshop of Biozentrum we developed a prototype pressurized box to multiplex the reservoirs for the input media, which is being used in our experiments.

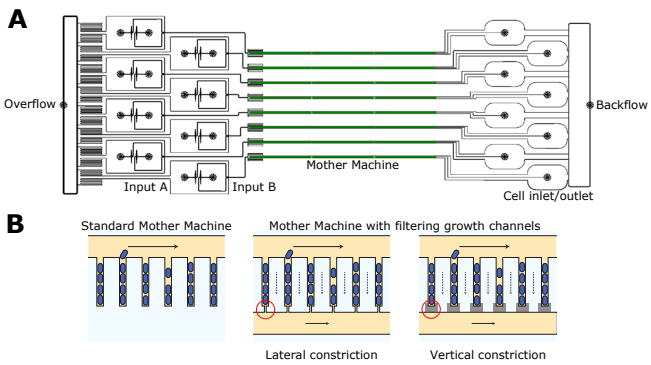

Fig. 1: Design of the microfluidic chips. A) Multiplexed DIMM. B) Different filter constriction designs.

To address the cell loading, we wanted to design a modified version of the standard Mother Machine where the closed end of growth channels is replaced by constrictions that act as filters. These filter structures are shallower and/or narrower than the growth channels, connected to the main flow channel, but also connected to a backflow channel so that media can flow through, but not the cells. This allows loading of the growth channels by simply 'filtering' a diluted bacterial culture through the chip. In addition, with these filters, there is no nutrient gradient inside the channels and the addition or the removal of chemicals of interest is immediate. Lastly, the flow through the growth channels can help retaining motile cells by mechanically pushing them toward the filter end. These filter channels have already been produced using a lateral constriction [4]. Because of the small size of these structures, they are very challenging to manufacture, and require e-beam lithography which is not widely available.

To establish the production of the filter channels we have pursued two strategies (Fig. 1B). On the one hand, together with Dr. Vitaliy Guzenko at PSI we used the e-beam lithography system Raith EBPG 5000Plus to microfabricate lat-

eral constrictions. With this strategy the design consists of two layers of different thicknesses; the main flow channels (20 µm wide and 10 µm deep) and the narrow (<1 µm) and shallow (900 nm deep) growth channels. The lateral constriction reduces the width of the channels to 250 nm. This design was unstable in first tests, but we produced newer versions of it that look promising.

An alternative strategy led by Dr. Thomas Julou is based on a 3-layer design, where the third layer is shallow enough to produce a vertical constriction, reducing the channel height by 250 nm. The vertical constriction consists of a reservoir-like structure surrounding the growth channel. This design has been tested and has already been successfully used in experiments.

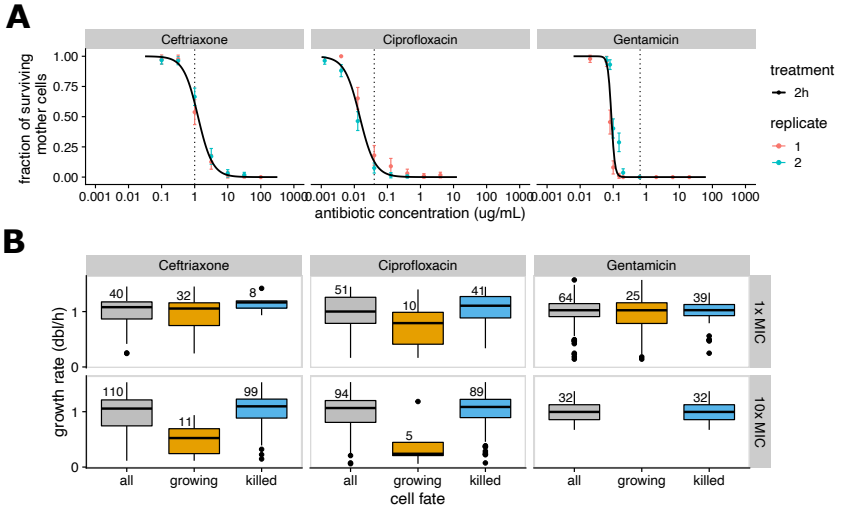

Fig. 2: A) Survival rates of mother cells at different antibiotic concentrations. The coloured dots show the fractions of surviving cells for each replicate, with 2 standard deviation error bars. The lines show Hill function curves fitted to the data of each antibiotic. Vertical dashed lines show MIC values measured in bulk. B) Boxplots showing the growth rate distribution all cells just before the treatment (gray), cells that survived (orange) and cells that died (blue). Two antibiotic concentrations are shown: the MIC and 10 times MIC for each antibiotic.

Characterization of single-cell responses to antibiotic treatment

We focused on 3 clinically relevant antibiotics for Urinary Tract Infection (UTI) treatment: Ciprofloxacin (CIP), Ceftriaxone (CEF), and Gentamicin (GEN). Our experiments consisted of treating cells of E. coli lab strain MG1655 with different concentrations of each antibiotic, ranging from the maximum concentration measured in serum during clinical treatment, to sub-Minimal Inhibitory Concentration (MIC). The experimental timeline consisted of 6 hours of exponential growth in M9 minimal media with 0.2% glucose, followed by 2 hours of antibiotic treatment, after which the survival was assessed by exposing the bacteria to fresh media for 16 hours.

We calculated the survival rates for all the conditions by tracking the 'mother' cells at the bottom of the growth channels across the treatment and counting the cells that produced viable progeny afterwards. We found that, although the fraction of surviving cells drops with concentration for each antibiotic, the concentration range over which survival rates fall varies between antibiotics (Fig. 2A).

We obtained quantitative data from the experiments using the DeepMoMA software, a new version of the MoMA software, that integrates the U-Net convolutional neural network architecture, developed by Dr. Michael Mell in our group. In particular, DeepMoMA has been adapted to different cell morphologies that result from the treatment with antibiotics. These morphologies include lysis, filamentation and loss of phase contrast, which are observed at different rates for different antibiotics and concentrations.

We reconstructed cell lineages across the 2-hour antibiotic treatment experiments, and we quantified various single-cell variables, including instantaneous growth rates. We then analysed how the growth rate of cells just before the treatment affected their survival. Surviving cells generally were growing more slowly just before the CIP and CEF treatment, than cells that died (Fig. 2B). Interestingly, as we increase the antibiotic concentration, surviving cells reduce their growth rate even further. We are currently working on analysing the raw traces using a Bayesian inference method developed by Björn Kscheschinski in our group (based on a maximum entropy process prior), called RealTrace, to obtain de-noised traces of cell length and GFP content as well as instantaneous growth and GFP production rates.

These results were obtained with a lab strain in minimal synthetic media. One of our goals is to compare these results with the behaviour of Uropathogenic E. coli (UPEC) strains. For that, we established the workflow in the lab to work with the UPEC strain strain CFT073, and we tested how it grows in the new Mother Machine designs in previously defined Synthetic Human Urine (SHU) [5], which is closer to real urine than laboratory-defined media. We are currently optimizing the workflow and expect to soon analyse the single-cell responses of CFT073 to antibiotics while growing in SHU.

References

[1] D. Hughes and D. I. Andersson, Environmental and genetic modulation of the phenotypic expression of antibiotic resistance, FEMS microbiology reviews 41 (2017)

[2] E. Rotem, A. Loinger, I. Ronin, I. Levin-Reisman, C. Gabay, et al., Regulation of phenotypic variability by a threshold-based mechanism underlies bacterial persistence, PNAS 107 (2010)

[3] M. Kaiser, F. Jug, T. Julou, S. Deshpande, T. Pfohl, et al., Monitoring single-cell gene regulation under dynamically controllable conditions with integrated microfluidics and software, Nat. Commun. 9 (2018)

[4] Ö. Baltekin, A. Boucharin, E. Tano, D. I. Andersson, J. Elf, Antibiotic susceptibility testing in less than 30 min using direct single-cell imaging, PNAS 114 (2017)

[5] D. S. Ipe and G. C. Ulett, Evaluation of the in vitro growth of urinary tract infection-causing gram-negative and gram-positive bacteria in a proposed synthetic human urine (SHU) medium, J. Microbiol. Methods 127 (2016)

Image the twist!

Project P1806: Image the twist!
Project Leader: V. Scagnoli and P. Maletinsky
Collaborators: S. Treves (SNI PhD Student), J. White, V. Ukleev

Introduction and motivation

The aim of this project is to determine the formation mechanism of skyrmions, a topologically protected magnetic structure [1]. Currently it is not fully understood what drives the formation and annihilation events in skyrmion hosting materials; such knowledge is particularly important if they are to be implemented into improved technological applications in the future [2]. Observations of these events are made easier through the use of materials which host skyrmions in ambient conditions.

A system of recent interest for hosting room temperature skyrmions with no need of an applied magnetic field is $NdMn_2Ge_2$, a rare-earth based centrosymmetric material. This bulk material has been observed to host different metastable magnetic textures stabilized by high- and low- magnetic field cooling protocols. Metastable skyrmions have been nucleated with a field cooling procedure and then observed using topological Hall effect measurements [3,4] and Lorentz transmission electron microscopy (LTEM) [5]. We have also confirmed these findings and demonstrated the effects of temperature and an applied magnetic field on the skyrmion lattice in previous years of the project.

Issues were encountered when using the measurement technique Nitrogen Vacancy (NV) magnetometry on the lamella sample used for the x-ray imaging experiment. Due to the sample being too thick (~200 nm, required to have sufficient magnetic signal in the x-ray measurements), the stray fields that it produced saturated the NV sensor, making it challenging to collect sensible NV data. We therefore aimed at producing thinner samples in a reliable and less invasive way as using focused ion beam (FIB), which is required to extract lamella out of larger crystal.

We found that the solution was to grow thin films of $NdMn_2Ge_2$ with the goal of replicating the bulk material properties. Thin films offer a unique set of advantages compared to bulk crystal samples. They offer more control of the magnetic properties and the ability to create microstructures. Furthermore, their provide versatility and make it possible to miniaturize the system, allowing for easier integration into pre-existing devices or sensors.

The sputter grown $NdMn_2Ge_2$ films were characterized, using x-ray diffraction and magnetization measurements. Magnetic Force Microscopy (MFM) measurements were then undertaken in ambient conditions, whilst applying an external magnetic field. Overall, our measurements indicate that it is possible to form skyrmions in these thin films and that their behaviour is like those observed in the bulk samples.

Key experimental results

The initial milestone was to successfully grow a thin film of stoichiometric $NdMn_2Ge_2$ and compare its properties to the bulk ones. Note that there are no reports in the literature about the growth of thin film of this material. Plasma sputtering was used to deposit the material from a target onto a MgO substrate. This procedure underwent several iterations, with a range of growth times, growth temperatures and annealing temperatures used.

To characterise the thin films x-ray diffraction (XRD) patterns and magnetometry data were collected. These results could then be compared to the results for the bulk crystal sample (Fig. 1) used in our previous experiments. The XRD pattern for a thin film with 45 nm of thickness can be seen in figure 2a. It exhibits the same Bragg peaks as the bulk. There is, however, an additional peak, which is due to the signal from the MgO substrate.

The magnetisation of the sample with changing temperature (Fig. 2b), also shows a similar behaviour to the bulk sample. This measurement is initialised by heating above the Curie temperature (T_C = 330 K), of the sample. A magnetic field of 0.01 T is then applied, out-of-plane (OOP), and the sample is cooled. There is a noticeably smaller magnitude of the thin film's magnetisation when comparing it to the bulk's magnetisation. This is due to the thin film being 20 nm in thickness, whereas the bulk crystal was closer to being mm in thickness when measured.

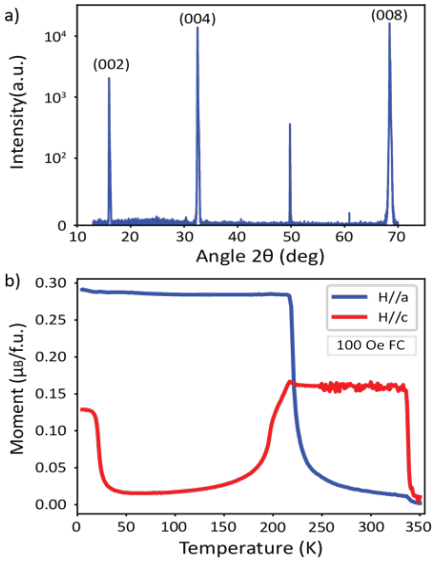

Fig. 1: Bulk $NdMn_2Ge_2$ crystal characterization. a) X-ray diffraction pattern showing selected Bragg peaks. b) The sample magnetization vs temperature under the application of a small magnetic field.

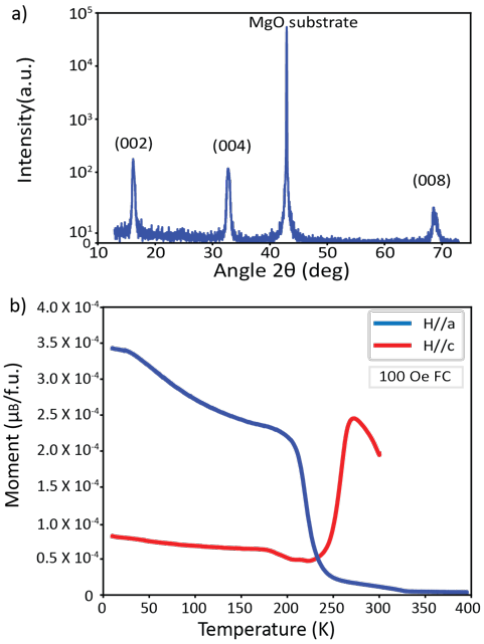

Fig. 2: Data for $NdMn_2Ge_2$ thin film (45 nm thickness). a) X-ray diffraction peaks indicating the position of the Bragg peaks of the crystalline planes. b) The magnetization of the thin film with reducing temperature and a small out-of-plane magnetic field applied.

Once the ideal growth conditions for the thin film had been identified, we began to grow thicker films. A film thickness of 90 nm was found to have the closest match for the magnetisation with respect to temperature to bulk samples in literature. With this knowledge, we conducted measurements using magnetic force microscopy (MFM). These measurements allowed for the sample's magnetic configuration at the surface to be imaged, allowing us to try to nucleate skyrmions, and be able to check immediately.

Several different measurement protocols were carried out: The sample was imaged in its as grown state, then it was imaged with an applied magnetic field; The sample was then field cooled and imaged in ambient conditions.

Our first goal with the MFM measurements was to nucleate skyrmions within the sample. When the thin film was imaged in ambient conditions its magnetic configuration was a a maze domain. When increasing an applied OOP magnetic field from 0 mT to 30 mT the maze domains shrank and eventually formed skyrmion like objects (Fig. 3). These objects remained stable up until 50 mT where the MFM images lose contrast due to the domains becoming too small. Furthermore, if the applied field is removed once the skyrmions have formed, the skyrmions collapse and merge together to form a maze domain state.

The next goal was to nucleate skyrmions, which would remain stable in ambient conditions. This was achieved via a field cooling method, which is as follows. The sample was heated above its T_C. Then an OOP magnetic field of 30 mT was applied whilst the sample cooled to room temperature. This process was repeated several times, with the sample imaged in ambient conditions after each field cool. After each of these field cools skyrmions were observed to be stable in the thin film. This confirms that like the bulk samples, it is possible to host skyrmions, which remain stable in ambient conditions in these thin film systems.

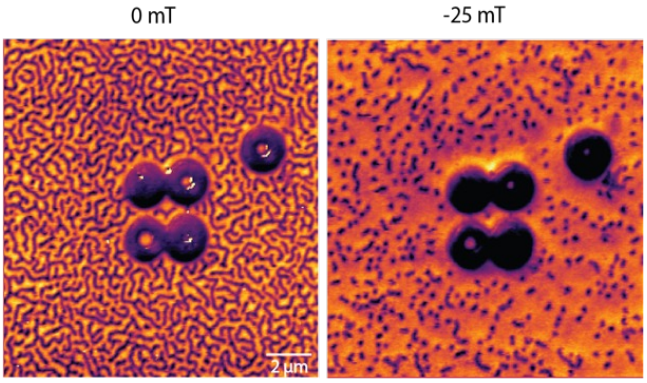

Fig. 3: MFM data for the 90 nm thin film. At 0 mT a maze domain pattern can be seen as the systems preferred magnetic state. When the field is ramped to -25 mT, the domains shrink and separate into skyrmions.

Outlook

The demonstration of metastable skyrmions within the thin films systems is a novel observation. Further investigation will be undertaken to explore the range of applied magnetic field values that they remain stable for. These studies will be undertaken with MFM and NV magnetometry, as 90 nm produces a stray field that does not saturate either probe. Further films of different thicknesses will also be grown, allowing for a study to be conducted on the thicknesses influence on skyrmion formation and stability within the sample.

References

[1] T. H. R. Skyrme, A unified field theory of mesons and baryons, Nuclear Physics 31, 556–569 (1962)

[2] S. S. P. Parkin, H. Masamitsu, L. Thomas, Magnetic Domain-Wall Racetrack Memory, Science, 320, 190 (2008)

[3] S. Wang, Q. Zeng, D. Liu, H. Zhang, L. Ma, et al. Giant Topological Hall Effect and Superstable Spontaneous Skyrmions below 330 K in a Centrosymmetric Complex Noncollinear Ferromagnet $NdMn_2Ge_2$, ACS Applied Material Interfaces, 12, 24125 (2020)

[4] X. Zheng, X. Zhao, J. Qi, X. Luo, S. Ma, et al., Giant topological hall effect around room temperature in noncollinear ferromagnet $NdMn_2Ge_2$ single crystal, Applied Physics Letters 118, 072402 (2021)

[5] Z. Hou, L. Li, C. Liu, X. Gao, Z. Ma, et al. Emergence of room temperature stable skyrmionic bubbles in the rare earth based $REMn_2Ge_2$ (RE = Ce, Pr, and Nd) magnets, Materials Today Physics, 17, 100341 (2021)

Experimental demonstration of an ion-nanooscillator hybrid system

Project P1808: Quantum dynamics of an ultracold ion coupled to an nanomechanical oscillator
Project Leader: S. Willitsch and M. Poggio
Collaborator: M. Weegen (SNI PhD Student)

Introduction

Ultracold trapped ions in radiofrequency traps are well-established and highly controllable quantum systems with a variety of applications in fields such as precision spectroscopy, cold chemistry, clocks and quantum technologies [1]. Nanomechanical oscillators are highly sensitive force transducers representing an attractive choice for the development and implementation of hybrid quantum systems [2]. Their nanoscopic size makes them excellent candidates for the study of physics on the border of classical and quantum physics in miniaturized devices.

The goal of the present project is the realization of an ion-nanowire hybrid system to explore new methods of quantum state engineering and readout via the mutual electrostatic interaction of its constituents. For this purpose, a charged Ag_2Ga nanowire is positioned in close proximity to trapped ions. By mechanically driving the nanowire around a mechanical resonance matched to the frequency of an oscillation of the ions in the trap, the nanowire vibrations couple to the motions of the ions. Previous theoretical modelling of the ion-nanowire interaction has shown a motional excitation of the ions by the mechanical drive of the nanowire in the classical regime, as well as the generation of highly excited coherent states and other exotic quantum states in a quantum-mechanical treatment of the ion motion [3].

Here, we report the successful experimental demonstration of such an ion-nanowire hybrid system [4]. We showed the resonant drive of trapped ions by the mechanical oscillations of the nanowire and characterized the strength of the coupling for a variety of salient experimental parameters.

Experimental Setup

The core of the experiment is the combination of a miniaturized linear radiofrequency wafer ion trap with a conductive Ag_2Ga nanowire (Fig. 1). The nanowire was positioned on the tip of a metallic tungsten holder and could be translated in all spatial directions with nanopositioners. Oscillations of the nanowire were driven with a piezo actuator mounted to the holder. The 397 nm fluorescence of trapped laser-cooled Ca^+ ions was split by a 50:50 beam splitter and guided onto an EMCCD camera as well as a photomultiplier tube (PMT) (Fig. 1a). The camera was used for spatial imaging of the trapped ions (Fig. 1b) while the PMT enabled a time-resolved determination of the ion fluorescence rate using a photon-correlation method (see below). A dual-element photodiode was used for the optomechanical readout of the nanowire resonance spectrum.

Photon-Correlation Method

A key element for the success of the present experiments was the implementation of a highly sensitive photon-correlation method to detect periodically driven motion of the trapped ions [5]. The underlying principle is the time-resolved measurement of the ion fluorescence exhibiting modulations due to a periodic Doppler shift with respect to the cooling lasers experienced during a driven motion. The fluorescence of the ions collected on a PMT was correlated with the drive frequency fdrive applied to the nanowire. Figure 2 shows the time-resolved fluorescence for a) a strong and b) a weak drive.

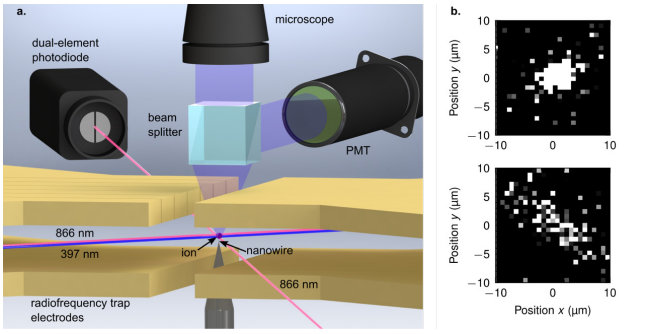

Fig. 1: a) Schematic of the experimental setup. The charged nanowire is positioned in close proximity to the trap center for strong coupling to trapped ions. The nanowire resonances are measured with a dual-element photodiode. The ion fluorescence is collected on an EMCCD camera (microscope) and PMT. b) EMCCD camera image of an ion at rest (top) and motionally excited by the mechanical drive of the nanowire (bottom).

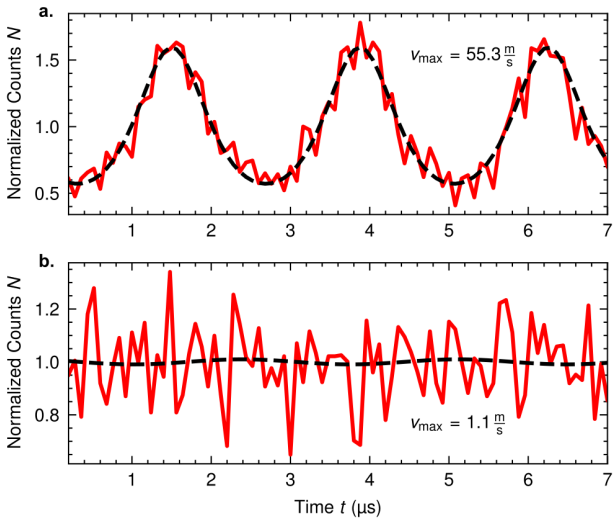

Fig. 2: a) Photon-correlation measurement for a strongly driven ion. The ion fluorescence as a function of time shows a clear periodic behavior. b) Time-resolved fluorescence trace for a weakly driven ion.

Ion-Nanowire Coupling

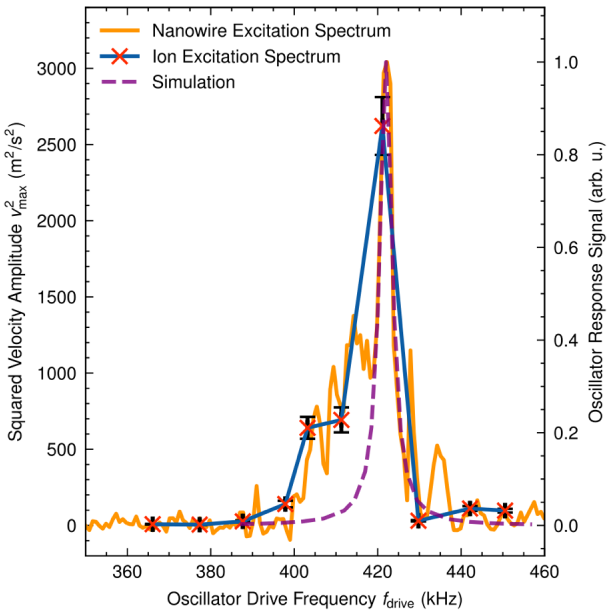

Fig. 3: Squared maximum velocities of the motion of trapped ions driven by the nanowire for different drive frequencies f_{drive}. The motional excitation of the ions (red crosses) shows a clear correlation with the mechanical excitation spectrum of the nanowire (orange trace), indicating the mechanical nature of the drive. Theoretical simulations (purple trace) confirm the mechanical motional excitation of the ions around the main resonance at 422 kHz.

We have applied this photon-correlation method to study the frequency dependence of the motional excitation of the ion by the mechanical drive of the nanowire. In these experiments, the frequency of the piezo drive applied to the nanooscillator was scanned across a mechanical resonance while the motional excitation of the ion was simultaneously measured. Figure 3 shows the ion velocity amplitudes obtained for different nanowire drive frequencies around a mechanical resonance at 422 kHz of the nanooscillator. A clear correlation between the nanowire mechanical excitation and the drive of the ion motion can be observed, demonstrating the mechanical nature of the ion excitation.

The strength of the motional excitation of the ion was mainly governed by three parameters: the amplitude of the nanowire drive, the ion-nanowire distance and the electric potential applied to the nanowire. Figures 4a-c show the velocity amplitudes of the driven ion motion as a function of these coupling parameters. Figure 4d shows the velocity amplitudes for varying ion numbers ranging from 1 to 4 ions.

Conclusions & Outlook

We have demonstrated the successful coupling of trapped ions to a charged nanowire, thus realizing a novel hybrid system. Our data reveals the mechanical drive of ion motion by the nanowire and its dependence on salient experimental parameters. The present results lay the foundations for manipulating the ion motion in the quantum regime as a means to engineer, inter alia, exotic motional quantum states for applications in the quantum sciences [3].

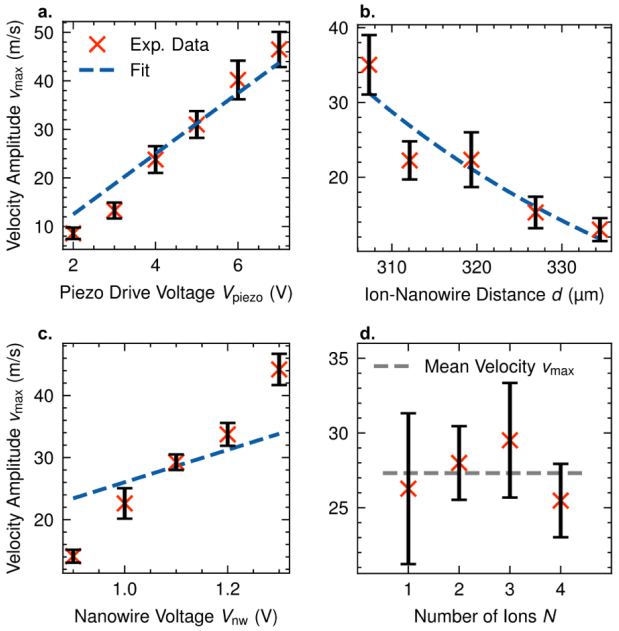

Fig. 4: a-c) Velocity amplitudes of the mechanically driven ions as a function of different coupling parameters. The obtained experimental trends correspond to the expectations and are confirmed by a fit to a theoretical model (dashed lines [3]). d) The mechanical drive of the ions is independent of their number.

References

[1] S. Willitsch, Coulomb-crystallised molecular ions in traps: methods, applications, prospects, Int. Rev. Phys. Chem. 31, 175 (2012)

[2] P. Treutlein, C. Genes, K. Hammerer, M. Poggio, P. Rabl, Hybrid Mechanical Systems, Springer (2014)

[3] P. N. Fountas, M. Poggio, S. Willitsch, Classical and quantum dynamics of a trapped ion coupled to a charged nanowire, New J. Phys. 21, 013030 (2019)

[4] M. Weegen, M. Poggio and S. Willitsch, Coupling trapped ions to a nanomechanical oscillator, arXiv-Preprint 2312.00576 (2023)

[5] D. J. Berkeland, J. D. Miller, J. C. Bergquist, W. M. Itano, D. J. Wineland, Minimization of ion micromotion in a Paul trap, J. Appl. Phys. 83, 5025 (1998)

Studying amyloid processing in single cells and brain homogenate

Project P1901: Microfluidics to Study Huntington's Disease by Visual Proteomics
Project Leader: T. Braun and E. Pecho-Vrieseling
Collaborator: A. Fränkl (SNI PhD Student), A. E. Schneider

Introduction
Maintaining proper protein balance in post-mitotic neurons is vital. Aging is the leading risk factor for spontaneous neurodegenerative diseases, and a loss of protein homeostasis and mitochondrial dysfunction are two hallmarks of aging. The impairment of proteostasis dynamics reduces the cell's ability to clear misfolded proteins, and the likelihood of α-syn misfolding increases. Unfortunately, cells appear poorly adapted for chronic proteotoxic stress, and misfolded amyloids accumulate. Potentially, this is an initial step in the pathomechanisms of the degeneration. Once misfolded, α-syn can recruit other α-syn-molecules, and the fatal cascade of the prion-like spreading starts.

It is unclear if the accumulation of lewy bodies (LBs) or glial cytoplasmic inclusions (GCIs) leads to neuronal cell death or is a rescue operation of an overwhelmed cell by disposing proteotoxic, misfolded amyloid proteins. Recently, a potential link between amyloid accumulation and cell death was reported for Alzheimer's disease (AD) [1], and a similar mechanism may play a role in synucleinopathies.

Here, we aim to develop methods for the single-cell analysis of the (i) prion-like infection of healthy cells and (ii) the fate of the infecting amyloid nanoparticles in cells and brain homogeneity of diseased patients. We use fluorescent labeled α-syn fibril-fragments for our cellular experiments to "infect" human, neuron-like SH-SY5Y cells. This allows the correlative analysis by fluorescent light and electron microscopy.

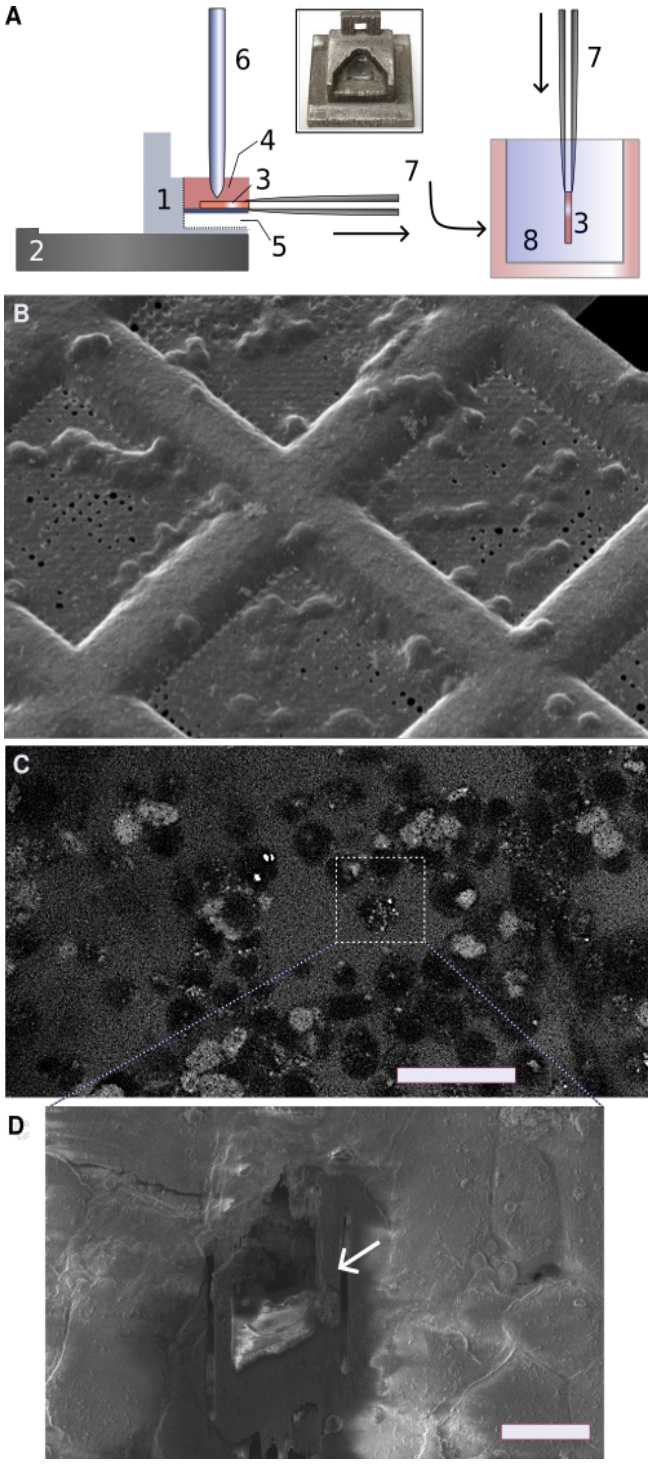

Fig. 1: Whole-cell vitrification using the cryoWriter system. The cells are grown on cryo electron microscope (cryo-EM) grids and infected with fluorescence-labeled α-syn nanoparticles derived from fibrils. A) We use a 3D-printed (inset) cell growth platform (1), which is placed on a temperature-controlled stage (2) before sample preparation. Cells grow on a grid (3) in cell culture media (4). The grid is placed on a thin PDMS support layer above a small pressurized chamber (5). The surplus liquid is removed with the cryoWriter's nozzle under a controlled atmosphere (not shown). Subsequently, the robot withdraws the tweezer with the EM-grid, flips it down, and plunges the sample into a bath of liquid ethane (8) for vitrification. B) Vitrified SH-SY5Y on a cryo-EM grid visualized in the scanning electron microscope (SEM). C) Vitrified SH-SY5Y-cells in the fluorescence light-microscope for target selection before FIB milling of a lamella. D) Lamella after FIB milling. The lamella (indicated by an arrow) will now be analyzed by cryo-EM tomography.

Blotting-free whole-cell vitrification of amyloid-infected cells

We developed a platform for the growth of adherent eukaryotic cells on cryo-EM grids, which can be directly mounted on the cryoWriter [2] for subsequent blotting-free vitrification (Fig. 1). We expect that this method is less stressful for cellular structures than the classical sample preparation. Furthermore, the platform allows a correlative analysis of the cell by fluorescence microscopy before and after vitrification.

The fluorescence label of the α-syn seeds helps target the "infected" cells and find the location for Focused Ion Beam Scanning Electron Microscopy (FIB-SEM) for milling thin lamellas (Fig. 2). These lamellae are now investigated by correlative light and electro-tomography.

Cells were grown on conducting slides in miniaturized cell culture plates, seeded with fluorescently labeled α-syn fibril fragments, and incubated and washed for a specified period. "Infected" cells, detected by the fluorescence signal, were lysed by electroporation, and cryo-EM grids were prepared. The latter is only possible using a new cryoWriter module for the spraying surface effector molecules [3].

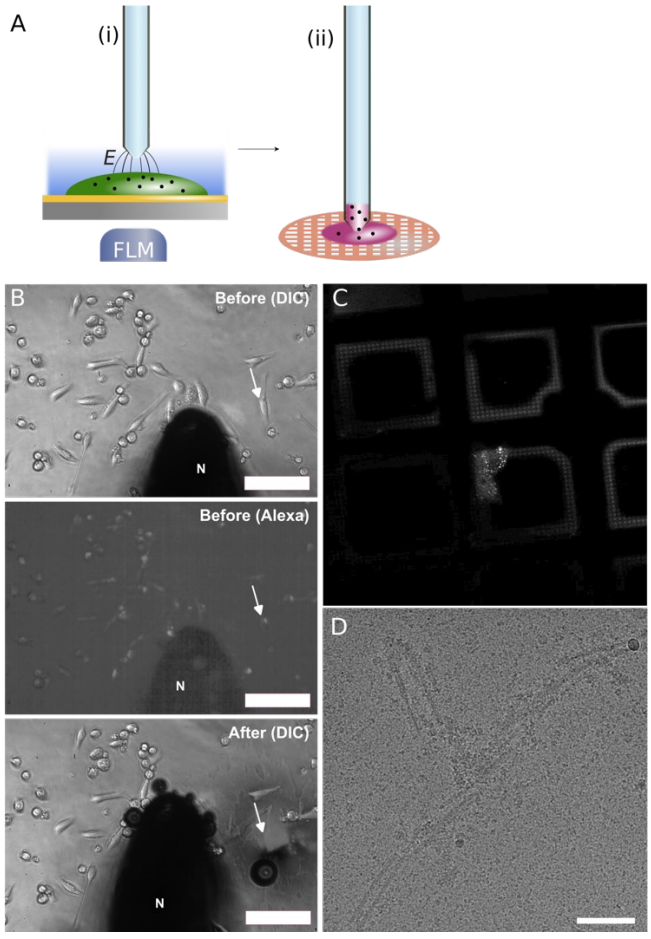

Fig. 2: Single-cell lysis and cryo-EM of α-syn fibrils [2, 3]. A) targeting and electroporation of a selected cell. The process is monitored by fluorescence light microscopy (FLM). B) Selection and monitoring of cell lysis. C) Fluorescence microscopy of vitrified single-cell lysate. The fluorescence signal shows that labeled α-syn fibrils were prepared. D) cryo-EM image of an extracted fibril.

Our results show that the host cell processes the fibril fragments. We suspect that the proteasome ubiquitin system modifies the α-syn particles. However, the average fibril length does not change.

Microfluidic biochemistry screening platform

To investigate the fibrils' processing further, we immobilized synthetic fibrils in the microfluidic system and performed a nano incubation with (i) cell lysate and (ii) brain homogenate of diseased patients. Photoelution of the fibrils allows the investigation of the effects of EM. Initial results show that patients' brain homogenate indeed modifies the fibril appearance (data not shown).

References

[1] S. Balusu, K. Horré, N. Thrupp, K. Craessaerts, A. Snellinx, L. Serneels et al. MEG3 Activates Necroptosis in Human Neuron Xenografts Modeling Alzheimer's Disease. Science 381(6663) (2023)

[2] S. A. Arnold, S. Albiez, A. Bieri, A. Syntychaki, R. Adaixo et al. Blotting-free and lossless cryo-electron microscopy grid preparation from nanoliter-sized protein samples and single-cell extracts, J. Struct. Biol. 197 (3) (2017)

[3] L. Rima, M. Zimmermann, A. Fränkl, T. Clairfeuille, M. Lauer et al. cryoWriter: a blotting free cryo-EM preparation system with a climate jet and cover-slip injector. Faraday Discussions 240, (2022)

3D-Bioprinting of cardiac tissue models with a novel cost-effective and versatile bioink

Project P1902: Directional 3D nanofiber network to mimic in-vivo myocardial syncytium towards guiding contraction patterns in in-vitro heart models
Project Leader: M. Gullo, M. Poggio and A. Marsano
Collaborator: F. Züger (SNI PhD Student)

Introduction
In cardiac tissue engineering, the urge for novel biofabrication methods is high since myocardial infarction is one of the most common causes of hospitalization and death in the world [1]. An impairment of heart functionality, after a myocardial infarction combined with a low intrinsic regenerative capability of cardiomyocytes (CMs) leads to a loss of cardiac tissue. This loss needs to be replaced with tissue that mimics and replicates natural tissue and its environment to achieve physiologically relevant conditions (Fig. 1) [2,3].

In order to improve our dual-scale approach, where 3D-printed micrometer scale and electrospun nanometer scale structures are combined, the formulation and refinement of our bioink was pushed further [4]. A bioink for tissue regeneration relies on, among other things, hydrogels with favorable rheological properties. These include shear thinning for cell friendly extrusion, post-printing structural stability as well as physiologically relevant elastic moduli needed for optimal cell attachment, proliferation, differentiation, and tissue maturation.

Therefore, the newly formulated bioink based on a novel cost-efficient gelatin-methylcellulose hydrogel, showed promising results in cardiac tissue biofabrication. Its rheological properties were optimized for ideal printability and cardiac tissue culture consisting of neonatal rat cardiomyocytes and fibroblasts (NRCM, NRFB). Moreover, due to its adjustable stiffness, it might be used for other cell types as well. After continuous optimization of the tissue engineering process (bioink production, 3D-printing process, and cell culture conditions) long-term cell culture experiments (21 d) were successfully conducted, assessing cell viability, and beating behavior at several timepoints.

Fabrication of Cardiac Constructs
The bioink, consisting of a blend of gelatine and methylcellulose (GMC) was freshly prepared, loaded with cardiac cells (>4 mio/mL) and subsequently 3D-bioprinted (70-100 kPa flow rate, 12 mm/s print speed; RegenHU Switzerland) into a predefined multi-layered construct, with the following dimensions: a 10 x 10 mm square, with 1 - 1.5 mm spacing and a strand size of 300 - 400 µm (Fig. 2A/B). A crosslinking solution composed of transglutaminase (TG; 120 mg/mL) was poured over the printed construct and incubated for 5 - 10 min. After this shape stabilization process the constructs were washed in PBS, submerged in full NRCM medium, and incubated for up to 21 d. Every 48-72 h the medium was changed and a life/dead assay at several timepoints was conducted, using a Propidium Iodide (PI)/Hoechst staining. Thereafter for each time point the viability was evaluated by fluorescence microscopy and ImageJ analysis. After 7 d in culture, cardiac tissue construct started to beat (Fig. 2C).

After the successful culture of two-layer high constructs, with >80% viability for up to 21 d post-print, the whole process of bioink formulation, cell cultivation and 3D-bioprinting was optimized to print higher constructs, consisting of

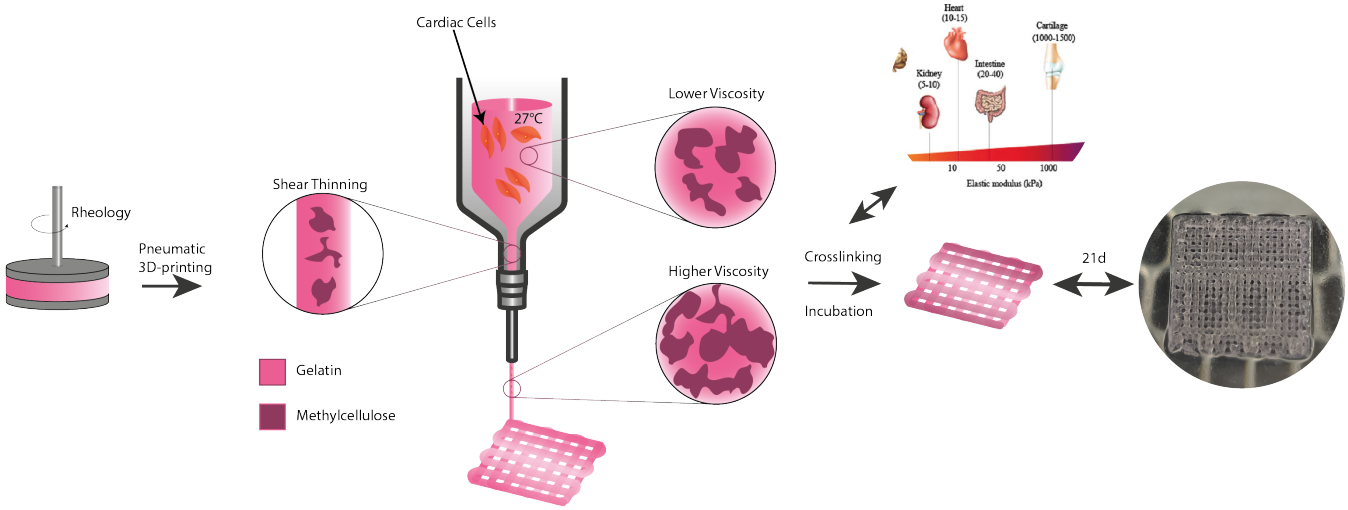

Fig. 1: Schematic representation of a typical workflow of a bioink formulation process for further utilization in long term 3D-printed cardiac cell culture experiments. Printed construct can be used in the dual-scale approach, combining nanoscale and microscale structures to resemble natural cardiac tissue closer.

up to 5 layers in z-direction. First results of bigger constructs indicate that cell extrusion and structural stability of the hydrogel remain in physiological favourable regimes, without affecting the cell survival, yielding a cardiac cell viability of > 80% after 21 d in culture. Further experimental data is currently being collected. Constructs with up to 10 layers, could be achieved and have been assessed. Further process optimization to increase satisfactory cell viability in such big constructs is currently being investigated.

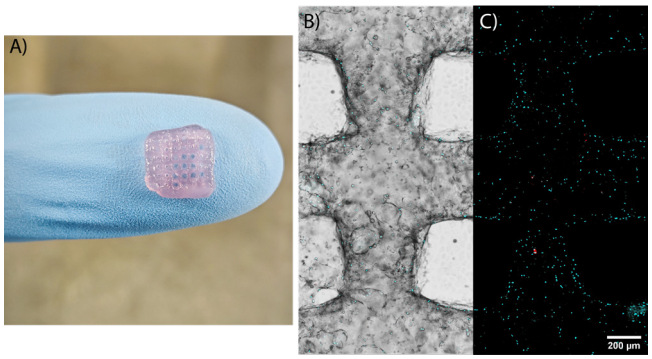

Fig. 2: A) Photograph of a 3D-bioprinted construct 21 days post-printing and incubation at 37°C, bioink contains cardiac cells (4 mio/mL), construct dimensions: 10x10 mm and 10 layers; (B&C) Fluorescence microscopy image of 21 d post-print construct stained with Hoechst 33342 (blue) and PI (red), stacking of brightfield (BF, only in B), Hoechst and PI channel (in C), scale bar = 200 µm.

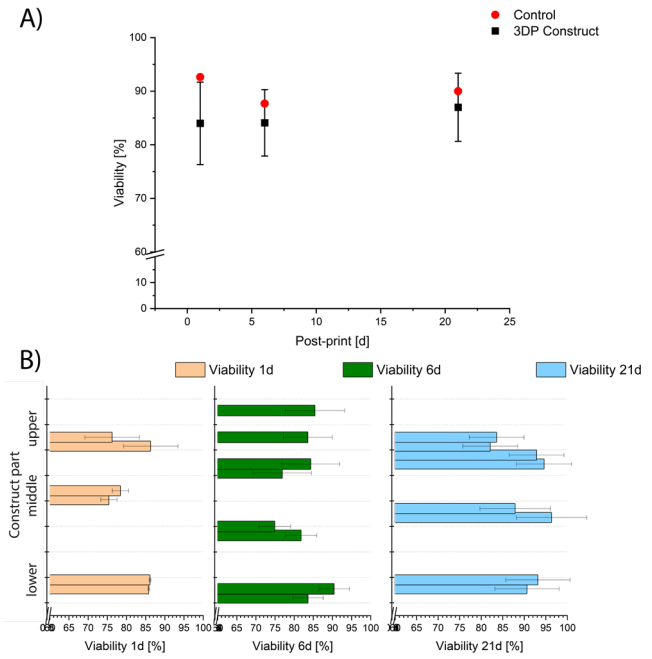

Fig. 3: A) Graphical illustration of NRCM cell viability in a two-layered 3D-printed construct at day 1, 7, 21 post-printing. Cell viability for 1 d= 84% ± 7.7, for 7 d= 84.2% ± 6.2 and for 21 d= 87.5% ± 6.4. Controls are slightly higher for all days, indicated by red dots. B) Graphical illustration of NRCM cell viability split into z-localization (upper, middle, lower part) of the printed construct. No significant decrease of cell viability in the center of the construct, referring to proximity to media source.

Analysis of Cardiac Constructs

At several timepoints of the cell culture (1 h, 7 d, 14 d and 21 d) the 3D-printed constructs were stained and the viability of the cells within the construct was assessed. Therefore, the constructs were washed, stained with PI and Hoechst 33342 for 30 min and washed again before imaging on a confocal fluorescence microscope. Single images as well as z-stacks were taken throughout the whole construct height. Subsequently, the images were analyzed with ImageJ, where the number of viable cells and the number of dead cells was determined. Two-layered constructs showed cell viabilities of more than 80%, for up to 21 d post-print (Fig. 3A). The viability of cells throughout the z-axis of the construct was in every region above 80%, leading to the assumption that all cells within the construct were close enough to cell culture media (Fig. 3B). This could arise from the design and the advantage of the 3D-printed construct compared to otherwise engineered cardiac tissue.

Spontaneous beating of NRCMs could be observed, after 7 d post-print until up to 5 weeks in culture.

Outlook

The ability to design and biofabricate a micrometer scale construct with the formulated bioink and high viability, paves the way to implement it into a dual-scale construct, together with electrospun nanometer scale conductive fibers (previously described). Combining these two structures could yield electrophysiological conditions and mimic human cardiac tissue and its cell environment [5]. Therefore, aligned electrospun nanofibers will be layered between 3D-bioprinted constructs and its viability, contraction and maturation will be assessed as next step. Furthermore, using a cell culture pacing system, higher cell maturation might be achieved, which in turn would lead to even closer cardiac tissue substitutes.

References

[1] J. Gopinathan, I. Noh, Recent trends in bioinks for 3D printing, Biomater Res. 22, 11 (2018)

[2] N. Freemantle, J. Cleland, P. Young, J. Mason, J. Harrison, Beta Blockade after myocardial infarction: systematic review and meta regression analysis. BMJ 318, 1730–1737 (1999)

[3] F. Züger, A. Marsano, M. Poggio, M. R. Gullo, Nanocomposites in 3D Bioprinting for Engineering Conductive and Stimuli-Responsive Constructs Mimicking Electrically Sensitive Tissue. Advanced NanoBiomed Research 2, 2100108 (2022)

[4] F. Züger, N. Berner, M. R. Gullo, Towards a Novel Cost-Effective and Versatile Bioink for 3D-Bioprinting in Tissue Engineering. Biomimetics 8, 27 (2023)

[5] D. Baruffaldi, G. Palmara, C. Pirri, F. Frascella, 3D Cell Culture: Recent Development in Materials with Tunable Stiffness. ACS Appl. Bio Mater. 4, 2233–2250 (2021)

Integration of neutron nanomediators in fuel cells

Project P1903: Neutron nanomediators for non-invasive temperature mapping of fuel cells
Project Leader: M. Kenzelmann and P. Boillat
Collaborator: A. Ruffo (SNI PhD Student)

Introduction
In this project, we integrate magnetic particles into fuel cell porous media called gas diffusion layers (GDLs) in order to measure the spatial temperature variation in-situ. The general measurement concept is to use the depolarization of a neutron beam as a measurement of the particle's magnetic saturation, which is temperature dependent. In previous work, we characterized how different materials and particle sizes impact the neutron beam depolarization and its temperature dependence. Here, we demonstrate how such particles can be introduced in a real fuel cell structure to conduct in-situ measurements.

a)

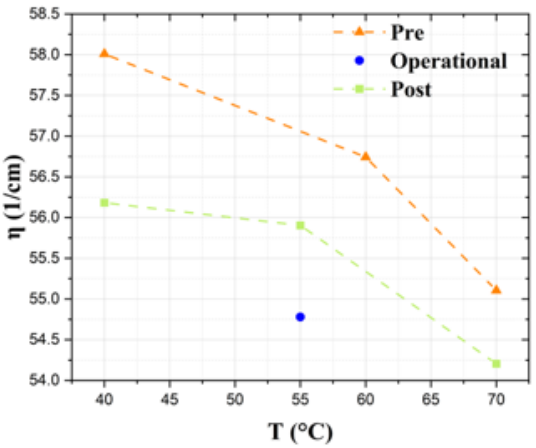

b)

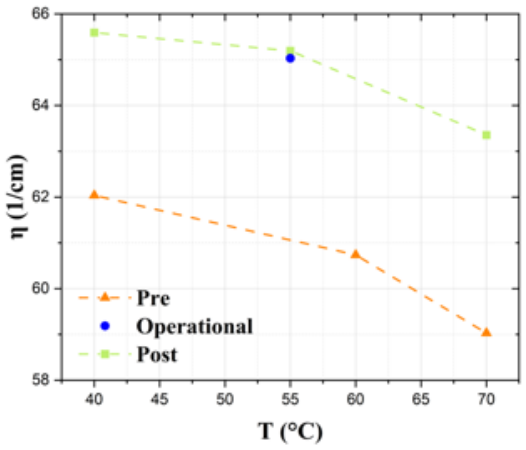

Fig. 1: Depolarization coefficients of samples taken from the a) anode and b) cathode at various stages of the operation. The data is segmented into three distinct periods: before operation, during operation, and after operation.

Measurement of the temperature in a fuel cell structure
To conduct the measurements, we included micrometric size magnetic particles. These particles were synthesized by ball milling from a coarser NdFeB powder. The milled powder is denominated NdFeB-415 based on the parameters used for the milling (4 hours, 15g of balls). The particles were integrated into the fuel cell GDLs by spray coating them together with a PTFE powder dispersion used as a hydrophobic treatment for the material. In order to be able to work with a neutron imaging setup with a limited resolution (aprox. 200 µm), we used a thicker porous layer than is usual fuel cell structures by stacking 5 GDL pieces on each side of the fuel cell.

As seen in figure 1, the impact of artificially imposed temperature variation could be observed in the real fuel cell structure, both before and after operation. Meaning that the mediators are functional even after being exposed to the fuel cell operating conditions. A measurement during operation shows a deviation from the measurement at the same temperature which could be indicative of a temperature elevation to cell operation. However, it is not fully clear whether this difference is outside the measurement margin of error.

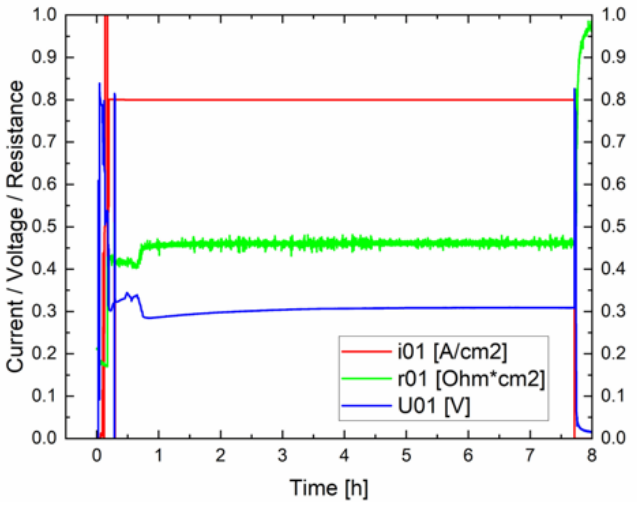

Fig. 2: Outcomes of an operating fuel cell containing a stack of GDLs coated with NdFeB-415, capturing three main parameters over a 7-hour operation period: the selected current density (red), the high-frequency resistance (green), and the cell voltage (blue).

Stability of cell operation
A potential concern with the proposed approach is whether part of the NdFeB particles could leach and poison either the catalyst or the membrane of the fuel cell. In the present study, the cell was operated for approximately eight hours at

a temperature of 55°C. As seen in figure 2, the stability of the cell high frequency resistance (indicative of the membrane conductivity) indicates that these is no significant poisoning of the membrane. If it would occur, catalyst poisoning would be evidenced as a decrease of voltage over time. As the voltage is stable (the slight increase is commonly observed in fuel cell testing and is attributed to catalyst surface change during fuel cell operation), we conclude that there is no indication of catalyst poisoning.

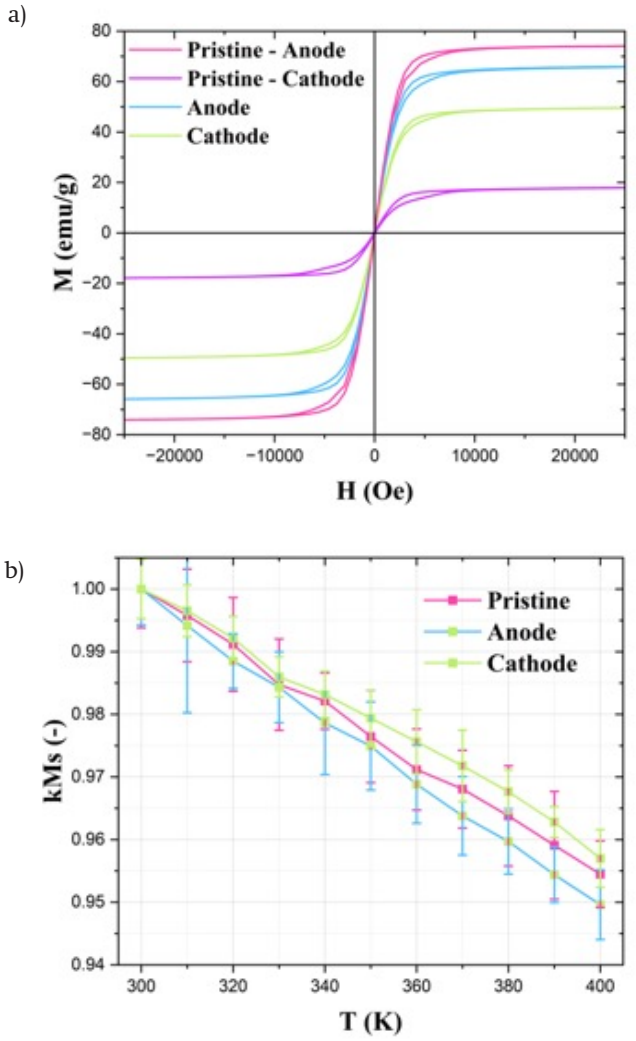

Fig. 3: a) Magnetic hysteresis loops of various samples: the pristine sample designated for the anode side (in pink), the pristine sample for the cathode side (in violet), and samples after operation in both the anode (in blue) and cathode (in green) sections. b) Relative magnetic saturation variation of the pristine (pink), anode (blue), and cathode (green) samples over a temperature range extending from 300 K to 400 K.

Stability of mediators

Besides the potential damage to the fuel cell, a further concern was the possible degradation of the mediator particles following their exposure to the fuel cell operating conditions. To assess this, magnetometer and EDX measurements were conducted on pristine samples and on samples having been used for the fuel cell anode and cathode. For figure 3a, we can see that the estimated magnetic saturation is reduced for the samples used after operation when compared to one of the pristine samples. However, a second pristine sample shows an even lower saturation, which means that the differences are possibly related to the uncertainties in the coating process by hand spraying, resulting in imprecisions in the amount of coated material. In figure 3b, we can see the relative saturation as a function of temperature. Because this value is normalized to the saturation at 30°C, the effect of the imprecisions in the amount of coated material is compensated. In this case, the temperature dependence is the same for the materials before and after exposure to fuel cell conditions. This indicates that the use of the particles in fuel cell does not significantly alter their composition, at least not in a way affecting their function as temperature sensors. This is consistent with the neutron depolarization measurements presented in figure 1.

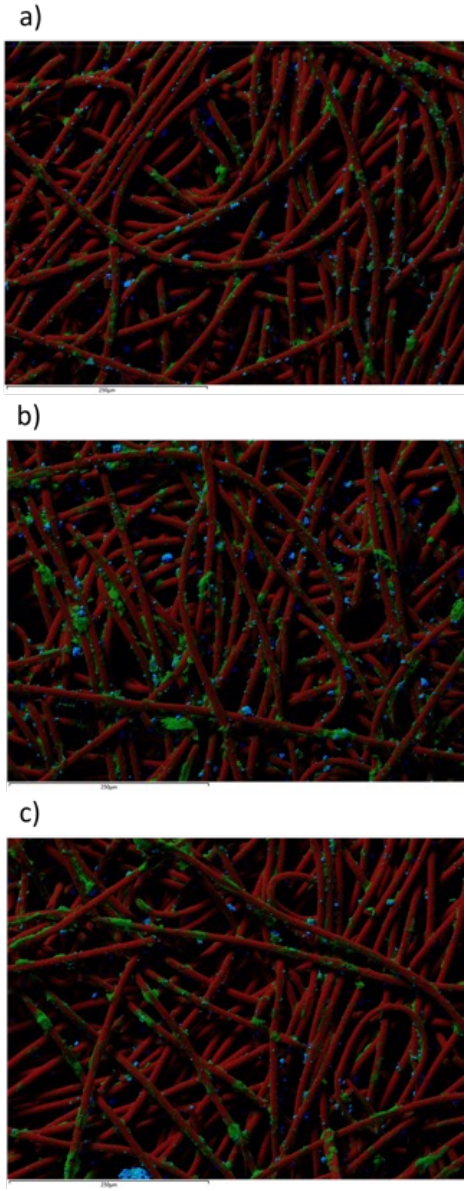

Fig. 4: EDX results of a) pristine, b) used in the anode, and c) used in the cathode samples, with elemental mapping shown in distinct colors: iron (dark blue), oxygen (light blue), neodymium (yellow), carbon (red), and fluorine (green).

The SEM-EDX results presented in figure 4 also show no significant qualitative differences between the pristine and used GDLs. In conclusion the results show that the Nd-FeB-415 powder used in this study can effectively be integrated in fuel cells without resulting in poisoning or being degraded by operation.

Tracing molecular reactions with XFELs

Project P1904: Revealing protein binding dynamics using time-resolved diffraction experiments at SwissFEL
Project Leader: C. Padeste and T. Ward
Collaborators: M. Carrillo (SNI PhD Student), D. Chen, Y. Hua, T. Weinert, J. Beale

Time-resolved serial protein crystallography is an emerging method to elucidate molecular reactions with high temporal and spatial resolution. Here we report on our developments of fixed-targets for serial crystallography at the Swiss Free Electron Laser (SwissFEL), to trace light-induced reactions such as binding of photocaged biotin to streptavidin after laser-induced uncaging.

Serial protein crystallography at X-ray Free Electron Lasers (XFELs)

X-ray Free Electron Lasers (XFELs) represent a groundbreaking technology in the realm of scientific research, particularly in the field of structural biology. They are advanced light sources generating high intensity, coherent, femtosecond x-ray pulses that allow for studying materials at an atomic and molecular level with sub-millisecond time resolution [1]. This results in the ability to determine structures and structural changes of biological macromolecules, such as proteins and viruses using crystallographic approaches. Due to the XFEL's high-intensity x-ray pulses, crystals undergo radiation damage after exposure to the x-ray. However, due to the short duration of the x-ray pulses, scientists are able to record diffraction patterns before the onset of radiation damage of the single crystal. To collect a full data set, a method called serial crystallography (SX) was developed, in which series of fresh crystals are sequentially exposed to the x-ray. Time-resolved serial crystallography (TR-SX) provides the ability to observe dynamic processes at the atomic level. By initiating a reaction within a crystal and capturing X-ray diffraction images at different time points, researchers can create a molecular movie that illustrates the structural changes occurring during a chemical or biological event. This capability provides invaluable insights into the fundamental mechanisms governing various processes, from enzyme catalysis to the dynamics of light-sensitive proteins.

SwissFEL, Switzerland's XFEL, was built in 2016 and since then has been a state-of-the-art facility. One of its newest constructed experimental stations, CristallinaMX, focuses on serial protein crystallography through fixed-target sample delivery method.

Fixed-Targets for Pump-Probe Studies

Fixed-targets are used as a sample delivery method for serial crystallography, which enables two types of data-collection, one of which is the aperture aligned method [2]. An aperture aligned polymer-based fixed-target called the Micro-Structured Polymer chip (MISP-chip; Fig. 1a)[3] was recently developed at the Paul Scherrer Institute (PSI) and is implemented as the designated sample delivery method for CristallinaMX at SwissFEL. The MISP-chip contains fiducials in each corner (Fig. 1c) to help aligning the chip to the laser and x-ray beam. The central membrane is composed of inverted pyramidal cavities (Fig. 1c) with cavity sizes of 100 µm and aperture sizes of 5 - 7 µm. These cavities serve to extract the excess mother liquor of the crystallization solution from the chip but also to funnel the crystals to single cavities. Once the crystals are centered inside the cavities, their location is known.

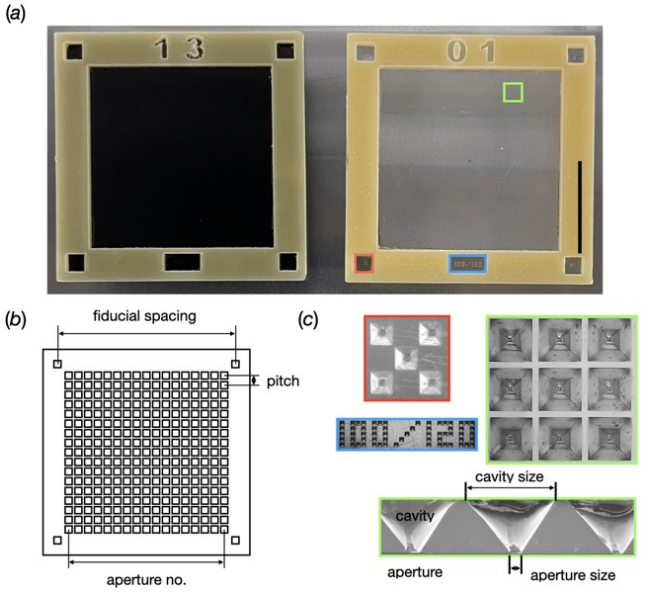

Fig. 1: a) The two current versions of the MISP-chip with black COC and transparent COP membrane. Scalebar represents 10 mm. b) Parameters used to identify the location of crystals. c) Magnified fiducials (red), membrane cavities (green), membrane labeling system (blue).

One of the frequently performed experimental techniques at XFEL facilities is pump-probe crystallography. This method involves two laser pulses: an optical "pump" pulse that initiates a rapid change in the sample (such as a photocaged ligand cleaving before binding onto the protein, or a conformation change in a photodynamic protein), and an x-ray "probe" pulse that measures the structural response with X-ray diffraction. Pump-probe experiments have allowed to study photodynamically controlled events within crystals by precisely controlling the timing between the pump and probe pulses. This allows for researchers to create a temporal sequence of snapshots that reveal the progression of a process with femtosecond to picosecond time resolution. CristallinaMX has been designed to enable pump-probe experiments (Fig. 2). However, a challenge arises concerning the prevention of light contamination between cavities to avoid premature initiation of light-triggering processes given that the original MISP-chips were transparent.

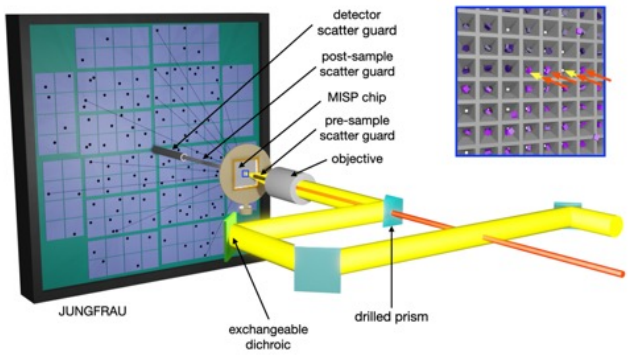

Fig. 2: Schematic of the pump-probe experimental set-up at Cristallina, SwissFEL. The pump laser (yellow) is coupled to the sample position via the endstation OAV. An exchange dichroic mirror (light green) enables different pump wavelengths to be reflected whilst transmitting light for the chip alignment. The X-rays pass through the center of the drilled objective and prism of the final part of the laser coupling. Air scatter from the X-ray is minimized using pre-and post-sample scatter-guards. The blue box highlights an area of the chip showing a 50:50 interleaved light:dark scheme, where X-rays are delivered to every well and laser pump only to every other.

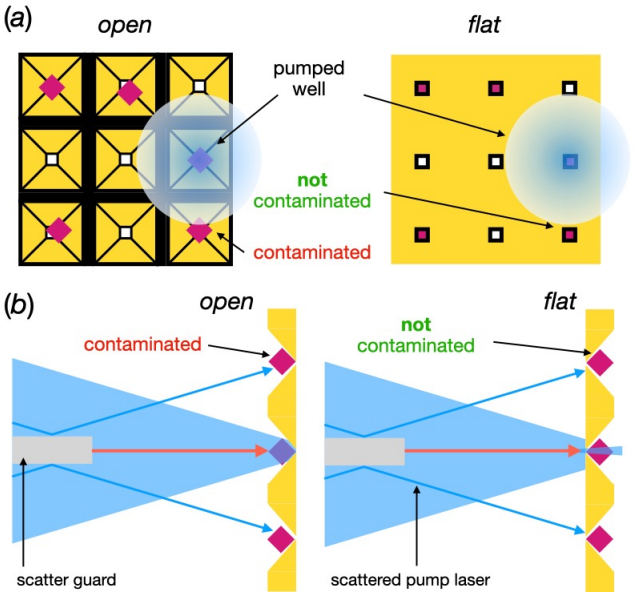

Fig. 3: Schematic of black COC MISP-chip for pump-probe experimental set-up at Cristallina, a) Schematic of the X-ray/pump laser view of the chip in the open and flat orientation. In the open view, the entire crystal is visible, enabling contamination via a large laser profile. The same large laser profile in the flat orientation does not give rise to contamination due to the restricted view of the crystals. b) A schematic showing how potential scattered pump laser from the pre-sample scatter guard could give rise to light contamination. Again, restricted view of the crystals in the flat orientation prevents contamination of crystals in adjacent well.

To resolve this issue a carbon-black COC membrane was developed at PSI to create the black MISP-chip (Fig. 1a) allowing for the laser light to be absorbed between cavities, avoiding light contamination to occur between cavities. Tests were conducted to assess the contamination rate of the black COC MISP-chips, examining both the open and flat sides of the chip. The findings revealed that the chip's orientation is crucial in preventing light contamination. Exposure to light from the open side (Fig. 3) resulted in neighboring wells being affected by light contamination. Conversely, when the chip was flipped to the flat side, no instances of light contamination were observed between neighboring crystals (Fig. 3).

Binding of Streptavidin – Photocaged Biotin

The ability to conduct TR-SX at CristallinaMX with the black COC MISP-chips creates numerous possibilities for studying photodynamic molecular processes, one of which is capturing the binding of biotin into the binding pockets of streptavidin. Streptavidin is a tetrameric β-barrel protein, derived from the bacterium Streptomyces avidinii, with a remarkably high binding affinity for biotin. Linking a specific coumarin derivative to biotin yields a photolabile protective group (photocage) that can be selectively removed upon exposure to 397 nm light (Fig. 4b). This process when initiated with a short light pulse, results in the controlled release of biotin, allowing for TR-SX experiments.

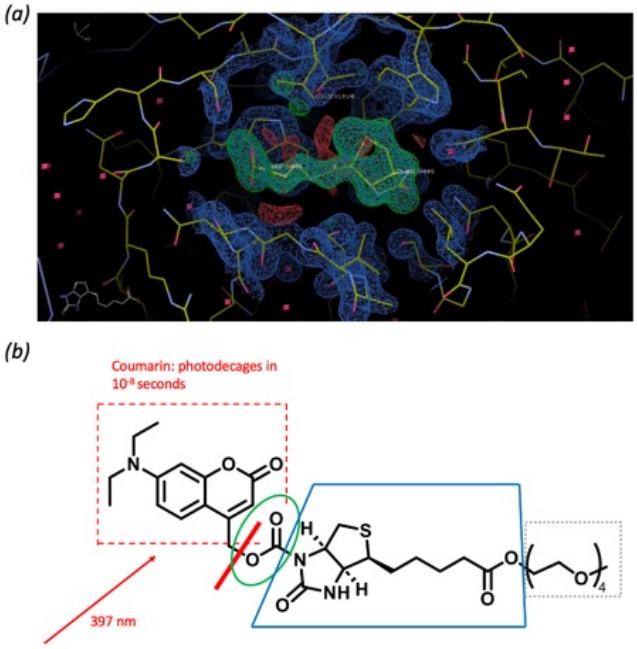

Fig. 4: a) XFEL room temperature structure determination (Fobs – Fobs) of biotin (green electron density) inside the binding pocket of streptavidin (blue electron density) after soaking biotin into streptavidin crystals. b) Photocaged biotin used for TR-SX at CristallinaMX. Biotin is highlighted in blue, the photocaged coumarin is highlighted in red, cleaving off with 397 nm.

References

[1] H. N. Chapman, P. Fromme, A. Barty, T. A. White, R. A. Kirian et al., Femtosecond X-ray protein nanocrystallography, Nature, 73, 470 (2011)

[3] S. Oghbaey, A. Sarracini, H. M. Ginn, O. Pare-Labrosse, A. Kuo et al., Fixed target combined with spectral mapping: approaching 100% hit rates for serial crystallography, Acta Crystallogr D Struct. Biol., 72, 8, (2016)

[4] M. Carrillo, T. J. Mason, A. Karpik, I. Martiel, M. W. Kepa, et al., Micro-structured polymer fixed-target for serial crystallography at synchrotrons and XFELs, IUCrJ, 10, 6, (2023)

Applying nanowire MFM to 2D materials

Project P1905: Magnetic force microscopy with nanowire transducers
Project Leader: M. Poggio and E. Meyer
Collaborator: L. Schneider (SNI PhD Student)

Introduction

Recent years have seen rapid progress in nanometer-scale magnetic imaging technology, with scanning probe microscopy driving remarkable improvements in both sensitivity and resolution. Among the most successful tools are magnetic force microscopy (MFM), spin-polarized scanning tunneling microscopy, as well as scanning magnetometers based on nitrogen-vacancy centers in diamond, Hall-bars, and superconducting quantum interference devices. Over the past three years, we have been using nanowire (NW) force sensors as ultra-sensitive MFM probes. Using NWs functionalized with magnetic tips, we strive to map magnetic fields and dissipation with enhanced sensitivity and resolution compared to the state of the art and to apply these new capabilities to study magnetization in 2D materials.

The key component of a force microscope is the force sensor, which consists of a mechanical transducer, used to convert force into displacement, and an optical or electrical displacement detector. In MFM, "top-down" Si cantilevers with sharp tips coated by a magnetic material have been the standard transducer for years. Under ideal conditions, state-of-the-art MFM can reach spatial resolutions down to 10 nm, although more typically around 100 nm. These cantilevers are well-suited for the measurement of the large forces and force gradients produced by strongly magnetized samples. The advent of NWs and carbon nanotubes grown by "bottom-up" techniques now gives researchers access to much smaller force transducers than ever before. This reduction in size implies both a better force sensitivity and potentially a finer spatial resolution. Sensitivity to small forces provides the ability to detect weak magnetic fields and therefore to image subtle magnetic patterns; tiny concentrated magnetic tips have the potential to achieve nanometer-scale spatial resolution, while also reducing the invasiveness of the tip on the sample under investigation. Such improvements are crucial for imaging nanometer-scale magnetization textures in 2D systems.

Recent efforts have demonstrated the use of single NWs as sensitive scanning force sensors [1]. When clamped on one end and arranged in the pendulum geometry, i.e. with their long axes perpendicular to the sample surface to prevent snapping into contact, they probe both the size and direction of weak tip-sample interactions. NWs have been demonstrated to maintain excellent force sensitivities around 1 aN/$Hz^{½}$ near sample surfaces (<100 nm), due to extremely low noncontact friction. As a result, NW sensors have been used as transducers in force-detected nanometer-scale magnetic resonance imaging and in the measurement of tiny optical and electrical forces. In a proof-of-principle microscopy experiment in the Poggio lab, we showed that a magnet-tipped NW can be sensitive to magnetic field gradients of just a few mT/(m $Hz^{½}$), equivalent to the gradient produced by a few tens of Bohr magnetons or a few nA of flowing current at a distance of a few hundred nanometers [2]. Such sensitivity compares favorably to that of other magnetic microscopies, including scanning Hall microscopy, scanning SQUID microscopy, and scanning nitrogen-vacancy magnetometry [3].

Goals

Despite these promising features, until now, only proof-of-principle NW MFM experiments have been carried out on the well-known magnetic field profile of a current-carrying wire [2, 4]. We intend to move past this demonstration stage by:

1. optimizing the magnet-tipped NW transducers to achieve the highest possible sensitivity and resolution;

2. using the new scanning probes to image magnetism in 2D vdW systems and the surface of bulk chiral magnets.

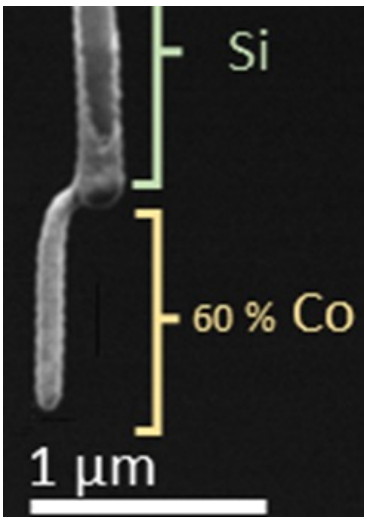

Fig. 1: Scanning electron micrograph of a Co tip deposited by FEBID (at the SNI Nano Imaging Lab) on the free end of a Si NW. The Si NW (length: 20 µm) was grown by the Budakian group (Waterloo).

Results

In the fourth year of work, we have been focusing on imaging experiments on 2D magnets as well as the surface of bulk chiral magnets. Both of these systems present a number of open questions relating to the spatial configuration of magnetic phases and phase transitions. NW MFM, which combines high magnetic field sensitivity and high spatial resolution, is ideally suited for this task.

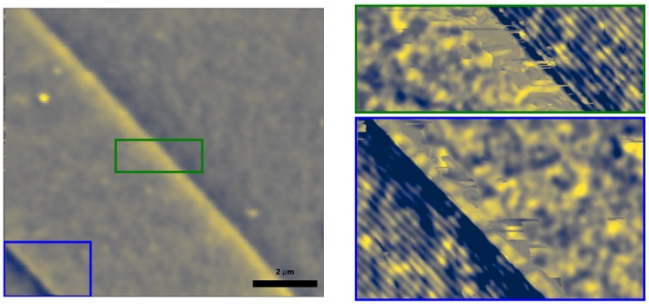

Fig. 2: NW MFM images of the (001) surface of Cu_2OSeO_3. The images show the sample after zero-field cooling in an applied field of 32 mT applied along [001]. 3 domains of the helical phase with modulations of 60 nm along <100> are visible. The domains with clear modulation visible have in-plane modulation vectors while the third domain has an out-of-plane modulation vector.

In collaboration with the Maletinsky group, who is studying the 2D magnet $EuGe_2$ using scanning nitrogen-vacancy (NV) microscopy (SNVM), we have studied bilayer samples of $EuGe_2$ [4] via NW MFM. The NW MFM images are complementary to the SNVM images, because they provide different contrast, i.e. magnetic field gradients and magnetic susceptibility, and can function under much higher magnetic fields. Using our NW MFM technique, we find a phase-separated state and follow its evolution with temperature and magnetic field. Spatial maps reveal that the characteristic length-scale of magnetic domains is in the hundreds of nanometers. These observations strongly shape our understanding of the magnetic states in 2D materials at the monolayer limit and contribute to engineering of ultra-compact spintronics. A manuscript on this work has been written and is currently under submission.

To exploit the high-spatial resolution of around 50 nm offered by NW MFM, we have also started imaging periodically modulated magnetic phases in the insulating cubic helimagnet Cu_2OSeO_3. These measurements complement scanning superconducting quantum interference device (SQUID) microscopy (SSM) measurements carried out in our own group on the same material. They have given us new insights about modulated phases with spatial periods around 60 nm, which were too small to be apparent in SSM images.

In Cu_2OSeO_3, like in other non-centrosymmetric cubic crystals, such as MnSi, MnGe, and FeGe, the lack of inversion symmetry induces an antisymmetric exchange interaction known as the Dzyaloshinskii-Moriya interaction (DMI), which is proportional to the spin-orbit coupling. This interaction and a common hierarchy of magnetic energy scales in these materials result in a similar set of modulated magnetic phases, including helical and skyrmion lattice phases, and the corresponding transitions between them. Cu_2OSeO_3, however, deviates from this universal behavior, exhibiting a tilted conical (TC) phase and a low-temperature skyrmion (LTS) phase, arising from the competition between anisotropic magnetic interactions. These states appear only under magnetic fields applied along ⟨100⟩, highlighting the role of cubic magnetocrystalline anisotropy for their stabilization. Until now, observations of these phases have been based on small angle neutron scattering (SANS), as well as measurements of magnetization and susceptibility. Although these techniques provide a wealth of information on the magnetic phases in the bulk, they do not provide information on their microscopic real-space configuration or their properties near the surface.

We now image the stray magnetic field at the surface of bulk Cu_2OSeO_3 at low temperature and with a magnetic field applied along ⟨100⟩ using both SSM and NW MFM. We map the real-space configuration of the field-polarized (FP), TC, and the LTS phases, as well as the helical domains in low field. Images taken as a function of applied magnetic field show how the transitions between these states unfold and proceed through intermediate states, which include coexisting domains of FP, TC, and LTS phases. The NW MFM images shed particular light on the presence of domains and surface states in low field. A manuscript on the results is currently in preparation.

The success of NW MFM in imaging non-collinear phases at the surface of Cu_2OSeO_3, has pushed us to start further experiments in collaboration with researchers at the PSI to confirm the presence of suspected surface states and transitions between different types of skyrmion states in on different crystalline surfaces of Cu_2OSeO_3.

References

[1] N. Rossi, F. R. Braakman, D. Cadeddu, D. Vasyukov, G. Tütüncüoglu, A. Fontcuberta i Morral, and M. Poggio, Vectorial scanning force microscopy using a nanowire sensor, Nat. Nanotechnol. 12, 150 (2017)

[2] N. Rossi, B. Gross, F. Dirnberger, D. Bougeard, M. Poggio, Magnetic Force Sensing Using a Self-Assembled Nanowire, Nano Lett. 19, 930 (2019)

[3] E. Marchiori, L. Ceccarelli, N. Rossi, L. Lorenzelli, C. L. Degen, M. Poggio, Nanoscale magnetic field imaging for 2D materials, Nat. Rev. Phys. 4, 49 (2022)

[4] A. M. Tokmachev, D. V. Averyanov, A. N. Taldenkov, O. E. Parfenov, I. A. Karateev, et al., Lanthanide f^7 metalloxenes – a class of intrinci 2D ferromagnets, Mater. Horizons 6, 1488 (2019)

Heteromeric nm-sized assembly characterisation

Project P1906: Machine learning assisted design of heteromeric self-assembled molecular capsules
Project Leader: K. Tiefenbacher and A. von Lilienfeld
Collaborator: I. Martyn (SNI PhD Student)

Introduction
Self-assembled supramolecular capsules have been shown to exhibit biomimetic catalytic properties, due to their rigid internal cavity modelling the active site of an enzyme. These nm-sized molecular containers can encapsulate guest molecules and stabilise reactive intermediates by means of non-covalent interactions, catalysing reactions such as terpene cyclisation [1]. However, most known hydrogen-bonded capsules are homomeric (self-assembled from only one building block). Due to the high symmetry of their internal cavity, homomeric capsules are limited in their ability to impose specific conformations on the encapsulated substrate, resulting in limited product selectivity [2]. Our screening results revealed a strong preference for thermodynamic self-sorting, nonetheless, two novel heteromeric capsules have been discovered.

Assembly Discovery and Characterisation
Two stable heteromeric supramolecular assemblies have been discovered in this project. Assembly I, as discussed in the previous Annual Report, consists of six bowl-shaped modules, two of one and four of the other. These modules form a hexameric assembly formed by recognition of complementary hydrogen bonding motifs, similar in size and internal volume to the well-known resorcin[4]arene hexamer. This unprecedentedly large heteromeric capsule (approx. 1270 Å³) is capable of C60-fullerene uptake.

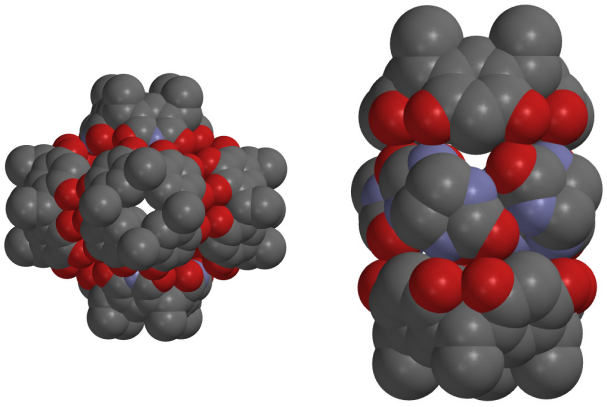

Fig. 1: a) Assembly I, b) Assembly II

Assembly II is smaller in size, consisting of two bowl-shaped modules and a belt motif of four smaller modules. Both modules are known in the literature to form heteromeric assemblies with other modules featuring hydrogen-bonding sites, showcasing the power of the undirected screening method to discover previously overlooked combinations. With a smaller internal volume of approx. 270 Å³, the possibility for guest uptake within Assembly II is limited, and ionic guests such as ammonium salts or hexafluorophosphate were found to cause capsule dissociation. However, in benzene, a bulky solvent which does not fit well inside the cavity of the capsule, addition of n-octane causes a characteristic upfield shift of the terminal methyl group of the guest, indicating guest uptake due to the improved fit inside the host cavity. Two small broad peaks at 0.05 and -0.38 ppm are also visible in the upfield region, indicative of the diastereotopic C2 protons of the guest, which are exposed to the chiral microenvironment of the belt. As the other alkyl signals belonging to the guest do not experience the C-H-π interaction with the aromatic cavity at the capsule ends, and therefore do not give signals in the upfield region, it can be surmised that the guest is bound within a cavity featuring both aromatic and aliphatic walls, supporting the proposed molecular model of assembly II.

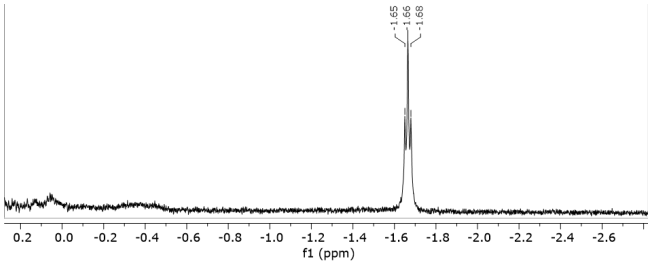

Fig. 2: Upfield region of the 1H NMR spectra (C_6D_6) of n-octane (15.5 mM) and assembly II (1.5 mM).

Furthermore, several cases have been discovered in which interaction between modules does not lead to a single well-defined heteromeric assembly, that is the only species observed at thermodynamic equilibrium. These interactions, in which a complete hydrogen-bonding network cannot be formed due to incomplete matching of donors and acceptors, steric considerations preventing the formation of energetically favourable hydrogen bonds, or competition with the respective homomeric assemblies, are similarly important in helping inform future design of heteromeric assemblies.

Fragrance Compound Design Project
The targeted computer-aided structural design (CASD) of fragrance compounds was also investigated, by exploring the use of a genetic algorithm (GA) to apply mutations to known fragrance compounds and evaluate the 3D structural properties of the resulting molecules.

Current open-source tools for designing compounds with similar properties to a target molecule are pervaded by a bias towards druglike molecules in existing databases. In particu-

lar, “fragrance-like” molecules are small, volatile, and more lipophilic than “drug-like” molecules [3]. In the absence of extensive crystallographic data on odorant receptors, which would enable ligand design via molecular docking, a widely-used drug design method, a ligand-based approach is typically used, based on modification of known fragrance compounds.

In this project, to generate molecules with similar properties to a target molecule, basic hydrocarbon skeletons were initially functionalised using custom RDKit functions. However, this process was prohibitively slow due to the generation and manipulation of molecular graphs it entailed. Instead, a text-based evolutionary algorithm was deployed, which is capable of quickly generating millions of SMILES strings using a mutation protocol [4]. In this protocol, a pre-defined list of characters (i.e. elements) can be added to the SMILES string at a random point. Other mutations include the deletion or replacement of random characters, and rearrangement of the SMILES string.

The large database of generated strings is then evaluated according to both pre-defined chemical feasibility and valid SMILES rules and the invalid results are discarded. Subsequently, a function is applied to generate all possible stereoisomers for each quartenary carbon in each molecule, to ensure representation in the dataset of and the valid structures are transformed to a molecular graph representation for further analysis.

The results of the molecule generation are filtered according to user-defined criteria, such as the number of rings or the presence of certain function groups. In this case, generated molecules that were either linear or had only one ring were prioritised, due to their desirable biodegradability properties and relative ease of synthesis compared to similar molecules with multiple rings. Results are then evaluated by combining shape and electrostatic surface potential (ESP) similarity to the target into a single score. 200 conformers are generated for each molecule to account for the flexibility of linear compounds, and each conformer was scored. The conformer that gave the best similarity score to the target was subjected to a simple energy evaluation relative to the most stable conformer, to ensure that the conformer was energetically feasible.

The synthetic feasibility of the generated molecules was investigated by means of fragment-based scoring methods such as SYBA and SAScore, however, these methods only provide a rough estimate of ease of synthesis. The synthetic accessibility of the molecules of interest was assessed individually, but unfortunately, the highly substituted products that give high similarity scores to the fragrance molecules are prohibitively difficult to synthesise.

Outlook

The novel heteromeric capsule results are being prepared for publication. Future work regarding these species will focus on the investigation of potential applications, such as the possibility of catalysis within the internal cavities of the heteromeric assemblies, which may provide different substrate reactivity than within homomeric assemblies.

References

[1] Q. Zhang, L. Catti, K. Tiefenbacher, Catalysis inside the Hexameric Resorcinarene Capsule, Acc. Chem. Res. 51, 2107-2114 (2018)

[2] I. Némethová, L. Syntrivanis, K. Tiefenbacher, Molecular Capsule Catalysis: Ready to Address Current Challenges in Synthetic Organic Chemistry?, Chimia 74, 561-568 (2020)

[3] L. Ruddigkeit, M. Awale, J-L Reymond, Expanding the Fragrance Chemical Space for Virtual Screening, J. Chem. Inf. 6, (2014)

[4] A. Nigam, R. Pollice, M. Krenn, G. Gomes, A. Aspuru-Guzik, Beyond Generative Models: Superfast Traversal, Optimization, Novelty, Exploration and Discovery (STONED) Algorithm for Molecules using SELFIES, Chem. Sci. 12, 7079-7090, (2021)

Towards quantum coherent coupling between a nanomechanical membrane and an atomic ensemble

Project P1907: Spin-opto-nanomechanics
Project Leader: P. Treutlein and P. Maletinsky
Collaborators: G.-L. Schmid (SNI PhD Student), M. Ernzer, M. Bosch Aguilera

Using atomic spins to control the vibrations of a nanomechanical membrane oscillator is interesting for fundamental quantum science as well as for applications in quantum sensing. The atomic spins can be initiated and manipulated very reliably using the well-established toolbox of atomic physics developed in the last decades. The mechanical oscillator on the other hand is a massive device with a very high force sensitivity and thus has potential applications in force sensing. Coupling the two systems on the quantum level enables us to use the toolbox of atomic physics to manipulate the vibrational state of the membrane on the quantum level and opens up many exciting opportunities for quantum measurement and control.

One possible application of this coupling is to cool the mechanical oscillator: the atomic spin can be initialized in its ground state while the membrane is in a thermal environment. Exploiting the strong coupling of the membrane to the spin ensemble [1], we performed state-swaps between the membrane vibrational state and the atomic spin [2]. In this way, the membrane could be cooled to 216 mK in 200 µs. In analogy to a classical feedback loop, our system can be described as a coherent feedback loop controlling the membrane with the atoms. In coherent feedback, a quantum system is controlled through its interaction with another one, in such a way that quantum coherence is preserved. In contrast to measurement-based, classical feedback, coherent feedback does not rely on measurements, thus avoiding the associated quantum backaction.

In future experiments, we will use the coherent control for further protocols. The coupling between the membrane and the atomic spins can be used to generate entanglement between the systems. This entanglement can serve as a resource for measurements of the membrane vibrations with a precision below the standard quantum limit.

To this end, we have to engineer quantum coherent coupling between the two systems. While in the so-called strong coupling regime, the coupling rate 2g is larger than the average decay rate of the systems, $4g > \gamma_s + \gamma_m$, for quantum coherent coupling the coupling rate must exceed the average decoherence rate, $4g > \gamma_s + \gamma_m \cdot (2n_{th}+1)$. In our experiment, we have achieved strong coupling of the membrane oscillator to the spin [1,2] while demonstrating the more stringent condition of quantum coherent coupling is still outstanding.

Hybrid setup

The coupling of the atomic spin to the mechanical oscillator is mediated by laser light such that the two systems can be separated by a macroscopic distance, in our case by about one meter. To achieve a Hamiltonian coupling between the two systems, the light forms a loop: The coupling laser interacts first with the spin, then with the membrane and once again with the spin, as sketched in figure 1 and detailed in [2]. By shifting the phase of the quantum signal on the light by $\phi=\pi$ before the second interaction with the spin, the second spin-light interaction is the time-reversal of the first one. This way, the backaction of the light onto the spin can be cancelled.

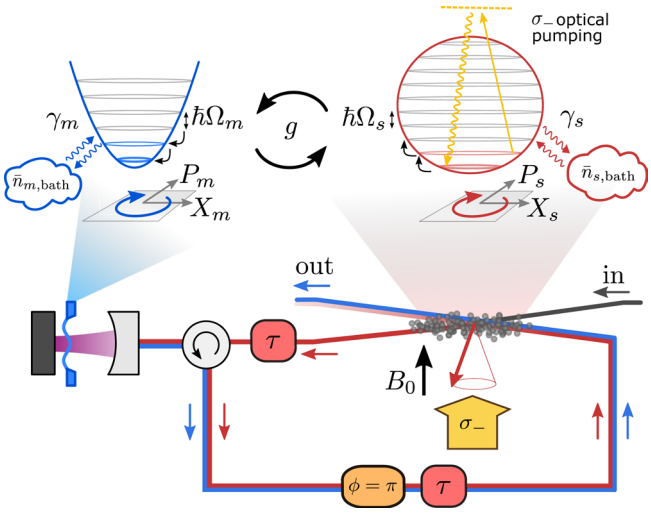

Fig. 1: Sketch of the light-mediated spin-membrane coupling. Light interacts first with the spin, then with the membrane, and then again with the spin. On the way back from the membrane to the spin, a π-phase is imprinted on the light, rendering the spin-membrane interaction effectively Hamiltonian for zero delay τ=0. The systems can be approximated by harmonic oscillators of frequencies Ω_m and Ω_s with damping rates γ_s and γ_m coupling them to a bath with $\bar{n}_{(m,bath)}$ and $\bar{n}_{(s,bath)}$ phonons, respectively. The oscillators are coupled at a rate g.

Membrane Oscillator

The membrane used in our previous works [1,2] is a 100 nm thin SiN square oscillator surrounded by a phononic crystal patterned into the Si support structure. The 2,2-mode of the oscillator used in the coupling experiments has a frequency of 1.96 MHz and a quality factor of 1.4×10^6 at room temperature. It is embedded in an optical cavity of linewidth $\kappa = 2\pi \times$ 77 MHz such that we are in the fast cavity limit.

Recently, we have upgraded the system by placing a so-called soft-clamped membrane [3] in the optical cavity. In these membranes, the phononic crystal structure is directly patterned into the SiN-membrane. In the middle of the membrane, there is a defect of the crystal which supports vibra-

tional modes at this position. The oscillation amplitude of these localized modes decays exponentially in the crystal and bending losses at the clamping points are strongly reduced [3]. This results in much higher mechanical quality factors. Our soft-clamped membrane has a mode at 1.19 MHz with a quality factor of 10^8 and a mode at 2.19 MHz with a quality factor of 7.5×10^7. It is mounted in an optical cavity with a linewidth of $\kappa = 2\pi \times 25$ MHz. Currently, the membrane is used to perform optical coherent feedback measurements as described in [4].

Atomic Spin

The collective atomic spin is formed by an ensemble of 2×10^7 ultracold 87Rb atoms in an optical dipole trap. The depth of the trapping potential and the number of trapped atoms were increased compared to [1,2] by upgrading the trapping laser. Moreover, by optimizing the dipole trap geometry, the shape of the atomic cloud could be matched to the probe light mode such that the scattering cone of the atoms overlaps better with the incoming probe light. The atoms are pumped into the state $|F=2,m_F=-2\rangle$. Using a static magnetic field, the atomic Larmor frequency can be tuned in resonance with the membrane frequency. The atomic spin interacts with the light by the off-resonant Faraday interaction.

For quantum coherent coupling of the spin and the membrane, we must understand the spin-light interface and be able to operate it in a regime where quantum fluctuations dominate, corresponding to a cooperativity of the spin-light coupling larger than unity. To characterize the spin-light coupling, we measure the light after the first interaction with the spin instead of sending it to the membrane. If the atoms are well polarized and not excited, we can detect the quantum noise of the atoms on the light.

Measuring the light after the spin-light interaction yields three noise terms: the first is the intrinsic quantum noise of the light which is called shot noise. The second arises from the intrinsic quantum fluctuations of the spin that are imprinted on the light, called projection noise. The third contribution arises from the quantum noise of the light driving the spin, whose induced fluctuations are then read out by the light again. This part is called backaction noise.

The different noise sources have a different scaling with atom number and optical power. By scanning those two parameters, we can distinguish the contributions. In figure 2, a measurement of the spin noise is shown for different numbers of atoms. While the shot noise is independent of atom number, the projection noise scales linearly and the backaction noise scales quadratically with atom number. In the regime of the measurement shown in figure 2, the backaction noise is dominant. The spin-light interface is in the quantum regime and the agreement with the theoretical expectation is good.

Outlook

The next step is to couple the soft-clamped membrane to the atomic spin in the quantum regime. The parameters of our improved setup should allow us to achieve ground-state cooling of the membrane by this interaction [2]. Exploiting the quantum coherent coupling, we could then create quantum entanglement of the spin and the membrane over a distance of more than one meter.

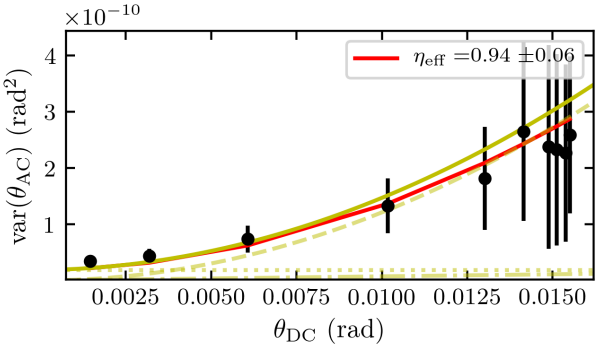

Fig. 2: Measurement of the quantum noise on the light after the interaction with the spin. Here, the vertical axis shows the quantum noise on the light measured with the spin aligned orthogonal to the probe beam, while the horizontal axis shows the DC Faraday signal measured with the spin parallel to the probe beam, which is proportional to the atom number. The yellow lines show theoretical expectations: the dotted line shows the shot noise, the dashed-dotted line (at the bottom) the projection noise, the dashed line the backaction noise, and the solid line the sum of all contributions. The red line shows a fit to the data with one fitting parameter for the overall spin-light coupling.

References

[1] T. M. Karg, B. Gouraud, C. T. Ngai, G.-L. Schmid, K. Hammerer, and P. Treutlein, Light-mediated strong coupling between a mechanical oscillator and atomic spins 1 meter apart, Science 369, 174 (2020).

[2] G.-L. Schmid, C. T. Ngai, M. Ernzer, M. Bosch Aguilera, T. Karg, and P. Treutlein, Coherent feedback cooling of a nanomechanical membrane with a spin, Phys. Rev. X 12, 011020 (2022)

[3] Y. Tsaturyan, A. Barg, E.S. Polzik, A. Schliesser Ultracoherent nanomechanical resonators via soft clamping and dissipation dilution, Nat. Nanotechnol. 12, 776 (2017)

[4] M. Ernzer, M. Bosch Aguilera, M. Brunelli, G.-L. Schmid, T. M. Karg, C. Bruder, P. P. Potts, and P. Treutlein, Optical coherent feedback control of a mechanical oscillator, Phys. Rev. X 13, 021023 (2023)

Chiral luminescent Pt(II) complexes – towards functional nanowires

Project P1908: Chiral Recognition in Molecular Nanowires from Square-Planar Platinum(II) Complexes
Project Leader: O. Wenger and C. Sparr
Collaborator: A. Huber (SNI PhD Student)

In the context of chiral recognition, we designed new nanostructured "chiral nose"-type materials to selectively sense chiral volatile organic compounds (VOCs)[1,2]. Controlled helical superstructures composed of stacked square planar platinum (II) complexes are of key interest to us. In theory, interactions of small chiral molecules with the crystal lattice can provoke changes in photoluminescence, vapochromism [3], or electrical conductance, thus leading to sensing behavior. Chiral recognition based on molecular nanowires seems underexplored until now.

Ideally, stereoisomers of specific VOC analytes could interact with the nanowire crystal lattice by intercalation, or through C-H-π, π-π, or other interactions directly at the atropisomeric moieties of the complexes.

The tendency of square planar Pt(II) complexes to form stacked aggregates arises from weak metal-metal interactions between the $5d_{z2}$ orbitals upon close contact (<3.5 Å)[4].

Stereogenic Pt(II) isocyanide complex synthesis
Taking advantage of the Sparr group`s expertise on atroposelective oligo-naphthylene synthesis [5], the selective formation of (Ra)- or (Sa)- di-naphthylenes was achieved. The iterative addition of building block (BB in Scheme 1a) to aromatic aldehydes was followed by an enantioselective arene-forming aldol-condensation[5].

The atropisomeric scaffold was then transformed into the isocyanide ligand, following methods developed in the Wenger group (Scheme 1b)[6]. Suzuki cross-coupling of the atropisomeric moiety with the ortho methylated aromatic formamide was followed by a dehydration to yield the isocyanide.

The sterically demanding monodentate ligand was introduced to perturb the intermolecular stacking in order to induce a helical supramolecular arrangement. On the other hand, metal-metal interactions were intended to stabilize the oligomeric nanowire structures [3,4].

The obtained atropisomeric isocyanide ligand could now be used for the formations of various planar Pt(II) systems [7,8]. Complex (1) was obtained after applying optimized reaction conditions and purification.

Absorption, luminescence and aggregation analysis of complexes (1)
With the desired complexes (1) in hand, we first studied the absorption and emission in solution.

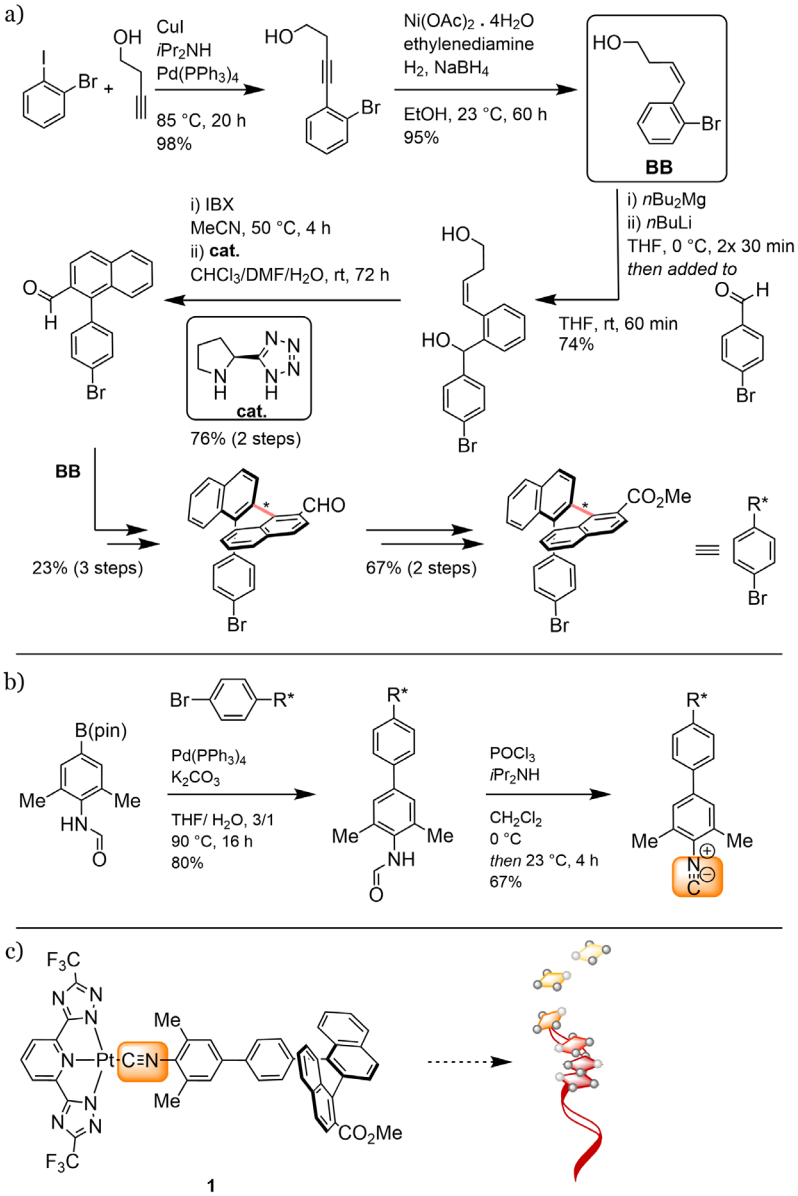

Scheme 1: Synthesis of the monodentate atropisomeric isocyanide ligand (a, b). Structure of complex 1 and schematic representation of the anticipated supramolecular aggregation c).

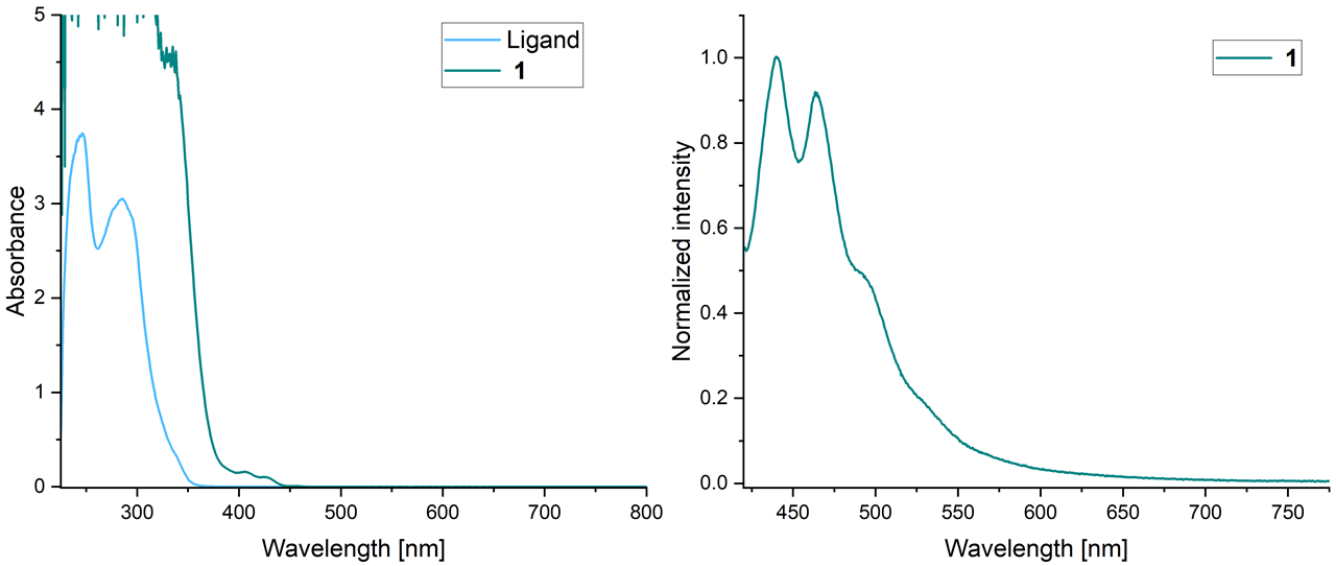

Fig. 1: UV-vis absorption (left) and emission (right) spectra of (1) in CH_2Cl_2 ($2.7 \cdot 10^{-4}$ M).

Figure 1 shows the UV-vis absorption (left) and emission (right) spectra of (1) in dichloromethane. The UV-vis absorption spectrum contains a metal to ligand charge transfer band at 420 nm. In the emission spectrum, a structured emission band between 430 - 600 nm is observed. A preliminary solid state emission measurement showed a weak but broad emission at 520 nm. We expect such a broadened emission of the nanowire assembly due to close metal-metal contacts.

Outlook

We now study the assembly behavior of our chiral Pt complex. Therefore, the physical characterization will focus on UV-Vis absorbance, photoluminescence, and circular dichroism. If possible, the nanostructures will be studied by X-ray- or electron diffraction. Finally, we will investigate changes of the aforementioned physical properties upon exposure to chiral VOC analytes.

References

[1] A. Prabodh, D. Bauer, S. Kubik, P. Rebmann, F. G. Klärner et al., Chirality Sensing of Terpenes, Steroids, Amino Acids, Peptides and Drugs with Acyclic Cucurbit[n]urils and Molecular Tweezers, Chem. Commun. 56, 4652-4655 (2020)

[2] Z. A. De los Santos, C. Wolf, Optical Terpene and Terpenoid Sensing: Chiral Recognition, Determination of Enantiomeric Composition and Total Concentration Analysis with Late Transition Metal Complexes, J. Am. Chem. Soc. 142, 4121–4125 (2020)

[3] O. S. Wenger, Vapochromism in Organometallic and Coordination Complexes: Chemical Sensors for Volatile Organic Compounds, Chem. Rev. 113, 3686-3733 (2013)

[4] W. B. Connick, R. E. Marsh, W. P. Schaefer, H. B. Gray, Linear-Chain Structures of Platinum(II) Diimine Complexes, Inorg. Chem. 36, 913-922 (1997)

[5] D. Lotter, A. Castrogiovanni, M. Neuburger, C. Sparr, Catalyst-Controlled Stereodivergent Synthesis of Atropisomeric Multiaxis Systems, ACS Cent. Sci. 4, 656–660 (2018)

[6] L. Büldt, X. Guo, A. Prescimone, O. S. Wenger, A Molybdenum(0) Isocyanide analogue of Ru(2,2'-Bipyridine)$_3^{2+}$: A strong reductant for photoredox catalysis, Angew. Chem. Int. Ed. 55, 11247-11250 (2016)

[7] S. Chakraborty, A. Aliprandi, L. De Cola, Multinuclear PtII Complexes: Why Three is Better Than Two to Enhance Photophysical Properties, Chem. Eur. J. 26, 11007–11012 (2020)

[8] V. W. Yam, V. K. Au, S. Y. Leung, Light-Emitting Self-Assembled Materials Based on d^8 and d^{10} Transition Metal Complexes, Chem. Rev. 115, 7589– 7728 (2015)

Targeted hafnium oxide nanoparticles for contrast enhanced computed tomography: towards more reliable diagnosis

Project P2001: Imaging cardiovascular macro- and micro-structure using HfO_2 nanocrystals as X-ray tomography
Project Leader: J. De Roo and A. Bonnin
Collaborator: E. Maksimova (SNI PhD Student)

Introduction
In 2019, cardiovascular diseases were responsible for 32% of all global deaths [1]. Heart transplantation is nowadays a routine surgery to treat heart failure or coronary artery disease. The early stages of transplant rejection can be monitored by endo-myocardial biopsy (EMB).

2D histology is the conventional technique to clinically assess the microstructure of removed cardiac tissue. However, this analysis is mainly qualitative and time-consuming. On the other hand, Synchrotron Radiation X-ray Phase Contrast Imaging (SR X-PCI) is a non-destructive tomography technique, providing 3D information. Nevertheless, while SR X-PCI measurements can provide 3D virtual histology, it is currently difficult to automatically identify early stages of rejection. Furthermore, for clinical implementation, X-PCI should be compatible with laboratory-source X-rays that are usually less sensitive. Therefore, the development contrast agents that target immune cells is essential to both improve cell differentiation and increase sensitivity [2].

In this project, we aim to develop hafnium oxide (Z=72) nanocrystals as novel contrast agents and apply them in cell-targeted 3D histology. To retain colloidal stability in physiological conditions, nanocrystals should be coated with biocompatible ligands. To couple nanocrystals with antibodies, we aim to use click-chemistry as highly specific, biocompatible and fast way of conjugation.

Solvothermal synthesis of nanocrystals
Hafnium oxide nanoparticles were synthesized via well-established solvothermal process [3]. Hafnium tert-butoxide and benzyl alcohol were heated at 220°C for 96 hours in muffle furnace (Fig. 1a). After synthesis, the nanocrystals are isolated, purified and stabilized with 2-[2-(2-methoxyethoxy) ethoxy]acetic acid (MEEAA) to impart colloidal stability of nanoparticles.

The synthesis resulted in the formation of monoclinic (Fig. 1b) ellipsoidal nanoparticles with major axis length of (3.4 ± 0.5) nm and minor axis length of (2.3 ± 0.3) nm, as confirmed by TEM (Fig. 1c).

Bioconjugation strategy
From the variety of bioconjugation options, we have chosen strain promoted alkyne azide cycloaddition also known as copper-free click-chemistry as highly specific, biocompatible and bioorthogonal reaction. It is a fast reaction with no catalyst required and it occurs under physiological conditions [4]. To enable this reaction, we provided azide groups on the surface of nanocrystals and functionalized antibodies with dibenzocyclooctyne (DBCO) group.

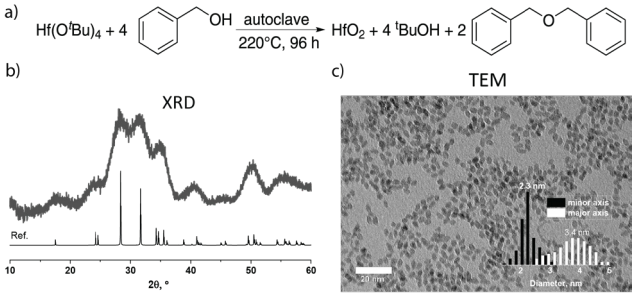

Fig. 1: a) Synthetic route of HfO_2 nanoparticles; b) powder x-ray diffraction analysis of the formed nanocrystals; c) TEM picture of nanocrystals.

Initially synthesized nanocrystals capped by MEEAA are known to be stable in water but only until pH = 3 maximum. To provide good colloidal stability at higher pH, more relevant for use in biological applications, and to provide the desired functional group we conducted a ligand exchange of native carboxylic acid the mixture of homemade catechol-based ligands, as they are known by their greater binding affinity to nanocrystal surface [3].

For the bioconjugation we aim to have one-to-one ratio of nanoparticles to antibodies. However, it is important to note that the presence of multiple functional groups on each species can potentially lead to the formation of larger aggregates or conjugate networks.

Specificity of bioconjugates
Next, prepared conjugates were tested in vitro using fluorescence activated cell sorting (FACS). For this, along with antibody cargo, we labeled nanocrystals with sulfo-Cy_5 DBCO ($\lambda_{ex/em}$ = 650/671 nm).

As the model system, CD_4-positive immune cells (helper immune cells) were chosen. Fresh spleen cells were isolated and stained with either dye-labeled nanoparticles or nanoparticles targeted with anti-CD_4 antibodies prepared as described before. Then the cell populations were analyzed using flow cytometry.

It was demonstrated that targeted nanocrystals can specifically recognize helper T cells among other immune cell types present in spleen, with minimal non-specific staining (Fig. 2). Since fluorescence only comes from nanocrystals, this result shows that the conjugation process successfully worked and that antibodies' targeting capabilities were preserved despite the chemical functionalization.

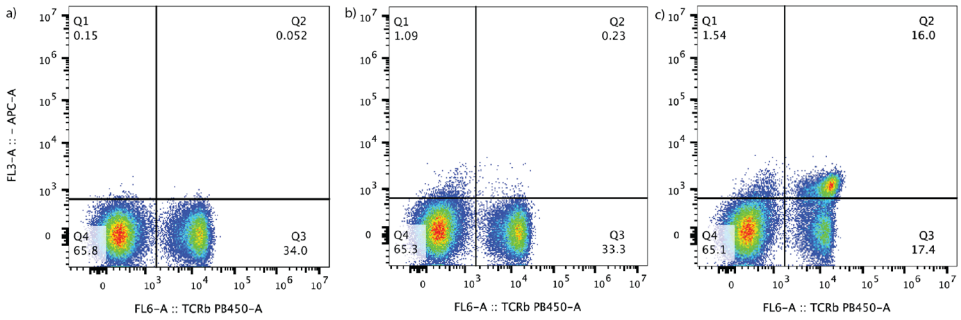

Fig. 2: The results of flow cytometry. For each sample, anti-TCR antibody staining is used to distinguish between B and T cells (represented on X-axis). Y-axis represents Cy_5 fluorescence intensity. a) Unstained fresh spleen cells; b) Cells stained with Cy_5-labeled nanocrystals; c) Cells stained with nanocrystals carrying Cy_5 dye and anti-CD_4 antibody.

Hafnium oxide as ex vivo contrast agent

As a side project, we explored the use of hafnium oxide nanocrystals to enable direct imaging of cardiovasculature ex vivo [5]. Vascular corrosion casting is a method used to visualize the three dimensional anatomy and branching pattern of blood vessels. A polymer resin is injected in the vascular system and, after curing, the surrounding tissue is removed. The latter often deforms or even fractures the fragile cast. Here, we developed a method that does not require corrosion, based on in situ micro computed tomography (micro-CT) scans. To overcome the lack of CT contrast between the polymer cast and the animals' surrounding soft tissue, hafnium oxide nanocrystals were introduced as CT contrast agents into the resin. The NCs dramatically improve the overall CT contrast of the cast and allow for straightforward segmentation in the CT scans. Careful design of the NC surface chemistry ensures colloidal stability of the NCs in the casting resin. Using only 5 m% of HfO_2 NCs, high-quality cardiovascular casts of both zebrafish and mice could be automatically segmented using CT imaging software. This allows to differentiate even µm scale details, without having to alter the current resin injection methods. This new method of virtual dissection by visualizing casts in situ using contrast enhanced CT imaging greatly expands the application potential of the technique. This project was executed in collaboration with various other actors, also in the context of the NCCR molecular systems engineering. The specific contribution of the SNI members was the high resolution imaging at the TOMCAT beamline at PSI (see Fig. 3).

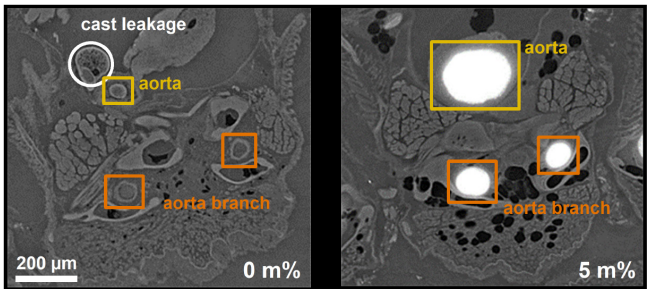

Fig. 3: Synchrotron CT scan slices of a zebrafish injected with resin containing 0 m% HfO_2 NCs (left) and 5 m% HfO_2 NCs (right) show the high contrast improvement with the surrounding soft tissues.

Conclusions and outlook

We have successfully synthesized nanocrystals that are colloidally stable in physiological conditions due to tightly bound catechol-based ligands. Alkyne azide cycloaddition of antibodies and nanocrystals was enabled by functionalization of antibodies with DBCO groups and providing azide groups on the surface of nanocrystals. The prepared bioconjugates were successfully tested in vitro to target CD_4-positive cells within other spleen cells.

Nevertheless, optimization of the bioconjugates preparation is needed. Further focus will be put on enhancing the versatility and purification by size exclusion chromatography.

References

[1] Cardiovascular diseases (who.int)

[2] H. Dejea, P. Garcia-Canadilla, A. C. Cook, E. Guasch, M. Zamora, et al. Comprehensive analysis of animal models of cardiovascular disease using multiscale x-ray phase tomography, Sci Rep 9(1):6996 (2019)

[3] L. Deblock, E. Goossens, R. Pokratath, K. De Buysser, J. De Roo. Mapping out the Aqueous Surface Chemistry of Metal Oxide Nanocrystals: Carboxylate, Phosphonate, and Catecholate Ligands. JACS Au, 2(3): 711-722 (2022)

[4] L. Taiariol, C. Chaix, C. Farre, E.Moreau. Click and biorthogonal chemistry: the future of active targeting of nanoparticles for nanomedicines? Chem. Rev. 122, 1, 340-384 (2021)

[5] E. Goossens, L. Deblock, L. Caboor, D. Van den Eynden, I. Josipovic, et al. From corrosion casting to virtual dissection: contrast-enhanced vascular imaging using hafnium oxide nanocrystals. ChemRxiv. Cambridge: Cambridge Open Engage (2023)

Mechanosensitive responses in live bacteria

Project P2002: A death-dealing nanomachine
Project Leader: R. H. Y. Lim and M. Basler
Collaborators: M. Brüderlin (SNI PhD Student), P. Cedro

Introduction
Bacterial cells activate specific signaling pathways in response to various signals from the environment [1]. However, bacterial cells are also sensitive to interbacterial and bacteria-host contact interactions [2]. Recent studies have attributed many of these interactions to mechanosensitive pathways. In this project, we have investigated the reaction of bacteria to mechanical stress by means of atomic force microscopy (AFM). Specifically, we use AFM in combination with live-cell fluorescence microscope (FM) to quantify how bacteria respond to force in a highly controlled matter [3] (Fig. 1).

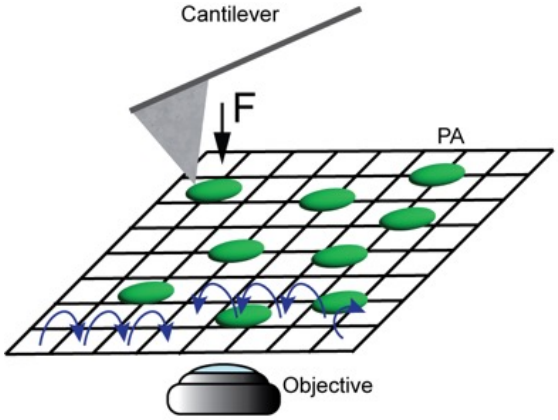

Fig. 1: Cartoon of the experimental set-up. The green rods indicate bacterial cells and the blue arrows show the path of the AFM cantilever during a force mapping experiment.

Mechanosensitivity of bacterial cells
Specific proteins were labeled with the fluorescent protein mNeonGreen to track the bacterial cell response by FM. The flagellar motility protein FliC was also knocked out to increase the attachment of bacteria to the Petri dish during imaging.

We tested a wide array of different stimuli conditions varying both the applied force as well as the velocity at which the force was applied. Bacterial cells reacted to the nanomechanical stimuli by driving an accumulation of labelled proteins to the point of tip impact. The elapsed time between tip contact and appearance of the fluorescent foci gave an overall response time of 13.23 ± 1.49 s. The number of mechanosensitive bacterial cells showed a positive correlation with the magnitude of applied force that reached an 8-fold higher response at the largest force.

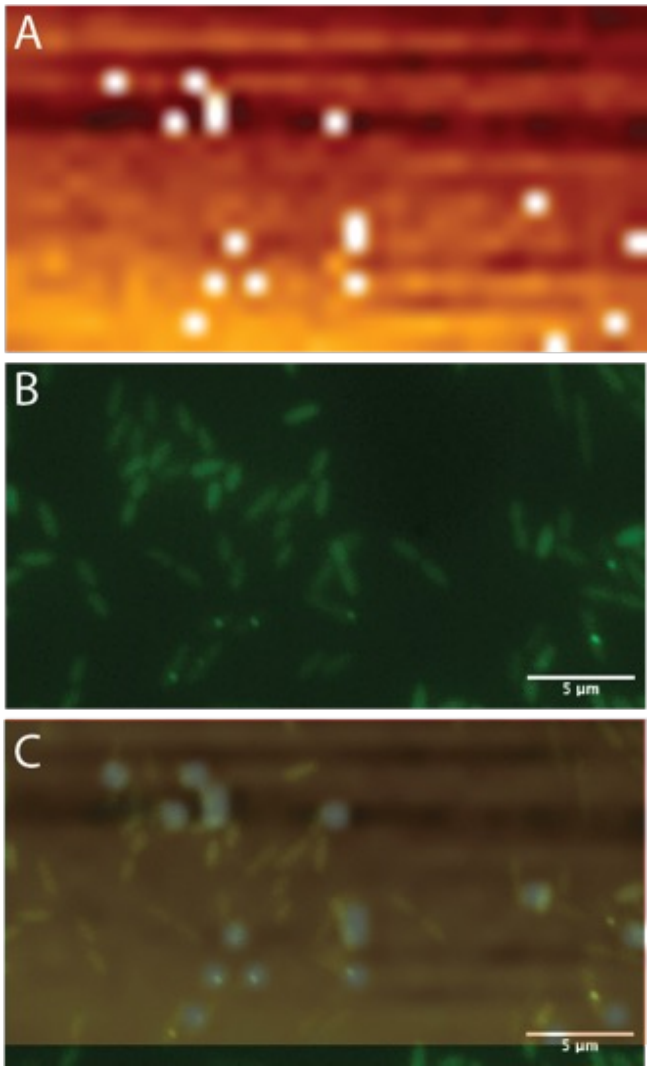

Fig. 2: A): AFM force map image. The bright spots indicate hits of the bacterial sample. B): Fluoresence image of the same field of view. The bright spots indicate of fluorescence indicate cells react to the AFM. C): overlay of the two images showing that cells hit by the AFM, react to the physical stimuli.

Force Curve analysis
To understand the significant increase in mechanoresponsiveness, an extensive force curve analysis was carried out. Viable curves typically reveal two membrane breaking points (Fig. 3) at T_1 (6.76 nN) and T_2 (23.98 nN). These breakage points corresponded to a puncture of the outer membrane and a subsequent breakage of the inner membrane, respectively. Strikingly, this is consistent with the large in-

crease in foci assembly rate above 20 nN, and suggests that membrane breakage plays a key role in regulating the bacterial response to mechanical stress.

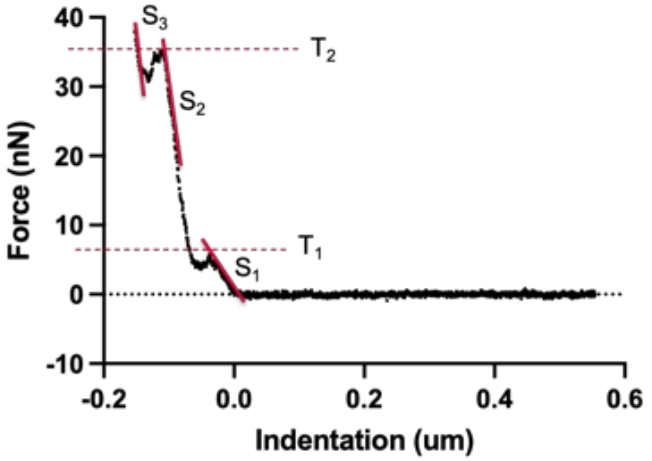

Fig. 3: Example force curve from a force mapping experiment. The continuous red lines show the slopes (stiffness) of different parts of the cell envelope when applying pressure. The dotted lines indicate membrane breaking thresholds. T_1 being the outer membrane and T_2 being the inner membrane.

Additionally, the force curves provided information about the stiffness of the individual parts of the bacterial cells. Using a modified Hertz-Sneddon model for the area of contact we determined the bacterial contact stiffness to be 749.9 ± 367.4 kPa.

Signaling cascade proteins

To further elucidate the mechanism of such a bacterial response, we identified and knocked out four key proteins in a stepwise manner. All AFM experiments for these knock-out mutants showed a complete lack of fluorescent foci regardless of applied force. Hence, these proteins are essential for mediating the mechanosensitive bacterial response.

Conclusion and Outlook

Our results show to elucidate the biophysical mechanism of bacterial contact responses. We propose that membrane damage is required to reliably cause a bacterial retaliation. This model is supported by the observation that higher forces lead to more membrane breaks in the force curves. It also explains why there is a significant increase in firing rate exceeding 20 nN of force since the median membrane breaking threshold is 23.5 nN. This implies that more cells would be primed to respond at higher forces.

For the future, we will study the mode action of how key bacterial proteins sense mechanical signals and how these signals are transferred to initiate assembly events.

References

[1] B.-J. Laventie, U. Jenal, Surface Sensing and Adaptation in Bacteria. Annual Review of Microbiology 74, 735-760 (2020)

[2] S. Peterson, K. Bertolli, J. Mougous, The Central Role of Interbacterial Antagonism in Bacterial Life. Current Biology 30(19), R1203-R1214 (2020)

[3] L. Mulder, J. H. Koolstra, J. M. J. den Toonder, T. M. G. J. van Eijden, Intratrabecular distribution of tissue stiffness and mineralization in developing trabecular bone. Bone 41, 256–265 (2007)

Towards all-optical single-spin scanning magnetometry

Project P2003: Nanoscale quantum sensing of complex spin systems in extreme environments
Project Leader: P. Maletinsky and M. Poggio
Collaborator: J. Zuber (SNI PhD Student)

Introduction
Group IV defect centers in diamond have attracted increasing attention in recent years, being investigated for all three directions of quantum technology applications, computing, communication, and sensing. The negatively charged silicon vacancy center (SiV^-) shows particular promise, as it is straight-forward to produce, exhibits excellent spin-coherence times at mK-temperatures and offers interesting optical properties, such as short lifetimes and a high Debye-Waller factor [1]. This project aims at establishing the SiV^- center as an alternative to the NV center in single-spin scanning probe magnetometry [2] for a regime where the latter is challenging to deploy, particularly in ultra-low temperatures and high magnetic fields. A noteworthy advantage is the perspective of all-optical single spin magnetometry in scanning probes using the SiV^- center. To achieve this, it is paramount to bring the emitter as close to the surface of the diamond as possible while retaining its favorable optical and spin properties in nanostructures. This year, we have shown that we can reliably create single and shallow (<50 nm) SiV^- centers that exhibit exceptional optical coherence over long timescales in diamond parabolic reflectors (PR) [3]. Additionally, we have continued investigating the charge state dynamics between SiV^- and its charge neutral state, SiV^0, a promising candidate for a spin-photon interface [4].

Coherent single silicon vacancy centers in diamond [3]
As shown in figure 1 we achieve lifetime-limited optical coherence in our shallow SiV centers in PRs with a combination of two high-temperature (>1200°C) annealing steps, one before and one after PR nanofabrication and an optical charge stabilization method whereby we expose the emitters to high powered (>5 mW) 445 nm laser light for extended durations (>1 h).

While the first high-temperature anneal serves the purpose of creating SiV centers, the second heals damage dealt to the diamond lattice during the nanofabrication. After this procedure, 30% of our emitters (population 1) already exhibit comparatively narrow optical linewidths close to the lifetime limit of ~100 MHz in charge-repump free photoluminescence excitation (crf-PLE). The remaining emitters either exhibit blinking under resonant excitation (population 2) and therefore display the need for continuous off-resonant charge repump laser pulses in charge-repump (cr)-PLE (introducing additional inhomogeneous broadening) or they appear dim with broad linewidths (population 3). Subsequently we discovered that, when exposed to the aforementioned 445 nm laser light, populations 2 and 3 of SiV centers with sub-optimal optical properties can be converted to population 1, enabling crf-PLE and reducing the linewidths, at times, to the lifetime limit. This conversion to population 1 of bright and coherent emitters is permanent and not sample specific.

Our results constitute a major step towards the use of SiV^- as nanoscale quantum sensors for applications under extreme conditions, such as single spin scanning magnetometry at sub-kelvin temperatures and tesla-range magnetic fields. Furthermore, our easy-to-implement charge-stabilization scheme will find immediate applications in other quantum technology applications of SiV^-, including the development of quantum repeaters, quantum networks, or indistinguishable single photon sources.

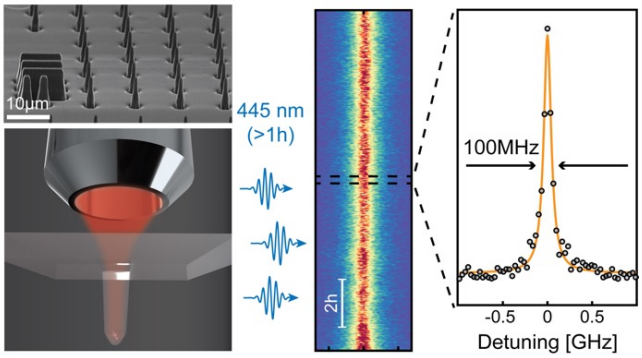

Fig. 1: Lifetime-limited and charge stable optical linewidths in diamond parabolic reflectors (PRs). Top left: SEM image of a PR array as fabricated on the diamond. Bottom left: Illustration of setup geometry in use, imaging our emitters through the diamond. Middle: Extended time trace of the resonance optical transition line of a single SiV center. Right: Linecut of the time trace, revealing a lifetime limited linewidth of the shallow emitter over a measurement time of more than six minutes.

Stabilizing SiV^0 through surface termination and continuous optical charge state tuning [4]
The predominantly stable charge state of the SiV center is negatively charged and stabilization of its neutral charge state hitherto required complex and error-prone Fermi-engineering by boron doping during diamond growth. We have found that hydrogen terminating diamond samples prepared in the way outlined above stabilizes SiV_0 in undoped samples by the band-bending introduced by the combination of the H-terminated surface and the intermittent water layer that is associated to all diamond surfaces in atmosphere. SiV_0 stabilized this way exhibit similar properties as its counterpart in boron doped samples and offers higher reproducibility as well as optional continuous optical charge state tuning; the latter is brought about by exposing the emitter in question to high-energy (>2.3 eV) laser light. These results pave the way for the use of the neutral charge state of the SiV center for quantum applications, specifically as a spin-photon interface, as it combines both excellent spin coherence and favorable optical properties [5].

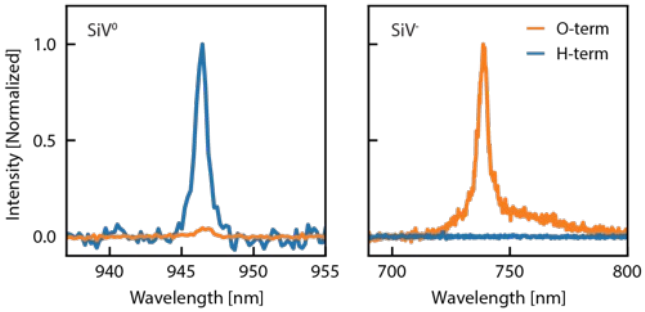

Fig. 2: Emission spectra of an SiV center in an undoped electronic grade diamond under different surface terminations.

Summary

Project P2003 has reached significant milestones this year, including the investigation of a method to optically stabilize the charge environment of single emitters, producing lifetime-limited optical linewidths in shallow emitters, a defining requirement for single-spin magnetometry Additionally, we have continued the charge state dynamics of the SiV center in diamond, having found a way to stabilize SiV^0 as well as converting it back to SiV^-. The next steps for this project include the nano-fabrication of scanning probe cantilevers containing SiV centers, achieving all-optical spin control [6] and finally, proof-of-principle all-optical single-spin magnetometry at high magnetic fields and ultra-low temperatures.

References

[1] L. J. Rogers, K. D. Jahnke, M. W. Doherty, A. Dietrich, L. P. McGuinness et al., Electronic structure of the negatively charged silicon-vacancy center in diamond, Physical Review B, 89(23), 235101 (2014)

[2] L. Thiel, Z. Wang, M. A. Tschudin, D. Rohner, I. Gutiérrez-Lezama et al., Probing magnetism in 2D materials at the nanoscale with single-spin microscopy. Science, 364 6444, 973-976 (2019)

[3] J. A. Zuber, M. Li, M. Grimau Puigibert, J. Happacher, P. Reiser et al., Shallow Silicon Vacancy Centers with Lifetime-Limited Optical Linewidths in Diamond Nanostructures, Nano letters 2023, 23, 23, 10901-10907 (2023)

[4] Z-H. Zhang, J. A. Zuber, L. V. H. Rodgers, X. Gui, X., P. Stevenson, et al., Neutral Silicon Vacancy Centers in Undoped Diamond via Surface Control, Phys. rev. letters, 130 166902 (2023)

[5] B. C. Rose, D. Huang, Z-H. Zhang, A. M. Tyryshkin, S. Sangtawesin, S. Srinivasan, et al., Observation of an environmentally insensitive solid-state spin defect in diamond, Science, 361 6397, 60-63 (2018)

[6] J. N. Becker, B. Pingault, D. Groß, M. Gündoğan, N. Kukharchyk, et al., All-optical control of the silicon-vacancy spin in diamond at millikelvin temperatures, Phys. rev. letters, 120(5), 053603 (2018)

Complex surface structure of the multiferroic Rashba semiconductor (GeMn)Te

Project P2004: Local manipulation of spin domains in a multiferroic Rashba semiconductor
Project Leader: M. Muntwiler and T. Jung
Collaborator: M. Heinrich (SNI PhD Student)

Introduction
Multiferroic materials are promising candidates to bridge the gap between traditional electronics and spintronics, since they exhibit coupled ferroic orders, such as ferromagnetism, ferroelectricity and ferroelasticity in the same system [1]. Such coupling could be used to manipulate spins via electric fields (magnetoelectric coupling) rather than energy consuming high magnetic fields and would allow to design smaller and faster computation devices.

Project goals
α-GeTe is a ferroelectric semiconductor with a rhombohedral bulk lattice which recently gained renewed attention due to the discovery of a large Rashba spin splitting in both bulk and surface bands. It was shown that doping with Mn induces ferromagnetic order in $Ge_{1-x}Mn_xTe$ which couples to the ferroelectric polarization. This magnetoelectric effect allows us to switch the surface spin polarization via an applied electric field [2]. As the polarizability of the material on the one hand and the atomic structure on the other hand seem to differ between the surface and the bulk, in this project, we conduct a multi-technique and multi-scale investigation of the surface atomic, electronic and magnetic structure of (GeMn)Te(111). We study the correlation between atomic structure and ferroic polarization as well as the role and importance of ferroic domains and domain walls.

We use synchrotron based photoelectron spectroscopy (XPS, ARPES) and diffraction (XPD, PhD) techniques as well as scanning tunneling microscopy (STM) and spectroscopy (STS) to probe complementary aspects of atomic and electronic structure at the surface of the materials. Using x-ray photoelectron diffraction (XPD, PhD) measurements and corresponding multiple scattering calculations [3], we determine the surface relaxation of GeTe(111) in the static case as well as in operando under an applied external field. In addition, we probe the electronic structure of (GeMn)Te(111) using angle-resolved photoelectron spectroscopy (ARPES) and, on the local scale, scanning tunneling spectroscopy (STS).

Results
The project started in July 2021. In the past months, we performed STM and STS measurements of GeTe(111) and $Ge_{1-x}Mn_xTe$(111) samples with different Mn concentrations. Figure 1a is an overview topographic picture of a high quality GeTe(111) thin film grown by molecular beam epitaxy (MBE). The film exposes large, flat terraces with an average step height of 3.6 Å (single Ge-Te layer). Zooming in to atomic resolution on a flat terrace, panel c) shows the Te terminated hexagonal surface lattice with a lattice constant of 4.16 Å interspersed with triangular shaped atomic defects in the top or sub-surface layers. In addition, we observe minority domains resembling a scale pattern, shown in figure 1b), accompanied by small steps at their sides. These domains originate from a rhombohedral bulk lattice distortion in oblique directions (i.e. in [11-1] and equivalent directions) and the observed small steps help to release the strain caused by the crystallographic mismatch between neighboring domains.

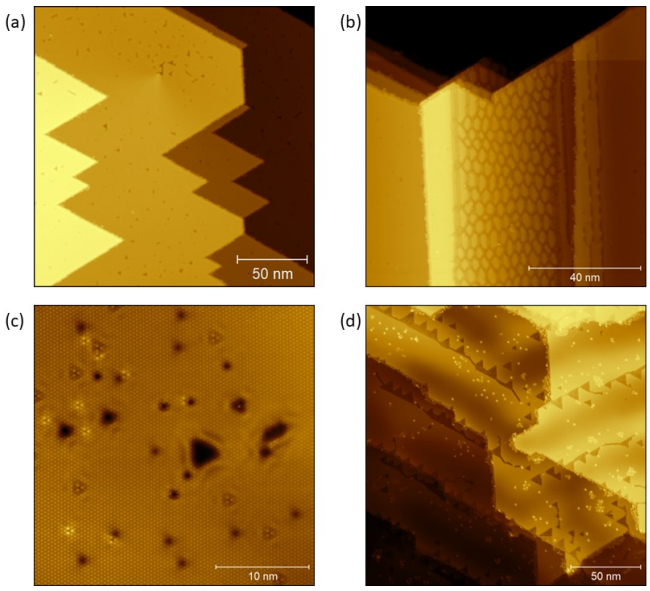

Fig. 1: a) Overview STM image of the regular GeTe(111) surface. b) Oblique domain in the form of a scale pattern observed on GeTe(111). c) Atomic resolution image of GeTe(111). d) Overview STM image of $Ge_{0.85}Mn_{0.15}Te$(111) depicting surface modulations and numerous triangular surface defects.

Figure 1d shows an overview STM picture of the surface of a $Ge_{0.85}Mn_{0.15}Te$(111) thin film. On top of a large-scale terrace structure similar to pure GeTe(111) (Fig. 1a-c), we observe numerous triangular shaped defects, adsorbed clusters (bright dots) and slight surface modulations visible by elongated bright and dark areas. The structural details and origin of these surface structures are currently under investigation.

The electronic structure of regular Te terminated hexagonal GeTe(111), as measured by ARPES and STS is depicted in figure 2. dI/dV curves, representing the local density of states, exhibit three dominating features that are attributed to two surface states (SS1 and SS2) as well as a surface resonance (SR1) based on a comparison with theoretical calculations [4]. Though STS normally probes the momentum-integrated density of states, momentum information can be extracted in Fourier transform STM (FT-STM) [5] from standing wave patterns like the ones visible around the dark defects in fig-

ure 1c. Such a local Fermi surface map of GeTe(111) is shown in figure 2b and compared to spatially averaged ARPES data (Fermi surface slice in figure 2c. We can clearly identify and distinguish the Rashba split surface states in both the FT-STM picture as well as in the ARPES Fermi surface slice. The goal here is to distinguish electronic band structures of different ferroelectric domains and understand their contribu tion to the multiferroic coupling.

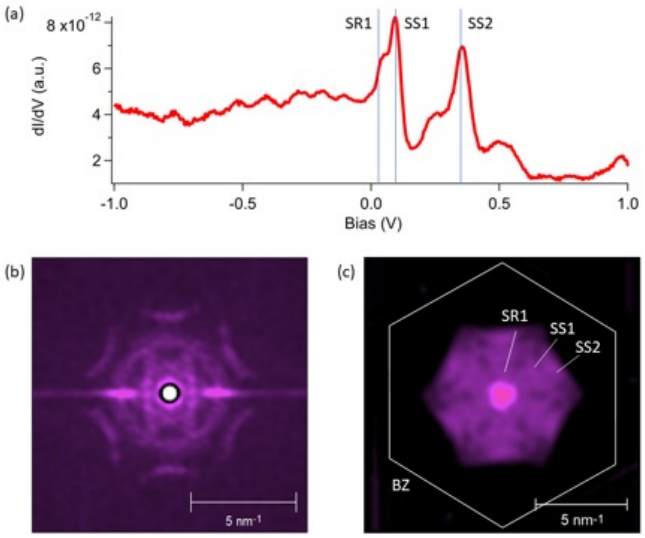

Fig. 2: a) dI/dV curve of the LDOS acquired on a Te terminated GeTe(111) surface. Distinctive features such as the onset of both surface states SS_1 & SS_2 as well as a surface resonance SR_1 are visible. b) and c) show Fermi surfaces measured by FT-STM and ARPES respectively. The Rashba split surface states SS_1 & SS_2, a surface resonance feature SR_1 as well as the Brillouin zone are indicated in c).

Outlook

Our focus in the coming months is to study the surface magnetic structure and the magnetoelectric coupling in $Ge_{1-x}Mn_xTe$(111). To this goal, a superconductive magnetic coil able to produce out-of-plane magnetic fields up to 150 mT has been installed in our STM and first spin-polarized STM measurements on reference samples are scheduled. SP-STM and SP-STS will allow us to map the surface spin orientation on an atomic scale and to probe the magnetoelectric coupling under the applied electric field of the STM tip.

References

[1] N. Spaldin, S. Cheong and R. Ramesh, Multiferroics: Past, present, and future, Physics Today 63, 38-43 (2010)

[2] J. Krempaský, S. Muff, J. Minàr, N. Pilet, M. Fanciulli et al., Operando Imaging of All-Electric Spin Texture Manipulation in Ferroelectric and Multiferroic Rashba Semiconductors, Phys. Rev. X 8, 021067 (2018)

[3] J. García de Abajo, M. A. Van Hove, and C. S. Fadley, Multiple scattering of electrons in solids and molecules: A cluster-model approach, Phys. Rev. B 63, 075404 (2001)

[4] J. Krempaský, M. Fanciulli, N. Pilet, J. Minàr, W. Khan et al., Spin-resolved electronic structure of ferroelectric α-GeTe and multiferroic $Ge_{1-x}Mn_xTe$, J. Phys. Chem. Solids 128, 237-244 (2019)

[5] L. Petersen, P. T. Sprunger, P. Hofmann, E. Laegsgaard, B. G. Briner et al., Direct imaging of the two-dimensional Fermi contour: Fourier-transform STM, Phys. Rev. B 57, R6858(R) (1998)

Employing a bacterial toxin component for controlled compartment fusion and cargo transfer in artificial systems

Project P2005: Transmembrane protein-mediated loading of synthetic compartments
Project Leader: C. G. Palivan, R. A. Kammerer and S. Gros
Collaborator: P. Jaśko (SNI PhD Student)

Compartmentalization, a prerequisite for the spatiotemporal control of biochemical pathways in cells, is a fundamental concept in designing new materials for medical and technological applications. Synthetic nano- and micro-compartments (NCs, MCs), with their chemical versatility and superior stability provide the basis for developing catalytic compartments, artificial organelles, or cell mimics that can be tailored and loaded with specific biomolecules. However, a higher selective loading efficiency and better permeability of the synthetic membrane remain hurdles that need to be overcome to increase the efficacy of in situ reactions [1, 2].

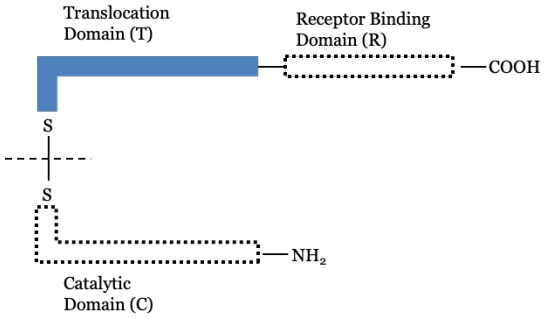

Fig. 1: Schematic representation of the architecture shared by the studied toxins. Our recombinant toxins are devoid of the receptor-binding domain (R) and catalytic domain (C).

Engineering bacterial toxins which inherently exert their cytotoxic activity through membrane remodeling to deliver enzymes into cells, hold great potential to tackle these hurdles (Fig. 1). Despite three decades of extensive research on this type of bacterial toxins, little is known about the structural and molecular basis underlying their interaction and insertion into the membrane, a prerequisite for their protein cargo release [3]. By improving our understanding of how the toxins operate in the presence of native-like (liposomes) and synthetic amphiphilic block copolymer (polymersomes) membranes, we aim to confer the feature of protein-mediated cargo delivery on NCs. In particular, we are interested to explore a novel mode of action of one of the studied toxins which proposes the toxin's ability to mediate vesicle fission and fusion [4]. We aim to test further whether in situ vesicle fusion is a feasible process that can be controlled in spatiotemporal manner ultimately leading to the fabrication of biohybrid systems whose content is modulated through the NCs fusion.

This interdisciplinary project encompasses the design and production of recombinant toxin components and the development of compartments with native-like and synthetic membranes made of phospholipids and amphiphilic block copolymers, respectively. Purified recombinant proteins are used initially to scrutinize conditions that promote their interactions with the membrane, ultimately resulting in their integration with the compartment membrane. Moreover, mutagenesis of the bacterial toxin allows us to systematically dissect the specific regions of the toxin responsible for facilitating its interaction with the NC. This detailed examination provides insights into the mechanism leading to the fusion of NCs, orchestrating the formation of MCs with precise spatiotemporal control over the entire process. By exploring the structural and functional features of the toxin proteins, we plan to develop a tool for functional coupling of distant biohybridized NCs. Preloaded vesicles will merge upon toxin addition facilitating their content mix as an alternative for cargo delivery (Fig. 2).

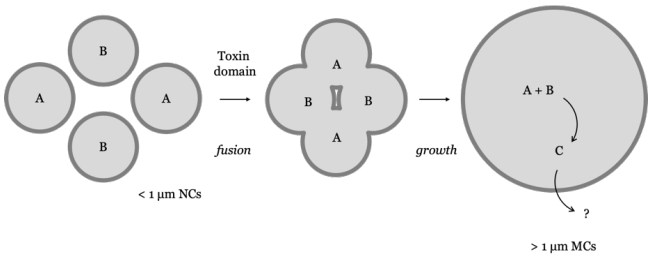

Fig. 2: Model of enzyme delivery by compartment fusion mediated by bacterial toxin-based vehicles.

The toxin domain we use shares an affinity towards negatively charged membranes. Under physiological conditions, the toxin domain effectively induces fusion between membranes with similar compositions, leading to the fusion of different nano-compartments. As a result, contents of vesicle A and B are combined facilitating in situ reactions within the emerging MC. In addition to testing MC stability, we will evaluate their membrane permeability.

We applied molecular biology techniques that allowed us to establish the production of recombinant proteins. In order to study the interaction between the recombinant toxin and the native-like and synthetic membranes, we introduced mutations in key amino residues believed to mediate this interaction. Using biophysical techniques such as circular dichroism (CD) and nano-differential scanning fluorimetry (nanoDSF), we examined the mutants' stability. The goal was to uncover any connections between toxin stability, its interaction with membranes, and its involvement in vesicle fusion. We produced large lipid unilamellar vesicles (LUVs) with varied negative charge content as well as we modulated the vesicle size, to mimic cell membranes for in situ functionality assessment of protein variants. In addition, we monitored the interaction of the purified toxin variants with vesicle membranes by a calcein-release assay and evaluated

the stability of proteoliposomes by means of fluorescence correlation spectroscopy (FCS), light scattering techniques, and electron microscopy (EM). The fusion process was examined using confocal laser scanning microscopy (CLSM). To visualize giant unilamellar vesicles (GUVs), we enhanced our LUVs preparation by implementing fluorescent lipids. The results on lipidic compartments represent a first step to demonstrate the interaction of the recombinant toxins with lipid membranes. This will serve to indicate the properties the synthetic membranes should possess for functional insertion. Therefore it will allow selection of the suitable amphiphilic block copolymers, e.g., functionalized with specific end groups (negatively charged) that will cope with the toxin-membrane interaction.

Our studies suggest that the interaction of the studied toxin with lipidic LUV membranes depends highly on negatively charged groups on the membrane surface. Moreover, our results indicate a novel role in nano-vesicle fusion for one of the bacterial toxins. In particular, a mutant toxin fragment had the tendency to mediate fusion of two adjacent membranes. The fusion of NCs results in the formation of MCs of homogenous size NCs (Fig. 3). In addition, studies carried out with polymersomes (polymeric LUVs) revealed that the fusion of polymersomes into polymeric GUVs is also possible (Fig. 4). Owing to the chemical versatility and size tunability of amphiphilic block copolymers parameters of lipidic systems that yielded the most desirable results in the toxin-mediated vesicle fusion can be easily modified. We plan to optimize the synthetic compartments such that they serve as a platform for the interaction with recombinant toxins ultimately.

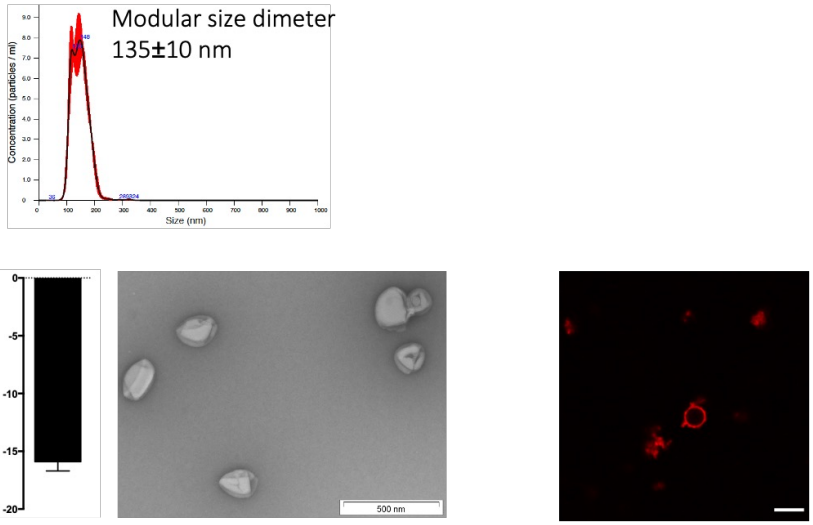

Fig. 4: Nanoparticle tracking analysis (NTA) of polymersomes (top panel) carrying negative charge corroborated by the zeta potential measurement with their typical morphology represented by negative-stain TEM (bottom left panel) – scale bar 500 nm. Polymersomes fuse into polymeric GUVs upon toxin addition as revealed by CLSM imaging with BODIPY dye-stained membrane (bottom right panel)—scale bar 5 µm.

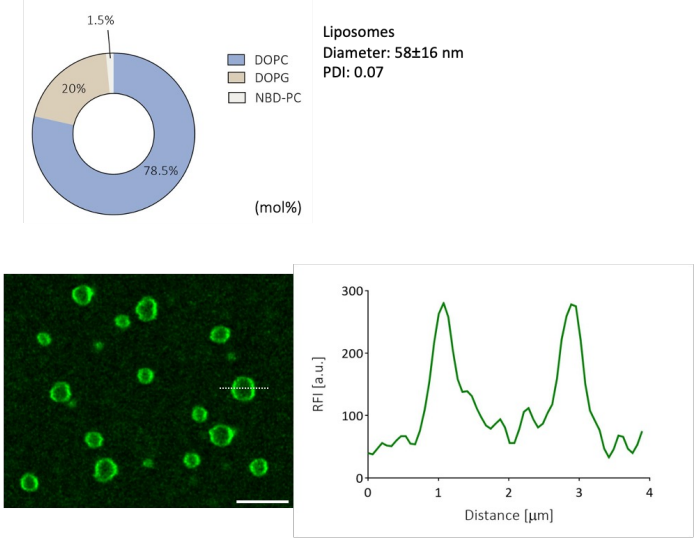

Fig. 3: DLS analysis of liposomes with their composition (top panel). The presence of DOPG ensures negative charge whereas NBD-PC fluorescent signal that is further recorded by CLSM (bottom left panel) in fused liposomes upon toxin addition. Emerged GUVs are of homogenous size with a typical 2 µm diameter (bottom right panel). Scale bar 5 µm.

References

[1] E. C. Dos Santos, A. Belluati, D. Necula, D. Scherrer, C. E. Meyer, R. P. Wehr, E. Lörtscher, C. G. Palivan, W. Meier, Combinatorial Strategy for Studying Biochemical Pathways in Double Emulsion Templated Cell-Sized Compartments. Adv Mater. 32, 48 (2020)

[2] V. Maffeis, A. Belluati, I. Craciun, D. Wu, S. Novak, C. A. Schoenenberger, C. G. Palivan, Clustering of catalytic nanocompartments for enhancing an extracellular non-native cascade reaction, Chem Sci. 12, 37 (2021)

[3] R. A. Kammerer, R. M. Benoit, Botulinum neurotoxins: new questions arising from structural biology, Trends Biochem. Sci. 39, 11 (2014)

[4] D. Pei, How Do Biomolecules Cross the Cell Membrane?, Acc. Chem. Res. 55, 3 (2022)

Surface chemistry and self-assembly studies of zirconium and hafnium oxo clusters

Project P2006: RESTRAIN – Reticular chemistry at interfaces as a form of nanotechnology
Project Leader: P. Shahgaldian and J. De Roo
Collaborator: A. Roshan (SNI PhD Student)

Introduction

Group IV metal oxo clusters are considered the smallest conceivable atomically precise nanocrystal prototypes due to their structurally analogous inorganic core capped with organic ligand shell [1]. Owing to the same, oxo clusters are being used as precursors for the synthesis of nanocrystals [2], and metal-organic frameworks [3]. Oxide nanocrystals are the compositionally closest ones to metal oxo clusters (Fig. 1). Though the field of group IV nanocrystals is not directly bridged with clusters so far, both classes of compounds have many features in common, including the same precursors. The formation mechanism, size-, shape-, and surface-tuning of oxide nanocrystals are widely explored. Such a broad investigation on the surface chemistry of group IV metal oxo clusters with different classes of ligands has not been done yet. Here, we study the surface chemistry of fully condensed zirconium and hafnium oxo clusters through ligand exchange reactions, both computationally and experimentally. We evaluate the influence of different phosphorus ligands on cluster surface and core. The insights on cluster surface chemistry will be further used to make 2D metal-organic frameworks (MOFs) in a controlled fashion.

Surface chemistry of oxo clusters

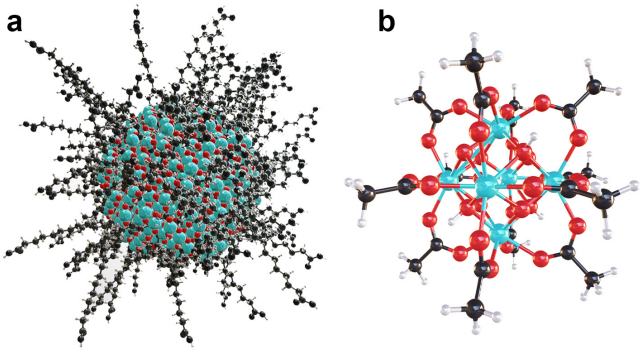

Fig. 1: a) Schematic representation of a colloidally stable zirconium/hafnium oxide nanocrystal depicting the inorganic core and organic ligand shell. b) The structure of fully condensed metal oxo cluster - $M_6O_4(OH)_4(OOCR)_{12}$, where the M_6O_8 core is capped with twelve carboxylate ligands, M=Zr/Hf.

The solubility and thereby the stability of colloidally stable nanocrystals are provided by capping ligands. Recently, surface chemistry studies elucidated the binding affinity of different classes of ligands on nanocrystals with an order of phosphonic acids ($RPO(OH)_2$) > phosphinic acids ($R_2PO(OH)$) > carboxylic acids (RCOOH)[4]. Similarly, we aim to manipulate the surface and morphology of Zr/Hf oxo clusters through ligand exchange reactions. We started from a fully condensed carboxylate-capped cluster and reacted them with phosphinic and phosphonic acids. As cluster model systems, we choose Zr12-acetate, which is a dimer of Zr6 cluster and synthesized according to our earlier report [5]. Regardless of dimer or monomer structure, each $Zr_6O_4(OH)_4^{12+}$ octahedron is coordinated by 12 carboxylate ligands. The original carboxylate ligands were exchanged by phosphinic or phosphonic acids, with varying sterical hindrance. To assess ligand exchange reactions, we choose to gradually titrate with the new ligand. In case of irreversible exchange, the complete ligand shell should be exchanged upon the addition of 12 equivalents.

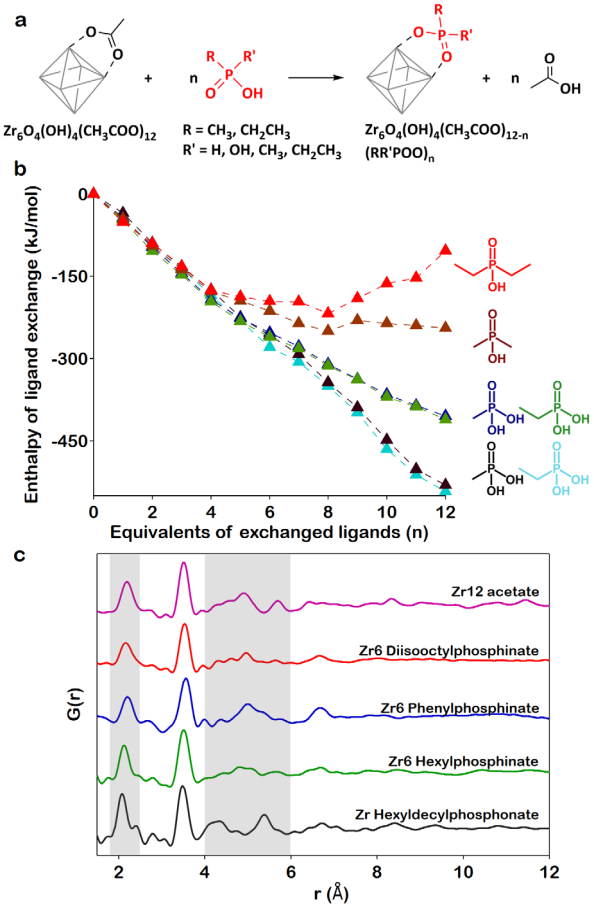

Fig. 2: a) Scheme representing the exchange of phosphonic acids and mono and dialkyl phosphinic acids with acetate ligands on a fully bridged Zr6 cluster. (b) Enthalpy of ligand exchange reactions as a function of equivalents of exchanged ligands obtained from DFT calculations. (c) PDF pattern obtained after ligand exchange. The major changes in the structural features are indicated.

Prior to experimental titrations, we evaluated the surface compatibility of ligands of interest on zirconium oxo clusters through density functional theory (DFT) calculations. Starting from a Zr6 monomer structure, each acetate ligand was exchanged with the ligand of interest in twelve steps. The enthalpy of ligand exchange reactions as a function of the equivalent of incoming ligands was plotted in figure 2b. Monoalkylphosphinate and phosphonate-capped clusters were thermodynamic-cally stable even after full exchange, and the length of the aliphatic chain has a minimal impact. The extra stability of phosphonate-capped clusters can be attributed to the presence of hydrogen bonds from the second hydroxyl functionality. Interestingly, in the case of dialkyl phosphinic acids, the ligand exchange beyond eight equivalents was not thermodynamically favorable. The bulkier the ligands, the harder the complete ligand exchange. To evaluate the DFT results, we performed the ligand exchanges experimentally and characterized with pair-distribution analysis (PDF) (Fig. 2c). We figured out that monoalkylphosphinic acids (phenyl and hexyl) can be fully exchanged to yield phosphinate capped Zr6 clusters. In line with the computational calculations, dialkylphosphinates cannot be fully exchanged resulting in mixed-shell clusters with both acetate and dialkylphosphinate as capping ligands. Surprisingly, after phosphonate exchange, cluster core structure is no longer preserved and is being disrupted to form layered zirconium phosphonate structures. This is macroscopically observed as a gel. This can be attributed to the second acidic group of phosphonates, enabling to bind the metal in tridentate mode. In summary, we infer that despite similarities with nanocrystals, the surface chemistry of clusters is quite different.

Self-assembly of oxo clusters

Metal oxo clusters are the secondary building units (SBUs) of group IV 2D MOFs. 2D MOFs consist of a single layer or stacked multiple layers of organic-inorganic hybrid material nanosheets in one direction. Such a layered structure enables 2D MOFs to increase the active metal sites, which reflects in higher catalytic activity, improved porosity and specific surface area, and better electrical conductivity than 3D MOFs [6]. One of the most widely used bottom-up approaches to synthesizing 2D MOFs is the interface-assisted method, where the metal ions/clusters and organic linkers are forced to react and grow at a confined interface. Herein, we report the first air-water interface-assisted synthesis of group IV 2D MOFs starting from tailor-made metal oxo cluster SBUs at room temperature. We target the 2D analog of the well-known MOF - UiO-66, where the terephthalic acid links the Zr6 SBUs. To confine the anisotropic growth of 2D MOFs at the surface, we produced a series of amphiphilic terephthalates bearing hydrophobic alkyl chains and hydrophilic carboxylate groups (Fig. 3a). We infer that these designer amphiphiles can readily form rigid monolayers at the surface of an aqueous cluster solution through Langmuir monolayer studies. The self-assembled monolayers produced at the air-water interface were transferred onto hydrophobic substrates (highly oriented pyrolytic graphite, HOPG), using the Langmuir-Schaefer (LS) technique.

High-resolution images of the transferred monolayer were obtained by means of atomic force microscopy (Fig. 3c). The average thickness of the monolayer was measured at 1.6 ± 0.5 nm; this is in good agreement with the theoretical values of the oxo cluster-amphiphilic terephthalate molecular model (Fig. 3b). Additionally, XPS analysis (Fig. 3d) indicates the incorporation of Zr oxo clusters in the monolayer confirming the formation of a 2D MOF.

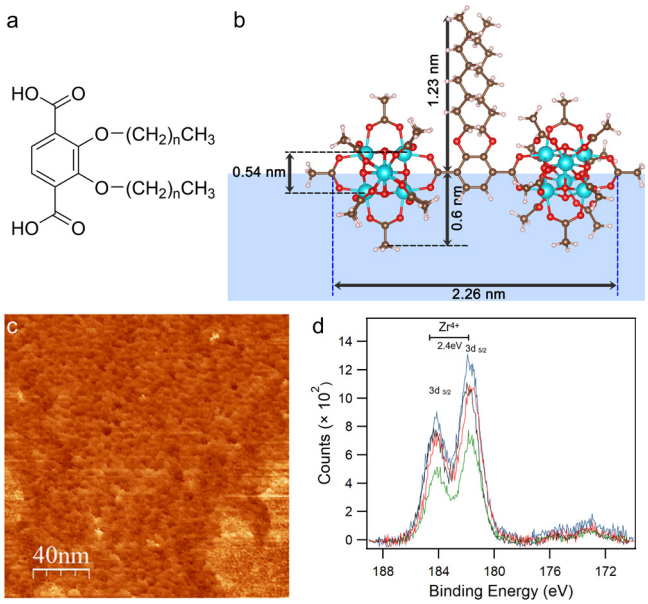

Fig. 3: a) Structure of amphiphilic organic linkers - terephthalates (n = 2, 7, 11). b) Proposed schematic molecular model of 2D MOF at the air-water interface with dimensions. c) High-resolution AFM micrographs and d) X-ray photoelectron spectra of zirconium acetate cluster-2,3-bis(octyloxy)terephthalic acid monolayer.

References

[1] D. Van den Eynden, R. Pokratath, J. De Roo, Nonaqueous Chemistry of Group 4 Oxo Clusters and Colloidal Metal Oxide Nanocrystals. Chem. Rev. 122, 10538–10572 (2022)

[2] M. A. Sliem, D. A. Schmidt, A. Bétard, S. B. Kalidindi, S. Gross et al. Surfactant-Induced Nonhydrolytic Synthesis of Phase-Pure ZrO2 Nanoparticles from Metal–Organic and Oxocluster Precursors. Chem. Mater. 24, 4274–4282 (2012)

[3] A. A. Bezrukov, K. W. Törnroos, E. Le Roux, P. D. C. Dietzel, Incorporation of an intact dimeric Zr12 oxo cluster from a molecular precursor in a new zirconium metal–organic framework. Chem. Comm. 54, 2735–2738 (2018)

[4] E. Dhaene, R. Pokratath, O. Aalling-Frederiksen, K. M. O. Jensen, P. F. Smet et al. Monoalkyl Phosphinic Acids as Ligands in Nanocrystal Synthesis. ACS Nano 16, 7361–7372 (2022)

[5] D. Van den Eynden, R. Pokratath, J. P. Mathew, E. Goossens, K. De Buysser et al. Fatty acid capped, metal oxo clusters as the smallest conceivable nanocrystal prototypes. Chem. Sci. 14, 573-585 (2023)

[6] G. Chakraborty, I.-H. Park, R. Medishetty, J. J. Vittal, Two-Dimensional Metal- Organic Framework Materials: Synthesis, Structures, Properties and Applications. Chem. Rev. 121, 3751–3891 (2021)

Focused acoustic radiation for efficient acousto-fluidic manipulation

Project P2007: Development of nanoscale acoustic tweezers for mechanobiology application
Project Leader: S. Tsujino and R. H. Y. Lim
Collaborator: S. Jia (SNI PhD Student)

Introduction

We are developing an acoustic tweezer driven by the surface acoustic wave (SAW) ultrasound transducers. To reach the goal of achieving high-spatial-resolution and high efficiency acoustofluidic manipulation of particles as well as soft matters in liquid environment, we explore the focusing of ultrasound into the fluidic channel.

Acoustic tweezers reported in literature commonly comprise the fluidic bath fabricated from PDMS (polydimethylsiloxane) and the ultrasound transducers such as SAW devices fabricated on the surface of a piezoelectric substrate [1]. However, their efficiency is normally limited since PDMS strongly attenuates the incident ultrasound radiation [2], which results in low acoustic transmission into the fluid [3]. This hinders efficient particle handling by acoustic radiation force. However, higher excitation efficiency is desired for high throughput sample handling with limited heating of the fluidic channel, especially for the manipulation of biological samples. To surmount the limitation, various efforts have been made on SAW transducers [4], microfluidic channels [5] and also the way these two are integrated [3]. In our approach, we combine a SAW device fabricated on a piezoelectric substrate with a microfluidic chip separately fabricated on a silicon substrate together with the geometrical shaping of the chip via deep reactive ion etching (RIE) for enhanced acoustic coupling. Our preliminary results described below show the effectiveness of this approach with an order of magnitude enhancement in the acoustic radiation force in the channel.

Materials and methods

We fabricated microfluidic chips on a silicon wafer by photolithography and deep RIE. The channel widths were chosen to be an integral multiple of the half wavelength of the ultrasound frequency which is to be determined by the device structure of the SAW chip. The SAW chip was fabricated on a SAW-grade $LiNbO_3$ substrate: the interdigitated electrodes were patterned by evaporation and etching. Using the direct laser writer DWL66$^+$, SAW chips with the SAW frequencies of 10, 20, 50, 100 MHz have been fabricated so far. For the manipulation of particles up to ~20 μm in water, we focused on the use of 50 MHz SAW chip with the finger width and spacing between two adjacent electrodes being 20 μm. For the acoustofluidic experiments, the silicon microfluidic chips are mounted on the SAW chip with intimate acoustic transmission. The top of the silicon microfluidic chip is sealed by thin glass plates.

Enhancing acoustic radiation by acoustic horns

The results of characterizing the acoustofluidic chips using 3-micron polyethylene particles in DI water are displayed in figure 1 and figure 2. The images in figure 1 are taken

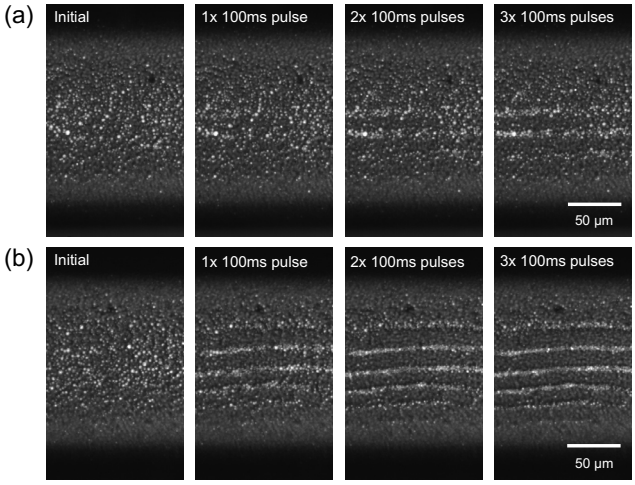

Fig. 1: a)-b) From the left to the right: particle distribution in the initial state, and after one, two, and three 100 ms ultrasound pulses, observed in the silicon chip with and without acoustic horns, respectively.

from above the acoustofluidic channels, at the centre of those, where the ultrasound power is the highest. The fluidic channel and its walls lie along the horizontal direction. The sequence of the recorded images in figure 1 display the distribution of the particles, from the left to the right, as the particles, initially randomly distributed, are moved along the lines with the spacing of ~16 micron as 100 ms ultrasound pulses are applied multiple times. The spacing corresponds to the ½ wavelength of the ultrasound in water. The width of the fluidic channels is chosen to be an integral multiple of the ultrasound wavelength driving the chip as described before. In this standing wave condition, the acoustic radiation force moves the polyethylene particles in the water toward the node lines that are parallel to the acoustic fluidic channels.

In the case of figure 1b, we enhanced the coupling of the ultrasound radiation into the fluidic channel by patterning the silicon chip in the shape of a focusing horn. As a result, the particles are moved to the acoustic node lines much more strongly, even with a single pulse (second from the left) with the same duration and nominally the same ultrasound output from the SAW chip as in the case of figure 1a.

For quantifying the acoustic radiation pressure in the acoustofluidic channels, we analysed the particle trajectories and calculated their velocities. Then the acoustic radiation force F_y^{rad} is obtained by equating it with the viscous Stokes drag force in y direction (transverse direction) [6], i.e., $F_y^{rad} = 6\pi\eta r v_y$, where η, r, and v_y are the dynamic viscosity of water, the radius of particle, and the particle velocity in the

y direction (transverse direction), respectively. The inertial effect is neglected. The results are shown in figure 2a as functions of the particle position in the y-direction for two cases, when the estimated acoustic pressure (excitation voltage) is increased by a factor of 2.

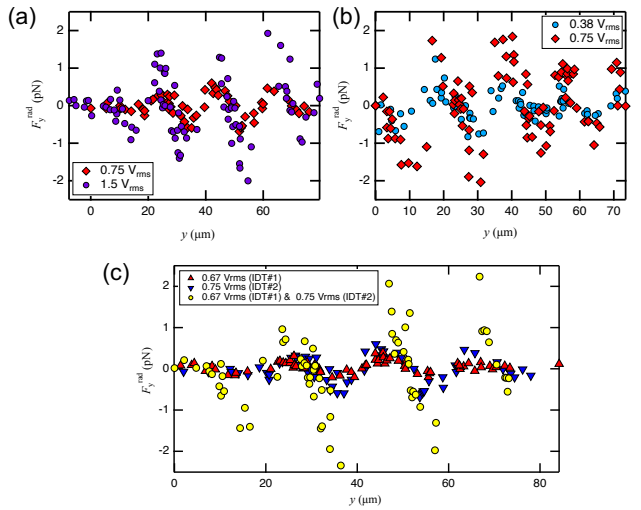

Fig. 2: Acoustic radiation force as a function of the particle position in the y axis in the microfluidic channels a) with and b) without acoustic horns. c) Acoustic radiation force as a function of the particle position in the y axis in the microfluidic channel without acoustic horns when two IDTs are driven simultaneously.

The comparison of the two results shown in figure 1a and b as well as in figure 2a and b indicates that the focusing of the ultrasound in our chip was effective to increase the acoustic radiation force per unit excitation power more than a factor of 4.

The acoustic radiation force was further enhanced by using two SAW transducers at both sides of the acoustofluidic chips: As figure 2c shows, the ultrasound input from both sides with the same nominal acoustic pressure resulted in a factor-of-4 increase as expected to the coherent superposition of the two inputs.

Summary

In our development of the acoustic tweezers based on SAW devices, we have introduced a new way of improving the efficiency of acoustofluidic manipulation. The dominant dependence of such enhancement on the structure of the silicon chip brings versability to this concept in that a conventional linear SAW interdigital transducer (IDT) can be integrated with a silicon chip tailored for specific needs. Further enhancement of the ultrasound excitation efficiency, increasing the driving frequency, and application of the developed method for soft matters and biological specimens are under way.

References

[1] Y. Gao, Y. Li, X. Ding, Acoustofluidic technology for cell biophysics, Micro and Nano Systems for Biophysical Studies of Cells and Small Organisms, 153-171 (2021)

[2] T. Franke, S. Braunmüller, L. Schmid, A. Wixforth, D. A. Weitz, Surface acoustic wave actuated cell sorting (SAWACS), Lab Chip 10, 789-794 (2010)

[3] S. M. Langelier, L. Y. Yeo, J. Friend, UV epoxy bonding for enhanced SAW transmission and microscale acoustofluidic integration, Lap Chip 12, 2970-2976 (2012)

[4] D. J. Collins, A. Neild, Y. Ai, Highly focused high-frequency travelling surface acoustic waves (SAW) for rapid single-particle sorting, Lab Chip 16, 471-47 (2016)

[5] M. Cui, S. K. Dutcher, P. V. Bayly, J. M. Meacham, Robust acoustic trapping and perturbation of single-cell microswimmers illuminate three-dimensional swimming and ciliary coordination, Proc. Natl. Acd. Sci. USA 120 (2023)

[6] H. Bruus, Acoustic Radiation Force on Small Particles, Microscale Acoustofluidics, The Royal Society of Chemistry, ch. 4, pp. 65-80 (2014)

Integrating a nanowire quantum dot on a scanning probe tip

Project P2008: Scanning nanowire quantum dot
Project Leader: D. Zumbühl and M. Poggio
Collaborator: L. Forrer (SNI PhD Student)

Introduction

In this project, we intend to develop a new kind of scanning probe microscope, which employs gated quantum dots (QDs) embedded in semiconductor nanowires (NWs), integrated on the tips of standard force microscopy cantilevers. These sensors will be sensitive scanning probes of charge and electronic density [1]. The sensors will be used to characterize the spatial profile of charge noise, quantum dots, and electric fields [2] in spin qubit devices, aiding the design of coherent quantum computation processors. This is particularly relevant here in the Department of Physics of the University of Basel, where the NCCR SPIN, aimed at producing scalable spin qubits in Si was established in summer 2020.

Our scanning probe method builds on previously developed scanning single-electron transistors (SETs) made from metallic islands [1] and scanning QDs defined in carbon nanotubes (CNTs) [2]. Research efforts using such devices have been extremely fruitful, due to the high sensitivity to electric field. Indeed, QD-based sensors are the preferred sensors of charge in applications in quantum computation with spins in QDs, where they are incorporated on the same substrate as the sample of interest. Such charge sensors make use of sharp spikes in the electrical conductance of the QDs (Coulomb peaks) and are capable of detecting a small fraction of an electronic charge at micron distance. Until now, however, both scanning SETs and scanning QDs in CNTs have been relatively cumbersome to use, extremely delicate, and limited in their design. These drawbacks are a result of the specialized processes involved in their fabrication.

Our approach addresses this shortcoming by using standard AFM cantilevers as the scanning probe combined with NWs as the QD hosts. By developing a scheme for patterning leads, gates, and contacts directly to the cantilever tip [3], we will have maximum flexibility for the design of our sensors. AFM levers allow easy tip-sample distance control, topographic contrast. NW QDs possess many qualities that make them suitable for use in scanning probes: they are small (~10-50 nm), need few gates because of the natural 1D confinement, and can due to the low-dimensional geometry of the NW be easily brought closer than 100 nm to a sample. Importantly, their strong confinement and tunable nature endows NW QDs with a higher sensitivity to electric fields and nearby charges than their SET counterparts. Moreover, NW crystals can be grown with an exceptional control over material composition. The specific NW material composition can pass on useful properties to the embedded probe QDs, such as a strong spin-orbit interaction, which may offer interesting new modalities of sensing.

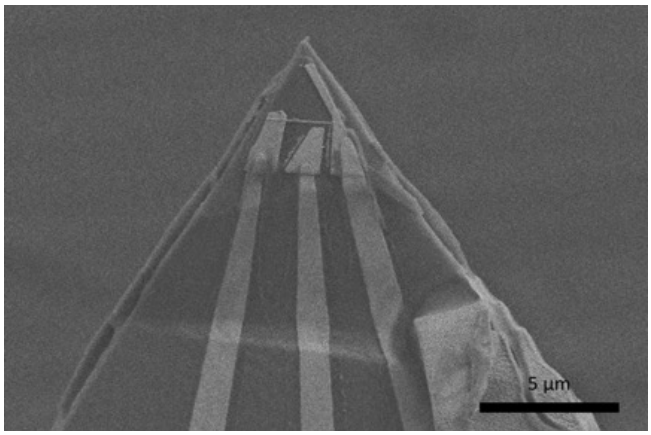

Fig. 1: A scanning electron micrograph of a patterned cantilever tip with a gate-controlled NW QD at its tip. We have recently realized such a working device and will soon implement it as a scanning probe as a highly sensitive tool for measuring small electric fields with nanometer-scale resolution.

Goals

The main goals of this project are to: 1) Fabricate scanning probe cantilevers hosting a NW with embedded gated QDs; 2) Image the electronic density of nanoscale samples with unprecedented sensitivity; 3) Implement high-bandwidth scanning probe imaging using microwave reflectometry techniques; 4) Image and study the dynamics of charge fluctuators in semiconducting devices.

Results

Early in this project, we developed new methods to pattern scanning probe cantilevers with nanostructures such as gate electrodes and contacts, using electron-beam lithography [3]. Our process involves coating cantilevers with a floating resist layer, which is then patterned with nanometer resolution (Fig. 2). We have tested the method for various kinds of cantilever shapes, which we pattern using focused-ion-beam milling. Summarizing, we are now able to make wide variety of gates, with dimensions down to 50 nm, and contacts suitable for QD control. This method gives us the opportunity to fabricate gates on the tip of our lever and contact NWs by evaporation of metal as done on conventional planar substrates [4,5].

We have demonstrated QD formation on substrates using our fabrication techniques and – very recently – we have successfully fabricated a NW QD on the tip of a cantilever designed for atomic force microscopy (AFM), seen in figure 1. We are currently characterizing this device and preparing a scanning probe experiment both to demonstrate its function and to take advantage of its capabilities to sensitively image electric fields.

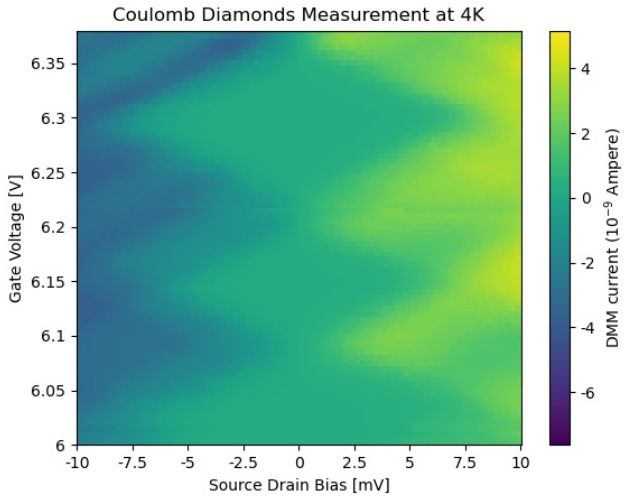

Fig. 2: Source-drain current measured as a function of source-drain bias and gate voltage in a NW QD device. Recently, we have realized a similar measurement for the NW QD on a cantilever tip shown in figure 1 [3].

Particularly important for this work is our design and construction of a custom-built high-vacuum and low-temperature scanning probe system to host such experiments. Building on designs using in the lab for magnetic force microscopy and scanning superconducting quantum interference device (SQUID) microscopy, the setup includes AFM control and a means to contact both low and high-frequency lines directly to both the sample and the scanning probe. In the next year, this design will be modified and applied to a new dilution refrigerator system, for which we recently obtained funding R'Equip funding from the Swiss National Science Foundation. This new instrument will allow us to reach the ultimate sensitivity of our probes by working at below 100 mK and allow us to investigate samples, such as superconducting qubits and topological insulators showing the quantum anomalous hall effect, that only function at very low temperature. Having assembled all the necessary instrumentation for implementing high-bandwidth microwave reflectometry read-out techniques and having developed a fabrication technique for patterning contacts and gates on AFM tips, we are also preparing advanced scanning gate microscopy experiments. In these measurements, we use our multiple on-tip gates to induce QDs in the substrate below and measure their charge state using both DC and microwave reflectometry techniques.

Outlook

In the final year of the project, we will apply the techniques that we have developed so far to to study defects and charge noise, which are the main source of decoherence in spin and superconducting qubit devices. Furthermore, by combining our multi-gate cantilevers with microwave reflectometry read-out techniques, we will be able to image QD formation and QD properties such as energy level splittings in pristine samples, such as ungated heterostructures, thin Si quantum wells, and NWs.

References

[1] M. J. Yoo, T. A. Fulton, H. F. Hess, R. L. Willett, L. N. Dunkleberger, et al., Scanning Single-Electron Transistor Microscopy: Imaging Individual Charges. Science 276, p. 579 (1997)

[2] L. Ella, A. Rozen, J. Birkbeck, M. Ben-Shalom, D. Perello, et al., Simultaneous voltage and current density imaging of flowing electrons in two dimensions, Nat. Nanotechnol. 14, p. 480 (2019)

[3] L. Forrer, A. Kamber, A. Knoll, M. Poggio, and F. Braakman, Electron-beam lithography of nanostructures at the tips of scanning probe cantilevers, AIP Adv. 13, 035208 (2023)

[4] F. S. Thomas, A. Baumgartner, L. Gubser, C. Jünger, G. Fülöp, et al. Highly symmetric and tunable tunnel couplings in InAs/InP nanowire heterostructure quantum dots, Nanotechnology. 31 (2020)

[5] F. N. M. Froning, M. Rehmann, J. Ridderbos, M. Brauns, F. A. Zwanenburg, et al., Single, double, and triple quantum dots in Ge/Si nanowires, APL. 113 (2018)

Graphene-organic interfaces for vertical electronic devices

Project P2009: Hybrid Van der Waals heterostructures for vertical permeable-base organic transistors
Project Leader: M. Calame
Collaborators: J. Oswald (Associate SNI PhD Student), D. Beretta, M. Stiefel, R. Furrer, S. Lohde, D. Vuillaume

Introduction
This report synthesizes the findings of two studies focusing on the unique properties and applications of graphene in the field of vertical organic transistors. Graphene, well known for its exceptional conductivity, flexibility, and optical transparency, plays a pivotal role in the development of advanced electronic devices. The content and figures of this report are partially reproduced from references [1] and [2]. Jacopo Oswald successfully defended his PhD thesis [3] entitled on Nov 15, 2023.

1. Effects of Organic Thin Films on Graphene's Charge Transport Properties
In a recent study [1], the interaction between graphene and organic molecules, particularly C60 and Pentacene, has been examined. Conducted on a sample of 300 graphene field-effect transistors, we explored how these molecules affect graphene's electrical characteristics under vacuum conditions. The study reveals that C60 thin films significantly increase the hole density in graphene by approximately 1.65 × 10^{12} cm^{-2}. This increase leads to a downshift in graphene's Fermi energy by about 100 meV. Conversely, Pentacene thin films are found to elevate the electron density by around 0.55 × 10^{12} cm^{-2}, resulting in an upshift of the Fermi energy by approximately 120 meV. Both types of molecular interaction result in a reduction of charge mobility and an increase in graphene's sheet resistance, approximately 3 kΩ at the Dirac point. Notably, despite these changes, the contact resistance, which varied be-tween 200 Ω and 1 kΩ, did not show significant alterations due to the deposition of these organic films.

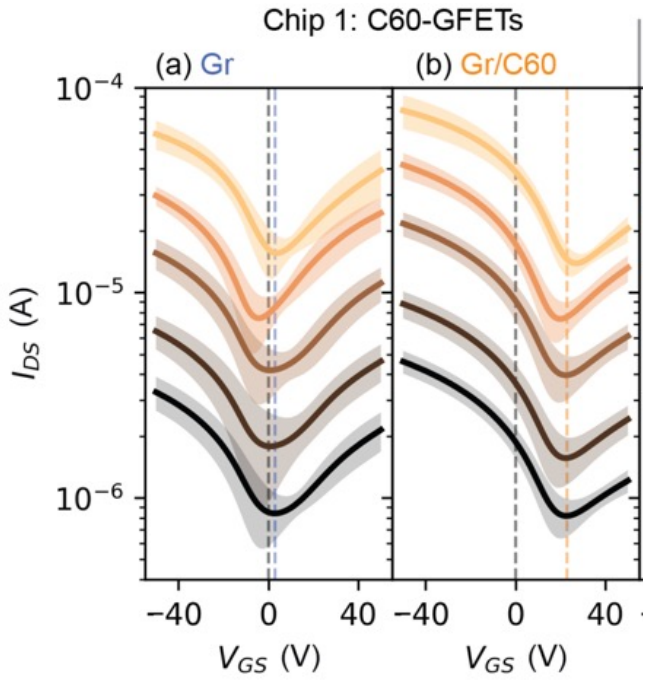

Fig. 1: Reproduced from [1]. GFETs' electrical measure-ments. a) Average transfer characteristic (IDS vs. VGS) of pristine CVD graphene FETs before C60 deposition (Chip 1, 101 devices, all L included). The shaded areas are the standard deviations. b) Average transfer char-acteristic of the C60-GFETs (Chip 1, 101 devices, all L included). L = 5 (light orang line), 10, 20, 50, 100 µm (black line).

2. Exploring Charge Injection Mechanisms in Graphene/Organic Semiconductor Interfaces
We also investigated the role of graphene in hybrid van der Waals heterostructures, particularly examining Gr/C60 interfaces, which are suitable for n-type vertical organic transistors. This study shows that the charge transport mechanism across vertical heterostructures (Au/C60/Gr) is predominantly injection limited.

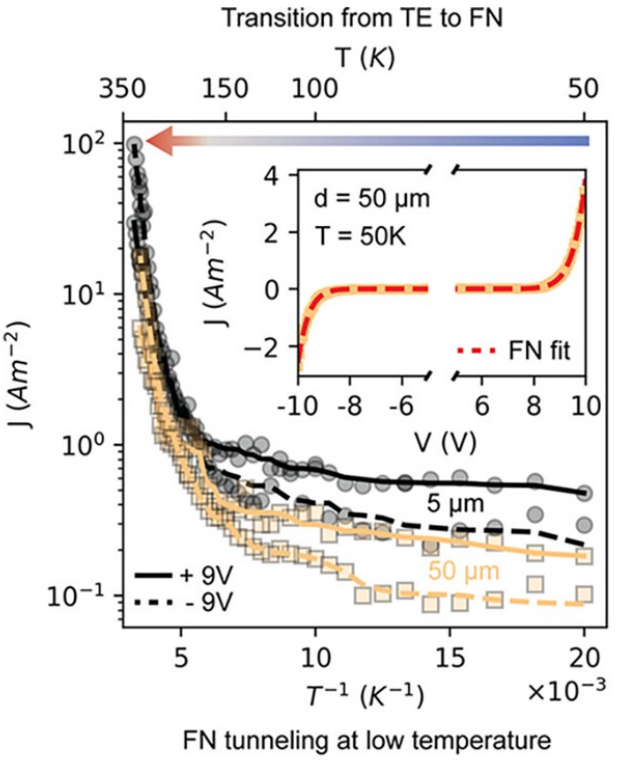

Fig. 2: Reproduced from [2]. Temperature-dependent current density of two representative devices of 5 and 50 µm at fixed biases of ±9 V. The inset shows the FN tunneling model fits for J–V data at 50 K.

At lower temperatures, the primary transport mechanism is identified as Fowler–Nordheim tunneling, while at room and higher temperatures, it transitions to non-ideal thermionic emission. The energy barriers at room temperature are found to be around 0.58 eV and 0.65 eV at the Gr/C60 and Au/C60 interfaces, respectively. Further analysis through impedance spectroscopy confirms that the organic semiconductor is depleted, resulting in two electron-blocking interfaces. The rectifying nature of the Gr/C60 interface, as revealed in this study, holds significant promise for its application in organic hot electron transistors and vertical organic permeable-base transistors.

Conclusions and outlook

The integration of graphene in vertical electronic devices reveals a complex interplay between graphene and the organic molecules, significantly impacting the electronic properties and potential applications.

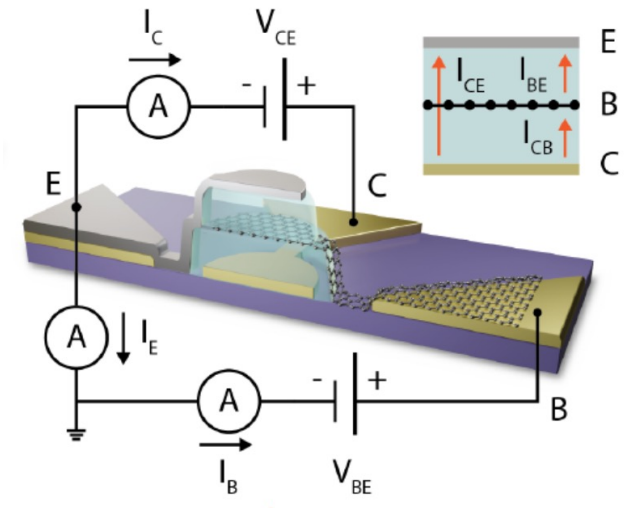

Fig. 3: Reproduced from [3]. 3D schematic and cross-secction of a n-type Vertical Organic Graphene Base Transisor (VOGBT) illustrating the applied voltages and measured currents in the common emitter configuration. The inset shows the internal currents, which are not directly measurable.

The variation of charge densities, shifts in Fermi energy, formation of Schottky barriers and the observed transport mechanisms underscore graphene's potential as a material in advanced electronic interfaces.

A particularly interesting device architecture exploiting graphene-Organic Semiconductors (OSCs) interfaces, the Vertical Organic Permeable Base Transistor (VOPBT), is depicted in figure 3. In this common emitter configuration, three parallel electrodes are separated by two OSCs. Electric charges are injected from the upper metal contact, i.e. the emitter (E), and enter the nearby OSC. They then traverse the permeable graphene electrode, i.e. the base (B), and the second OSC before being collected by the lower metal contact, i.e. the collector (C). The amount of charges collected by the base will depend on the electrical potential applied to it, while some charges will be emitted from the base and injected into the collector. The electrical (external) currents I_E, I_C and I_B are measured at the three terminals of the device. The internal currents (not directly accessible) I_{CE}, I_{CB} and I_{BE} are depicted in the inset. This VOPBT device geometry holds great promise for various applications, including amplifiers, inverters, ring oscillators, and control of OLEDs [3]. The vertical architecture and operational characteristics of these devices make them well-suited for these applications. We emphasize here that the specific properties of graphene, in terms of conductivity and optical transparency, make it also a good electrode material to contact light emitting layers.

Further exploration of the interplay between graphene and the organic molecules interactions will pave the way for innovative electronic devices such as the VOPBT, leveraging the unique properties of graphene.

References

[1] J. Oswald, D. Beretta, M. Stiefel, R. Furrer, D. Vuillaume et al. The Effect of C60 and Penta-cene Adsorbates on the Electrical Properties of CVD Graphene on SiO2. Nanomaterials, 13, 1134 (2023)

[2] J. Oswald, D. Beretta, M. Stiefel, R. Furrer, S. Lohde et al. Field and Thermal Emission Limited Charge Injection in Au–C60–Graphene van der Waals Vertical Heterostructures for Organic Electronics. ACS Appl. Nano Mater, 6, 11, 9444–9452 (2023)

[3] J. Oswald, Graphene-organic interfaces for vertical electronic devices, PhD thesis (2023)

Towards a tantalum-based planar architecture for bosonic qubits

Project P2101: A planar nanofabrication process for coupled Schrödinger-cat qubits in parametrically-driven nonlinear superconducting resonators
Project Leader: A. Grimm and C. Bruder
Collaborator: A. Bruno (SNI PhD Student)

Introduction

Quantum two-level systems are routinely used to encode qubits but tend to be inherently fragile, leading to errors in the encoded information. Quantum error correction (QEC) addresses this challenge by encoding effective qubits into more complex quantum systems. Unfortunately, the hardware overhead associated with QEC can quickly become very large.

In contrast, a qubit that is intrinsically protected against a subset of quantum errors can be encoded into superpositions of two opposite-phase oscillations in a resonator, so-called Schrödinger-cat states. This "Schrödinger-cat qubit" has the potential to significantly reduce the complexity of QEC, because it can replace a large number of two-level-system qubits in a QEC code [1]. In a recent experiment, we have demonstrated the stabilization and operation of such a qubit through the interplay between Kerr nonlinearity and single-mode squeezing in a superconducting microwave resonator [2]. This type of Schrödinger-cat qubit is typically referred to as the "Kerr-cat qubit".

Previous implementations of Kerr-cat qubits relied on three-dimensional microwave cavities. This counteracts the reduction in hardware complexity achievable with this system and is not fundamentally required. In this project, we are developing a nanofabrication process for fully planar Kerr-cat qubits. This will result in an easily scalable platform enabling us to investigate interactions between several such qubits.

In the first year of this SNI project we built up the basics required for the fabrication, measurement, and operation of Kerr-cat qubits in line with the ramping up of the research activities of the host group. In addition to experimental tasks, such as building a measurement and control setup, we implemented an Al/AlO_x/Al Josephson junction fabrication process for standard superconducting transmon qubits and benchmarked it by characterizing the coherence times of these devices. We furthermore reported on building a first prototype of a quantum-limited parametric amplifier in our group.

This year, we have built on these results by replacing the material of large portions of our circuits with tantalum. This has been shown to reduce losses and improve coherence times [3]. We will describe our work in more detail in the following.

A tantalum-based nanofabrication process for superconducting circuits

Even though bosonic qubits are intrinsically robust against errors, they profit from high coherence properties of the underlying superconducting circuits. Therefore, we can build on developments made for standard superconducting qubits and apply them to our devices. A standard superconducting qubit consists of a capacitive element connected to one or several Josephson junctions acting as a nonlinear inductor. The capacitive element and the embedding superconducting circuitry is generally made from thin metal films, such as aluminum or niobium, patterned on a substrate, such as Si:SiO_2 or sapphire. In bosonic or protected qubits, more complex circuit elements are used, but the basic fabrication principle is similar.

Losses in high-coherence superconducting circuits originate primarily in the three interfaces present in the devices: metal-vacuum, substrate-metal, and substrate-vacuum [4]. It is therefore crucial to improve the quality of these surfaces and interfaces. This has led to the emergence of tantalum (Ta) as a new circuit material in recent years [3,5]. Ta can be deposited directly and cleanly onto sapphire and has a naturally low-loss surface oxide that is stable at room temperature. It furthermore resists aggressive cleaning steps aimed are removing contaminants at the substrate-vacuum interface.
Over this past year, we have implemented a tantalum-based fabrication process and benchmarked it by measuring the internal quality factors of superconducting coplanar waveguide (CPW) resonators. We currently source HEMEX quality sapphire substrates with 200 nm of α-phase Ta films externally (STAR Cryoelectronics), but plan to transition to in-house deposition by the end of the coming year. We clean the wafers with a piranha etch (H_2SO_4:H_2O_2) after we receive them. We then perform optical lithography (AZ1518 and Heidelberg DWL66$^+$ laser writer), an oxygen descum, wet etching (HF:HNO_3:H_2O), resist stripping, dicing, and additional piranha and buffered oxide etch (BOE) cleaning. All these steps have been implemented by us in the PSI cleanroom.

Benchmarking with CPW resonators

The first series of test samples we designed and fabricated consist of a CPW transmission line (feedline) through which measurement signals can propagate and up to twelve laterally coupled resonators (so-called "hanger" coupling geometry) as shown in figure 1. The resonator frequencies as shown are evenly spaced so that we can test multiple devices in a single experimental run and quickly build up measurement statistics.

Our samples are bonded into a Qcage.24 sample holder, which is mounted on the baseplate of one of our dilution refrigerators. The cryogenic wiring of these instruments is partially made and completely assembled in-house to be optimized for filtering and routing of fast, low-noise microwave frequency control and measurement signals.

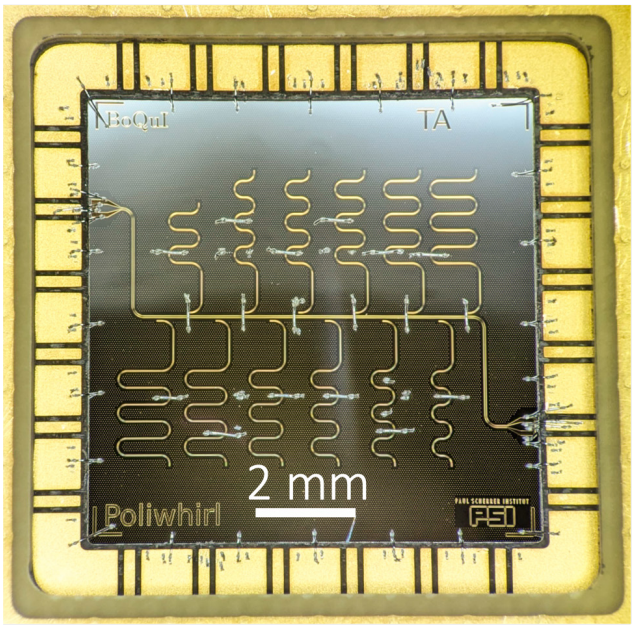

Fig. 1: CPW resonator test sample bonded to the PCB of our sample holder. The feedline runs from the top left to the bottom right of the chip. Twelve meandering resonators are laterally coupled to it. Wire bonds that suppress spurious chip modes (across feedline and resonators) and connect the chip to the sample holder (at the edges) are also visible.

We then measure the microwave response of our devices with a room-temperature vector network analyzer connected to the input and output lines of our dilution refrigerator. By fitting this response to theoretical predictions [6], we extract the internal quality factor which is inversely proportional to the losses present in the device. Importantly, we do this at an average photon population of approximately one in the resonator to avoid saturating loss mechanisms and overestimating the quality factors.

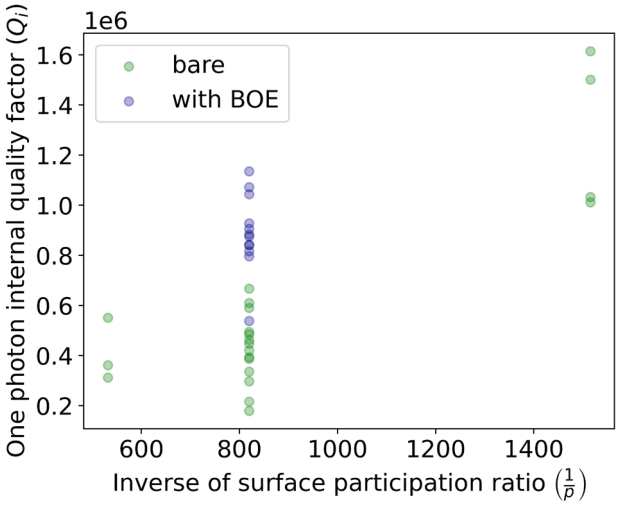

Fig. 2: Internal CPW-resonator quality factors as a function of surface participation ratio. Each dot represents a different device. "With BOE" ("bare") denotes samples that have (have not) been treated with a buffered oxide etch.

Figure 2 shows the results of these measurements for resonators with three different geometries. Varying the geometry changes the ratio of the resonator electric field energy stored in the surfaces and interfaces of the device to the total electric field energy. Our results illustrate nicely the expected increase of the quality factor with decreasing surface participation ratio. Our best devices have internal quality factors in excess of 1 million which is on par with the state of the art in the field [5]. Note that performing a BOE etch on a separate but similar sample additionally increases the quality factor twofold as expected from the literature [6].

Building on these promising results, our next steps in this project will be to integrate tantalum-based low-loss circuits with our Josephson junctions. The goal of this task is to first demonstrate superconducting qubits with coherence times longer than 100 microseconds, which should be achievable with our fabrication process [3]. Once this goal is reached, we will implement bosonic qubits in this long-lived planar superconducting circuit architecture. This will create a platform to both perform quantum error correction experiments on coupled bosonic qubits and to explore the associated fundamental physics of coupled quantum parametric oscillators.

References

[1] A. S. Darmawan, B. J. Brown, A. L. Grimsmo, D. K. Tuckett, and S. Puri, Practical Quantum Error Correction with the XZZX Code and Kerr-Cat Qubits. PRX Quantum 2, 030345 (2021)

[2] A. Grimm, N. E. Frattini, S. Puri, S. O. Mundhada, S. Touzard, M. Mirrahimi, S. M. Girvin, S. Shankar & M. H. Devoret, Stabilization and operation of a Kerr-cat qubit. Nature 584, 205-209 (2020)

[3] A. P. M. Place, L. V. H. Rodgers, P. Mundada, B. M. Smitham, M. Fitzpatrick et al. New material platform for superconducting transmon qubits with coherence times exceeding 0.3 milliseconds. Nat. Commun. 12, 1779 (2021)

[4] C. Wang, C. Axline, Y. Y. Gao, T. Brecht, L.Frunzio et al. Surface participation and dielectric loss in superconducting qubits. Appl. Phys. Lett. 107, 162601 (2015)

[5] K. D. Crowley, R. A. McLellan, A. Dutta, N. Shumiya, A. P. M. Place et al. Disentangling Losses in Tantalum Superconducting Circuits. Phys. Rev. X 13, 041005 (2023)

[6] S. Probst, F. B. Song, P. A. Bushev, A. V. Ustinov, M. Weides, Efficient and robust analysis of complex scattering data under noise in microwave resonators. Rev. Sci. Instrum. 86, 024706 (2015)

Structural basis of NINJ1-mediated plasma membrane rupture in cell death

Project P2102: Structure and Assembly Mechanism of the Ninjurin-1 Membrane Perforation Pore in Executing Cell Death
Project Leader: S. Hiller and D. J. Müller
Collaborator: M. Degen (SNI PhD Student)

Introduction
This project is centred on deepening our understanding of how cells die – a fundamental process essential for multicellular life. Cells can naturally undergo a process called Programmed Cell Death (PCD), which is vital for maintaining healthy tissues. However, when PCD goes awry, it can cause serious illnesses like cancer, neurodegenerative diseases, autoimmune disorders, and chronic inflammation. Our focus is on a 19 kDa protein named Ninjurin-1 (NINJ1), which plays a pivotal role in the final stages of certain subtypes of lytic PCDs such as pyroptosis and secondary necrosis [1].

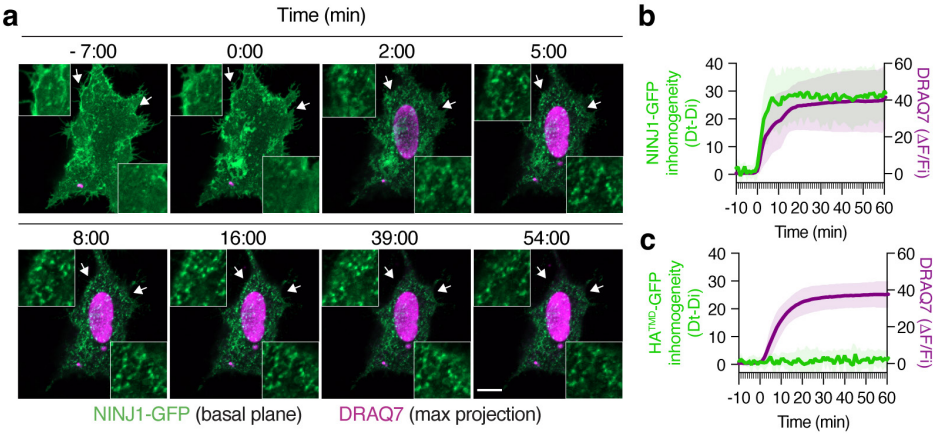

Fig. 1: NINJ1 clusters upon induction of pyroptotic cell death. a time-resolved fluorescent microscopy showing speck formation upon cellular insult. b and c fluorescent read-out signal inhomogeneity over time.

The membrane protein NINJ1 is crucial for PCD. Its primary role is to facilitate the completion of lytic PCD by breaking apart the plasma membrane. This event releases important molecules, such as HMGB1 and LDH, which trigger further immune responses. The key objective of our study is to understand how NINJ1 works, particularly how its structure influences its function [2].

Establishing recombinant protein expression and purification
Our initial steps involved producing NINJ1 in a controlled environment. We inserted human NINJ1 into a suitable vector for expression in Escherichia coli. To purify NINJ1, we isolated it from the cells, solubilized it from the bacterial membranes using detergents and then utilized a combination of different chromatography-based purification techniques.

After purification, we used two types of electron microscopy to study NINJ1. Negative stain transmission electron microscopy helped us understand the size and overall arrangement of NINJ1 assemblies at a basic and low-resolution level. For a more detailed view, we employed cryogenic electron microscopy (cryo-EM), revealing the three-dimensional structure of NINJ1 at atomic resolution.

NINJ1 polymerizes to into filaments to exert its function
Intriguingly, our investigation revealed that NINJ1 undergoes a significant structural transformation during pyroptosis. Using time-lapse fluorescence microscopy, we observed NINJ1 clustering at the plasma membrane, concurrent with the influx of cell death-indicating dyes (Fig. 1a, b). This clustering was specific to NINJ1 and was not observed in other plasma membrane proteins (Fig. 1c). These observations underscore the unique role of NINJ1 in pyroptosis, distinct from other plasma membrane proteins.

To elucidate NINJ1's structural basis, we utilized cryo-EM. This revealed long (up to µm size) NINJ1 filaments with varying degrees of bending. These filaments, comprising stacked subunits, exhibited a combination of a hydrophobic and a hydrophilic side (Fig. 2.). The hydrophilic face of the filament interacts with the aqueous environment, while the hydrophobic face, typical of membrane associating, pore-forming proteins, likely engages with the lipid bilayer of the plasma membrane, enabling membrane rupture. This amphipathic nature explains NINJ1's ability to form stable structures at membrane edges, that we have shown to be essential for its role in lytic cell death.

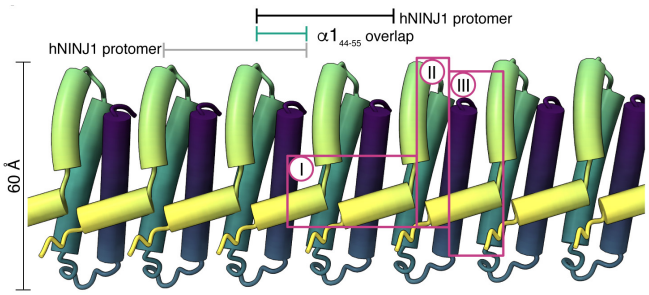

Fig. 2: NINJ1 Cryo-EM Structure of the NINJ1 filament. Individual protomers are colored by gradient (yellow-green-purple). Main interfaces of NINJ1 protomers are indicated by magenta boxes.

Molecular Dynamics and Mutagenesis Studies
Molecular dynamics simulations further supported our structural findings. These simulations demonstrated the stability of NINJ1 filaments at membrane edges and their

ability to form variable arrangements, proving crucial for membrane perforation. The simulations also highlighted the importance of specific helices, in maintaining the structural integrity of NINJ1 filaments.

To validate our structural model, we engineered single-amino-acid mutants of NINJ1 and assessed their impact on in vitro filament formation and cell lysis (Fig. 3 a, b). Mutants designed to disrupt filament formation generally reduced or abolished cell lysis, aligning with our structural understanding of NINJ1. These findings were corroborated in both in vitro settings and in cellular models, cementing the functional significance of NINJ1's structural arrangement in mediating cell death.

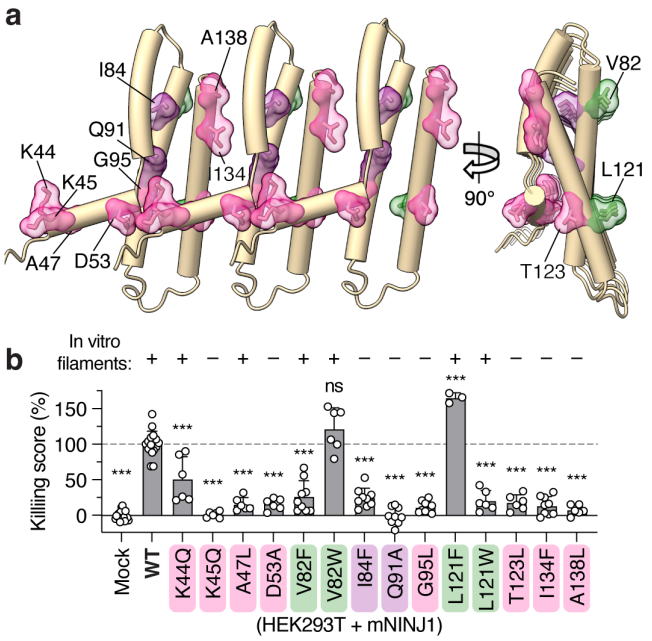

Fig. 3: Rational design of mutants and their effect on NINJ1 filament formation and effect on lytic ability.

a NINJ1 structure with mutated residues shown as side chains and surface. b Effect of mutations on in vitro polymer formation and lytic ability upon transfection into HEK293T cells.

Conclusion

This project has so far illuminated the critical role of NINJ1 in PCD, particularly in the context of pyroptotic cell death (Fig. 4). By elucidating the structural and functional aspects of NINJ1, we have advanced the understanding of the molecular mechanisms underpinning inflammatory active, lytic cell death. This knowledge not only contributes to basic biological science but also opens new avenues for therapeutic interventions in diseases characterized by dysregulated cell death [3].

Looking ahead, our focus will shift towards examining and visually capturing the immediate impact of reassembled NINJ1 polymers on lipid bilayers. This will be achieved through the application of atomic force microscopy, allowing us to observe and possibly quantify membrane disruptions. This study is anticipated to further elucidate the mechanisms triggering NINJ1 activation, a critical yet unresolved aspect of our research. Emerging studies suggest that this activation might be linked to cellular blebbing which is a common hallmark across different forms of PCD [4]. In addition, it has been proposed by us and others that membrane lipid composition and therefore fluidity / rigidity could play a role in activation which we aim to investigate further.

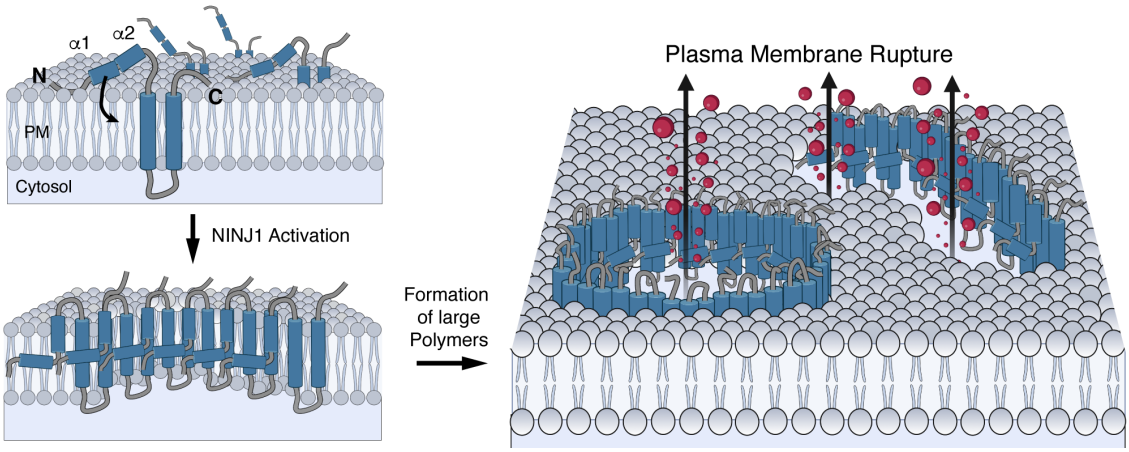

Fig. 4: Schematic model summarizing the current understanding of NINJ1-mediated plasma membrane rupture.

References

[1] N. Kayagaki, O. S. Kornfeld, B. L. Lee, I. B. Stowe, K. O'Rourke et al. NINJ1 mediates plasma membrane rupture during lytic cell death. Nature 591, 131–136 (2021)

[2] M. Degen, J. C. Santos, K. Pluhackova, G. Cebrero, S. Ramos et al. Structural basis of NINJ1-mediated plasma membrane rupture in cell death. Nature 618, 1065–1071 (2023)

[3] N. Kayagaki, I. B. Stowe, K. Alegre, I. Deshpande, S. Wu et al. Inhibiting membrane rupture with NINJ1 antibodies limits tissue injury. Nature 618, 1072–1077 (2023)

[4] Y. Dondelinger, D. Priem, J. Huyghe, T. Delanghe, P. Vandenabeele et al. NINJ1 is activated by cell swelling to regulate plasma membrane permeabilization during regulated necrosis. Cell Death Dis 14, 755 (2023)

Gold nanoparticles for intraoperative visualization of ovarian cancer cells

Project P2103: Gold nanoparticle assemblies for SERS based detection of EGFR expressing ovarian cancer cells in tumor xenografts
Project Leader: S. Saxer, S. McNeil and V. Heinzelmann
Collaborator: A. Stumpo (SNI PhD Student)

Introduction

Ovarian cancer (OC) is the gynecologic malignancy with the highest mortality. Several reports suggested that overexpression of the epidermal growth factor receptors (EGFR) family plays an important role in OC, leading to clinical trials of different EGFR inhibitors such as gefitinib and erlotinib [1]. Nevertheless, the most common OC treatment approach remains the debulking surgery followed by chemotherapy. A precise pre/intra-operative visualization is essential because patients with post-surgical residual tumors less than 1 cm have higher survival rates than those with more residual tumor masses [2]. Currently, the most common imaging methods include computed tomography, magnetic resonance, positron emission tomography, and fluorescence-guided surgery which is the current gold standard for surgical guidance.

Recently, Raman microscopy is emerging as a label-free, sensitive, and non-invasive imaging and diagnostic technique [3]. The combination of Raman microscopy with anti-EGFR functionalized gold nanoparticles (AuNPs) allows a sensitive detection of OC cells exploiting Surface Enhanced Raman Scattering (SERS).

Early detection requires a strong SERS signal to provide high sensitivity but also a selective target. Hence the AuNPs have to be functionalized with a proper mixture of Raman reporter for the Raman signal, inert polyethylene glycol (PEG) coating for stabilization and to prevent unspecific adsorption, and the anti-EGFR antibody as an active targeting functionality.

However, not only the ratio matters but also the type of surface chemistry, and the orientation of the molecules. For instance, the commonly used carbodiimide crosslinker chemistry may randomly orient antibodies on the surface, potentially affecting their binding affinity. Moreover, the residual negative carboxyl groups could induce non-specific uptake of the AuNPs. Both might influence sensitivity and selectivity of the AuNPs.

Hence, we compared this surface chemistry to the Light Activated Site-Specific Conjugation (LASIC), which conjugates IgGs by binding to the fragment crystallizable (Fc) region through one covalent bond, therefore without affecting its binding site [4]. The anti-EGFR antibody was linked to the DBCO PEG-SH on the 60 nm AuNPs by photo crosslinking chemistry. The physicochemical properties (PCs) were characterized after each step. Finally, the anti-EGFR AuNPs capability to distinguish EGFR-positive and EGFR-negative ovarian cancer cell lines is evaluated in vitro using OVCAR8, OVCAR5 and TOV-112D cells (Fig. 1).

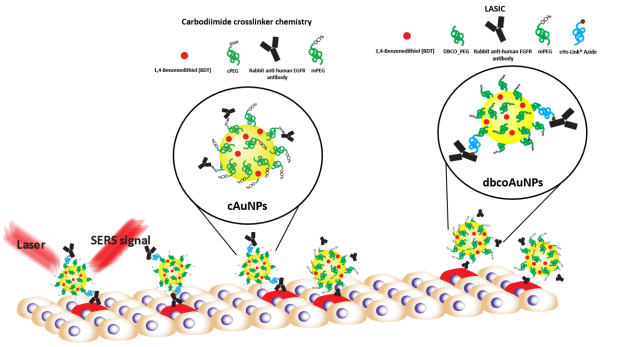

Fig. 1: Schematic illustration of AuNPs with the two surface chemistries targeting ovarian cancer cells expressing the EGFR protein on the surface (in red).

Results and discussion

The ideal ratio of surface chemistry between Raman reporter, protective PEG layer and anti-EGFR antibodies, essential for achieving the ideal properties of AuNPs, was previously outlined by Burgio et al. [5] and adopted for our AuNPs. First, the Raman reporter benzene-1,4-dithiol (1,4-BDT) is bond to the AuNPs by its dithiol groups. The 1,4-BDT Raman spectrum with the main peaks around 330, 740, 1090 and 1575 rel. 1/cm is then measured and the stability of the SERS signal of AuNPs with both surface chemistries proved. Furthermore, each functionalization step was characterized by dynamic light scattering and as expected, for both chemistries an increase in size is shown after each individual modification, with a significant increase of 20 nm after adding α-methoxy-ω-mercapto PEGs (mPEG), due to a consistent increase in PEG molecules surface density. Unexpectedly, regarding the surface charge of the two surface chemistries no difference was observed, with a decrease after the mPEG functionalization step from -41.2 ± 0.5 mV to -22.4 ± 0.7 mV for Carbodiimide chemistry and from -41.2 ± 0.5 mV to 21.8 ± 0.6 mV for LASIC conjugation (Fig. 2). Then the Carboxy-PEG-SH or the DBCO-PEG-SH were used to link the anti-EGFR antibodies to the surface, using either carbodiimide crosslinker chemistry (EDC/NHS) or an OyO link with the LASIC site-specific label only on the Fc region of the antibody. The antibody conjugation to the AuNPs was then proven with a dot blot method (Fig. 3). Thereby a very bright red spot is only visible when AuNPs are fully functionalized on the surface (Fig. 3.1, 3.2) whereas without antibodies no spot is observed (Fig. 3.3, 3.4), proving that the interaction between nanoparticles and antigen is mediated by antibody-antigen recognition. However, when only the OyO Link or the EDC/NHS is absent, a faint red spot remains visible, indicating unspecific absorption of antibodies on the surface (Fig. 3.5, 3.6). Dot blot is not capable to quantitively reveal any difference in antibody conjugation nor binding affinity between the two surface chemistries.

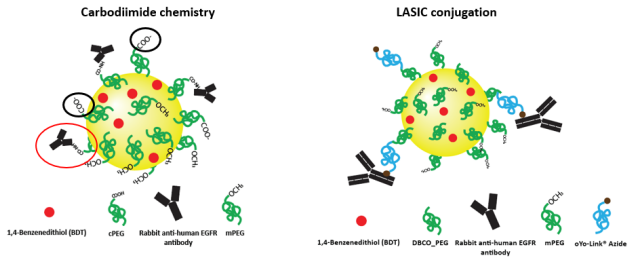

Fig. 2: Schematic illustration of the two different surface chemistries. Carbodiimide chemistry does not allow to control the antibodies orientation, possibly affecting their binding sites (red circle). The remaining carboxyl groups are deprotonated in physiological conditions, displaying a negative charge (black circles). LASIC conjugation, controlling the antibody orientation, enables to increase the number of mPEG molecules, then decreasing the surface negative charge and the AuNPs unspecific uptake.

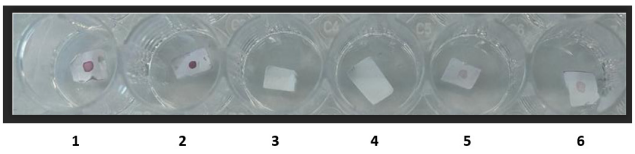

1. DBCOPEG_OyoLink_Ab, 2. cPEG_EDCNHS_Ab, 3. DBCOPEG_OyoLink_**NoAb**, 4. cPEG_EDCNHS_**NoAb**, 5. DBCOPEG_**NoOyoLink**_AB, 6. cPEG_**NoEDCNHS**_Ab

Fig. 3: Photograph of the dot blot method used to test anti-EGFR AuNPs binding to the recombinant human EGFR protein blotted on a nitrocellulose membrane. A clear red spot is visible when the AuNPs contain anti-EGFR antibodies on the surface (1,2). A faint red spot is visible for the reference with anti-EGFR but without linker molecules (OyOLink and EDC/NHS) (5,6). No red spot is visible without anti-EGFR antibodies (3,4).

In order to evaluate the potential of anti-EGFR AuNPs to specifically target ovarian cancer cells by their EGFR expression level, the following cell line were employed: OVCAR5 and OVCAR8 that exhibit positive EGFR expression; TOV-112D that is EGFR-negative. Nonspecific staining is evident on the TOV-112D cell line (Fig. 4). These results were confirmed by western blot.

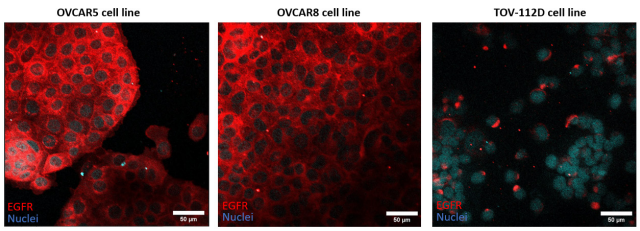

Fig. 4: Confocal microscopy picture of the EGFR expression of 3 selected ovarian cancer cell lines: OVCAR8, OVCAR5 and TOV-112D. EGFR expression in red; Nuclei stained in blue. Scale bar: 50 µm.

To better understand how the surface chemistries influence the anti-EGFR AuNPs functionality, we eventually tested the AuNPs capability to distinguish EGFR-positive and EGFR-negative ovarian cancer cells using Raman microscopy. AuNPs with both surface chemistries were found on the EGFR-positive OVCAR8 cell line, suggesting their capability to recognize the antigen expressed on the cell surface. Still, the unspecific uptake remains our main issue for both surface chemistries, with AuNPs without the antibodies found occasionally on OVCAR8 cells (Fig. 5).

Fig. 5: Fluorescence microscopy images of OVCAR8 cells treated with: A, AuNPs displaying antibodies conjugated by LASIC approach; B, AuNPs displaying antibodies conjugated by Carbodiimide chemistry; C,D, AuNPs without antibodies with DBCO_PEG (C) and cPEG (D). Nuclei stained with DAPI; Scale bars: 200 µm. Inserts: Raman images of OVCAR8 cells. AuNPs presence highlighted by black boxes. Scale bar: A, D, 10 µm; B, C, 20 µm.

For this reason, we are currently working on reducing the unspecific binding by adjusting AuNPs concentration, incubation time and washing steps in order to get a significant discrimination of EGFR-positive and EGFR-negative ovarian cancer cells and better evaluate the influence of the two chemistries. We consider this initial experimental cell line setup as optimal approach to evaluate the specificity and selectivity of SERS as an imaging tool for follow-up experiments, to continue for intra operative visualization of tumor cells.

References

[1] Q. Sheng & J. Liu, The therapeutic potential of targeting the EGFR family in epithelial ovarian cancer, British Journal of Cancer 104, 1241-1245 (2011)

[2] A. Musto, L. Rampin, C. Nanni, M. C. Marzola, S. Fanti et al., Present and future of PET and PET/CT in gynaecologic malignancies, European Journal of Radiology, 78 (1), 12-20 (2011)

[3] I. P. Santos, E. M. Barroso, T. C. Bakker Schut, P. J. Caspers, C. G.F. van Lanschot et al., Raman spectroscopy for cancer detection and cancer surgery guidance: translation to the clinics, Analyst 142, 3025-3047 (2017)

[4] J. Z. Hui, S. Tamsen, Y. Song, A. Tsourkas, LASIC: Light Activated Site-Specific Conjugation of Native IgGs, Bioconjugate Chem., 26 (8), 1456-1460, (2015)

[5] F. Burgio, D. Piffaretti, F. Schmidt, U. Pieles, M. Reinert et al, Tuning the surface chemistry of gold nanoparticles to specifically image glioblastoma cells using surface-enhanced Raman spectroscopy, ACS Appl Nano Mater. 3, 2447-2454 (2020)

RT-Xray as a tool to explain cryptic promisquities of halide methyltransferases

Project P2104: Methods to understand the role of ordered waters and disordered residues in enzyme catalysis using macromolecular crystallography at physiological temperatures
Project Leader: F. P. Seebeck and J. H. Beale
Collaborator: S. Bolotova (SNI PhD Student)

Abstract
The objective of this project is to implement room temperature (RT) crystallography methods to determine enzyme structures that are physiologically more relevant that those emerging from standard measurements at cryogenic temperatures. In the past year we have started to study the structural and dynamic requirements for the substrate specificity of halide methyl transferases.

Introduction
The structural determinants of the substrate specificity of enzymes are usually studied by inspecting static structures determined by cryo-X-ray crystallography. Although successful in many instances, this approach may fail when the substrate scopes of two enzymes diverge because of different dynamic behaviour. We plan to use room temperature (RT) crystallography to examine different dynamic behavior in enzymes that catalyze similar reactions but are characterized by different substrate scopes. In 2022 we developed a methodology for recording room temperature X-ray diffraction data on a routine basis. This year we focused on establishing the specific study system: halide methyltransferases (HMTs) that accept S-adenosylmethionine and halides as substrates to produce S-adenosyl homocysteine and methyl halide as products (Fig. 1). [4, 6] Our goal is to examine as to whether the different abilities of HMTs to accept non-natural SAM-derivatives or synthetic pseudohalogens as substrates may be explained by comparative B-factor analysis of the corresponding crystal structures [1].

Results and Discussion
Methyl-donor specificity. Methyltransferases (MTs) comprise a large group of enzymes catalyzing the methylation of a broad range of small and macromolecular substrates, including secondary metabolites, proteins and nucleic acids [2,3]. Methylation of these substrates changes their properties and regulates various biosynthetic processes, including gene expression and signal transduction. MTs could be classified by the type of the methylated nucleophilic atom (N, C, O, S), by the targeted function (amine, amide, catechol, carboxylate, phosphate), or by the reaction type (Sn_2, radical, ping-pong). The largest subgroup of this family is constituted by the S-adenosylmethionine dependent MTs. The structural and functional diversity of MTs is important for biocatalytic methylation of a wide range of substrates with high stereo-, regio- and chemoselectivity in pharmaceutical processes.

Large-scale application of MTs is challenging because of their dependence on SAM stoichiometric methyl donor, which is expensive, unstable and causes feedback inhibition of the by-product SAH. As a solution to this problem, our laboratory has developed a process that allows the recycling of SAH by HMT-catalyzed methylation using synthetic methyl donors, such as methyl iodide (Fig. 1) [5].

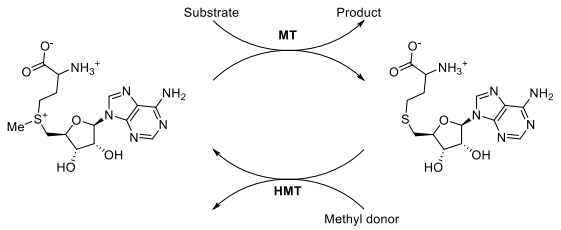

Fig. 1: MT-catalyzed methylation of nucleophilic substrates.

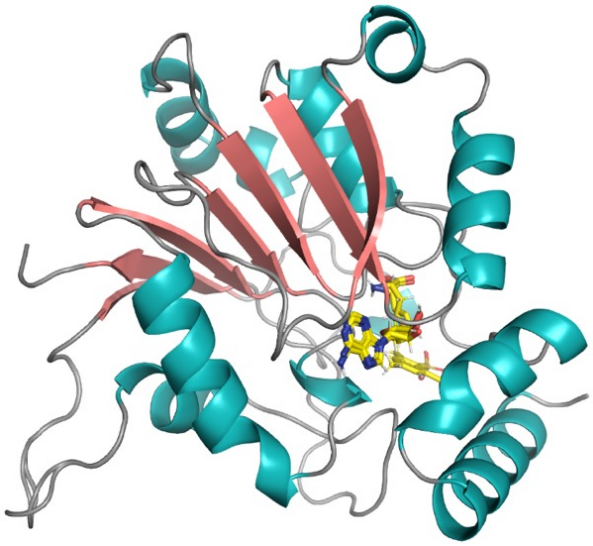

Fig. 2: Crystal structure of HMT from the orchid symbiotic fungus Tulasnella calospora (KioHMT) in complex with SAH and mesitylene sulfonate at a resolution of 1.90 Å. The KioHMT polypeptide chain was modeled for residues 12 – 246. A partially unresolved loop (residues 204-217) is shown in the lower left corner. The protein was produced in E. coli and crystallized after proteolytic removal of the N-terminal His-tag.

More recently, we have identified members of the HMT class that also accept sulfate- and sulfonate-based methyl donors [7]. These non-volatile reagents may be better suited for large-scale application than methyl halides. In order to understand as to why certain HMTs accept bulky and aromatic sulfonates in active sites that have evolved to bind small anionic halides, we have started to examine crystal structures of these enzymes in complex with SAH or sinefugin – a naturally SAM analog and MT inhibitor – and sulfonates (Fig. 2). Comparison of the crystal structures of several related HMTs

(from Arabidopsis thaliana, Paraburkholderia xenovorans and Tulasnella calospora) suggests that the differences in their structures alone does not explain their different abilities of accept bulky sulfonates as methyl donors (Fig. 3). In a second step we will collect room temperature diffraction data on HMT crystals to compare (B-factor analysis)1 the different dynamic behavior of HMTs from different organisms.

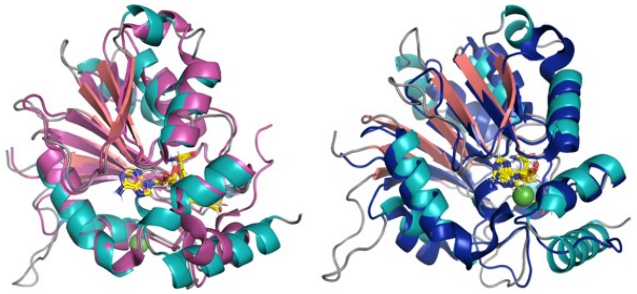

Fig. 3: Left: Alignment of the structures of KioHMT and AthHMT (pink, PDB ID: 3LCC, 1.8Å). RMSD = 0.977 (148 to 148 atoms). Sequence identity = 33.63%. The chloride atom is colored green, and SAH and MS are colored yellow. Right: Alignment of the structures of KioHMT and BxHMT (blue, PDB ID: 8AJP, 1.8Å). RMSD = 1.989 (145 to 145 atoms). Sequence identity = 28.16%. The chloride atom is colored green, and SAH and MS are colored yellow.

β-methyl SAM. A second study system emerges from our goal to identify HMTs that can methylate SAH derivatives with an additional methyl group attached to Cβ of the homocysteinyl moiety. Screening a panel of HMT homologs we identified HMT from the white-rot basidiomycete fungus Dichomitus squalens as an efficient catalyst (tbuHMT). We solved the crystal structure of this enzyme in complex with SAH. Comparison of this structure with that of other HMTs (see above) revealed no explanation as to why tbuHMT is significantly more efficient at methylating β-methyl SAH. As a next step we plan to crystallize tbuHMT with β-methyl SAH. We suspect that this unnatural substrate binds to HMTs via induced fit. This alternative conformation may not be available for other HMTs despite very similar structures of the native protein.

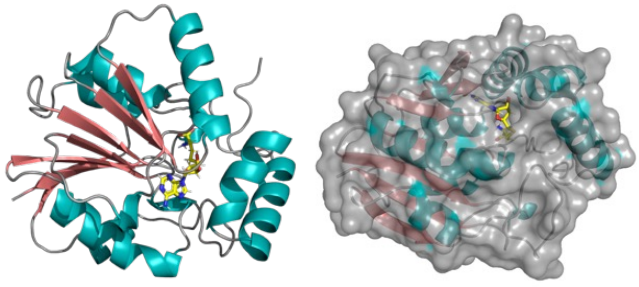

Fig. 4: Left: TbuHMT + SAH structure, resolution 1.60 Å. SAH is colored yellow. Right: Surface representation of the same structure.

Conclusion

We have crystallized HMTs in complex with non-natural SAM derivatives and synthetic methyl donors to examine the structural determinants for differences in substrate specificity among HMT homologs. In a next step we will apply RT-X-ray analysis and B-factor analysis to examine dynamic contributions to the observed substrate specificities.

References

[1] Z. Sun, Q. Liu, G. Qu, Y. Feng, M. T. Reetz Utility of B-Factors in Protein Science: Interpreting Rigidity, Flexibility, and Internal Motion and Engineering Thermostability. Chem Rev 119 (3), 1626 - 1665 (2019)

[2] L. C. Ward, H. V. McCue, A. J. Carnell Carboxyl Methyltransferases: Natural Functions and Potential Applications in Industrial Biotechnology. ChemCatChem 13, 121 - 128 (2021)

[3] Q. Tang, I. V. Pavlidis, C. P. S. Badenhorst, U. T. Bornscheuer, From Natural Methylation to Versatile Alkylations Using Halide Methyltransferases. Chembiochem 22(16), 2584 – 2590 (2021)

[4] J. W. Schmidberger, A. B. James, R. Edwards, J. H. Naismith, D. O'Hagan, Halomethane biosynthesis: structure of a SAM-dependent halide methyltransferase from Arabidopsis thaliana. Angew Chem Int Ed Engl 49(21), 3646 – 3648 (2010)

[5] C. Liao, F. P. Seebeck, S-adenosylhomocysteine as a methyl transfer catalyst in biocatalytic methylation reactions. Nat Catal 2(8), 696 – 701 (2019)

[6] T. S. Bayer, D. M. Widmaier, K. Temme, E. A. Mirsky, D. V. Santi, C. A. Voigt, Synthesis of methyl halides from biomass using engineered microbes. J Am Chem Soc 131(18), 6508 – 6515 (2009)

[7] X. Wen, F. Leisinger, V. Leopold, F. P. Seebeck, Synthetic Reagents for Enzyme-Catalyzed Methylation. Angew Chem Int Ed Engl 61(41), e202208746 (2022)

Exchange energy of the ferromagnetic ground-state in a monolayer semiconductor

Project P2105: Ferromagnetism of mobile electrons in a two-dimensional semiconductor
Project Leader: R. Warburton and M. Poggio
Collaborators: R. Kaiser (SNI PhD Student), N. Leisgang, D. Miserev, H. Mattiat, L. Schneider, L. Sponfeldner

Ferromagnetism represents one of the canonical magnetic states. It describes a state of matter in which spontaneous alignment of electronic spins leads to a net magnetisation. A key metric of a ferromagnet is the exchange energy, the energy required to flip one spin. The exchange energy determines the Curie temperature, the temperature at which there is a phase change from a ferromagnetic state (magnetically ordered) to a paramagnetic state (magnetically disordered). For the well-known metallic ferromagnets, e.g. iron, the exchange energy is large resulting in enormous Curie temperatures, ~1,000 K.

Recently, it was shown that electrons in two-dimensional (2D) systems become ferromagnetically ordered at low temperature. Ferromagnetic order has been observed in the semiconductor consisting of monolayer MoS_2 [1, 2]. However, the exchange energy characterising the ferromagnetic state is unknown.

Here, we present a way to determine the exchange energy of ferromagnetic MoS_2 (at low electron density). We argue that the energetic separation between two lines in the photoluminescence spectrum provides a direct measurement of the exchange energy, Σ. According to this method, the exchange energy is about 10 meV. This is a substantial energy, much larger than the thermal energy at cryogenic temperatures, suggesting that the ferromagnetic order should survive to temperatures of tens-of-Kelvin.

Monolayer MoS_2 is a semiconductor with direct band-gaps at the K- and at the K̃-point of the Brillouin zone (Fig. 1a). Resonant σ^+-polarised light creates an exciton at the K-point; σ^--polarised light creates an exciton at the K̃-point. An electron gas in monolayer MoS_2 forms a ferromagnetic state in which the Fermi surface consists of a circle at the K-point and a circle at the K̃-point [1]. If the electron spins point down, the K↓ and K̃↓ bands are occupied up to the Fermi energy; conversely, the K↑ and K̃↑ bands are pushed above the Fermi energy by the Coulomb interactions amongst the electrons and are unoccupied. The reconstructed band structure is sketched in figure 1b. The energy separation between the ↓ and ↑ bands is the exchange energy, Σ. The close-to-complete spin polarisation implies that Σ must be larger than the Fermi energy.

The sample consists of a MoS_2 monolayer sandwiched between two hBN layers, (Fig. 1c). Electrons are injected into the monolayer via a gate electrode; the electron density n is proportional to the applied electrode voltage. We perform a quasi-resonant, quasi-local photoluminescence (PL) experiment: the laser photon-energy is 1.96 eV, just above the exciton energy, 1.94 eV; the PL is collected from a region with diameter 500 nm. The excitation is either σ^+- or σ^- -polarised,

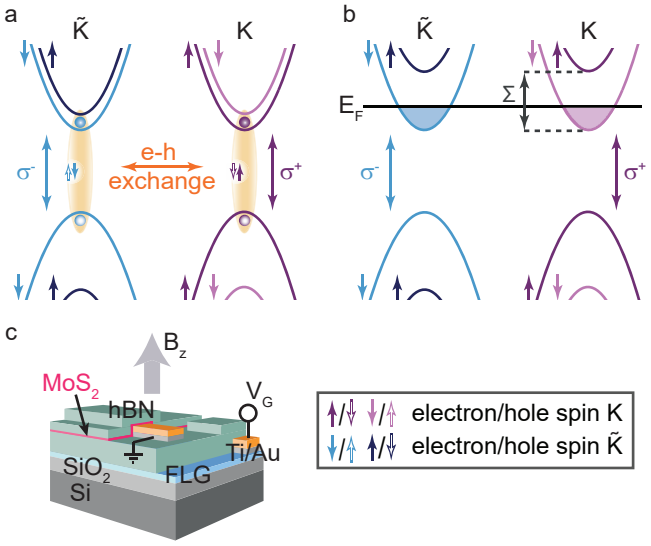

Fig. 1: a) Band structure of monolayer MoS_2 showing exciton formation, the associated selection rules at the K- and K̃-points, and the inter-valley exciton coupling provided by electron-hole exchange. b) Schematic of the reconstructed band structure of monolayer MoS_2 containing ferromagnetically-ordered itinerant electrons with spin-↓. The Fermi surface consists of two circles, one at the K-point, one at the K̃-point. Σ is the exchange energy. c) Schematic of the sample design. FLG stands for few-layer graphene.

thereby injecting an exciton with spin-↑ at the K-point or spin-↓ at the K̃-point, respectively. The PL is detected with σ^+- or σ^- -polarisation, allowing via the selection rules the responsible valley for each emission line to be determined. A magnetic field (perpendicular to the 2D layer) of +9.00T is applied, aligning all the spins ↓. The optical response is plotted as a matrix, figure 2: σ^+/σ^- refers to excitation with σ^+, collection with σ^-; and etc.

At very low *n* before an electron gas is established, the optical response is dominated by the neutral exciton, X^0. At higher *n*, a series of trions is observed, T_1 to T_4. Figure 2 reveals a pronounced dichroism at low n: the trions in σ^+/σ^+ are much stronger than those in σ^-/σ^-. This is one signature of ferromagnetism. The key to determining Σ is an identification of the trions, T_1 to T_4. This process proceeds using a model which accounts for the injection process, the Pauli exclusion principle, electron-hole scattering from one valley to the other, and recombination [3]. Detective work using the PL-polarisation and trion-linewidths as crucial clues leads to a robust, self-consistent identification (Fig. 3). According to this analysis, Σ can be determined from the splitting between T_2 and T_4.

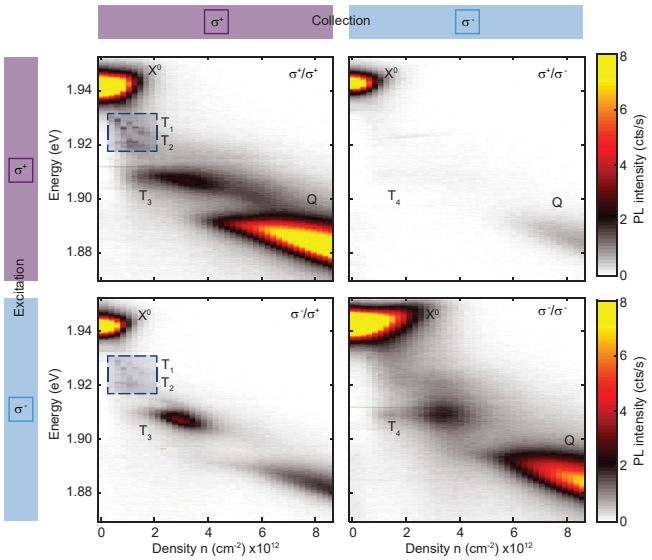

Fig. 2: Photoluminescence for quasi-resonant excitation on gated monolayer MoS_2 at +9.00 T and 4.2 K shown as a matrix: σ^+/σ^- excitation, σ^+/σ^- collection.

There are two striking points. First, the analysis of the trions is fully consistent with a close-to-complete electron spin-polarisation, i.e. ferromagnetism. Second, the crucial energy scale of the ferromagnetic phase, i.e. Σ, can read off from a PL spectrum. Previous work has not managed to identify the trions, and the idea of measuring the exchange energy via the optical response is a new one.

The optics here is used to probe the electronic ground-state. Crucially, the optical probe is sensitive to spin. However, the optical response has a degree of complexity, and injecting electron-hole pairs (the basis of a PL experiment) represents a local perturbation to the ferromagnetism. Furthermore, these experiments were performed at cryogenic temperatures, 4 K, yet at higher temperatures, the optical probe fails: the lines broaden on account of phonon scattering. The next crucial step is to detect the ferromagnetism directly by measuring the stray magnetic field. A nanoscale magnetometer is ideal. Such an experiment is challenging as the magnetism of the mobile electrons is much weaker than the magnetism of a two-dimensional magnet simply because there is just one electron per ten-thousand atoms. Nevertheless, estimates of the stray field suggest that state-of-the-art magnetometers developed by SNI groups are up to the job [4].

References

[1] J. G. Roch, G. Froehlicher, N, Leisgang, P. Makk, K. Watanabe, T. Taniguchi and R. J. Warburton, Spin-polarized electrons in monolayer MoS2, Nat. Nanotechnol. 14, 432–436 (2019)

[2] J. G. Roch, D. Miserev, G. Froehlicher, N. Leisgang, L. Sponfeldner, K. Watanabe, T. Taniguchi, J. Klinovaja, D. Loss and R. J. Warburton, First-Order Magnetic Phase Transition of Mobile Electrons in Monolayer MoS2, Phys. Rev. Lett. 124, 187602 (2020)

[3] N. Leisgang, D. Miserev, H. Mattiat, L. Schneider, L. Sponfeldner, K. Watanabe, T. Taniguchi, M. Poggio and R. J. Warburton, Exchange energy of the ferromagnetic electronic ground-state on monolayer semiconductor, arXiv: 2311.02164 (2023)

[4] H. Mattiat, N. Rossi, B. Gross, J. Pablo-Navarro, C. Magén, R. Badea, J. Berezovsky, J. M. De Teresa and M. Poggio, Nanowire Magnetic Force Sensors Fabricated by Focused-Electron-Beam-Induced Deposition, Phys. Rev. Applied 13, 044043 (2020)

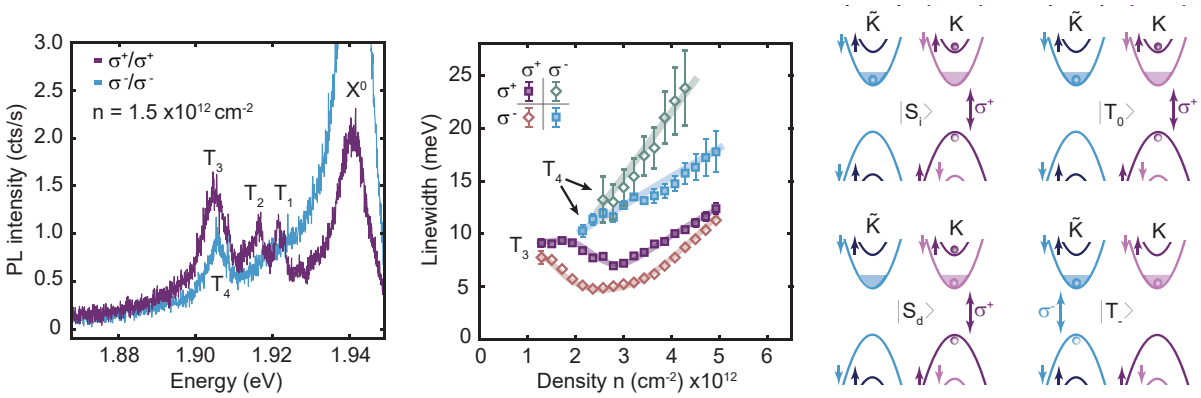

Fig. 3: Schematic of the trion eigenstates showing in each case the two electron states and the hole state from which the trion is constructed. T_1, T_2, T_3 and T_4 are identified as S_i, T_0, S_d and T-, respectively. S stands for spin-singlet, T for spin triplet.

Catalytic uncaging strategies for the in vivo release of cargoes

Project P2106: Innovative catalytic strategies to combat cancer
Project Leader: T. R. Ward and M. Fani
Collaborator: D. A. Graf (SNI PhD Student)

Abstract
Most traditional cytotoxic anticancer drugs used in chemotherapy indiscriminately target rapidly proliferating cells. Their mode of action mainly relies on either impairment of mitosis or induction of DNA damage and, therefore, affects both rapidly proliferating cancer cells and healthy cells. By utilizing a prodrug therapy, where a less cytotoxic form of the anticancer drug is administered, the undesirable and unspecific death of healthy cells can be minimized. Yet the accumulation and site-selective release of the cytotoxic drug in the vicinity of the diseased tissue is key to a successful outcome of the cancer treatment. The prerequisite for the accumulation is the over-expression of a membrane-bound receptor that can be actively targeted by its natural ligand, antagonist, or antibody (ADC, SMDC, ADEPT, Fig. 1)[1,2,3].

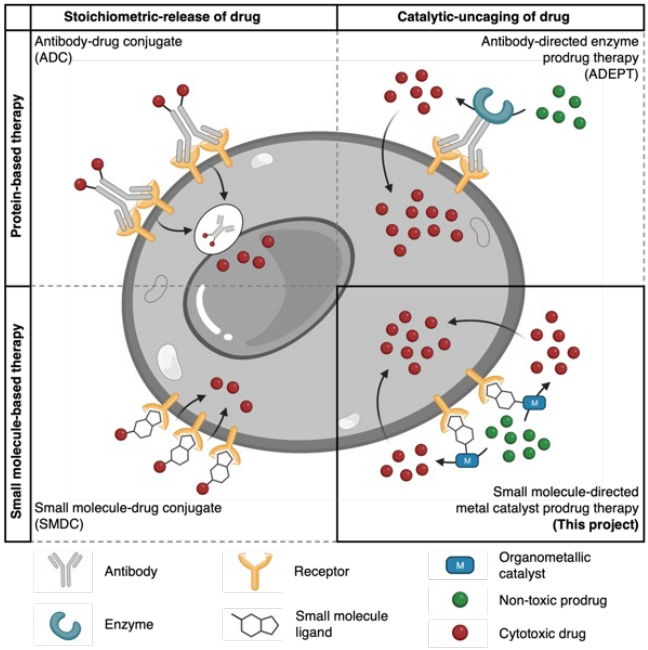

Fig. 1: Active targeting strategies used to accumulate chemotherapeutic drugs on cancer cells.

Our project is based on the development of an innovative therapy consisting of an organometallic catalyst conjugated to a targeting unit with a high affinity for a receptor that is over-expressed on the surface of cancer cells. Following selective accumulation at the surface of target cancer cells, the catalyst will site-specifically uncage a subsequently administered non-toxic prodrug to release a potent cytotoxic drug. Importantly, the small molecule-directed metal catalyst prodrug therapy (MCPT) is expected to be significantly more selective than current chemotherapies. Further, compared to antibody-drug conjugates (ADC), the small molecule components are more straightforward and inexpensive to produce and tailor for a given target. Importantly, they are expected to exhibit greater tissue diffusion rates. Building on our expertise with in cellulo metal-catalyzed carbene-insertion and cyclopropanation reactions [4,5], we set out to adapt this strategy to the metal-catalyzed intramolecular Buchner carbene insertion reaction of aryl diazoketones.

Results

Probing Buchner carbene insertion

The Buchner carbene insertion reaction is based on the formation of a metal carbene, which undergoes cyclopropanation on an aryl moiety to form a norcaradiene intermediate. This initial step is followed by a pericyclic concerted disrotatory 6π-ring expansion to afford a cycloheptatriene (Fig. 2). The systematic evaluation of copper, gold, rhodium, and iridium complexes revealed that i) Cu(Tp) predominantly produces the undesired β-lactam through the insertion into the benzylic C–H bond in polar, aprotic as well as in polar, protic solvents. ii) The Au(NHC) is inactive towards the carbene insertion into the aryl or C–H bond to form the cycloheptatriene or the β-lactam product. iii) $Rh_2(OAc)_4$ and Ir(mPIX) preferentially afford the ring expansion product and iv) are compatible with cell lysate. Due to the superior in vivo stability of Ir(mPIX) compared to $Rh_2(OAc)_4$ and the facile functionalization of the carboxylic acid moiety of the mesoporphyrin IX (mPIX), we selected Ir(mPIX) for future in vivo studies.

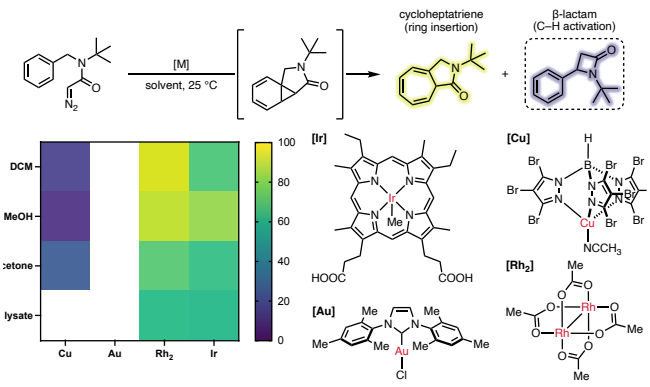

Fig. 2: Probing the Buchner carbene insertion with different transition-metal catalysts including copper, gold, rhodium, and iridium catalysts.

Design and synthesis of the caged substrate

With the aim of validating the feasibility of the uncaging strategy, we developed a caged substrate based on the aryl diazoketone model substrate (Fig. 2). The precursor was syn-

thesized in 6 steps with an overall yield of 21%. Next, the meta-benzylic alcohol moiety was used to cage cytotoxic drugs i.e. fluorouracil, doxorubicin or MMAE (Fig. 3). It additionally includes two methyl groups at the benzylic position to prevent the undesired C–H activation to afford the undesired β-lactam side-product. Following the Buchner carbene insertion, the cycloheptatriene intermediate spontaneously undergoes a 1,6-elimination, accompanied with the release of the drug. Gratifyingly, the uncaging of a para-fluorophenol substituted aryl diazoketone via Buchner carbene insertion was confirmed by LC-MS and 1H NMR spectroscopy.

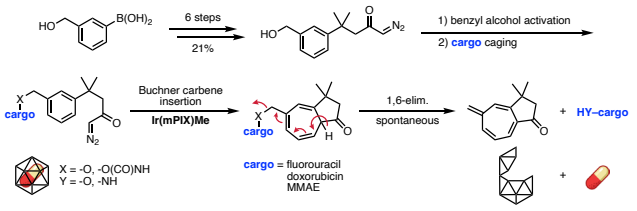

Fig. 3: Design and synthesis of an aryl diazoketone for the uncaging of cytotoxic drugs via Buchner carbene insertion, followed by spontaneous 1,6-elimination.

Targeted drug-delivery to cancer cells

The dimeric membrane protein human carbonic anhydrase IX (hCA IX) is highly over-expressed under hypoxic conditions, a common feature of the microenvironment of solid tumors. It has been extensively validated as a tumor target site. Acetazolamide-containing ligands (Fig. 4) have been widely used as sub-nanomolar hCA IX inhibitors. Importantly, these are not internalized upon binding to hCA IX.[6] For the selective accumulation of the organometallic catalyst on the cell surface, different iridium porphyrin catalysts are conjugated to the acetazolamide (AA) mono- and dual-inhibitors.

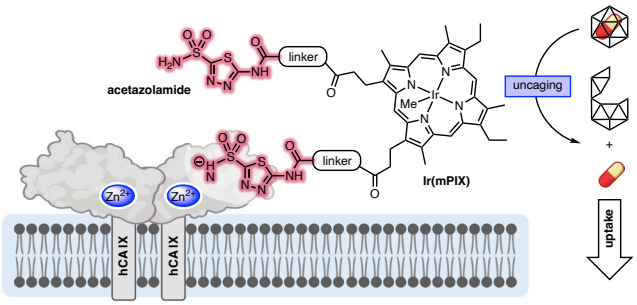

Fig. 4: Active accumulation of AA–Ir(mPIX) on the cell surface of cancer cells, using acetazolamide targeting moieties (red).

We are currently pursuing in vivo uncaging studies based on these iridium porphyrins with a fluorophore-bearing substrate on the cell surface of CT26 cell lines. Such engineered CT26 cell lines were generously provided by the group of Dario Neri and over-express hCA IX on their cell surface under normoxic conditions.

Outlook

Having demonstrated the uncaging based on the Buchner carbene insertion in silico, we are working on the in vivo uncaging of non-toxic prodrugs to afford their corresponding cytotoxic drugs. The most promising prodrug/drug couples and the AA–Ir(mPIX) catalyst will then be evaluated in a tumor-bearing mouse model to validate our developed small molecule-directed metal catalyst prodrug therapy (MCPT).

References

[1] J. Z. Drago, S. Modi and S. Chandarlapaty, Unlocking the potential of antibody-drug conjugates for cancer therapy, Nat. Rev. Clin. Oncol. 18, 327–344 (2021)

[2] G. Casi and D. Neri, Antibody-Drug Conjugates and Small Molecule-Drug Conjugates, J. Med. Chem. 58, 8751–8761 (2015)

[3] S. K. Sharma and K. D. Bagshawe, Translating antibody directed enzyme prodrug therapy (ADEPT) and prospects for combination, Expert Opin. Biol. Ther. 17, 1–13 (2017)

[4] C. Rumo, A. Stein, J. Klehr, R. Tachibana, A. Prescimone, et al. An Artificial Metalloenzyme Based on a Copper Heteroscorpionate Enables Sp3 C–H Functionalization via Intramolecular Carbene Insertion, J. Am. Chem. Soc. 144, 11676–11684 (2022)

[5] J. Zhao, D. G. Bachmann, M. Lenz, D. G. Gillingham and T. R. Ward, An Artificial Metalloenzyme for Carbene Transfer Based on Biotinylated Dirhodium Anchored within Streptavidin, Catal. Sci. Technol. 8, 2294–2298 (2018)

[6] M. Wichert, N. Krall, W. Decurtins, R. M. Franzini, F. Pretto, et al. Dual-display of small molecules enables the discovery of ligand pairs and facilitates affinity maturation, Nat. Chem. 7, 241–249 (2015)

Magnetic torque transducer in a phononic band-gap structure

Project P2107: High-sensitive torque magnetometry for 2D materials
Project Leader: I. Zardo and M. Poggio
Collaborator: M. Claus (SNI PhD Student)

Introduction
Progress in fabrication and development of nanomechanical resonators now allows measurement of mass, force, and torque with exquisite sensitivity. These improvements are mostly due to the dramatic reduction in the size of mechanical transducers over the last 30 years. Decreasing size and defect density reduces mechanical losses and therefore improves transducer sensitivity [1]. Recently, phonon engineering has also been exploited to diminish mechanical losses [2] via patterned mechanical supports engineered to have a phononic band-gap around a transducer's mechanical resonance frequency. In addition, the supports have been designed to optimally clamp the resonator, further reducing loss. These techniques have been used to make high-Q optomechanical devices [2] and are beginning to be applied in the design of ultra-sensitive force sensors. So far, however, no one has applied them to torque sensing.

Here, we intend to apply these techniques to fabricate ultra-sensitive mechanical torque sensors and to design these sensors especially for the investigation of 2D materials – including 2D magnets and van der Waals (vdW) heterostructures. In addition to being sensitive enough to measure ultrathin magnetic materials, our sensors will incorporate the possibility of making electrical contact to the sample as sketched in the envisioned device shown in figure 1.

Torque magnetometry is an established and highly sensitive technique for studying nanomagnets, correlated metals, and superconductors [3]. Dynamic torque (frequency shift), which is proportional to the curvature of the magnetic free energy with respect to rotations, is a particularly useful observable for identifying magnetic phase transitions [4], because – just like the magnetic susceptibility – it is discontinuous for both first and second order phase transitions. Torque magnetometry is broadband and capable of measuring both magnetostatic effects and magnetization dynamics, including spin resonance and relaxation processes [5]. The improved sensitivity of our planned torque sensors and the ability to integrate electrical leads and contacts to the sample will enable a whole series of experiments: e.g. detecting superconducting and magnetic phase transitions in twisted bi-layer graphene [5], vdW heterostructures, and other 2D materials, including the reported magnetic phase transition in gated monolayer MoS2 [6]. Our vision is to create and apply a new experimental platform for the investigation of magnetic and superconducting phase transitions in 2D systems.

Goals
Sensitive torque magnetometry has been used to determine the magnetic behavior of very small magnets [7], persistent currents in normal metal nano-rings [8], and tiny superconducting structures [9]. So far, however, its sensitivity has not been leveraged to measure any of the emerging class of 2D vdW materials and their heterostructures, which are far too thin for conventional SQUID or torque magnetometers. Recently discovered correlated states in these systems range from superconductivity, to highly insulating states, to magnetism. In some cases, transitions between these states can even be induced by electrostatic gates. Our specially designed torque sensors will allow us to measure these phase transitions, yielding the associated phase diagrams and giving new insight into these poorly understood condensed matter phenomena.

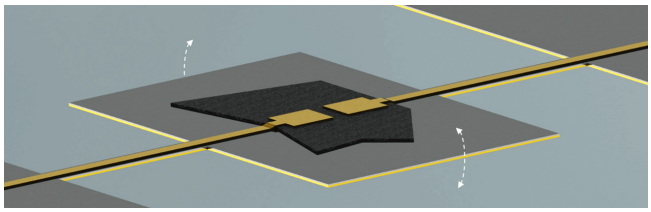

Fig. 1: Schematic diagram of a torque sensor with 2D sample, bottom back gate, and top contacts.

Accordingly, the goals of this project are to:
1) Fabricate torsional resonators allowing for electrical contact to the sample and integrate them within a phononic band-gap support with optimal clamping;

2) Demonstrate state-of-the-art torque sensitivity on samples with electrical contacts;

3) Use the transducers to measure magnetic and superconducting phase transitions in 2D materials as a function of applied gate voltage, magnetic field, and temperature.

Results
After development of fabrication techniques to make torsional torque transducers inside a phononic band-gap support made from silicon nitride during the first year, we have shifted towards studying and testing flexural beams with a phononic band-gap during the second year. An optical image of one such flexural torque transducers and its frequency response spectrum are shown in figure 2. The latter shows a band gap between 400 and 670 kHz, and the fundamental flexural resonance of the transducer at 490 kHz, well within the band-gap. With this phonon escape from the resonantor into the substrate is suppressed strongly by the band-gap. This is confirmed by the fact that the flexural mode at 490 kHz is only observed when it is driven with an ac magnetic field, while it cannot be excited with a simple piezo actuator shaking the entire chip.

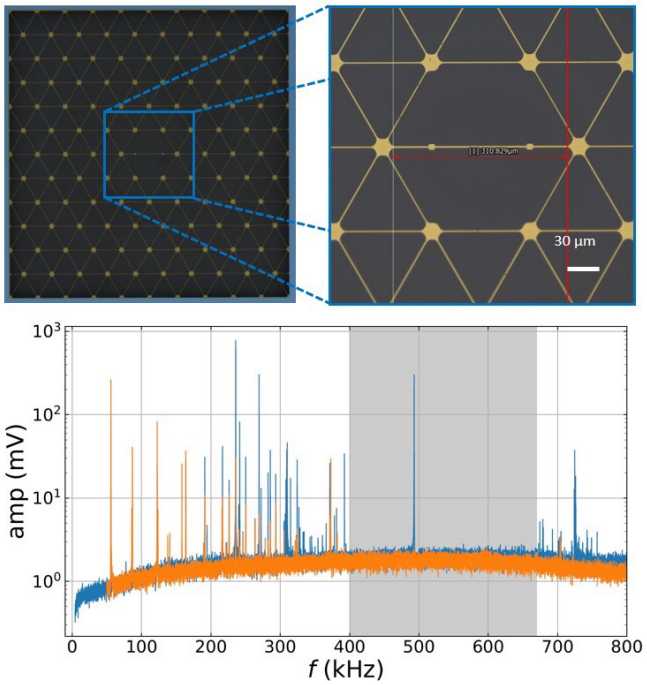

Fig. 2: Doubly clamped flexural torque transducer inside a phononic band-gap structure and measured frequency response spectrum with the band-gap highlighted by the gray background. The signal at 490 kHz is only visible when driving the device with an ac magnetic field (blue data), while it is not observed when a piezo actuator (orange data) is used instead.

In spite of successful fabrication of such a band-gapped flexural transducer, we did not observe a substantial improvement in the Q-factor compared to transducers that are not embedded within a band-gap. This indicates that mechanical dissipation of our flexural resonator is again dominated by bending and/or surface losses as was the case for the torsional transducers developed and studied previously. Again, this demands for optimization of the device on other premises as for example by performing a final surface passivation to reduce surface losses.

In addition, we have explored and developed a fabrication technique to make plain silicon nitride cantilevers with a 2D magnetic specimen attached: First, a simple silicon nitride membrane is fabricated based on the same microfabrication techniques that were used to make previous transducers. In a second step, crystals of a magnetic material are exfoliated to yield magnetic samples that are only few layers thick, which are then stamped directly on top of the suspended membrane by employing a standard PC-transfer protocol. In a last step, a cantilever is cut around the magnetic specimen by FIB-milling to yield the final torque transducer with a 2D magnetic specimen attached to it. The characteristics and magnetic signatures of such a transducer with a CrSBr antiferromagnetic specimen is currently under investigation.

Outlook

With the acquired expertise to produce suspended silicon nitride microresonators, we are able to design and fabricate high-sensitive torque transducers with high precision and good yield. With the addition of the ability to make transducers that have a 2D magnetic specimen attached to them, we are currently investigating the characteristics of such high-sensitive transducers and aim to study their magnetic signatures within the weeks to come. If successful, this will allow us to study many different magnetic 2D materials in the future even without reducing phonon dissipation by means of a phononic band-gap structure. Concerning our band-gapped transducers, we have learned that surface dissipation is the dominant loss mechanism. This will be addressed in the near future by exploring and testing different surface passivation techniques.

References

[1] F. R. Braakman and M. Poggio, Force sensing with nanowire cantilevers, Nanotechnol. 30, 332001 (2019)

[2] Y. Tsaturyan, A. Barg, E. S. Polzik, and A. Schliesser, Ultra-coherent nanomechanical resonators via soft-clamping and dissipation dilution, Nat. Nanotechnol. 12, 776 (2017)

[3] A. Mehlin, F. Xue, D. Liang, H. F. Du, M. J. Stolt et al., Stabilized Skyrmion phase detection in MnSi Nanowires by Dynamic Cantilever Magnetometry, Nano Lett. 15, 4839 (2015)

[4] J. E. Losby, F. F. Sani, D. T. Grandmont, Z. Diao, M. Belov et al., Torque-mixing magnetic resonance spectroscopy, Science 350, 798 (2015)

[5] U. Zondiner, A. Rozen, D. Rodan-Legrain, Y. Cao, R. Queiroz et al., Cascade of phase transitions and Dirac revivals in magic-angle graphene, Nature 582, 203 (2020)

[6] J. G. Roch, D. Miserev, G. Froehlicher, N. Leisgang, L. Sponfeldner et al., First-order magnetic phase transition of mobile electrons in monolayer MoS2, Phys. Rev. Lett. 124, 187602 (2020)

[7] A. Mehlin, B. Gross, M. Wyss, T. Schefer, G. Tütüncüoglu et al., Observation of end-vortex nucleation in individual ferromagnetic nanotubes, Phys. Rev. B 97, 134422 (2018)

[8] A. C. Bleszynski-Jayich, W. E. Shanks, B. Peaudecerf, E. Ginossar, F. von Oppen et al., Persistent currents in normal metal rings, Science 326, 272 (2009)

[9] J. Jang, D. G. Ferguson, V. Vakaryuk, R. Budakian, S. B. Chung et al., Phase-locked cantilever magnetometry, Science 331, 186 (2011)

Exploration of 2D layered transition metal based ferromagnets

Project P2202: Search for 2D ferromagnetism at room temperature
Project Leader: M. Ciomaga Hatnean and M. Kenzelmann
Collaborator: T. Geise (SNI PhD Student)

Introduction

Two-dimensional ferromagnets are of great interest in the scientific community since the discovery of intrinsic ferromagnetism in bilayer CrI_3 and $CrGeTe_3$ (CGT) [1,2]. Owing to the physical properties of these materials, they have great potential to be used in spintronics. One of the most studied layered van der Waals ferromagnets is CGT, which belongs to the compound class ABX_3, where A is a transition metal cation, B is dimerized ion (mostly Si, Ge) and X is a chalcogenide anion (S, Se, Te). Several other compounds isostructural with CGT have been synthesized and investigated.

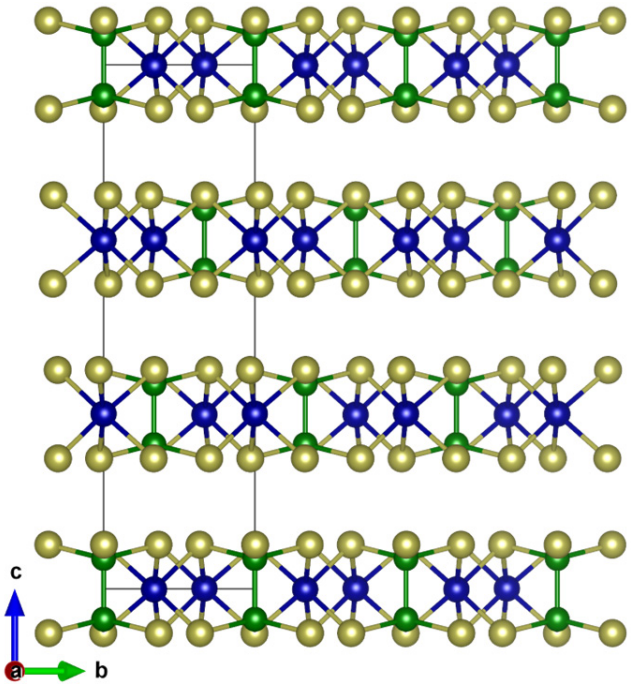

Fig. 1: Crystal structure of CGT viewed along a-axis. Van der Waals gaps are visible between the layers. Blue atoms: Cr, Green atoms: Ge, Yellow atoms: Te.

CGT crystallizes in a trigonal space group, $R\bar{3}$ (No. 148). The layered structure exhibits van der Waals gaps between the Tellurium atoms. The magnetic chromium ions are arranged in a honeycomb lattice. The existence of van der Waals gaps in materials is a rare behavior, but it is very useful for the exfoliation and preparation of atomically thin layers, which afterwards can be studied with techniques like MOKE.

The typical arrangement formed by the transition metal ions, i.e. a honeycomb lattice, can yield four different types of magnetic ground states. ABX_3 systems are expected to be either ferromagnetic or antiferromagnetic (Fig. 2).

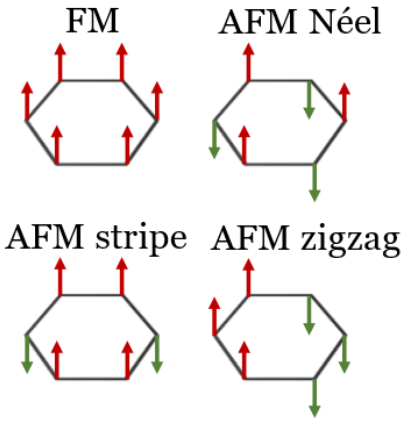

Fig. 2: Expected types of magnetic ordering in the ABX_3-class.

Previous studies suggested that the nature of the magnetism exhibited by CGT is correlated to the Cr-Te-Cr angle, i.e., if this angle is closer to 90°, the superexchange interaction is expected to become stronger, thus leading to a ferromagnetic ordering of the Cr-ions. In 2015, computational studies predicted an antiferromagnetic zig zag type ordering in the $CrSiTe_3$ monolayer [3]. This was later disproved experimentally, and a recent study showed that $CrSiTe_3$ exhibits ferromagnetic properties in the monolayer [4]. In $CrSiTe_3$, despite the fact that the Cr-Te-Cr angle is closer to 90° than in CGT, the magnetic transition temperature is significantly lower (31 K). These results suggest that the nature of the magnetic interactions in these systems is still not fully understood.

Furthermore, upon substitution of Cr with Mn, additional manganese cations are intercalated in the van der Waals gaps. Despite being isostructural with CGT, $Mn_3Si_2Te_6$ and $Mn_3Si_2Se_6$ compounds exhibit thus a ferrimagnetic long range ordering [5,6]. Moreover, it has already been observed that the TC in CGT also decreases as the number of atomic layers decreases [7]. The application of tensile strain has the potential to increase the TC in the atomically thin layers [8]. Using computational methods, several new materials in this class are predicted to form. The aim of our exploratory experimental work is the discovery of new ferromagnetic materials belonging to this family of compounds. In addition, we plan to investigate other classes of materials, different in structure and in chemical composition, but exhibiting similar properties (layered van der Waals crystal structures and ferromagnetic ordering with a high TC).

Various methods can be used to obtain powder or single crystals of layered van der Waals materials. In our work, we employed two techniques: solid-state reaction and flux growth method. Using the flux method, we were able to synthesize

large single crystals of CGT (Fig. 3). During our growth experiments, we varied the main parameters that affect the quality and size of the crystals, i.e. heat treatment conditions (temperature, duration and heating/cooling rates). The synthesis of polycrystalline materials by solid state reaction was only partially successful, as in most cases, the resulting powder was multi-phase. The presence of minor secondary phases was observed. We plan to adapt our procedure for the synthesis of polycrystalline material, by employing other methods, such as ball-milling, in order to eliminate the small amounts of secondary phases that form in the solid-state reaction.

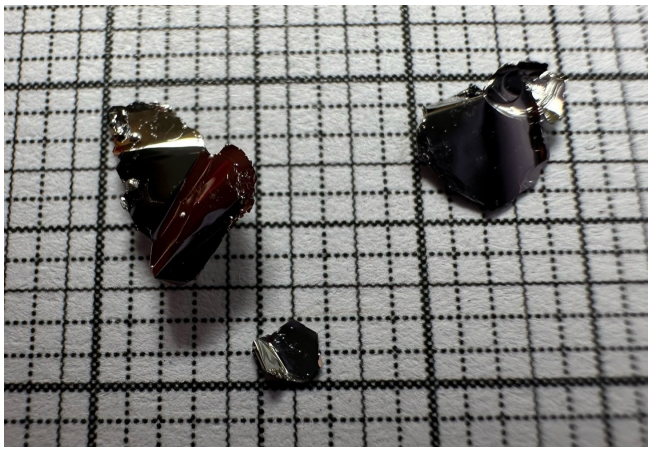

Fig. 3: CGT single crystals on mm-paper. Crystals were grown by the flux method.

The characterization of the polycrystalline and single crystal samples prepared was performed using several laboratory-based characterization methods. Powder and single crystal X-ray diffraction were used to identify phases and investigate the crystal structures of the prepared materials. When single phase materials were obtained, we carried out μ-XRF, MPMS and PPMS measurements on these samples. Laboratory-based characterization methods are part of the preliminary preparation of the samples for further neutron investigations, aimed at understanding the magnetic interactions in the studied materials. Once we identify new ferromagnetic materials that are ferromagnetic in the bulk, we will investigate if they exhibit similar properties in the atomically thin layers.

Results

In a first instance, we prepared single crystals of CGT, the archetypal ferromagnet belonging to the ABX_3 class of materials. We then investigated the structural and magnetic properties of CGT crystals prepared. Single crystal X-ray diffraction measurements confirmed that CGT crystallizes in the trigonal space group $R\bar{3}$ (No. 148). Magnetization measurements performed on our crystals showed, that the crystal has a paramagnetic-ferromagnetic transition at $T_C \sim 65$ K (Fig. 4). These experiments were performed to establish a growth procedure, and the results of the structural and magnetic properties investigations will be used as a standard for the new materials prepared.

Outlook

Furthermore, different synthesis attempts of new materials are ongoing. Following the investigations performed on the bulk crystals, we will prepare atomically thin layers (mono- to multilayers) of these materials by exfoliation, for studies of the magnetic properties at the 2D level. The magnetic behavior of the materials will be investigated to determine their potential role in future applications in novel spintronics.

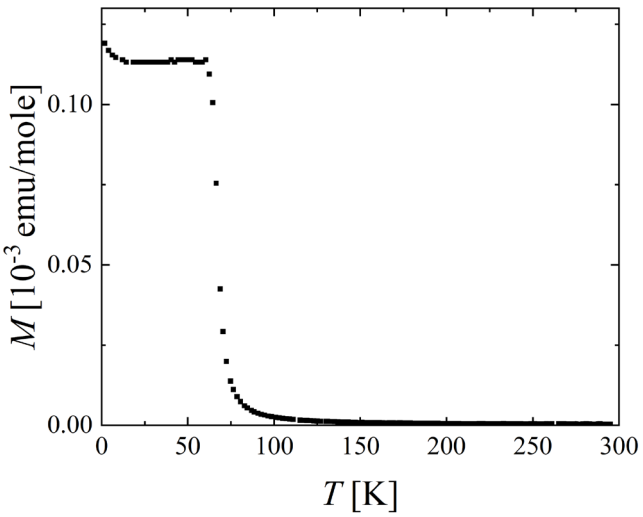

Fig. 4: Temperature dependence of magnetization measured on a CGT crystal.

References

[1] B. Huang, G. Clark, E. Navarro-Moratalla, D. R. Klein, R. Cheng et al., Layer-dependent ferromagnetism in a van der Waals crystal down to the monolayer limit, Nature 546, 270-273 (2017)

[2] C. Gong, L. Li, Z. Li, H. Ji, A. Stern et al., Discovery of intrinsic ferromagnetism in two-dimensional van der Waals crystals, Nature 546, 265-269 (2017)

[3] N. Sivadas, M. W. Daniels, R. H. Swendsen, S. Okamoto, D. Xiao, Magnetic ground state of semiconducting transition-metal trichalcogenide monolayers, Phys. Rev. B 91, 235425 (2015)

[4] J. Zhang, X. Cai, W. Xia, A. Liang, J. Huang et al., Unveiling Electronic Correlation and the Ferromagnetic Superexchange Mechanism in the van der Waals Crystal CrSiTe3, Phys. Rev. lett. 123,047203 (2019)

[5] A. F. May, Y. Liu, S. Calder, D. S. Parker, T. Pandey et al., Magnetic order and interactions in ferrimagnetic Mn-3Si2Te6, Phys. Rev. B 95, 174440 (2017)

[6] A. F. May, H. Cao, S. Calder, Magnetic properties of ferrimagnetic Mn3Si2Se6, J. Mag. Mag. Mat. 511, 166936 (2020)

[7] M. Gibertini, M. Koperski, A. F. Morpurgo, K. S. Novoselov, Magnetic 2D materials and heterostructures, Nat. Nanotechnol. 14, 208-419 (2019)

[8] L. Liu, X. Hu, Y. Wang, A. V. Krasheninnikov, Z. Chen et al., Tunable electronic properties and enhanced ferromagnetism in Cr2Ge2Te6 monolayer by strain engineering, Nanotechnology 32, 485408 (2021)

Understanding the promoting role of sulfur in cobalt phosphide nanocatalysts

Project P2203: Towards earth-abundant nanocatalysts for hydrogenation reactions: Understanding the promoting role of sulfur in cobalt phosphide nanocatalysts
Project Leader: M. F. Delley and M. Nachtegaal
Collaborator: C. Yuan (SNI PhD Student)

Introduction

Hydrogenation reactions are widely used for the production of chemicals in the chemical industry. For the development of sustainable processes highly efficient and highly selective catalysts are needed that are made of earth-abundant elements. In particular, transition metal phosphide nanomaterials have recently shown great promise as catalysts for chemical transformations in energy-related applications, such as water splitting [1]. These materials have also shown high catalytic activity for hydrodesulfurization (HDS), in which heteroatoms are removed from organic fuels by reaction with H_2, and more recently also for the hydrogenation of multiple bonds in organic substrates [2]. Empirical studies have shown that the catalysis of water splitting by transition metal phosphides can be enhanced when a hetero-element, especially sulfur, is incorporated in the catalytic material (e.g. by doping)[3]. Interestingly, a similar effect has been observed in HDS applications of these materials. During HDS sulfur is incorporated at the surface of transition metal phosphides and it is this in-situ formed phosphosulfide that is thought to be catalytically active [4]. However, due to the complexity of the sulfur-doped transition metal phosphide catalysts, it is challenging to establish clear structure-reactivity relationships for the sulfur-effect on the catalysis of these materials.

Goal of this research

The goal of this research is to understand the promoting role of sulfur on the hydrogenation catalysis by transition metal phosphide nanoparticles in order to develop a roadmap for the design of better catalysts. We aim to combine a strategy for a controlled sulfur-doping of transition metal phosphide nanoparticles with operando X-ray-based spectroscopic analysis for detailed information on the structure of the catalytic active site and especially the role of sulfur in the material under catalytic working conditions. This should enable the construction of structure-reactivity relationships for the rational development of efficient hydrogenation catalysts. At present, we are working on the preparation of suitable cobalt phosphide nanoparticles and the development of a controlled method of doping the nanoparticles with sulfur.

Result and Discussion

We adapted a previously reported method for the synthesis of cobalt phosphide nanoparticles [5]. Cobalt chloride as Co-precursor, 10 equivalents of triphenyl phosphite as P-precursor, and 10 equivalents of hexadecylamine (HDA) as ligand were dissolved and mixed in hexadecane. Hexadecane was chosen as solvent in order to avoid a possible oligomerization of the more typically used 1-octadecene solvent at 280°C [6]. The mixture was degassed for 2 h at 150°C and then heated to 280°C for 0.5 h. At this temperature a black precipitate formed, which suggested the successful formation of nanoparticles. These were then separated, washed, and redispersed. Optimization of the washing and centrifugation procedure enabled an increase in the yield of particles by 50%. Multiple batches of particles were prepared to test for reproducibility of our results. The thereby prepared particles were characterized by a range of physicochemical methods. Analysis by powder X-ray diffraction (pXRD) and X-ray photoelectron spectroscopy (XPS) was consistent with the preparation of cobalt phosphide particles that are largely amorphous. Transmission Electron Microscopy (TEM) pictures provided information on the shape and size of the particles and are shown in figure 1.

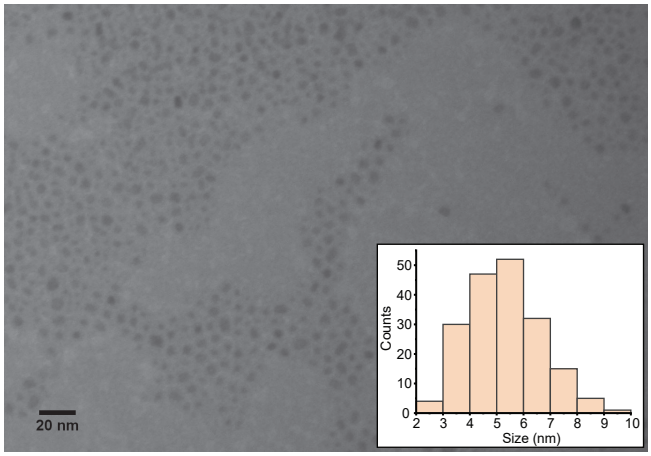

Fig. 1: The TEM picture of the prepared cobalt phosphide nanoparticles and their size distribution.

The particles had quasi-spherical shapes with an average size of 5 ± 1 nm. This differs from the shape and size obtained through original the procedure, which lead to rod-shaped particles with a size of width × length = 6.9 ± 0.8 nm × 33 ± 9 nm and a crystalline Co_2P structure, presumably due to differences in the synthetic method including the rate of the inert-gas-flow [5]. Characterization of the particles by FTIR showed bands near 3000 cm^{-1} that were assigned to the symmetric and asymmetric stretching from the -CH_2 and –CH_3 groups (Fig. 2). These bands show the presence of the HDA ligands having long alkyl chains on the particle surface. Combined XPS and TGA analysis of two different batches of cobalt phosphide nanoparticles suggested that the mass ratio of the ligand shell to cobalt phosphide particle (assuming a CoP phase) is approximately 30%.

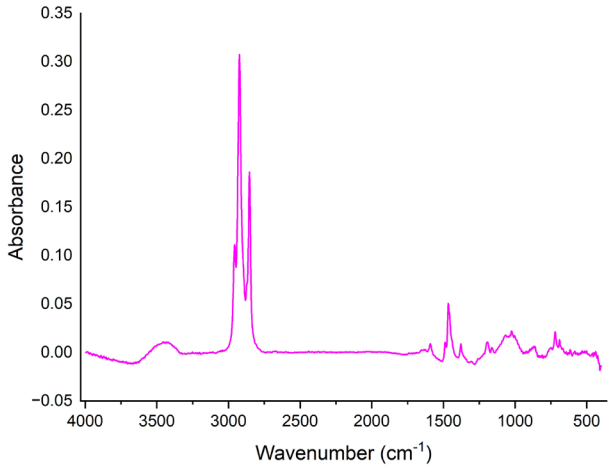

Fig. 2: The IR spectrum of the as-synthesized cobalt phosphide nanoparticles.

After successful synthesis of cobalt phosphide nanoparticles, we tested different soft chemical methods to remove the ligands on the surface [7]. A removal of the ligands from the nanoparticle surface is pursued as this should increase their catalytic ability through higher accessibility of the reactive surface. The thereby-treated particles were isolated, washed, and characterized by TEM, TGA, and IR. Figure 3 shows a representative TEM picture of nanoparticles after ligand removal. The ligand removal procedure has slightly decreased the size of the particles to 4 ± 1 nm with a quasi-spherical shape retained. TGA analysis was consistent with the removal of a significant fraction of the HDA ligands and suggested the presence of light, more volatile components on the particles, such as ethanol used for washing. We are currently using further characterization methods to quantify the amount of removed ligands per particle.

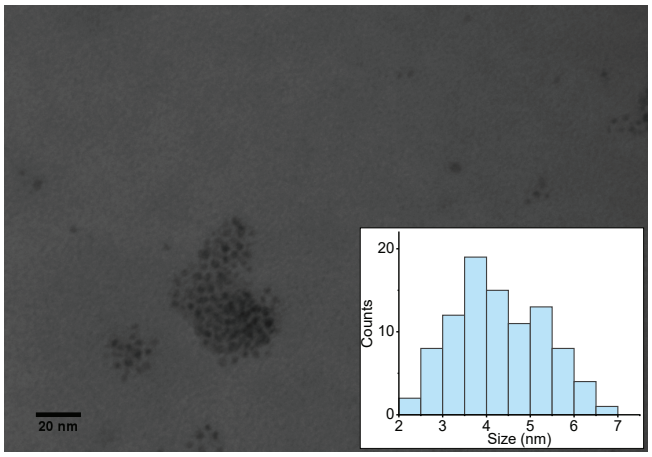

Fig. 3: The TEM picture of the cobalt phosphide nanoparticles after ligand removal and their size distribution.

Preliminary efforts to dope the cobalt phosphide nanoparticles with sulfur seem promising as ca. 0.014 mg sulfur per mg of cobalt phosphide nanoparticles can be achieved.

Conclusion and Outlook

Within 6 months, we successfully synthesized and characterized cobalt phosphide nanoparticles with long alkyl ligands. Further first results show that we can remove a substantial fraction of the ligands and dope the cobalt phosphide nanoparticles with sulfur. Next, we will be optimizing sulfur doping and test the catalytic properties of both as-prepared and sulfur-doped cobalt phosphide nanoparticles for hydrogenation reactions. Synchrotron-based operando experiments will also be designed in the next step in order to gain insight into the key structure-reactivity relationships of these materials.

References

[1] T. Shi, B. Zhang, Recent advances in transition metal phosphide nanomaterials: synthesis and applications in hydrogen evolution reaction, Chem. Soc. Rev., 45, 1529-1541 (2016)

[2] S. Oyama, T. Gott, H. Zhao, Y. Lee, Transition metal phosphide hydroprocessing catalysts: A review, Catal. Today, 143, 94– 107, (2009)

[3] J. Kibsgaard, T. Jaramillo, Molybdenum Phosphosulfide: An Active, Acid-Stable, Earth-Abudant Catalyst for the Hydrogen Evolution Reaction, Angew. Chem. Int. Ed. 53, 14433-14437, (2014)

[4] X. Duan, Y. Teng, A. Wang, V. Kogan, X. Li, Y. Wang, Role of sulfur in hydrotreating catalysis over nickel phosphide, J. Catal. 261, 232– 240, (2009)

[5] J. Liu, M. Meyns, T. Zhang, J. Arbiol, A. Cabot, A. Shavel, Triphenyl Phosphite as the Phosphorus Source for the Scalable and Cost-Effective Production of Transition Metal Phosphides, Chem. Mater. 30, 1799-1807, (2018)

[6] E. Dhaene, J. Billet, E. Bennett, I. Van Driessche, J. De Roo, The Trouble with ODE: Polymerization during Nanocrystal Synthesis, Nano Lett. 19, 7411-7417, (2019)

[7] A. Nelson, Y. Zong, K. Fritz, J. Suntivich, R. Robinson, Assessment of Soft Ligand Removal Strategies: Alkylation as a Promising Alternative to High-Temperature Treatments for Colloidal Nanoparticle Surfaces, ACS Mater. Lett. 1, 177-184, (2019)

Rubisco phase separation: from dynamics to structure

Project P2204: NanoPhase: A multi-scale view of phase separation from cells to nanostructure
Project Leader: B. Engel and M. Hondele
Collaborator: Ph. Van der Stappen (SNI PhD Student)

Small, dynamic, and liquid-like
Biomolecular condensation and liquid-liquid phase separation (LLPS) have recently become recognized as fundamental mechanisms underlying the formation and function of membraneless organelles (MLOs) and cellular organization. These dynamic compartments, devoid of a surrounding membrane, facilitate a variety of crucial biochemical processes, including RNA processing and carbon fixation. The essence of LLPS lies in its weak, multivalent interactions, which foster the creation of organelles that are highly dynamic, flexible, and reversible. These properties allow them to exhibit a remarkable diversity in size, composition, material characteristics, regulatory mechanisms, and functional roles [1].

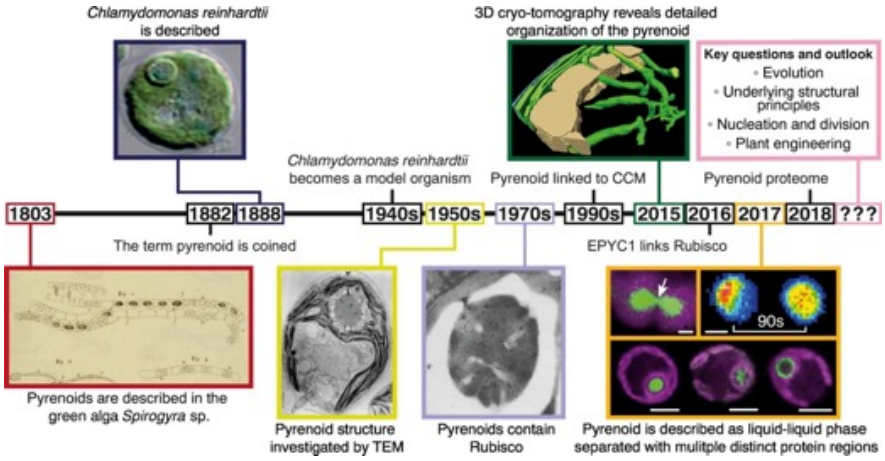

Fig. 1: A brief history of research into the pyrenoid and the model organism Chlamydomonas. Adapted from [2].

Both in vitro (when reconstituted from recombinant proteins) and inside cells, biomolecular condensates have mostly been studied at the microscale using light microscopy techniques such as fluorescence recovery after photobleaching (FRAP) and passive microrheology. In this project, our research will focus on investigating the mechanisms of phase separation across scales, ranging from cellular dynamics to molecular nanostructure.

The pyrenoid – a membraneless organelle fixates CO_2 in photosynthetic marine algae
Among all diverse biomolecular condensates, the pyrenoid [2] stands out as a pivotal element in Earth's biosphere. This MLO is predominantly found in the chloroplasts of algae, is filled with the carbon-fixing enzyme Rubisco (Ribulose-1,5-bisphosphate carboxylase/oxygenase), and is responsible for approximately one-third of the planet's photosynthetic CO_2 assimilation. Algae are a vital component of marine ecosystems, carrying out carbon fixation and oxygen production, while forming the foundation of aquatic food webs.

The model alga Chlamydomonas reinhardtii
In the model organism C. reinhardtii, it is known that an intrinsically disordered protein called EPYC1 interacts with Rubisco and is essential for the underlying phase separation that enables formation of the pyrenoid [3]. Figure 1 highlights the chronological history of key pyrenoid discoveries, from their first observation by light microscopy in 1803, to the recent rapid progress understanding their function, molecular composition, and LLPS.

Looking at the eukaryotic tree of life, we can observe various different algal pyrenoid morphologies (see Fig. 2). However, to this day, we only know about three essential linker proteins which form Rubisco condensates across species, and only the C. reinhardtii pyrenoid system is characterized well enough to allow in-depth biophysical study.

Thus, we are keen to apply our multiscale techniques to understand both the biochemical and structural mechanisms governing Rubisco phase separation in the C. reinhardtii pyrenoid.

Intrinsically disordered proteins are key
EPYC1 is a 30 kDa protein with intrinsically disordered regions (IDRs), high positive charge, and 5 repeating sequences. Each of these five repeats contains a Rubisco binding motif. This allows for weak multivalent interactions bridging adjacent Rubisco proteins which enables condensate formation (see Fig. 3). These biochemical properties of IDRs are crucial for LLPS. The Rubisco binding motifs is called a “sticker”, and the amino acids between a sticker is called a “spacer”. EPYC1 has 5 stickers and 5 spacers.

However, such Rubisco linker proteins are not conserved between different algal clades. No homology sequences are known, but functional homologs exist that share common properties such as IDR’s, weak multivalency, and a sticker-spacer model. Why evolution came up with a set number and length of stickers and spacers is a big mystery that we aim to explore in our project.

Cryo-electron tomography and the pyrenoid ultrastructure
Rubisco is the most abundant protein in the world, and its copy number inside a single algal pyrenoid is high. Additionally, the 550 kDa protein is big enough to be resolved by high-resolution cryo-electron tomography (cryo-ET, Fig. 4). By combining cryo-ET with different biophysical methods to

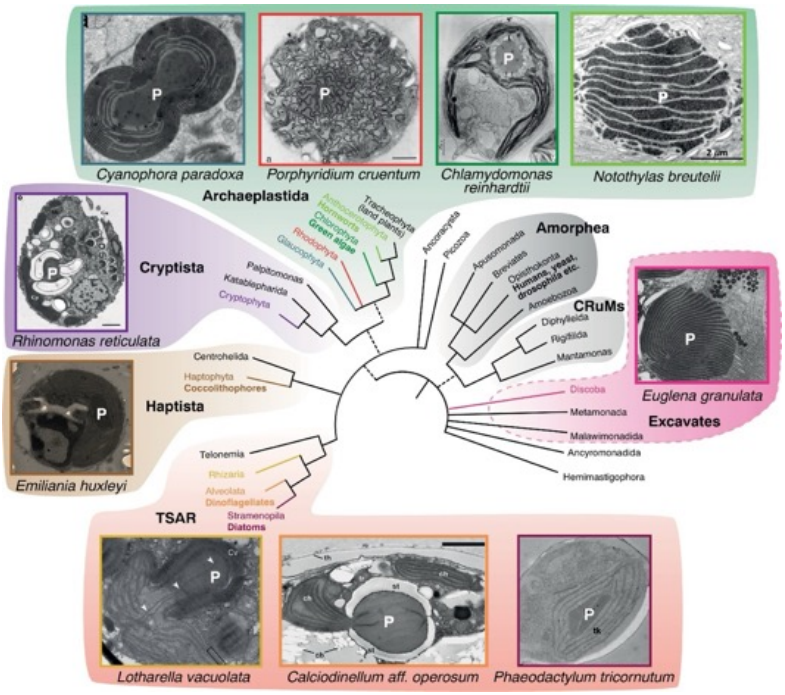

Fig. 2: Pyrenoid-containing algae are polyphyletic and found across the eukaryotic tree of life. Adapted from [2].

study biomolecular condensates – such as FRAP and microrheology – we aim to bridge our understanding of LLPS across scales.

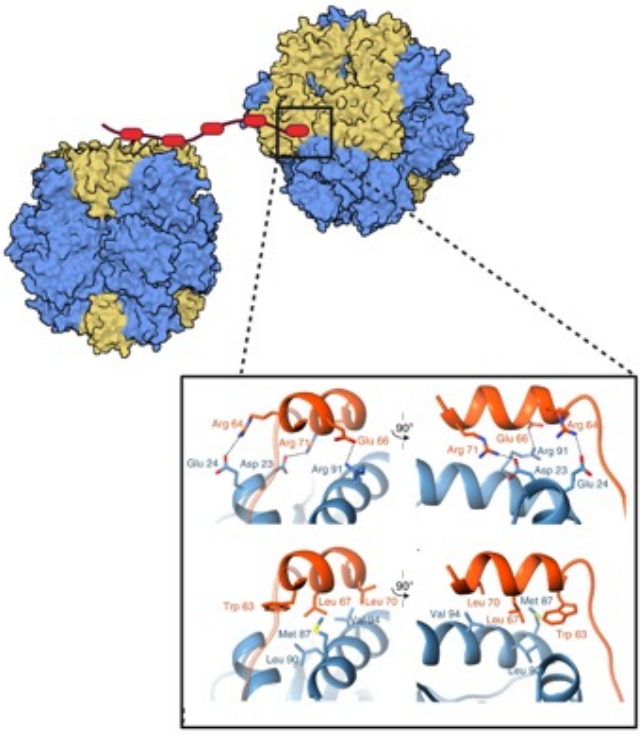

Fig. 3: Depiction of multivalent crosslinking between Rubisco by EPYC1. Zoomed in box shows residues involved in the binding. Adapted from [4].

We are developing a modular system to test several tunable properties of EPYC1 linker variants (sticker and spacer modifications) on the LLPS of Rubisco both in vitro and inside cells. By combining micrometer-scale measurements of condensate dynamics with nanometer-scale analysis of Rubisco organization, we aim to bridge the gap between the liquid-like fluid properties of the condensate and the ultrastructural arrangement of its components. This would be a first in the field of phase separation, and would also provide new insights into the globally-important pyrenoid compartment.

References

[1] Y. Shin, C. P. Brangwynne, Liquid phase condensation in cell physiology and disease. Science, 357.6357 (2017)

[2] J. Barrett, P. Girr, and L. C. M Mackinder, Pyrenoids: CO2-fixing phase separated liquid organelles. Biochim. Biophys. Acta Mol. Cell Res. 1868(5) (2021)

[3] L. C. M. Mackinder, M. T. Meyer, T. Mettler-Altmann, V. K. Chen, M. C. Mitchell et al. A repeat protein links Rubisco to form the eukaryotic carbon-concentrating organelle. Proc. Nat. Acad. of Sci. USA 113(21) (2016)

[4] S. He, H-T. Chou, D. Matthies, T. Wunder, M. T. Meyer et al. The structural basis of Rubisco phase separation in the pyrenoid. Nat. plants 6(12) (2020)

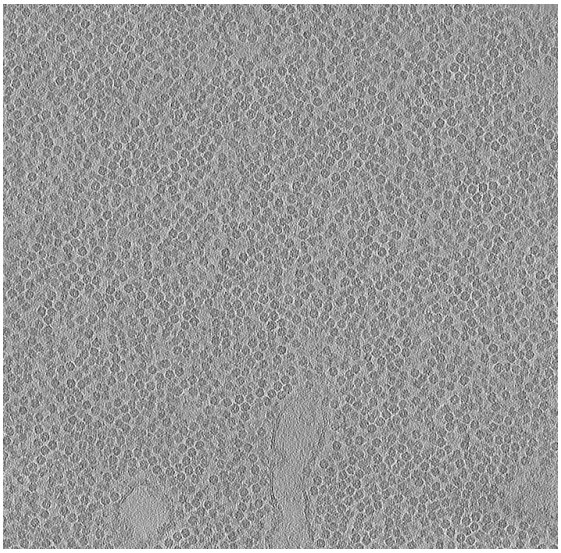

Fig. 4: A cryo-electron tomogram of the pyrenoid inside a frozen C. reinhardtii cell. Individual Rubisco protein complexes are visualized with high resolution.

Towards NIR-light triggered nanocarriers

Project P2206: Multi-compartment nanofactories for on-site and on-demand drug synthesis and delivery
Project Leader: O. Tagit and C. G. Palivan
Collaborator: A. Nikoletić (SNI PhD Student)

Introduction

Combination chemotherapy has been shown to provide a synergistic or additive attack on tumors. However, distinct pharmacokinetic and solubility profiles of individual drugs make the choice of correct dosages and drug ratio difficult and can hence lead to inefficient therapy [1]. Therefore, new drug delivery systems are emerging, with the ability to co-deliver dissimilar small molecules to the site of interest at an optimum dose using nanocarriers. Aqueous self-assembly of amphiphilic block copolymers into nano- and microscopic vesicles is commonly used to produce compartments used in an array of applications ranging from nanoreactors to cell mimicry and drug delivery [2]. Compared to liposomes (lipid vesicles), vesicles based on amphiphilic polymers offer both improved mechanical and chemical stability, as well as the possibility to tune thickness, permeability, and stimuli-responsive behavior. Stimuli-responsiveness is a key aspect to improve spatial and temporal control over delivery. Polymers that display either a lower critical solution temperature (LCST) or an upper critical solution temperature (UCST) in aqueous medium are used as building blocks to develop thermoresponsive nanocarriers that undergo structural change once heated above their critical temperature.

In this project, we aim to develop 'nanofactories' with multiple internal compartments capable of independently and selectively releasing content when triggered. Our nanocompartments are based on stimuli-responsive block copolymers and gold nanorods (AuNRs). Gold nanorods with different aspect ratios have different localized surface plasmon resonances (LSPR), and will generate heat when excited with photons of specific wavelengths [3]. By combining different AuNRs and thermoresponsive polymeric compartments, they can be selectively triggered at different excitation wavelengths (Fig. 1). We are synthesizing novel thermoresponsive block copolymers that self-assemble into polymersomes, to which we covalently attach AuNRs through appropriate end-group functionalization of polymers. Our 'nanofactories' will be produced in a bottom-up manner, by co-encapsulating different compartments inside giant unilamellar vesicles (GUVs).

Thermoresponsive block copolymers

We have developed a library of thermoresponsive block copolymers based on polydimethylsiloxane (PDMS) and poly(diethylene glycol acrylate) (PDEGA). This library consisting of hydrophobic PDMS and hydrophilic PDEGA blocks was synthesized to investigate the influence of block chain lengths on the thermoresponsive behaviour and architecture of self-assembled structures. Starting from PDMS-OH of varying degrees of polymerization, we synthesized PDMS-CTA macroinitiators using Steglich esterification. We then used photoinitiated RAFT polymerization to couple variable block lengths of hydrophilic PDEGA. RAFT end-group can be cleaved into a thiol group using aminolysis, resulting in a ω-thiol functionalized PDMS-b-PDEGA. Synthesized copolymers were characterized by 1H NMR spectroscopy and GPC, revealing the controlled nature of RAFT polymerization.

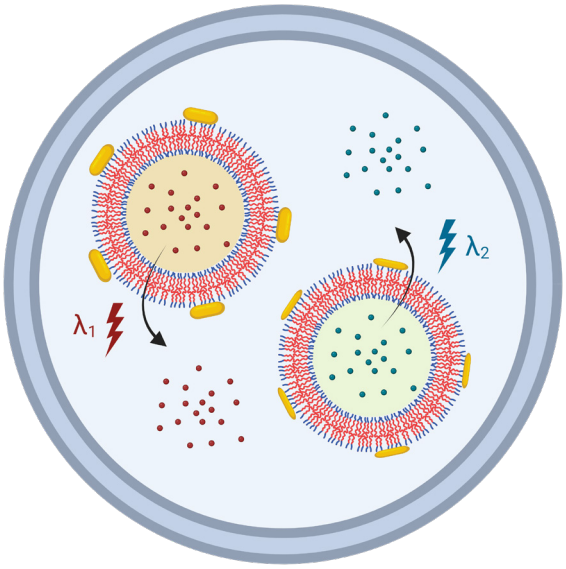

Fig. 1: Schematic illustration of the 'nanofactory'. Compartments with different AuNRs are triggered with light of different wavelengths.

To evaluate the thermoresponsive behaviour of PDMS-b-PDEGA, dynamic light scattering (DLS) and turbidimetry (cloud point) experiments were conducted in aqueous solutions in H_2O and PBS. The cloud point of PDMS-b-PDEGA¬ (f=68%) was determined to be 46°C in H_2O and 32°C in PBS using turbidimetry (Fig. 2a). This difference is due to the cations from the buffer interfering with the solvation shell of the PDEGA side chain. Analogous critical temperatures were obtained from DLS as the temperatures where sudden increase in size occurs due to aggregation and where PDI>0.5 (Fig. 2b). Other block copolymers with longer PDMS blocks exhibited lower LCST due to increased hydrophobicity of copolymer.

Gold nanorods

We have synthesized AuNRs in two steps using the seed-mediated growth method. First, CTAB-coated gold seeds were prepared by the reduction of $HAuCl_4$. Aged seeds were then added to the growth solution to allow for the formation of AuNRs. Plasmonic resonance wavelengths of synthesized AuNRs were obtained using the UV-Vis-NIR spectroscopy. By varying the gold seeds aging time and nanorods growth time

we obtained AuNRs with slightly different LSPR (Fig. 3a). Size and aspect ratio of the prepared AuNRs were determined by SEM (Fig. 3b) and TEM.

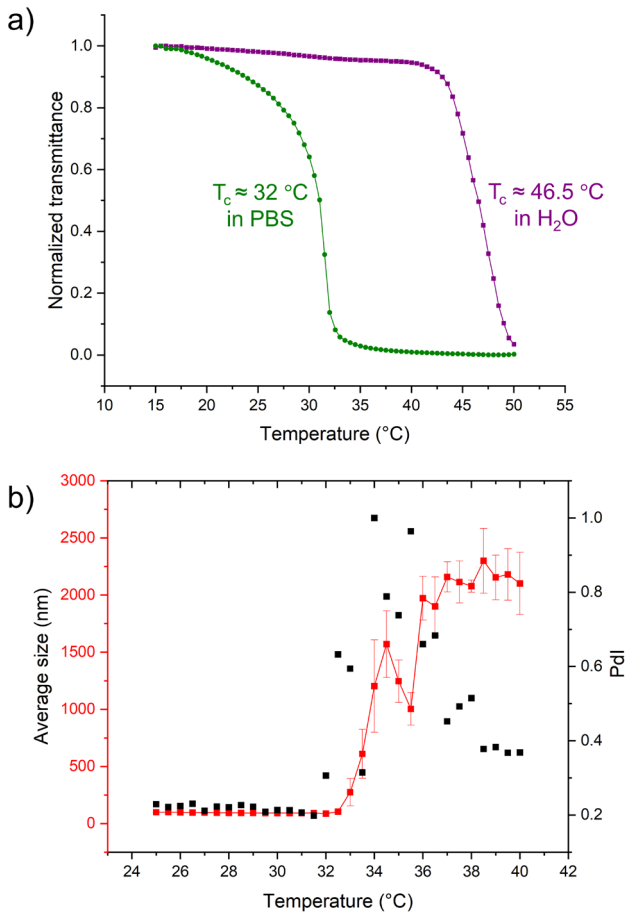

Fig. 2: Thermoresponsivity of PDMS-b-PDEGA (f= 68%) in aqueous solutions. a) Cloud point determination using turbidimetry in PBS (green) and H_2O (purple). Critical temperature was extracted at 50% transmittance drop in the transmittance versus temperature graph. b) Determination of LCST phase transition from DLS measurements performed at different temperatures in PBS.

The AuNRs synthesized this way are stabilized with CTAB and dispersed in water (hydrophilic AuNRs). They can be made hydrophobic by dispersing them in organic solvent with phase transfer through liquid-liquid interface, during which the stabilizing ligands are exchanged. We used alkanethiols to stabilize AuNRs in organic solvents.

Outlook

We are currently working on obtaining thermoresponsive polymersomes and combining them with AuNRs. In the next stage of the project, AuNRs will be covalently attached to the surface of thermoresponsive polymersomes. Such assemblies will be used for NIR-light triggered release studies. We will also prepare gold nanorods using different methodology in order to get LSPR wavelengths above 1000 nm. Finally, we will encapsulate polymersomes decorated with different AuNRs inside GUVs and test their selective release.

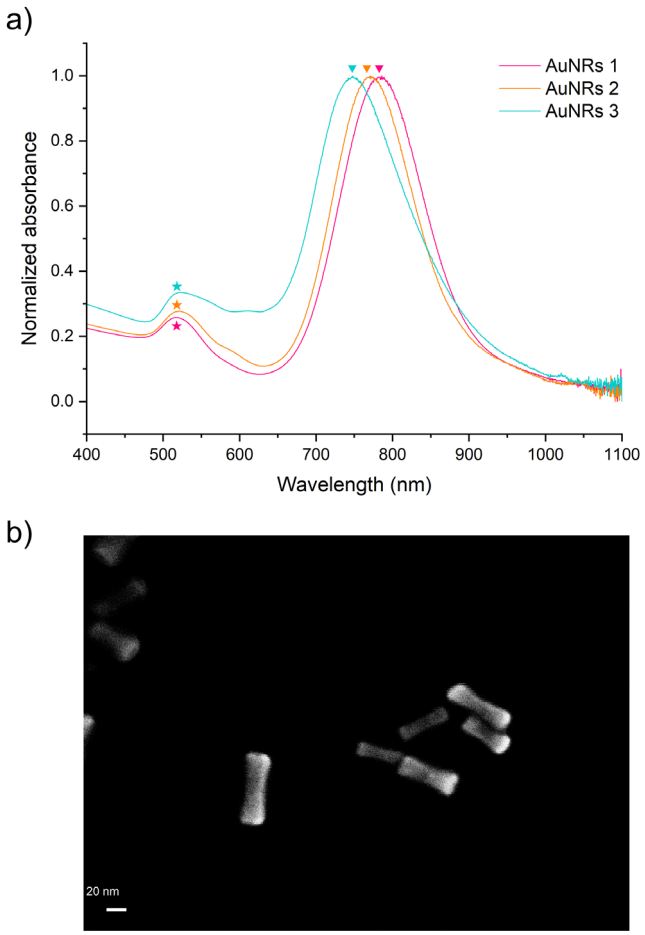

Fig. 3: Characterization of CTAB-stabilized AuNRs. a) UV-vis spectra of AuNRs. LSPR depends on the aspect ratio. b) SEM micrograph of AuNRs synthesized from 2h-aged seeds (aspect ratio 3.6).

References

[1] Q. Hu, W. Sun, C. Wang, Z. Gu, Recent advances of cocktail chemotherapy by combination drug delivery systems, Adv. Drug Deliv. Rev. 98, 19 (2016)

[2] R. Wehr, E. C. dos Santos, M. S. Muthwill, V. Chimisso, J. Gaitzsch, W. Meier, Fully Amorphous Atactic and Isotactic Block Copolymers and Their Self-Assembly into Nano- and Microscopic Vesicles. Polym. Chem. 12 (37), 5377 (2021)

[3] J. Zheng, X. Cheng, H. Zhang, X. Bai, R. Ai et al, Gold Nanorods: The Most Versatile Plasmonic Nanoparticles, Chem. Rev. 121 (21), 13342 (2021)

HfO_2 scintillating nanoparticles doped with Ln^{3+} for X-ray mediated optogenetics

Project P2207: Targeted scintillator nanoparticles for X-ray mediated optogenetics in behaving mice
Project Leader: A. A. Wanner, J. D. Roo and C. Padeste
Collaborator: E. Liari (SNI PhD Student)

Scintillating nanoparticles (SNPs) for X-ray mediated optogenetics

Optogenetics is considered a promising technique to study the function and connectivity of neuronal circuits in the brain tissue by manipulating the activity of neurons with high temporal precision [1,2,3]. In principle, this is achieved by either the excitation or inhibition of light switchable transmembrane proteins, such as channelrhodopsin, halorhodopsin or archaerhodopsin, with the assistance of visible light [4,5]. However, conventional optogenetics requires a light source that is invasively implanted into the brain, since the penetration depth of the visible light in the brain tissue is limited to a few hundred micrometers. However, this surgical intervention bears the risk of brain tissue damage and neuroinflammation [5]. The aim of this project is to develop and synthesize SNPs, as an alternative non-invasive means of optogenetics utilizing X-ray radiation which can achieve deeper penetration tissue depth compared to visible light [3,5,6]. SNPs will be modified appropriately to be colloidally stable in physiological conditions and to provide targeted adherence to the appropriate transmembrane opsin. Subsequently, they will be injected into the brain tissue, adhere to the targeted opsin, and convert X-ray radiation into visible light for the activation or inhibition of the selected protein (Figure 1). Their function will be tested both in vitro and in vivo in behaving mice. Overall, it is expected that SNPs will offer an alternative non-invasive tool for optogenetics and potentially, for the treatment of neurological diseases [3].

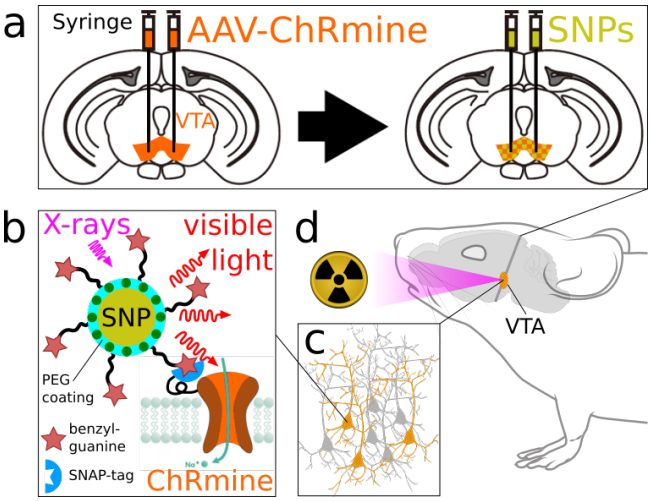

Fig. 1: Schematic overview: a) Injection of modified adeno-associated viruses (AAV) into the ventral tegmental area (VTA) and release of artificial DNA into infected cells that codes for light-switchable proteins such as the red-shifted channelrhodopsin ChRmine. Four weeks after the AAV injection the light-switchable proteins will be integrated into the cell membranes of the neurons of interest and SNPs are injected into the same area. b) The appropriately functionalized SNPs will associate with the light-switchable proteins. Upon irradiation with X-rays, the SNPs emit visible light which activates the light-switchable proteins in the neurons (see c)) to excite or inhibit them. d) Optogenetical manipulation of neuronal activity in deep brain regions in vivo in behaving mice by exposing them to focused X-rays.

HfO_2 is an appropriate material to act as a host matrix of SNPs, as the incorporation of atoms, such as Hf with high atomic number (Z= 72), is crucial for an efficient X-ray absorption [7]. Furthermore, it can host trivalent Ln ions, which act as efficient sensitizers for utilization in the final application. HfO_2:Ln NPs of around 3 nm diameter are being synthesized using a typical solvothermal reaction. A solution of $Hf(OtBu)_4$, BnOH and $Ln(OAc)_3$ is heated at high temperatures for 96 hours in a furnace to yield crystalline nanoparticles (NPs) [7]. After synthesis, the particles are further functionalized with the appropriate carboxylate ligand that makes them colloidally stable in non-polar solvents. 1H NMR spectroscopy indicates the binding of the ligand on the surface of the NPs by the broadening of the NMR signal of the bound compared to the free ligand. This broadening results from a) the restriction of rotational mobility of the bound ligand that speeds up T_2 relaxation (homogeneous line broadening) and b) the differences in solvation and ligand-ligand interaction (heterogeneous line broadening) [8]. Dynamic light scattering (DLS) measurements confirm the hydrodynamic size of the particles (around 7 nm), transmission electron microscopy (TEM) shows the size and morphology of the particles and thermogravimetric analysis (TGA) the amount of ligand bound on their surface (Fig. 2).

The synthetized and functionalized NPs are colloidally stable in non-polar solvents such as toluene and cyclohexane. Since we aim to utilize them in a biomedical related application, they need to be colloidally stable in aqueous environments at physiological conditions (pH= 7.4), instead. The colloidal stability of the particles plays an important role in cellular uptake, cytotoxicity, targeting of a molecule of interest, particle aggregation, etc. [9]. Therefore, the carboxylate that is initially bound to the surface of the NPs will be exchanged with an appropriate ligand that will provide colloidal stability of the particles in a physiological environment. Furthermore, the ligand chain should be end-functionalized with an appropriate moiety that can be chemically attached to specific molecules (e.g. SNAP tags) that will provide linkage of the NPs to the targeted protein in the brain. Non-doped HfO_2 particles are chosen to study the surface chemistry of the NPs, since they are compatible with 1H NMR spectroscopy and their surface chemistry is similar to that of doped particles. 1H NMR signals of HfO_2:Ln particles show an excessive broadening due to the paramagnetic effects of trivalent

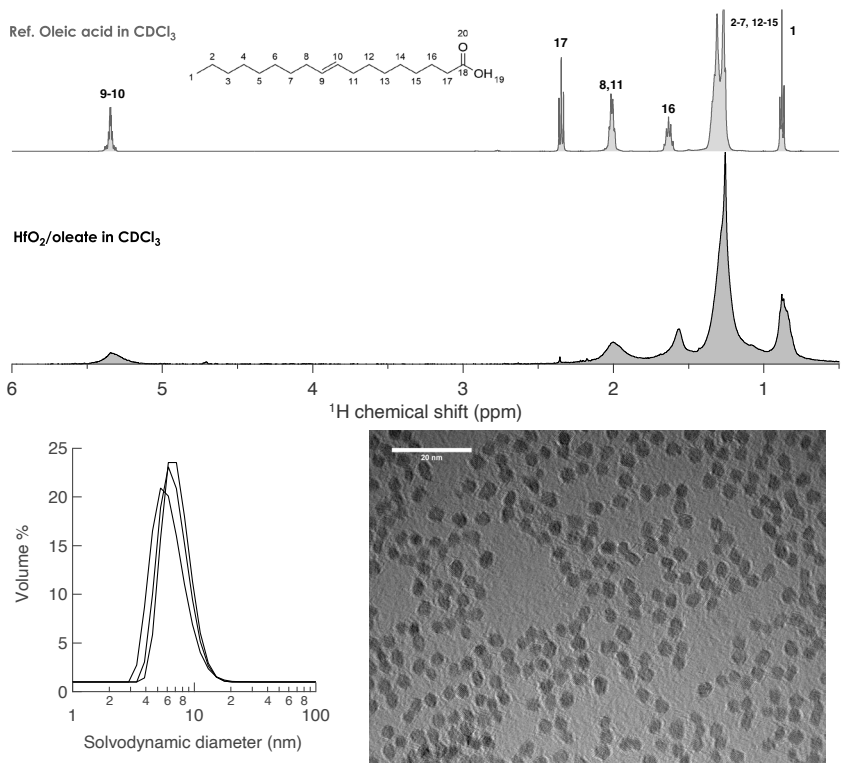

Fig. 2: Characterization methods of SNPs. a) 1H NMR of HfO_2 particles coated with oleate (HfO_2@OA). The broadening of the peak indicates the binding of the ligand on the surface of the NPs, b) DLS of HfO_2:Ln@OA showing a hydrodynamic size of around 7 nm and c) TEM of crystalline HfO_2:Ln@OA NPs.

Ln ions, making it difficult to study their surface chemistry. The synthesis of the non-doped particles is the same as for the doped particles with the main difference being that only $Hf(OtBu)_4$ and BnOH are used as precursors. So far, it has been proven that catechol provides the best colloidal stability of the NPs in physiological conditions [9]. However, in the case of optically active NPs, the benzene ring can act as a possible quencher of the luminescence and thus, cannot be used as a surface ligand. Hence, our focus is on synthesizing and testing bidentate bisphosphonic acids, instead, as they are thought to provide better colloidal stability compared to their monodante phosphonic acid analogues and they do not quench the luminescence of the NPs [10].

Important aspects of the SNPs are their excitation and emission profiles. The host matrix of the particles should absorb electrons in the X-ray region, transfer the absorbed energy to the Ln^{3+} ions, which emit in high yields at a wavelength that matches the excitation region of the protein of interest. The protein of interest chosen is a red-shifted channelrhodopsin, ChRmine, with peak response at 520 nm. Hence, we started performing photoluminescence measurements of the NPs to follow the excitation, emission and emission decay profiles of the SNPs capped with different bisphosphonate ligands.

In the future, we aim to measure the radioluminescence of the synthesized and functionalized particles in H_2O to get more insight in their optical properties. Afterwards, the ligand chain on the surface of the NPs will be further functionalized with specific binders that can specifically target the opsin of interest. Lastly, the NPs will be tested first in vitro in acute coronal slices of mouse brain, where the generated photocurrent will be monitored by electrophysiological recordings and then in vivo in behaving mice.

References

[1] J. Ditterich, M. E. Mazurek, M. N. Shadlen, Microstimulation of visual cortex affects the speed of perceptual decisions, Nat. Neuroscience 6, 891–898 (2003)

[2] C. D. Salzman, K. H Britten, W. T. Newsome, Cortical microstimulations influences perceptual judgements of motion direction, Nature 346, 174–177 (1990)

[3] B. Chen, M. Cui, Y. Wang, P. Shi, H. Wang, F. Wang, Recent advances in cellular optogenetics for photomedicine, Adv. Drug Deliv. Rev. 188, 114457 (2022)

[4] E.S. Boyden, F. Zhang, E. Bamberg, G. Nagel, K. Deisseroth, Millisecond-timescale, genetically targeted optical control of neural activity, Nat. Neuroscience 8, 1263–1268 (2005)

[5] R. Berry, M. Getzin, L. Gjesteby, G. Wang, X-optogenetics and U-optogenetics: Feasibility and Possibilities, Photonics 2, 23–39 (2015)

[6] A. Kamkaew, F. Chen, Y. Zhan, R. L. Majewski, W. Cai, Scintillating Nanoparticles as Energy Mediators for Enhanced Photodynamic Therapy, ACS Nano 10, 3918–3935 (2016)

[7] A. Lauria, I. Villa, M. Fasoli, M. Niederberger, A. Vedda, Multifunctional Role of Rare Earth Doping in Optical Materials: Nonaqueous Sol-Gel Synthesis of Stabilized Cubic HfO2 Luminescent Nanoparticles, ACS Nano 7, 7041-7052 (2013)

[8] J. D. Roo, The surface chemistry of colloidal nanocrystals capped by organic ligands, Chem. Mater. 35, 3781–3792 (2023)

[9] L. Deblock, E. Goosens, R. Pokratath, K. D. Buysser, J. D. Roo, Mapping out the Aqueous Surface Chemistry of Metal Oxide Nanocrystals: Carboxylate, Phosphonate, and Catecholate Ligands, JACS Au 2, 711–722 (2022)

[10] S. Kachbi-Khelfallah, M. Monteil, M. Cortes-Clerget, E. Migianu-Griffoni, J. L. Pirat et al., Towards potential nanoparticle contrast agents: Synthesis of new functionalized PEG bisphosphonates, Beilstein J. Org. Chem. 12, 1366–1371 (2016)

A laboratory transmission X-ray microscope based on an X-ray achromatic lens

Project A16.01: ACHROMATIX (Paul Scherrer Institut, University of Basel, XRnanotech GmbH, Untersiggenthal)
Project Leader: J. Vila Comamala
Collaborators: D. Qu, S. Zhao, G. Schulz, G. Rodgers, U. T. Sanli, P. Qi, A. Kubec, F. Döring, B. Müller, C. David

Introduction
Transmission X-ray microscopy (TXM) is a non-destructive tool for the analysis of the inner structure of intact samples at the micro- and nanoscale. However, its implementation at broadband X-ray tube sources suffers from the image blurring and long exposure time due to the chromatic aberration of the lenses and the inherent low available flux of laboratory sources.

Recent development of X-ray achromatic lens and capillary optics at Paul Scherrer Institute allows the efficient collection of a larger bandwidth of a polychromatic laboratory X-ray source. The X-ray achromatic lens consists of a focusing diffractive Fresnel zone plate and a defocusing compound refractive lens, focusing X-rays from a broader energy range at the same focal spot, as reported in the publications [1]. In order to avoid the lens alignment complexity in the X-ray imaging systems, these two lens components can be fabricated as monolithic lens. Depending on the diameter and outmost zone width of the Fresnel zone plate, the focal length and numerical aperture (NA) of this monolithic achromat lens are 95 mm and 1.0 mrad for the 7.1 keV X-rays.

The single-bounce monocapillary has an elliptical shape which can focus divergence X-rays onto the sample. Depending on the incident angle of X-rays in the capillary, the high energy X-rays can be filtered. Due to the high reflectivity of gold, the reflective surface of the capillary optics is gold coated. At a surface roughness of 1 nm, a monocapillary reflects more than 80% of 5-11 keV X-rays. The Au capillary is fabricated by electroplating and evaporation processes. However, the current fabrication processes lead to a surface roughness of 5 nm resulting in a reflectivity less than 50%. Low reflectivity causes low photon flux for imaging and also affects the quality of imaging. In further investigations, the surface roughness of capillary will be improved.

Designing the achromatic X-ray microscope
Figure 1 shows the sketch of our achromatic transmission X-ray microscope at PSI using a microfocus X-ray tubes, the monocapillary optics, a central stop, a pinhole, a monolithic achromatic lens and pixel detector. Designing a TXM involves several critical components and considerations:

X-ray source: a microfocus X-ray tube is selected for our microscope, which has a beam size of 10 µm. We also measured the spectra directly from the X-ray tube and from the reflected beam of the capillary, as shown in figure 2. The tungsten X-ray tube has three emission lines at 8.4 keV, 9.7 keV and 11.0 keV at a tube voltage of 50 kV and a tube current of 200 µA. Compared to the direct beam, the monocapillary suppresses the hard X-ray photons. Notably, to reduce the absorption of X-rays in the air, helium flight tubes were also utilized along the optical axis.

Optical system: our X-ray microscope has a magnification of 12x and a field of view of 50x50 µm². The distances from sample to achromat and from achromat to detector are approximately 115 mm and 1380 mm, respectively. The capillary focal length is 400 mm. Thus, the total length of the microscope is 1.9 m. In addition, it is important that the illumination angle of capillary must match the NA of the monolithic achromatic lens. Accordingly, the monocapillary has a semi-major axis of 200 mm, a semi-minor axis of 0.42 mm and a length of 12 mm.

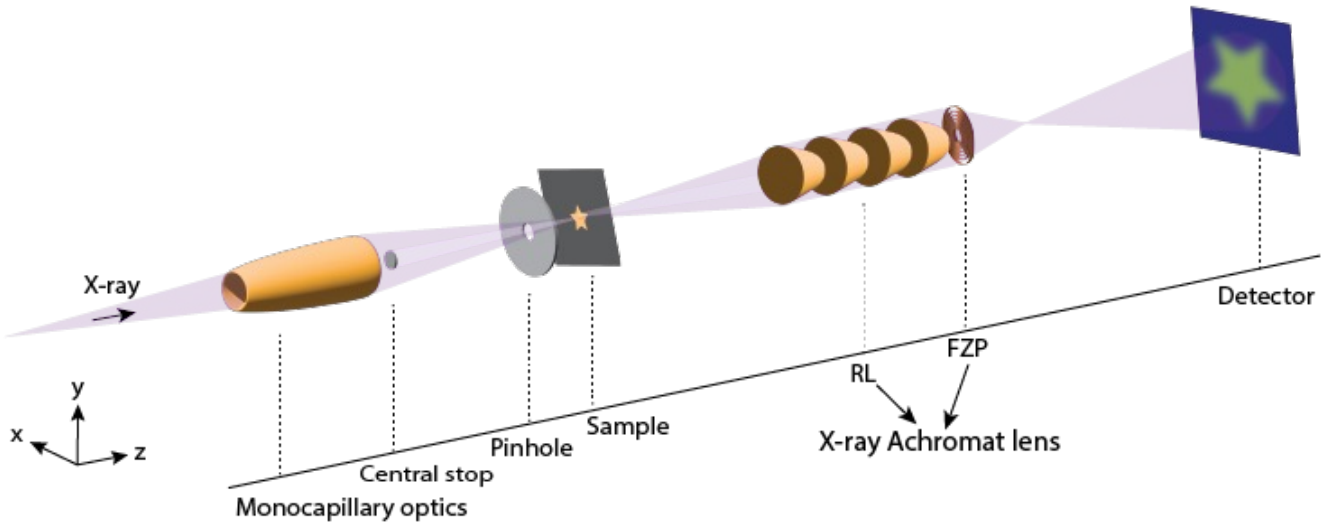

Fig. 1: The schematic design of a laboratory transmission X-ray microscope with an achromatic lens.

Detector: commonly, the X-ray detector is indirect and that involves a scintillator, an objective, a mirror and a CCD camera. A 25 µm-LuAG crystal was selected as scintillator because LuAG has an absorption edge at 9.25 keV. Although the spatial resolution can be further increase with optical magnification, a high photon flux is required for indirect X-ray detector. On the other hand, the direct X-ray detector can collect images at low photon flux. However, it has no optical magnification, for the high-resolution imaging, smaller pixel size or computing calculation are demanded. Both detectors were performed in our microscope as will be discussed below.

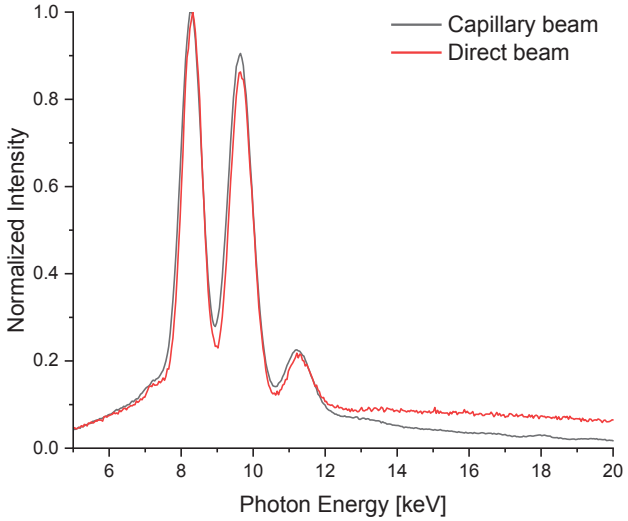

Fig. 2: The measured spectra of direct beam from X-ray tube and reflected beam from monocapillary at 50 kV and 200 µA.

Imaging by the achromatic X-ray microscope

In the case of indirect X-ray detector, the quality of the X-ray imaging was not only limited by the low reflectivity of the capillary, but also the efficiency of indirect X-ray detector, as shown in figure 3. The test sample is a gold mesh having a period of 25.4 µm. Figure 3a shows the raw image of the gold mesh with an exposure time of 30 min. With the flat image correction, an image of 4 hexagons was observed. However, noise is still evident in the image, limiting the spatial resolution of the image. Notably, the white ring around the image was caused by the reflected beam from the capillary.

MÖNCH is a hybrid silicon detector based on charge integration, featuring a pixel size of 25 x 25 µm², which has been developed at PSI [2]. It consists of an array of 400 x 400 identical pixels for a total active area of 1 x 1 cm². It is worthwhile mentioning that MÖNCH has very low electric noise and requires a low photon flux. The 200-seconds raw image acquired with MÖNCH is shown in figure 4a. The charge sharing in the MÖNCH allows the photo positioning and improving the spatial resolution using the interpolation algorithm. The interpolated image is shown in figure 4b with a binning of 5. The hexagons are separated by a line width of 8 pixels, which corresponds to 3 micrometers. Currently, our achromatic microscope can achieve a spatial resolution up to 1 µm.

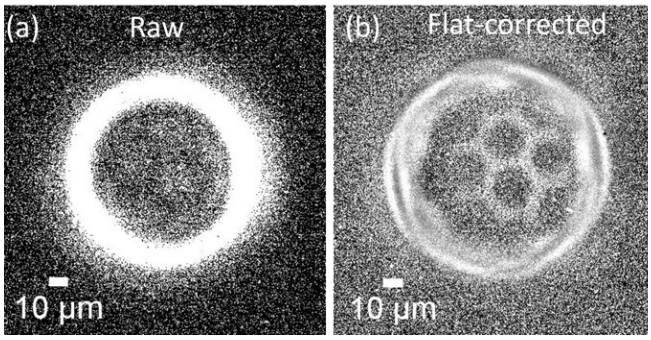

Fig. 3: 30-minutes exposure a) raw image and b) flat-corrected image of gold mesh sample with an indirect X-ray detector.

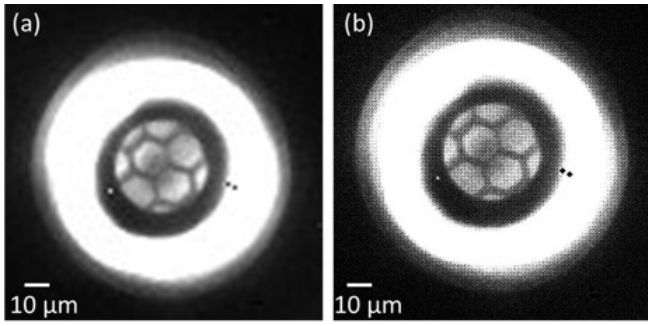

Fig. 4: 200-seconds exposure a) raw image and b) interpolated image of a gold mesh sample with MÖNCH detector.

Further developments of achromatic X-ray microscope

To further improve the spatial resolution of our X-ray microscope to 200 nm, the magnification can be increased by extending the distance between achromatic lens to the detector. Moreover, it remains challenging to improve the reflectivity of the monocapillary. Further investigation of capillary fabrication and its surface roughness remains to be explored. A new achromatic lens for the photon energies between 8.0 and 10.0 keV is under developing to match the X-ray tube emissions.

References

[1] U. Sanli, G. Rodgers, M, Zdora, P. Qi, J. Garrevoet et al., Apochromatic X-ray focusing, Light: Science & Application 12, 10107 (2023)

[2] A. Bergamaschi, M. Andrä, R. Barten, C. Borca, M. Brückner, et al. The MÖNCH detector for soft X-ray, high-resolution, and energy resolved applications, Synchrotron Radiation News 31(6), 11-15 (2018)

Theragnostic nanobody-polymer-conjugates targeting B7-H3 – An update

Project A17.1: B7H3 Nanobody PC (CIS Pharma AG, Bubendorf, FHNW Muttenz, Paul Scherrer Institut, Universitäts-Kinderspital Zürich)
Project Leader: Ch. Geraths
Collaborators: M. Behe, T. Villiger, O. Germershaus, J. Nazarian

Background and Concept
Conventional tumor chemotherapy or radiotherapy are efficient at eradication of tumor cells but often lack target cell specificity, resulting in significant side effects. Theragnostics are modalities which may be used for both diagnosis and treatment, facilitating improved disease management, and reducing risks and costs of cancer therapy.

B7-H3 is a transmembrane protein, acting as a suppressor of T-cell activation and proliferation as well as a potential checkpoint inhibitor ligand, which is overexpressed in different tumors, e.g., non-small cell lung cancer and prostate cancer. [1]

Nanobodies are derived from heavy-chain antibodies from Camelidae and are characterized by low molecular weight, high stability, low immunogenicity, excellent affinity and specificity as well as high solubility. [2] Therefore, nanobodies represent ideal targeting moieties in the development of immunoconjugates.

The aim of this project is the development of a nanobody-polymer conjugate targeting B7-H3 and allowing attachment of diagnostic tracers such as radionuclides and/or therapeutic agents such as cytotoxic drugs (Figure 1). By employing suitable polymeric carriers, the blood half-life of the conjugate may be tailored according to diagnostic or therapeutic requirements, off-target effects may be reduced and ultimately penetration of the blood-brain barrier may be achieved.

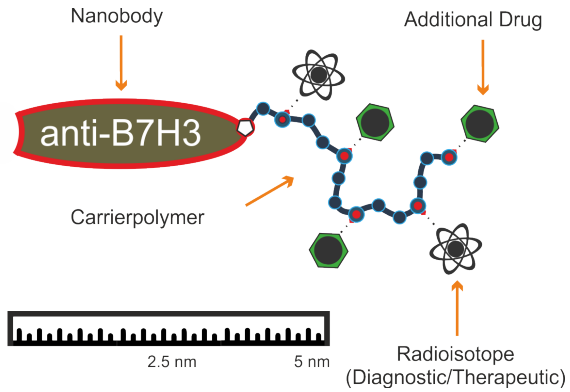

Fig. 1: Concept of B7-H3-nanobody-polymer conjugate.

Nanobody Characterization & Upscaling
The two nanobody candidates against B7-H3 VHH A & VHH B (see report 1st year) comprising an N-terminal His-SUMO1 tag and a C-terminal peptide linker with a surface exposed cysteine were expressed in E. coli, purified by affinity chromatography and cleaved by SENP1 enzyme to remove the His-SUMO tag. Subsequently, both candidates were tested for their affinity to the antigen B7-H3 using grating coupled interferometry (GCI); nanobodies still comprising the His-SUMO tag served as control.

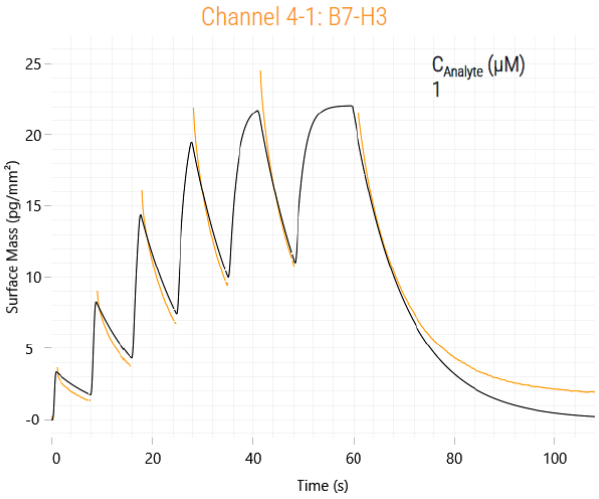

Fig. 2: Double referenced sensorgram of the interaction between B7-H3 (immobilized antigen) and VHH A (lead).

The His-SUMOtag had a negative influence on the binding characteristic as expected (KD in the range 360 nM). Candidate VHH A had the highest binding affinity with a KD of 180 nM (in a 1:1 kinetic model) and was defined as lead candidate for upscale and conjugation. Production upscaling was performed stepwise from shaking flask, to bioreactor with 2 L and 20 L culture volume. During this process culture conditions were optimized and the ideal downstream methods evaluated.

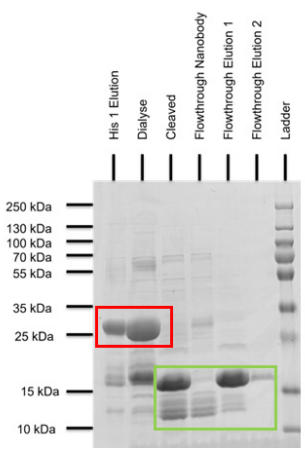

Fig. 3: SDS-PAGE of a VHH A fraction during downstream process.

Ladder: Pageruler Plus Protein. Gel: 10-20% Tris-Glycine. The red area marks the uncleaved construct consisting of nanobody-His-SUMO. The green area marks the individual fragments nanobody (13.7 kDa) and His-SUMO (12.1 kDa).
The purified nanobody was subsequently used for functionalization tests.

Labeling of Nanobody VVH A with Radionuclides

The purified nanobody (VHH A) comprises a surface exposed cysteine which can be used for attachment of linker-drugs or the polymer carrier. For this purpose, a mild reduction protocol was established to ensure that only this cysteine is reduced while the essential disulfide bridge in the nanobody remains intact. The step was monitored with an Ellman's reagent-based assay. Since in average only < 1 cysteine was detected, we assume that the nanobody's tertiary structure is preserved. Subsequently, we modified this reactive group with a maleimide-DOTA chelator to result in a nanobody-conjugate which can be labeled with radionuclides (figure 5). For the nanobody-polymer conjugates it is planned to switch to a maleimide-azide derivative that is coupled with the click reactive polymer carrier afterwards.

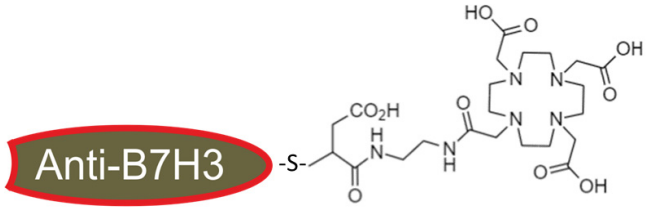

Fig. 4: Structure of chelator modifed nanobody.

In the next step the nanobody-conjugate was labeled with a therapeutic radionuclide Lu-177. Even though a labeling was achieved the yield was quite low. This was a result of small amounts of maleimide-DOTA still present in the solution. Therefore, the purification protocols were optimized with an additional column purification after the labeling process (Fig. 6). This led to a purified product suitable for first cell culture experiments.

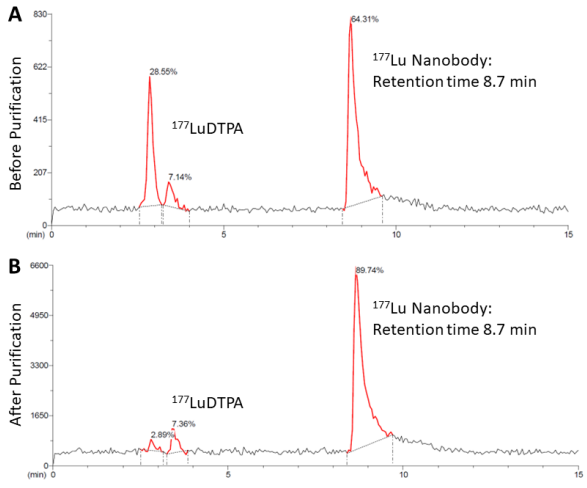

Fig. 5: Chromatogram of Lu-177 labeled nanobody

A: Radio chromatogram before purification by PD10 column (Nanobody 64.3% radiopurity). B: Radio chromatogram aft purification by PD10 column (Nanobody 89.7% radiopurity).

Polymer Carrier Syntheses and Characterization

Model polymer carriers comprising biocompatible monomers tested in the 1st year were synthesized by a controlled radical polymerization technique (RAFT polymerization). The polymer carrier chosen as a model is capable to deliver 8 active molecules in any combination (e.g., 3 tracers/ 5 radionuclides or drugs). After polymerization, the carriers were functionalized with amine-reactive DOTA chelators and fluorophores. In the last step the carries head group was modified with a click reactive DBCO-group for later attachment to the azide-modified nanobody. The schematic process is presented in figure 6. Furthermore, methods for the characterization of drug load were established using a picryl sulfonic acid-based assay for detection of amino groups as well as a competitive complexometric assay for the number of attached DOTA chelators. Originally it was intended to purify these modified carriers by dialysis and first results looked promising. However, due to a change in the composition of the dialysis membrane, by-products could not be removed (sticking to membrane). Therefore, a new purification method based on ultra-filtration was established. In the end this process led to a model polymer which can be used for cell internalization assays (detection by fluorescence) as well as radioactive labeling with diagnostic or therapeutic radionuclides (later mouse experiments).

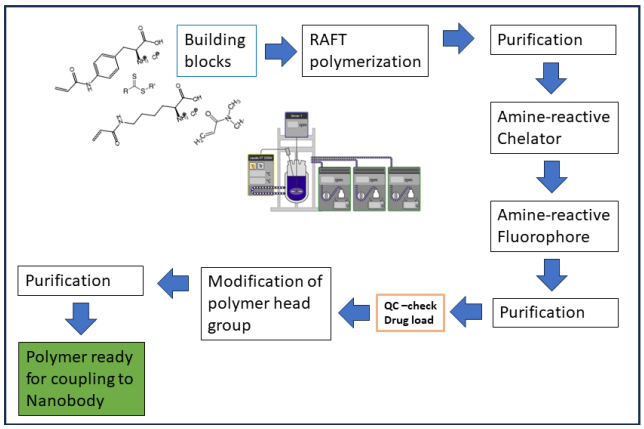

Fig. 6: Process scheme carrier synthesis

Summary

During the 2nd year of the project a lead was identified out of several nanobody candidates. The nanobody production was upscaled as well as downstream processes established. The nanobody lead was then successfully modified with a chelating agent and first radioactive labeling experiments were performed. Several model polymer carriers were developed and are ready for coupling to the nanobody. In the next steps the nanobody will be tested on tumour cells (binding to receptor) and in a mouse xenograft model (biodistribution). However, affinity of the lead nanobody for the target B7-H3 was specific (KD of 180 nM) but will have to be optimized by affinity maturation in another project.

References

[1] S. Yang, W. Wei, Q. Zhao, B7-H3, a checkpoint molecule, as a target for cancer immunotherapy, Int. J. Biol. Sci. 16, 1767 (2020)

[2] S. Sun, Z. Ding, X. Yang, et al., Nanobody: A Small Antibody with Big Implications for Tumor Therapeutic Strategy, Int. J. Nanomedicine 16, 2337 (2021)

Cosmic-ray reliability of nanoscale oxide layers in power semiconductors

Project A17.2: CRONOS (FHNW Windisch, ANAXAM, SwissSEM GmbH, Lenzburg)
Project Leader: R. Minamisawa
Collaborators: S. Rehm, L. Spejo, L. Knoll, R. Stark, V. Novak, B. Ammann, P. Würsch, N. Schulz

Motivation

Power semiconductors are the basis for electrification, being applied in a plethora of power electronic systems ranging from electric vehicles, to photovoltaics, to electricity transmission and so forth. In order to reduce losses in such devices, material properties and devices design needs to be optimized up to its limits. One such limit is cosmic ray failure, which makes the devices prone to breakdown because of the combination of high internal fields and cosmic ray induced ionization. This is usually tested with the gate (control input) shortened to the emitter (negative power connection). This however results in no field across the gate oxide. In real applications, the gate is usually charged to ±15 V with respect to the emitter. Since the gate oxide is very thin (<100 nm) the result is a very high field strength of more than 150 kV/mm. Further, it is not yet understood the impact of combined cosmic ray irradiation with stress on the gate oxide. The goal of this report is to test the effects of cosmic rays on the reliability of the IGBT gate oxide with a gate voltage applied.

Sample preparation

For the experimental investigations, 1200 V / 250 A trench-gate IGBTs from SwissSEM (product number SIS0250C120i20) have been selected as test vehicles. The sample assembly was done on a PCB specially designed by FHNW for this test. The assembly process consisted of the following steps:

1. Soldering of the IGBT chips to the PCB
2. Acoustic scan to check for solder voids
3. Wire bonding
4. Frame gluing and potting with silicone gel

The samples were then shipped to FHNW for a pre-stress characterization.

Cosmic ray test system

During cosmic ray tests, the samples were bombarded with high-energy protons (200 MeV) while simultaneously blocking high voltage (~60% of max. voltage). The voltage is increased stepwise, which increases the sensitivity of the samples to interactions with the protons or neutrons. If a particle interaction occurs in a critical area, the sample will fail. Each sample has its own electronic fuse which detects the increase in current and shuts down the failed sample.

Proton and neutron irradiation tests

The tests at the proton irradiation facility (PIF) were performed with 200 MeV protons (Fig. 1, left). The neutron irradiation was performed at the ChipIr beamline in ISIS, UK (Fig. 1, right). Figure 2 left shows a comparison between FIT of IGBTs irradiated with neutron or proton, interestingly showing that there is no significant difference.

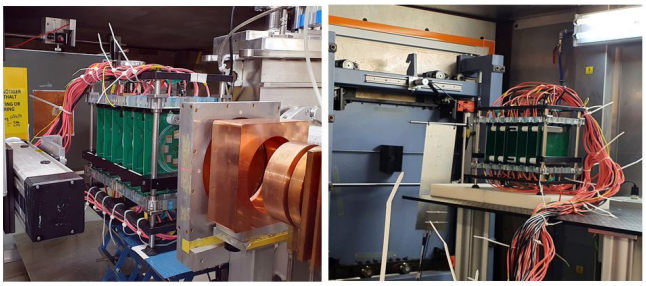

Fig. 1: Prepared IGBTs in the PIF beamline at PSI (right) IGBTs samples at the ChipIr beamline in ISIS (left).

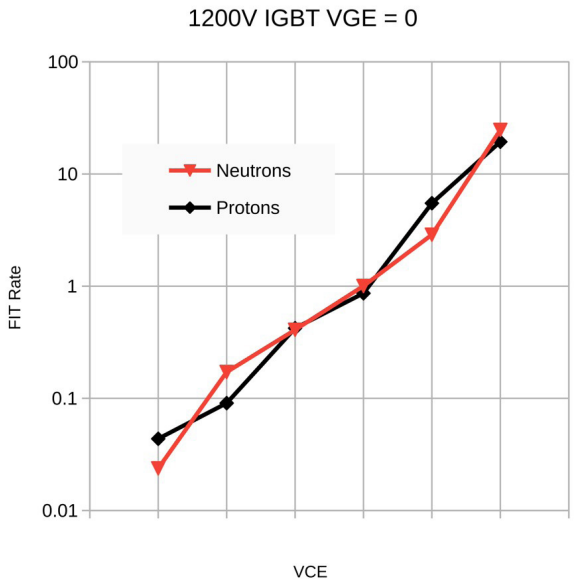

Fig. 2: Measured FIT rate of 1200 V IGBTs with gate voltage of 0 V irradiated with protons or neutrons.

Oxide reliability tests

The main objective of this project is to understand the impact of neutron and proton irradiation on the oxide reliability of IGBTs. As such, after irradiation, surviving samples have undergone oxide reliability tests.

The effects of proton and neutron irradiation on the electrical characteristics of IGBT devices were investigated based on the schematic shown in figure 8. Initially, the subthreshold curve characterization from all devices was performed with a Keysight B1505A Power Device Analyzer at 22°C and a fixed drain-source voltage of 0.875 V. Then, the devices under test (DUTs) were divided into 5 groups. One group is used as a reference, not receiving any irradiation. The other 2 groups were irradiated with protons at two distinct conditions: 0

Vge; 880 Vce (batches B1-B6) and -15 Vge; 880 Vce (batches B7-B12). The last two groups received neutron irradiation at two distinct conditions: 0 Vge; 880 Vce (batches B13-B18) and -15 Vge; 880 Vce (batches B19-B24). These devices are the survivors of the cosmic ray degradation experiment, where around half of the initial devices presented failures and were not considered during the static characterizations. The second characterization is performed after the particle irradiations to check the effect on the subthreshold characteristics.

Further, a high-temperature gate bias (HTGB) experiment is performed on the DUTs. Such an experiment is a standard industrial test to check the gate oxide robustness after stressed conditions. Initially, a + 40 V gate voltage (collector shorted to the emitter) is applied in the DUTs at 150°C for 84 h duration. At the end of the test, the devices are placed outside the chamber at 22°C to perform a new set of characterizations (Third characterization). Finally, one last HTGB test is performed on the devices at – 40 V gate voltage, followed by a fourth subthreshold characterization. The main objective is to investigate the possible effects of particle irradiation on the devices' gate oxide [1], as well as the effect of high gate voltage and high temperature on such devices [1]. As shown in figure 8, the reference samples that did not suffer irradiation are also tested under HTGB to compare with the irradiated samples. By performing such characterizations at each stage, we can compare the effect of experiment on the device's electrical characteristics. The subthreshold curve is one standard characterization that provides information about the gate oxide reliability, indicating the presence of gate oxide charges [1]. After cosmic ray exposure and gate oxide reliability testing, these characterizations were performed in the surviving samples. Thus, the effects of each procedure can be investigated individually and compared to the initial characterization of the samples. Figure 3 shows the 48-channel oxide reliability test set-up used to stress the IGBT.

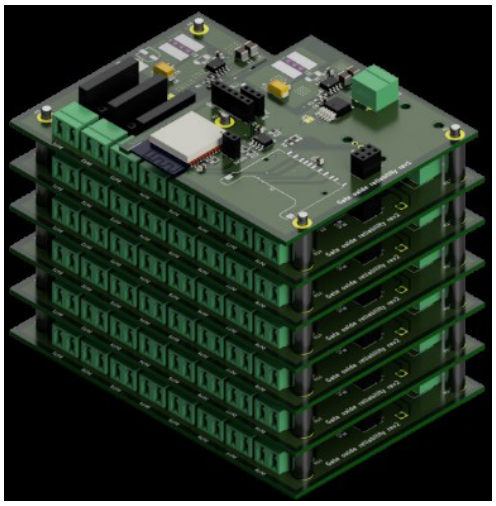

Fig. 3: 48-channel HTGB tester.

A typical parameter investigated from the subthreshold curves is the threshold voltage variation (ΔVt). Such parameter may indicate the presence of gate oxide charges, being a good representative if the devices suffered any gate degradation. All devices had their threshold voltage extracted using the constant current method at a fixed current value of 10 mA. The results are indicated in figure 4. Independently of the device group and experiment performed, no significant changes were observed in the threshold voltage values, confirming that the gate oxide structure preserved its characteristics. Such a similar effect is also observed in the reference samples, showing that the irradiation on the survived devices did not significantly alter the subthreshold electrical characteristics.

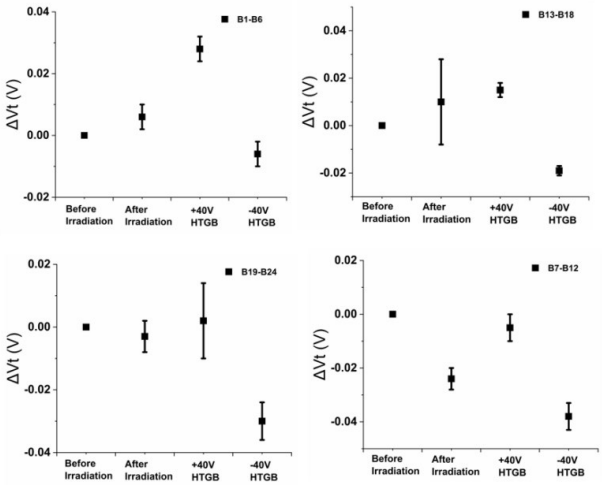

Fig. 4: Threshold voltage variation curve from an IGBT before irradiation, after irradiation, after +40 V HTGB and after -40 V HTGB, where (top-left) and (top-right) are samples irradiated with protons with Vge= 0 V and -15 V, respectively, and (bottom-left) and (bottom-right) are samples irradiated with neutrons with Vge= 0 V and -15 V, respectively.

Conclusions

The devices that survived the cosmic ray irradiation test presented no significant changes compared to reference devices (no irradiation). Particularly, irradiation with protons and neutrons exhibited similar FITs. Furthermore, all devices presented excellent preservation of the subthreshold characteristics after HTGB tests, indicating the good quality of the gate oxide structure and interface. Results have been submitted to the ISPSD 2024 conference.

References

[1] F. Principato, G. Allegra, C. Cappello, O. Crepel, N. Nicosia, et al, Investigation of the Impact of Neutron Irradiation on SiC Power MOSFETs Lifetime by Reliability Tests, Sensors 21, 5627 (2021)

[2] C. Martinella, R. G. Alia, R. Stark, A. Coronetti, C. Cazzaniga, et al., Impact of Terrestrial Neutrons on the Reliability of SiC VD-MOSFET Technologies, IEEE Trans on Nuclear Science 68(5), 634-641 (2021)

Functional cryo-EM sample preparation

Project A17.3: FuncEM (University of Basel, Biozentrum, Paul Scherrer Institut, cryoWrite AG, Basel)
Project Leader: T. Braun
Collaborators: I. Takashi, N. Zimmermann, A. Fränkl, L. Rima, N. Candia, A. Lorca, A. Engel, P. Frederix

Introduction
Cryogenic electron microscopy (cryo-EM) radically changed biomedical and fundamental research structural investigations. Unfortunately, sample preparation is still a bottleneck in the workflow. Notably, the classical process uses a lot of samples and tends to damage the specimen by the paper blotting step and the exposure to the harsh air-water interface. The cryoWrite system [1-3] minimizes sample consumption and loss, eliminates the paper blotting step, and allows unprecedented control over the preparation process.

In this project, we aim to improve the microfluidic preparation process further by (i) protecting the specimen better from the aggressive air-water interface, (ii) gently controlling the thickness of the sample, and (iii) developing a real-time system to monitor the sample activity immediately before vitrification. As a benchmark project, we analyze the 3D structure of motile cilia (or eukaryotic flagella in synonym) by cryo electron tomography.

Sample protection from air-water interface
The specimen is embedded in a thin buffer layer of 30 to 50 nm for cryo-EM. During preparation, the protein is exposed to physically and chemically harsh air-water interfaces, and a significant fraction of the protein particles fall apart (Fig. 1). For an average protein, the diffusion times are in the low microsecond range, and an outrunning of protein diffusion to the air-water interface is impossible. Therefore, we developed a climate jet to control the micro-environment of the grid [4]. The jet provides an oxygen-depleted environment of precisely controlled temperature and relative humidity and allows the spraying of effecter molecules onto the thin sample during specimen preparation. This enables the creation of a protecting layer at the air-water interface of the thin sample (Fig. 2).

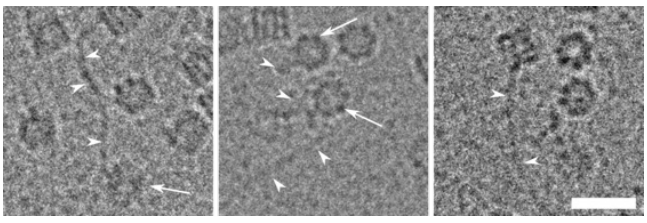

Fig. 1: Denaturation of protein particles at the air-water interface. Arrows indicate damaged Chaperonin 60 particles, a known sensitive protein. Arrow-heads point to unfolded protein chains. We interpret that the high contrast of the visible chain is due to the significant electron density difference at the air-water interface, where the chain adheres. We suspect that unfolded proteins are a major source of noise in cryo-EM images. Scale bar: 20 nm

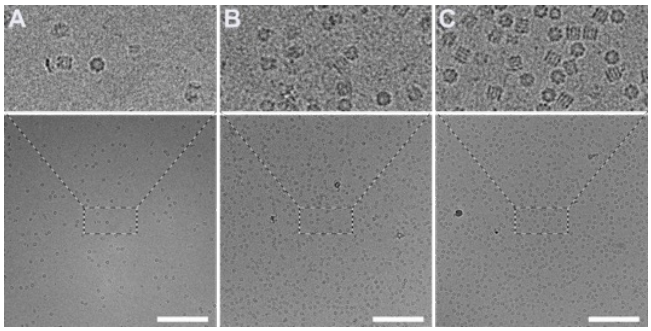

Fig. 2: cryo-EM sample preparation of Chaperonin 60 The grids were performed using A) the classical preparation (Vitrobot) with paper blotting, B) the cryoWriter without spray, and C) the cryoWriter with the pulse injection of an detergent during preparation. Scale bars: 200 nm. Adopted from [4].

Our experiments show that spraying surface modulating molecules can improve the quality of cryo-EM preparations (Fig. 2): For our test-protein chaperonin 60, the cryoWriter already significantly improved preparation quality (number of particles, fraction of intact particles, orientation distribution) and is additionally improved by the spray. Thereby, the signal-to-noise ratio is also significantly better. We believe unfolded proteins decrease cryo-EM images' signal-to-noise (SNR) ratio. Cryo-EM preparations using the spray exhibit a considerable improvement in SNR.

Functional Cryo-EM Sample Preparation for Flagellar Axoneme
The architecture of a eukaryotic flagella consists of a bundle of microtubule pairs with attached dynein motor proteins (among other proteins). Natively, a membrane surrounds this protein core (axoneme). Here, we studied demembranized axoneme protein assemblies isolated from Chlamydomonas, which allows the activation of flagella beating by ATP.

Isolated, de-membranized axonemes are long and fragile structures. Therefore, the preparation for cryo-EM is delicate; in particular, the paper blotting step used in classical preparation methods disturbs, flattens, or disrupts the ultra-structure. Even using the blotting-free preparation method by the cryoWriter system needed optimization to maintain the radial assembly without flattening (Fig. 3), which allowed the comparison of ATP activated with resting flagella (Fig. 4).

However, our initial cryo-EM tomograms revealed that the weekly attached dynein motors got lost during the preparation. Further optimization of the nozzle geometry and uptake and dispensing speed for the priming of the axonemes enabled the cryo-EM preparation with intact motor protein assembly (Fig. 5). Light-microscopy of ATP-activated axon-

emes on the cryo-EM grid revealed that these preparations contain functional assemblies. However, For these investigations, the grid must be transferred to the temperature-controlled stage before vitrification. We are currently developing an additional optic to avoid this transfer.

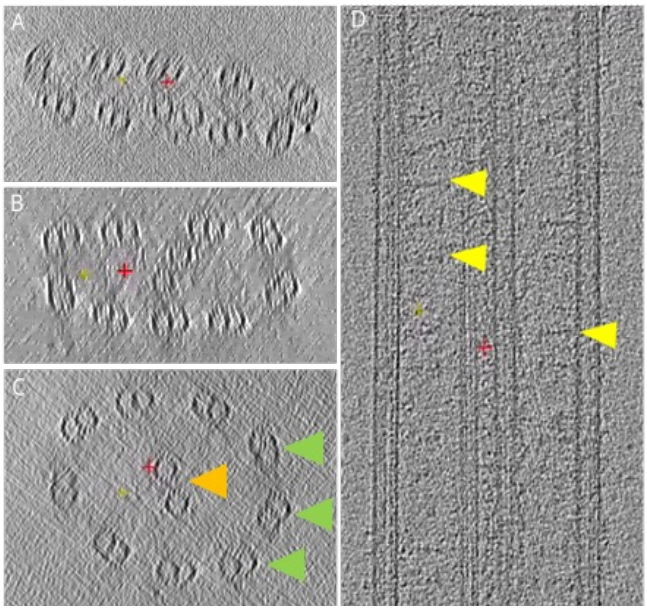

Fig. 3: Electron tomograms showing de-membraned Chlamydomonas flagella in various ice thicknesses. A) Chlamydomonas flagella in too thin ice, resulting in a crushed structure. B) Chlamydomonas flagella in a thicker layer of ice but still being warped by the ice being too thin C) Chlamydomonas flagella in an ideal amount of ice with both the central pair and outer doublets visible. Green arrows indicate microtubule doublets. The Orange arrow indicates the central pair. D) A top-side tomogram of the Chlamydomonas flagella assembly clearly shows the microtubule doublets and the central pair. Yellow arrows indicate radial spokes.

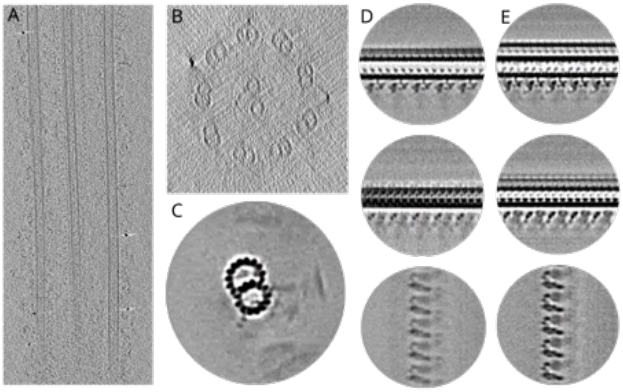

Fig. 4: Electron Tomograms of activated and non-activated Chlamydomonas axoneme. A) Regular tomogram of axoneme. B) Cross section of the tomogram. C) Initial sub-tomogram average without classification and refinement. D) Different sections of C) sub-tomogram average for activated (with ATP) axoneme. E) Different sections of the sub-tomogram average for non-activated axoneme. More protein densities are visible due to less conformational change occurring.

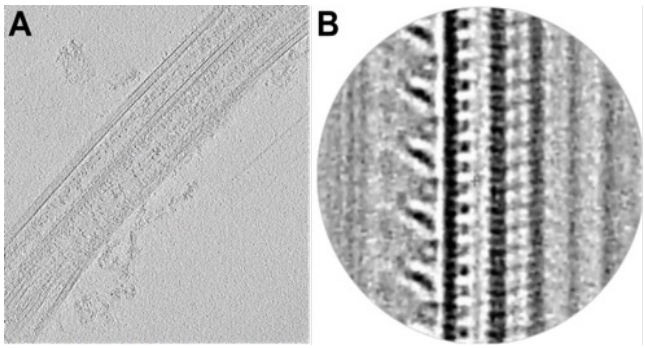

Fig. 5: An electron tomogram of a vitrified Chlamydomonas Axoneme shows the preservation of intact dynein attached to the microtubule structure. A) Lengthwise tomogram showing several dynein transporters. Both inner arm and outer arm conformations are seen. Dyneins are preserved through a slow aspiration and uptake of said sample (0.4 ul/min uptake, 0.2 ul/min aspiration). B) High-resolution refinement of protein densities found on axoneme.

Ongoing experiments and outlook

Several ongoing developments and experiments will be completed in 2024: (i) The preparation of complete axemenes using focused ion-beam milling and cryo-EM tomography. (ii) optics for in situ activity assays. (iii) Installation and usage of the new commercial cryoWriter currently developed by cryoWrite AG.

References

[1] S. A. Arnold, S. Albiez, N. Opara, et al. Total sample conditioning and preparation of nanoliter volumes for electron microscopy, ACS Nano 10 (5), (2016)

[2] S. A. Arnold, S. Albiez, A. Bieri, et al. Blotting-free and lossless cryo-electron microscopy grid preparation from nanoliter-sized protein samples and single-cell extracts, J. Struct. Biol. 197 (3), (2017)

[3] C. Schmidli, S. Albiez, L. Rima, et al. Microfluidic protein isolation and sample preparation for high-resolution cryo-EM, Proc. Natl. Acad. Sci. U.S.A. 116 (30), (2019)

[4] L. Rima, M. Zimmermann, A. Fränkl, et al. cryoWriter: a blotting free cryo-EM preparation system with a climate jet and cover-slip injector, Faraday Discussions 240, (2022)

Phase-shifting metasurfaces for flexible and foldable displays

Project A17.4: META-DISPLAY (CSEM Allschwil SA, Paul Scherrer Institut, Rolic Technologies Ltd., Allschwil)
Project Leader: B. Gallinet
Collaborators: L. Ciric, G. Basset, I. Giannopoulos, D. Kazazis, F. Federspiel, R. Frantz, D. Pires

Introduction

The rising market demand for thin, flexible, and foldable displays has initiated the quest for technologies that could facilitate their fabrication. To ensure sufficient flexibility, the display's thickness must be significantly reduced. A polarizer and a phase-retarding layer are stacked above the display's emitted layer with the aim to suppress back reflection from ambient light and maximize image contrast (Fig. 1). Additionally, the suppression of ambient light reflection must be minimized for a broad range of angles, ensuring that contrast is maximized at any viewer position. The phase-retarding layer, a quarter waveplate, must also have high transmission to maximize the brightness of the OLED display.

Standard phase-retarding materials based on liquid crystals typically have thicknesses of a few microns. Metasurface-based layers have the potential to replace existing bulky phase-retarding plates, as they can achieve the same functionality by inducing the desired electromagnetic field phase retardation within a single micrometer [1, 2].

Metasurface technology holds promising potential for applications in other segments of the consumer electronics market. One noteworthy example is its use as flat imaging elements in smartphones.

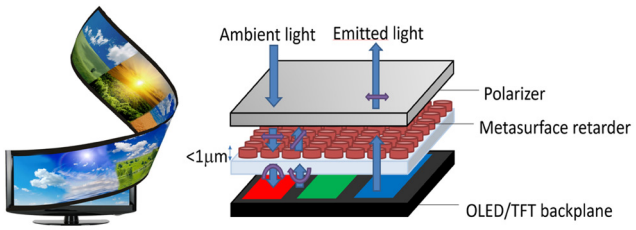

Fig. 1: Left, foldable screen illustration. Right, phase retardation stack with metasurface layer. Unpolarized light passes through an x-linear polarizer, becomes anticlockwise circularly polarized after 1/4 waveplate. Reflection from LED backplane results in clockwise polarization, by 1/4 waveplate further transformed back to linear polarization but orthogonal to initial linear polarization, thus preventing any light reflection.

Design and fabrication

In the first phase of the project metasurface phase retarders have been designed and simulated. Figure 2 illustrates the simulation results, showcasing the values of phase retardation and their minimal dependence on the incident angle of light, meeting the target requirements. The simulations demonstrate the feasibility of implementing these structures in various materials and substrates, providing additional flexibility.

A cost-effective and high-throughput approach, as depicted on the left in figure 2, involves UV nanoimprint lithography (UV-NIL). This method allows for the direct transfer of metasurface structures onto high refractive index material coated on a thin, flexible, transparent foil. Preliminary tests reveal challenges in sustaining the replication fidelity of high aspect ratio structures required for such metasurface designs.

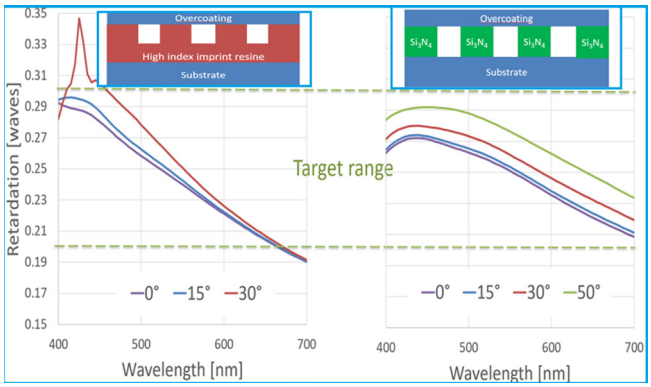

Fig. 2: Simulation of EM phase retardation with wavelength/angle of incidence. Left: case of UV NIL of high refractive index foil. Right: case of NIL approach on rigid dielectric (green color code). Between the dashed green lines is the range of retardation that is "nice to have". It should have a low angle and wavelength dependence.

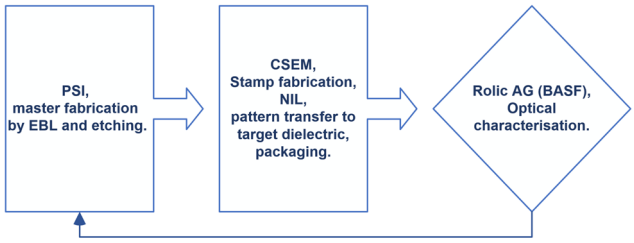

Fig. 3: Technical fabrication collaboration scheme.

Hence, the current focus in this stage of the project is on wafer-based fabrication utilizing thermal NIL as shown on the right in figure 2. The initial step in thermal NIL involves fabrication of a high-quality master with electron beam lithography (EBL) and reactive ion etching (RIE) on silicon (Fig. 3). Subsequently, the stamp is produced from the first copy of the master to ensure the correct polarity of the structures. Following the thermal NIL step, depicted in figure 4 on the right, the metasurface pattern is transferred into a dielectric layer through RIE of the residual layer, Cr, and the dielectric material.

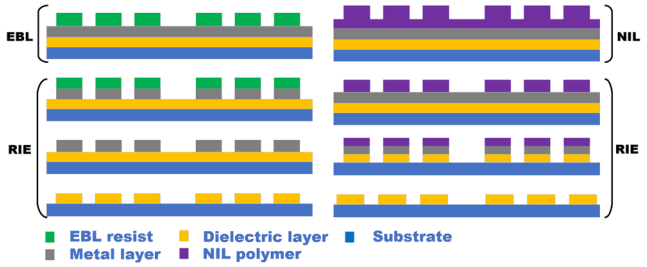

Fig. 4: Left, process flow of EBL (done ad hoc as a proof of concept) followed by RIE steps. Right, thermal embossing NIL with RIE.

Results

For the proof of concepts and simulation approval, the 1/4 waveplate grating was fabricated by EBL and RIE (see Fig. 4, left and Fig. 5). At the time, for this purpose thermal NIL was not employed because the etching of the residual layer required better process control. The lack of control on residual layer etching could provoke significant deviation from the original pattern and increase line edge roughness. However, even though EBL and RIE process have fewer steps and better process control, slight deviations from the nominal simulated structures were observed after etching and processing of the full stack.

Despite these deviations, the initial characterizations (Fig. 3) of a series of gratings fabricated by EBL and RIE exhibit promising results, with phase retardance ranging from 0.27 to 0.3, slightly above the desired 0.25. The fabricated structures maintain an aspect ratio within 10% of the simulated values. Moreover, the transmission is exceptionally high at around 85%, and there is notable angular stability. Overall, the results are encouraging; these metasurfaces demonstrate relatively good retardation values, indicating robustness regarding slight deviations coming from fabrication process steps.

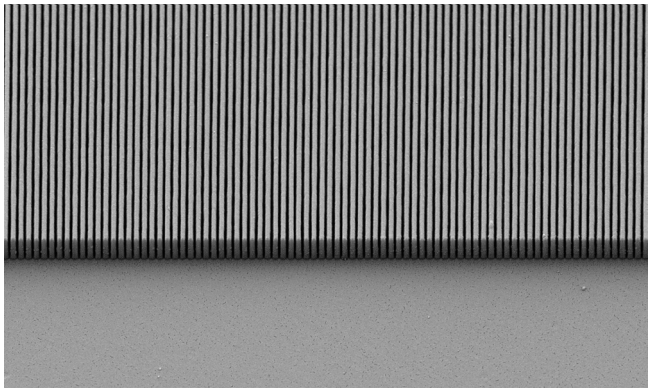

Fig. 5: SEM image of 1/4 waveplate in dielectric nanostructures fabricated by EBL and RIE in dielectric.

Having made significant progress in the control of residual layer etching, metasurfaces entirely based on thermal NIL have been finally successfully fabricated, as shown in figure 6. However, optical inspection of these metasurfaces is still pending.

Outlook

In the upcoming phase, a multitude of metasurfaces based on thermal NIL will be produced, characterized, and subjected to systematic analysis to determine precise geometrical specifications. The results of optical characterization will be meticulously crosschecked with the fabricated structures, and the most performative ones will be selected for the creation of a large-area metasurface master. Utilizing this large-area master in thermal NIL, the produced samples will then be integrated into a demonstrator device.

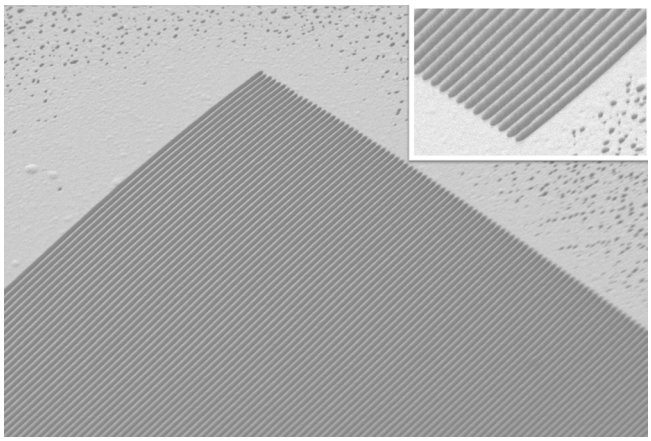

Fig. 6: SEM image of metasurface grating after thermal NIL, residual layer etching, RIE of Cr and dielectric.

Acknowledgments

The project partners (CSEM, Paul Scherrer Institut (PSI) and Rolic AG) express sincere gratitude for funding the project.

References

[1] A. Arbabi, Y. Horie, M. Bagheri, A. Faraon, Dielectric metasurfaces for complete control of phase and polarization with subwavelength spatial resolution and high transmission, Nature Nanotechnology 10, 937- 943 (2015)

[2] F. Lütolf, F. Friebel, I. Kuznetsov, B. Rudin, F. Emaury et al., Wafer-scale replicated gratings for compressing ultrafast laser pulses at telecom wavelengths, Optics Continuum 1, 1051- 1059 (2022)

Smooth focusing mirrors for X-rays

Project A18.01: CAPOFOX (Paul Scherrer Institut, FHNW Muttenz, XRnanotech, Villigen)
Project Leader: H. Schift
Collaborators: S. Saxer and F. Döring

In the Nano Argovia project CAPillary Optics for FOcusing of X-rays (CAPOFOX), an interdisciplinary team is further developing lithographic methods to produce micro-optical components with extreme low surface roughness. Researchers from the Paul Scherrer Institute PSI, the School of Life Sciences at the University of Applied Sciences and Arts, Northwestern Switzerland FHNW and the industrial partner XRnanotech are aiming for a process that produces tiny capillary mirrors suitable for both ultraviolet and X-rays.

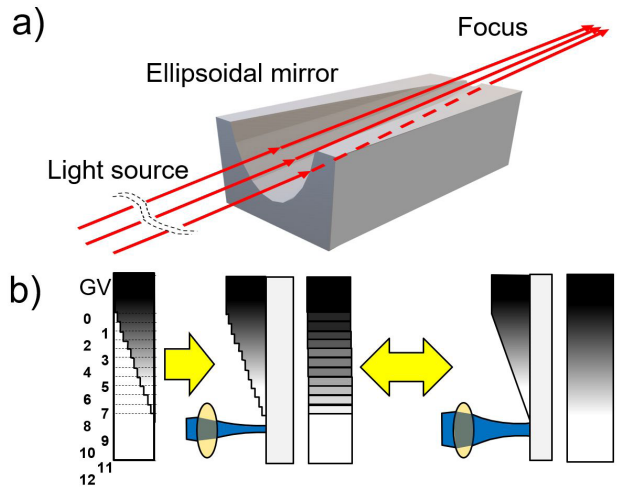

Fig. 1: a) Reflective focusing optics, b) influence of beam size for step smoothening in directly laser lithography.

Lenses and mirrors stand out as prominent examples among optical components. In case of focusing refractive lenses, the light passes through a bulky glass element and is, depending on the angle of its incidence, the refractive index, the thickness and thus the length of the path between two surfaces, directed to the focus point. Such a lens – for visible light – has a convex shape with spherical surfaces. For X-rays, however, the lens would absorb most of the light in transmission, therefore a mirror is created with a similar shape as the lens, that could focus the light by reflecting it by the surface. Ellipsoidal mirrors, or hollow tubes that are shaped like a funnel, can act as focusing elements for X-ray beams (Fig. 1) [1]. The light impinges on the internal walls at very shallow angles (called "grazing incidence"). Glass capillaries are widely used for this because they can be thermally drawn in well-established processes, e.g., for generating pipettes. They have outstanding smooth surfaces with RMS roughness below 1 nm. Yet, there is a restricted range of available geometrical shapes.

Arbitrary 3D shapes by gray-tone lithography

Gray-tone lithography allows to reproduce a three-dimensional (3D) surface topography from a computer aided design and could fill the gap to create surfaces, e.g., with parabolic shapes in lateral (x-y) direction, that could focus light more precisely. This can be done by exposing photosensitive materials (photoresist) with different laser energies and then etching the exposed resist away, leading to a ready to use 3D structure. A further advantage of gray-tone lithography is that it is capable to produce elements with specific 3D contours – for example lenses with continuous and stepped surfaces, such as those used in smartphone cameras. The different lateral exposure after subsequent processing results in resist layers of different thicknesses.

However, the number of applicable gray values of current direct laser writers is a discrete number between 128 and 1024 and limits the resolution in vertical direction (z). Thus, the method leads to exposure steps that add to the roughness of the surface. This significantly constrains its application in lenses and mirrors, because with every reflection, part of the light is lost due to scattering. The thicker the resist, the more pronounced the steps. The longer the steps, the more difficult to simulate a slope with continuously inclined surfaces.

In CAPOFOX, the project team wants to establish methods that are a) capable of generating such geometries with a limited number of gray values and b) characterize and optimize the roughness in the nanometer range, to finally achieve smooth waveguide structures in polymers that are similar or even better than those of glass capillaries.

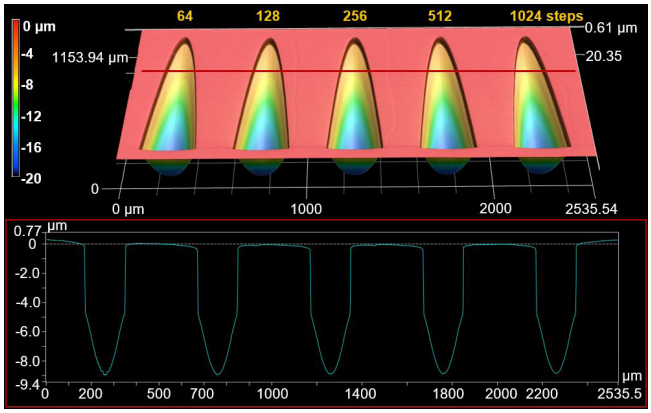

Fig. 2: Confocal scanning laser microscope (Keyence VK-X3100) images and cross-sections of five slopes produced with direct laser lithography (Heidelberg Instruments DWL 66+) in ma-P1275G novolak resist (micro resist technology) with different numbers of gray values.

Stepless nano-smooth surfaces

In previous Nano Argovia projects, a team led by Dr. Helmut Schift (PSI) had developed various methods for local smoothening of a surface, in which roughness was largely reduced by local melting [2]. However, this contactless polishing cannot be used for extended structures with longer steps, as required in capillary optics. The current strategy is to enhance the number of gray tones by creating intermediate steps between the steps provided by the direct laser writer, by superimposing multiple, tiled exposures with varying intensity. What sounds like a simply computational trick, is far more complex, since it involves the separation of the designed shape into multiple gray-tone designs, and the adaptation of the exposure. Once it is achieved it allows for writing a variety of shapes. Combination with surface smoothening by selective reflow, the addition of microscopic and even nanoscopic steps in a smooth surface would allow generating alignment structures that would allow the combination of different optical functions or even elements.

The difference between waviness and roughness

A general guideline is that the roughness of a surface should be at least 10 times smaller than the wavelength used. Even tiny steps in the order of magnitude of the wavelength interfere. For Extreme UV (13.5 nm), that is currently used for the high-volume manufacturing of microchips, this would require roughness of around 1 nm. For X-rays below 10 nm, roughness down to the atomic level is needed. To calibrate analytical methods that are coming to their limitations, we employed sapphire crystals that exhibit staircases with 0.3 nm high steps and are also promising molds for replication into polymers. They serve as high precision reference that mimic this roughness in a defined way.

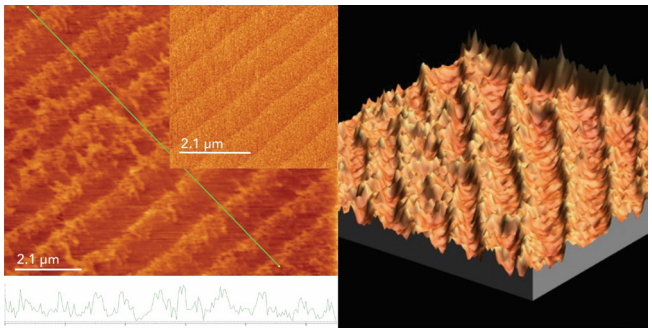

Fig. 3: Nanometer-sized steps of a polymer reference replicated from thermally treated sapphire (inset picture left image), measured using scanning force microscopy.

Roughness is measured by scanning the surface with mechanical or optical profilometers. However, they are not sensitive enough to measure the nano roughness anticipated for the waveguides. Scanning force microscopy (SFM) is the method of choice in this dimension although the latest optical techniques, e.g., confocal scanning laser microscopy (CSLM) and white light interferometry (WLI) advance in sensitivity and resolution. Surface topography is segregated in three parts: a) The form, i.e., the desired general shape of the surface, b) the waviness, often fabrication-related repetitive structures of larger height, and c) roughness coming from process- and material-related limitations. For our system, the slope represents the form, the writing steps the waviness and the resist structure the roughness.

Currently, only SFM enabled us to measure the sub-nanometer steps of the sapphire reference. In contrast to this, the structures that were thermally imprinted into polymers exhibited defects and an increased roughness of >10 nm (Fig. 3). Thus, the imprint process requires optimization. The gray tone slopes are currently showing a waviness of approx. 30 nm and roughness around 10 nm, whereas the waviness was also confirmed by CLSM. The measurement of the complete waveguide is currently done by using CLSM or WLI to characterize the geometry of the up to 5 mm long and 100 µm high slope with 1-50 µm long steps, followed by local roughness measurements with SFM.

An ongoing challenge lies in discerning a measured 1-10 nm roughness, which could originate from either the step height or the inherent roughness of the material. For this, we must differentiate between the three topography parts. However, most roughness analysis software does not differentiate, moreover automatic or manually applied filters distort the data and impede a comparison between the techniques. Dr. Sina Saxer (FHNW) and her team are writing a MatLab® script that allows to compare the measured profile of SFM, CLSM and WLI and segregate it in the three parts. We expect a better understanding of the limits of each method, the specific modification of the writer parameters and polymer surface post treatments to achieve nano roughness (< 0.3 nm).

As the next step, a concave reflective mirror for EUV will be produced using different number of gray values (Fig. 4). We will see what effect the optimized results from linear slopes will have on these more complex 3D shapes. The results will contribute to the development of ultra-smooth mirrors for focusing X-rays, which can be used in material processing, for example.

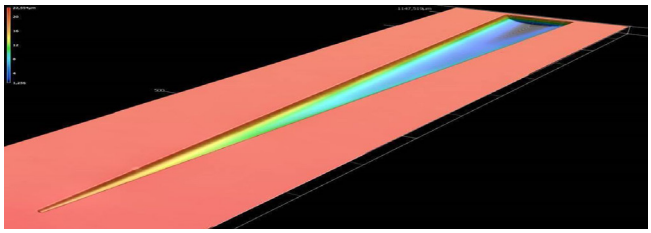

Fig. 4: An elongated half-pipe capillary 3D structure.

This project enables the young start-up XRnanotech to enhance their portfolio of microlenses for X-ray applications: “The CAPOFOX project combines excellent expertise in the production and investigation of ultra-smooth surfaces. The chosen methodology is innovative and is characterized by many future high-impact applications. We are very pleased to be able to accompany and support such developments.”, according to Dr. Florian Döring, CEO and founder of XRnanotech.

References

[1] H. Yumoto, T. Koyama, S. Matsuyama, Y. Kohmura, K. Yamauchi, et al., Ellipsoidal mirror for two-dimensional 100-nm focusing in hard X-ray region, Sci. Rep. 7, 16408 (2017)

[2] N. Chidambaram, R. Kirchner, R. Fallica, L. Yu, et al., Selective surface smoothening of polymer microlenses by depth confined softening, Adv. Mater. Technol., 1700018 (2017)

NanoFemto Tweezers: Tissue assembly with diffractive nano-optics tweezers and fs Alexandrite laser

Project A18.5: NanoFemto Tweezers (FHNW Windisch, FHNW Muttenz, TLD Photonics AG, Wettingen)
Project Leader: B. Resan
Collaborators: T. Grätzer, M. Gullo, R. Carreto

Abstract
We aim to build holographic optical tweezers by employing diffractive nano-optics and a novel ultra-short pulsed alexandrite laser. The optical tweezers will be able to manipulate multiple types of cells allowing for multi-cellular tissue assembly with minimal thermal impact due to a newly developed ultra-short pulsed alexandrite laser pumped by red laser diodes.

Introduction
Personalized medicine aims to tailor treatments, reducing adverse effects, using patient-derived organoids for drug testing. Yet, organoids alone can't replicate intricate inter-organ interactions. Body-on-chip platforms are vital, integrating multiple organoids in microfluidic setups, which requires precise bio fabrication, aligning diverse cell types with micrometer accuracy. Holographic optical tweezers offer promise, using lasers to manipulate cells. Conventional lasers risk cellular damage due to heat. To counter this, we propose femtosecond lasers, giving a minimal heat impact. Enhanced by nano-diffractive optical elements, lasers can form optimal trapping patterns. This synergy aims to establish a gentle holographic optical tweezer system towards body-on-chip creation.

The alexandrite oscillator developed for this application uses red laser diodes to directly pump the crystal. This provides multiple benefits to other pumping setups currently in use such as flash lamps, green laser diodes, and frequency doubled YAG-lasers. Pumping by red laser diodes provides superior quantum efficiency, lower cost, and complexity. Multi-watt level red laser diodes have become commercially available in recent years and have thus enabled the direct pumping of alexandrite lasers. Continuous-wave and Q-switched pulsed operation of alexandrite lasers pumped by red laser diodes has already been demonstrated [1]. Mode-locked operation of alexandrite, which is the method used for achieving ultrashort pulses in the femto- and picosecond range, has only been demonstrated using green pump light from expensive frequency-doubled solid-state lasers [2]. Therefore, to our best knowledge, the developed alexandrite laser would be the first femtosecond alexandrite laser pumped by red laser diodes. This new approach could make ultra-short pulsed lasers in the NIR more efficient and cost-effective compared to alexandrite lasers pumped by other means and the currently widely used Ti:sapphire lasers.

Experimental Setup
The experimental setup consists of a scientific setup of the diode-pumped alexandrite oscillator (see Fig. 1 and Fig. 4b) and an optical tweezer setup. The alexandrite oscillator is pumped by a fiberized output laser diode module with 5 W of nominal optical output. The cavity design was adapted from Ti:sapphire oscillators by considering the upper state lifetime and emission cross-section of alexandrite. The crystal is straight-cut and anti-reflection coated for the pump and lasing wavelengths.

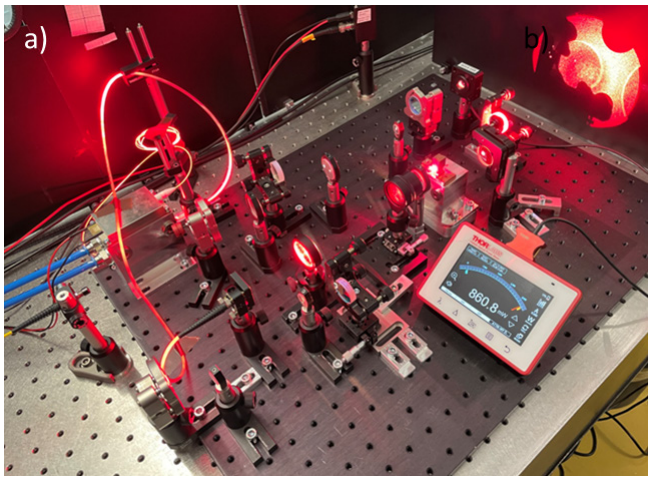

Fig. 1: Scientific setup of the red diode pumped alexandrite oscillator.

Results
An 80 MHz pulse repetition rate alexandrite laser oscillator was designed, and a scientific setup has been built, as shown in figure 1. The laser achieved 1 W of output power in CW mode at 8 W of pump power using a 1% output coupler. Using a SESAM as one of the end mirrors and incorporating GVD mirrors for dispersion compensation, we have achieved modelocked operation centered at 745 nm with a spectral width (FWHM) of 11.5 nm (see Fig. 2a). Assuming near transform-limited pulse duration and a sech2-shaped pulse, this corresponds to ~50 fs pulse width (FHWM). The output power was only 70 mW due to the losses introduced by the available sub-optimal SESAM. Figure 2b depicts the pulse train of the laser in modelocked operation measured by a fast photodiode. We are currently working on improving the stability of the modelocked operation.

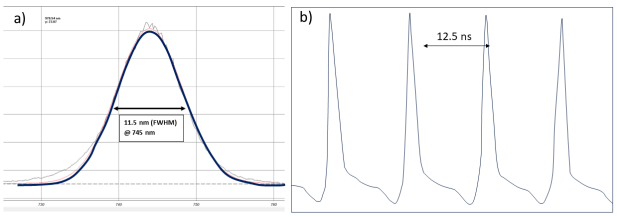

Fig. 2: a) Spectrum of the modelocked alexandrite laser. b) pulse train of the modelocked alexandrite laser measured by a fast photodiode.

To project holograms for optical trapping foci, nano diffractive optical elements (nDOE) were computed based on a kinoform addition algorithm. The kinoform shown in figure 3a is devised to induce a diffraction pattern aligning three points as exemplified in figure 3b. The gradation from black to white corresponds to a phase shift spanning from zero to one. The kinoforms were then used to compute a 3D nDOE structures (Fig. 3c). This transformation involved transposing each kinoform pixel into a physically tangible pixel measuring 10 x 10 µm, with its height based on the intended phase shift and the refractive index intrinsic to the employed polymeric ink. Subsequently, the nDOE as depicted in the micrograph figure 3d and SEM image figure 3e were fabricated by 2-photon lithography. Two types of nDOE were manufactured: one for reflective wavefront modulation and one for transmissive wavefront modulation. The reflective nDOE showed an important loss of intensity as only thin reflection coatings could be applied for keeping the nanopatterned structure conform. Therefore, the transmission nDOE was chosen for the continuation. To permit the trap arrangement modulation, e.g., trap distance, several nDOEs were fabricated side by side to enable switching between different configurations by lateral shifting of the nDOE plate.

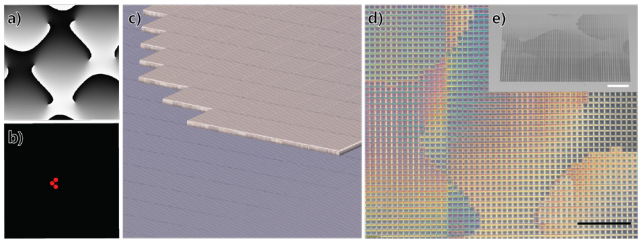

Fig. 3: a) Computed kinoform phase shift for b) three optical trap foci; c) Part of a computed 3D nDOE structures showing the 10 x 10 µm² phase pixels with the maximal height of 1.4 µm and resolution of 11 nm; d) Optical micrograph of the fabricated nDOE and e) corresponding SEM image. All scalebars are 10 µm.

A basic optical tweezer setup based on discrete nano-optical elements and a pilot laser matching the targeted wavelength as a temporary replacement for the pulsed laser, has been designed (Fig. 4a) and implemented (Fig. 4c). Preceding the nDOE integration into the optical path, an assessment of setup quality was performed via a singular focal point projection (Fig. 4b), which showed a focal spot size of 3 µm. Upon the introduction of the nDOE, the anticipated projection of three traps emerged in alignment with computations (Fig. 4d). As the phase modulation was implemented in a transmissive manner, the focal spot (orange arrow) emerging form from the principal beam remained present in addition to the foci generated by the nDOE (red arrows). Several nDOE projecting foci with increasing distance from the centre allowed a swift modulation of the foci position (Fig. 4d). The freely available micromanager software plugin for ImageJ was expanded to be able to computer control the optical tweezer setup such video camera, nDOE calibration, OpenCV image tracking and other automated tasks. A setup integration into a commercially available microscope is currently being evaluated.

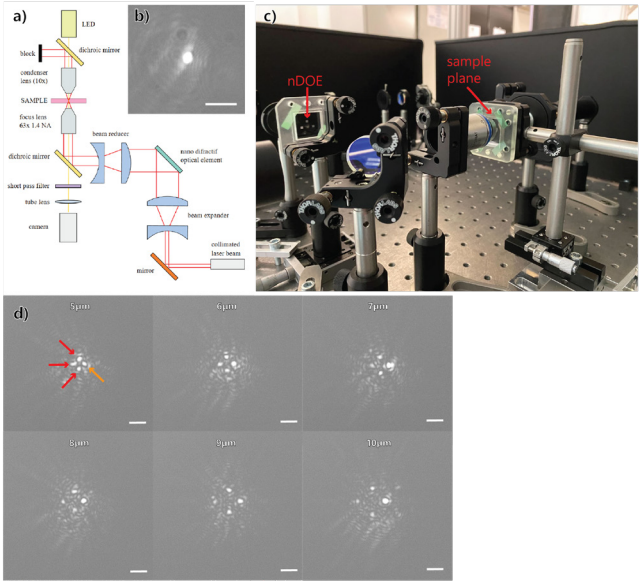

Fig. 4: a) Schematic illustration of optical trap setup; b) Single optical trap foci with a focal spot size of 3µm; c) projection and imaging part of the assembled optical trap setup showing the nDOE and sample planes; d) Projection of the different kinoforms for 3 foci resulting on different trapping distances form the center; orange arrow shows transmitted focal spot; red arrows show holographic foci.

References

[1] A. Teppitaksak, A. Minassian, G. M. Thomas, and M. J. Damzen, High efficiency >26 W diode end-pumped Alexandrite laser, Opt. Express 22, 16392 (2014)

[2] S. Ghanbari, K. A. Fedorova, A. B. Krysa, E. U. Rafailov, A. Major, Femtosecond Alexandrite laser passively mode-locked by an InP/InGaP quantum-dot saturable absorber, Opt. Lett. 43, 234 (2018)

NanoHighSens: A high bandwidth and nanoscale magnetic sensor for current measurements

Project A18.6: NanoHighSens (FHNW Muttenz, FHNW Windisch, Camille Bauer Metrawatt AG, Wohlen)
Project Leader: J. Pascal
Collaborators: H. Nicolas, A. Grana, J-B. Kammerer, R. Sousa, S. Gorenflo, M. Ulrich

Introduction

Contactless measurement at high bandwidth of electrical currents is nowadays required in quality control of electrical networks, while still remaining challenging, due to the difficulty to combine high bandwidth with low noise. In this context, the NanoHighSens project aims to use nanoscale spin transfer torque magnetic tunnel junctions (STT-MTJs) as nanoscale magnetic sensors with high bandwidth as well as high resolution. Such innovative sensors should meet the most recent quality standard requirements (e.g., IEC62020-1), requiring the measurement of high-frequency harmonics in electrical currents above 100 kHz.

Magnetic Tunnel Junctions

To operate the MTJs (Fig. 1) as sensing units, a low amplitude (< ± 400 mV) triangular voltage signal at high frequency is applied across the MTJ, typically 100 kHz and above, leading to periodical reversal of the magnetization of the free layer [1]. This reversal leads to a change in the resistance of the device, alternating from low resistive state (e.g. 4 kΩ) to high resistive state (e.g. 8 kΩ) and inversely. However, as a result of the spin transfer torque effect combined with the TMR effect observed in these devices, the time spent, over one period of the input signal, between the low resistive state and the high resistive state is directly a function of the external magnetic field [2].

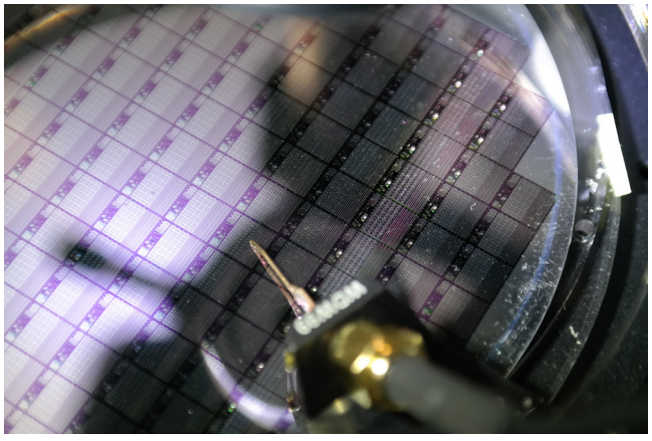

Fig. 1: MTJs on wafer under test.

Since the voltages to obtain these resistance reversals are proportional to the external magnetic field, sensing of the reversal voltages (low to high and high to low) allows the measurements of the magnetic field. In addition, since MTJs can be operated at high speed, being one of the reasons MTJs are well suited for memories, such sensing principle is inherently offering high-bandwidth capabilities (Fig. 2).

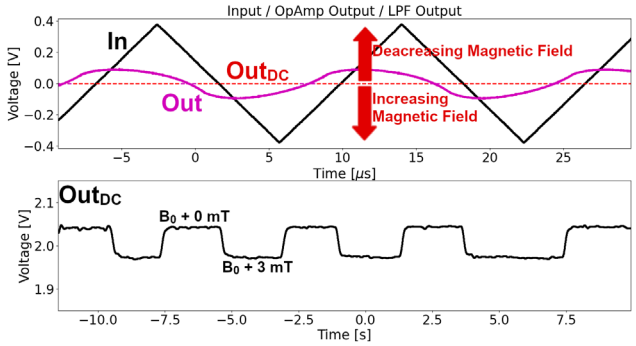

Fig. 2: Measurement principle of the proposed sensor [2].

Electronics and Signal Processing Platform

To achieve desired results, both signal processing electronics and conditioning electronics need to be developed to use the physical device as a sensing element. The conditioning electronics includes all the required analog hardware circuitry to output a signal proportional to the magnetic field, as depicted in figure 3. This includes only a few operational amplifiers combined with few passive components, making the design fully compatible with future CMOS monolithic integration. Since MTJs are originally designed for memory applications, these are also fully compatible, or will be in the short term, with CMOS standard processes. Such sensor will then be more easily available to mass production as monolithic integrated circuits, lowering the cost and increasing the range of applications.

On the other hand, the signal processing platform consists in multiple larger units, including microcontrollers or memories, each capable of handling the measurement of a sensing unit, creating the complete current probe prototype (Fig. 4). Each unit can measure the MTJs up to a bandwidth of 250 kHz, by including the developed conditioning electronics described above, synchronously with all the other units. This results in eight different, but synchronous, data point from multiple sensing units, each of them resulting from an array of MTJs, allowing the noise to be substantially lowered.

Consecutive data points are then stored until filling the embedded memory of the microcontrollers, then quickly collected, and sent to the computer for more advanced signal processing and analysis (e.g. FFT, filtering, …). The output of the whole system is a unique reconstructed signal proportional to the external field (i.e., current) with low noise and high bandwidth, allowing the assessment of high harmonics in the monitored power network.

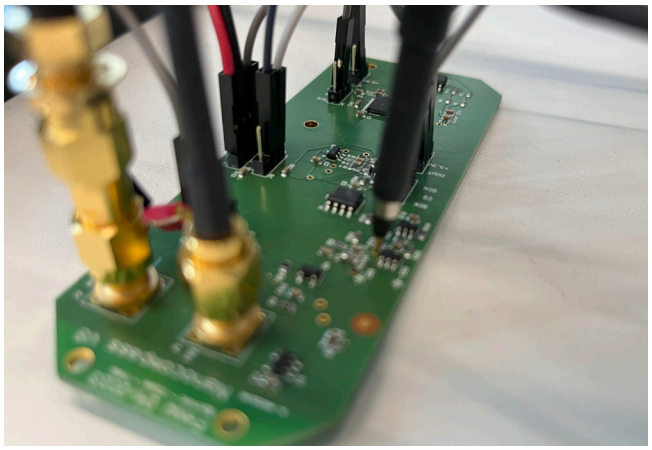

Fig. 3: Conditioning electronics, including all the analog electronics to operate the MTJs as sensing elements.

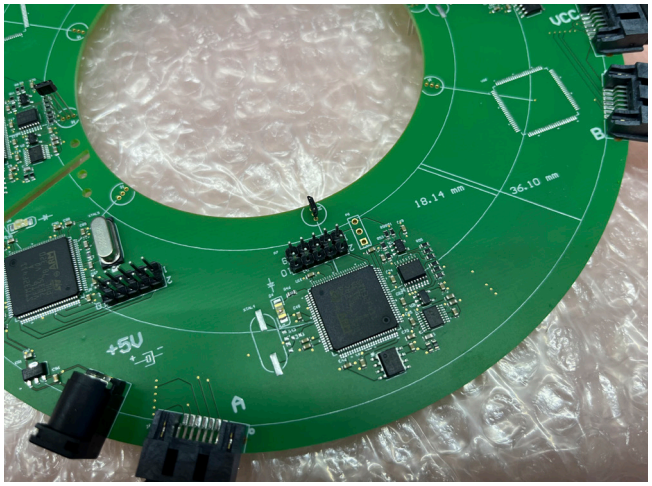

Fig. 4: Signal Processing Platform. One can see the different measurement units arranged in the circular shape, in charge of handling both the analog and digital processing of the MTJs.

Results

Using these devices with the electronics described in the previous sections, one could extract sensitivity of up to 25 mV/mT with noise level as low as 1 µT/√Hz on a single MTJ with diameter ranging from 20 to 100 nm. Further tests are being conducted to assess the different ways of optimizing the electronics and/or the stack of the junction to push the performance of single junctions even further.

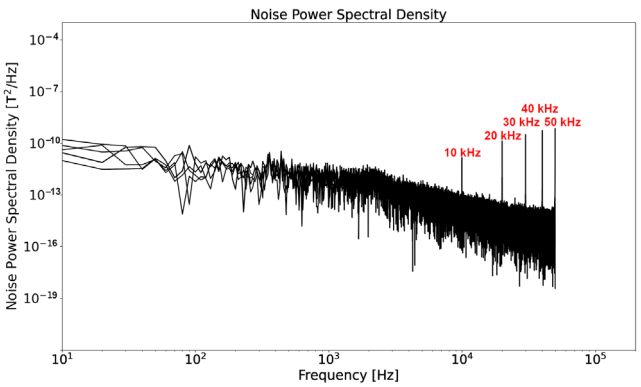

Fig. 5: Initial evaluation of the bandwidth of the sensor. Multiple measurements are superposed in this image, showing the capabilities of detecting different harmonics up to at least 50 kHz.

Current consumption is typically less than 30 µW for the sensing element. This also makes the prototype and MTJs compatible for future arrays of multiple junctions, as global power consumption of such array will remain in the order of few mW, easily manageable in an integrated circuit. Typical range of such sensing devices are between ± 8 mT to ± 20 mT while the bandwidth has yet to be determined but appears to be above the measured 50 kHz (Fig. 5, 6).

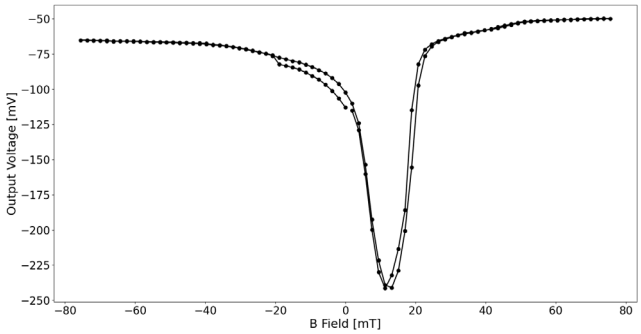

Fig. 6: Output voltage of the proposed sensor.

Conclusion

Using MTJs presenting low coercive fields of less than a mT with high-sensitivity, associated with the proper reading architecture, a high-bandwidth magnetic sensor could be demonstrated achieving a high bandwidth with a resolution of few µT/√Hz, while offering a low power consumption combined with nanometric dimensions. Thanks to these dimensions, an array of multiple MTJs is now being considered, allowing the resolution to be lowered down as explained previously.

Such sensing units will then be placed in the described circular pattern on the PCB of the current probe to create the final prototype, combining both high-bandwidth and low noise performance. However, different improvements are still required to obtain the lowest noise possible, almost exclusively induced by the stochasticity of magnetic tunnel junctions in the reversal events.

References

[1] H. Nicolas, R. C. Sousa, A. Mora-Hernandez, I.-L. Prejbeanu, L. Hebrard et al., Conditioning Circuits for Nanoscale Perpendicular Spin Transfer Torque Magnetic Tunnel Junctions as Magnetic Sensors, IEEE Sensors Journal 23(6), 5670-5680 (2023)

[2] H. Nicolas et al., Low-Coercivity Perpendicular Spin Transfer Torque Magnetic Tunnel Junctions as Nanoscale Magnetic Sensors, IEEE Intermag 2023, (2023)

Quantum sensors for brain imaging

Project A18.7: QSBI (Paul Scherrer Institut, CSEM Allschwil SA, Qnami AG, Muttenz)
Project Leader: K. Moselund
Collaborators: S. Kim, J. Meirer, T. Sjölander

Introduction
The diagnostics of neurological diseases and the study of brain health requires a detailed monitoring of brain activity. Magnetoencephalography (MEG) provides unique spatiotemporal accuracy. MEG is used clinically to diagnose epilepsy [1], as well as in neuroscience research where it is used to study for example depression and eating disorders. MEGs relative lack of market penetration is due to a number of issues with current state-of-the-art commercial technology, including cost of acquisition and maintenance. Our goal is to develop a new generation of MEG system, combining quantum sensors (NV centres) and artificial intelligence (AI). Such systems would enable measurements of brain activity in noisy environments and may be integrated into nano-probes for brain or cardiac endoscopy.

Strategy
The present project focuses on two key components. The first component is the development of a new quantum sensor based on optically addressable atomic defects in diamond known as NV centres. NV-diamond quantum sensors have the potential to revolutionize MEG by providing high enough sensitivity to measure signals from the brain while simultaneously having high enough dynamic range to enable measurements outside of magnetically shielded rooms. Further, the sensors could be mounted on a headcap and adjusted to patient's head shape, including children. However, the high refractive index of diamond, as well as the low absorption cross section of NV-centers means that getting enough light out of the crystal is a challenge. The conversion efficiency from excitation photons to detected readout photons is typically 1-3%. Ultimately this is one significant factor currently limiting sensitivity, and both excitation efficiency and photon collection efficiency needs to improve before it is possible to reach the sensitivity needed to detect magnetic signals from the brain. Within this project PSI and Qnami aims to use optics and nanofabrication expertise to overcome this challenge and design an optical collection system capable of a photon conversion rate of 10%.

The second component consists in advancements of AI algorithms to reconstruct the 3D brain activity map at high fidelity and robustness to noise. Reconstructing maps of brain activity from MEG data is an ill-posed inverse problem. Recent results in other areas of biomedical imaging indicate that this problem probably is better solved with an AI than current state-of-the-art classical methods [2]. A signal processing strategy is needed for decoding tiny (picotesla) brainwave signals while in the presence of the much larger (micro-tesla) ambient field of the earth in addition to environmental noise sources like other instrumentation and vehicles. A key result will be to benchmark our algorithm with already existing benchmark data.

Results & discussion
1) Design an optical assembly structure
Qnami has finished the design of a light collection system compatible with sensor packaging and miniaturization. The design consists of two parts: An NV-sensor diamond crystal cut into the shape of an elongated diamond rod with square end facets. The elongated shape and the high refractive index of diamond ensures that the majority of the photoluminescence from the crystal is guided towards the 2 square facets. Second, contacted with one of the facets is a parabolic light guide that reduces the NA of the emitted PL (while increasing the area). The lightguide is designed to optimize coupling into a 0.52 NA optical fiber. Large core diameter fibers with 0.52 NA are easily accessible commercially. Ray tracing simulations indicate that using this optical system we should be able to achieve a conversion ratio of green photons to collected red PL of 23%.

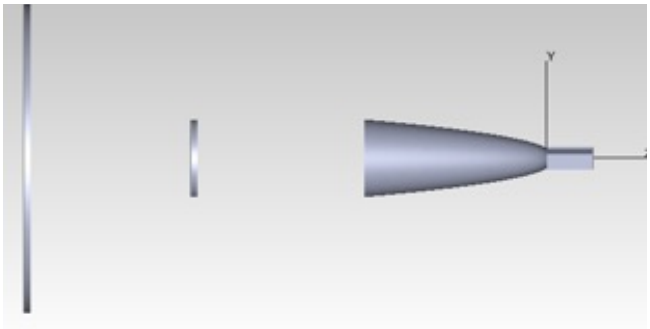

Fig. 1: The optical assembly design. Taken from a ray-tracing simulation. The cylindrical parabola is a diamond light guide, while the square rod represents the NV containing diamond crystal. The vertical planes are used to measure the angular distribution and intensity of the light that is coupled out of the diamond. This design is upgraded from the elliptical design we envisioned at the start of the project. Careful simulations showed that the performance of the elliptical design would be unsatisfactory.

2) Design and fabricate advanced photonic nanostructures on the diamond surface.
In order to selectively optimize the excitation and collection efficiencies we designed and fabricated wavelength dependent optical structures on the diamond. We evaluated different design approaches by simulation, developing structures both based on photonic bandgaps as well as optimized scattering. Qnami and PSI jointly developed fabrication routes to produce the designed structures. Based on our investigation of nanophotonic surface patterning, we believe this is a more promising route to improve efficiency rather than the simple solution of coating.

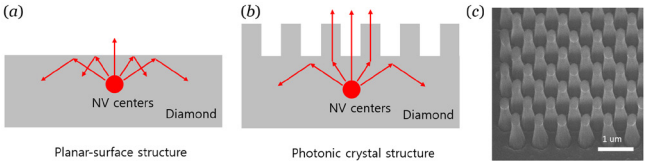

Fig. 2: a) Illustration of the challenge of out-coupling light due to the high refractive index of diamond, the out-coupling efficiency of the light is very low, which results in a low sensitivity. b) Illustration of the concept of how scatterers at the surface or photonic crystals might optimize out-coupling efficiency. c) Example of a diamond photonic crystal lattice fabricated in QSBI.

3) Development of optical measurement set-ups

PSI has developed an optical set-up (Fig. 3a) and test methodology which allows us to assess the impact of nano patterning of the diamond surface. It can operate in either a normal reflection mode or free-space via a fiber coupling to the side of the diamond crystal. As illustrated in figure 3b, we did observe an enhancement from the patterned region (stronger colour), however the current set-up does not allow for a quantitative comparison of the different designs, nor do we observe a clear dependence on wavelength. In the next period we will continue to work on improving both the fabrication route (reducing roughness and optimizing the profile), improving the resolution of the optical set-up for quantitative comparison as well as developing different designs.

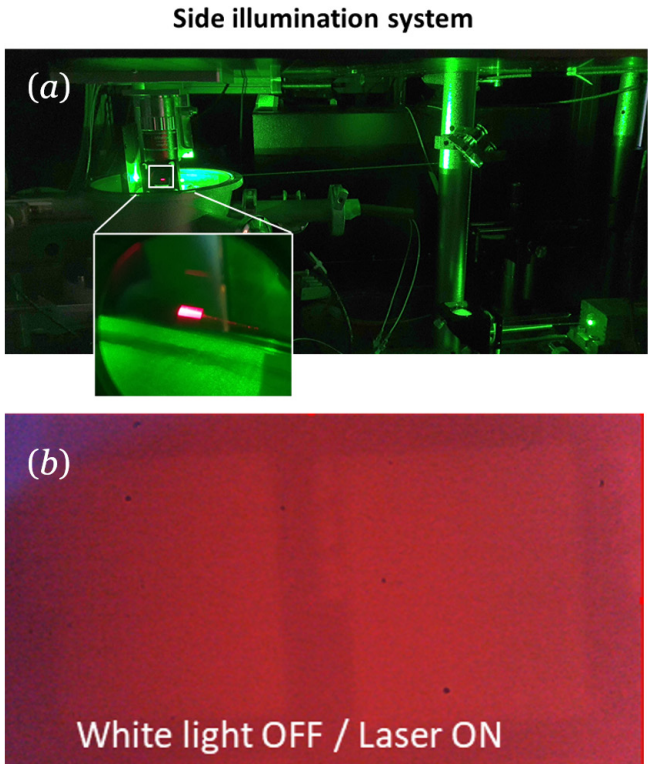

Fig. 3: a) photo of the optical set-up showing the light path from the fiber to the diamond chip. After introducing NV centers the diamond chip lights up in pink. b) image of two patterned regions. The fact that they are brighter than the surrounding indicates improved out-coupling efficiency.

4) Inverse mapping problem

We have implemented a forward model for how brain activity generates magnetic fields and adapted Qnami's previously developed AI architecture to work with 3D brain data rather than 2D semiconductor data. Based on the forward model, we simulated a dataset of MEG measurements and benchmarked the algorithm against existing methods. While the algorithm succeeded in reconstructing neural activities, it did not provide a significant benefit over recently published AI-based methods. We are therefore further developing and adapting the current state-of-the-art methods for the activity reconstruction task. In addition, we have obtained a phantom head dataset (recorded from a plastic head with current loops corresponding to magnetic dipole sources, so called MEG phantom data) and are using it as another benchmark for the evaluation of new methods. In parallel, we performed an extensive analysis using the phantom head MEG dataset to identify requirements for the number of sensors required to obtain accurate reconstructions. For this, we varied the number of sensors (ranging from 2 to 300) and performed the reconstruction task 100 times for each scenario to obtain a robust performance estimate. In the next phase of the project we will continue to develop and identify the best-performing model for brain activity reconstruction based on benchmarks against existing methods using both the simulated data and the MEG phantom head data.

Conclusion

In order to develop a sensor compatible with MEG application, we investigated different design approaches by simulation and measured qualitatively an enhancement of PL emission. Although the AI algorithm's initial performance is comparable to existing methods, ongoing work with benchmark data and the MEG phantom head dataset will guide further refinements. Future plans involve refining the optical assembly, optimizing nanostructures, and developing AI models for improved brain activity reconstruction. This interdisciplinary approach, combining quantum technology, nanofabrication, and AI, positions the project to revolutionize MEG technology, enabling precise brain activity measurements even in challenging environments. The ultimate goal is to contribute significantly to the diagnosis of neurological diseases and advance our understanding of brain health.

References

[1] M. J. Brookes, J. Leggett, M. Rea, R. M. Hill, N. Holmes, et al., Magnetoencephalography with optically pumped magnetometers (OPM-MEG): the next generation of functional neuroimaging, Trends in Neuroscienes 45, 621-634 (2022)

[2] G. Zeng, Y. Guo, J. Zhan , Z. Wang, Z. Lai, et al., A review on deep learning MRI reconstruction without fully sampled k-space, BMC Medical Imaging 21, 195 (2021)

Overcoming the drug delivery barriers with SmartCoat™

Project A18.8: SmartCoat (FHNW Muttenz, Paul Scherrer Institut, Palto Therapeutics AG, Allschwil)
Project Leader: J. Mosbacher
Collaborators: G. Lipps and R. Benoit

The challenge

De novo drug development is a highly resource-intensive, risky, and costly process. Despite tremendous efforts by the pharmaceutical industry to develop small-molecule and biologics, only 0.05% of the human genome has been drugged by the currently approved protein-targeted therapeutics. Many disease-causing proteins are inaccessible or lack specific clefts and pockets for small molecules binding. The difficulties associated with drug development have resulted in two main issues. First, conventional drugs have reached an efficacy ceiling, and many new therapies only bring marginal benefit to patients. Secondly, the costs to bring such drugs to market have increased to over one billion USD per registration. Common failure rates in the clinical development are 90%, or even 97% for cancer drugs.

RNA interference is a natural process through which a disease-causing gene can be eliminated in a highly specific manner. This mechanism enables precise and personalized treatment of diverse life-threatening diseases, including cancer, viral infections and rare genetic diseases. The discovery of small interfering RNA (siRNA) and its promise to provide a universal treatment for practically any disease has been awarded with the Nobel prize in 2006 (Andrew Fire and Craig Mello). However, in 2023, only six siRNA-based drugs have been approved, mainly due to the challenge of stably delivering such molecules to target cells in patients.

The safe and efficient delivery of siRNA to diseased cells remains an unsolved challenge. First, naked siRNAs are rapidly degraded in a biological environment. After years of research effort, it has been shown that siRNA can be stabilized with extensive chemical modifications, while maintain activity. However, even when stabilized, the major barrier to build functional RNA therapeutics remains their delivery to target tissues in the body. Current delivery strategies are to formulate of the siRNA into lipid or solid nanocarriers or to conjugate chemically-protected siRNA to triantennary N-acetyl-galactosamine (GalNac). The GalNAc–siRNA conjugate delivery platform is safe and effective, but only allows delivery to hepatocytes and restricts its therapeutic use to liver diseases.

The solution

Palto Therapeutics provides a novel approach, which is called SmartCoat™ to overcome the issues related to the delivery of siRNA. SmartCoats™ are defined, monodipserse structures that strictly allow a 1 :1 binding of siRNA (Fig. 1). They consist of safe and innocuous material which are not associated with immunogenicity.

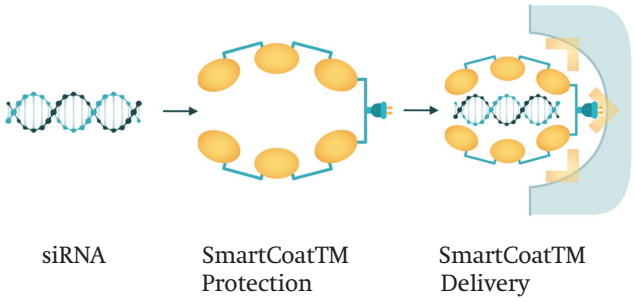

Fig. 1: Chemically unmodified therapeutic siRNA (left) is encapsulated in a single protective layer that protects the RNA (middle, SmartCoat™) and mediates cellular delivery (right).

SmartCoat™ novel design and structure differ significantly from conventional nanoparticles. Lipid or other particulate nanocarriers (Fig. 2) are plagued by inherent pharmacologic problems. Drug delivery is a complex problem and inacceptable properties, such as toxicity, poor tissue distribution and inadvertent immune activation must be avoided. For example, the high absorption of lipidic nanoparticles in liver and lung has prevented their generic use as siRNA delivery platform. Consequently, a breakthrough for the extra-hepatic transport of siRNA-based therapeutics is still urgently needed.

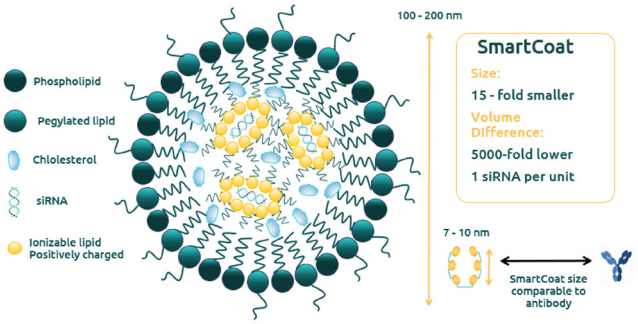

Fig. 2: Comparison between Lipid Nanoparticles (LNPs), a SmartCoat™ and an Antibody. Before siRNA can take effect in the cytoplasm of a target cell, it must be transported to the target site without clearance or degradation. Currently, lipids are the most used carriers for siRNA. LNPs are heterogeneous particles containing multiple lipids and chemically modified RNA molecules (left). SmartCoats™ are homogeneous particles containing an unmodified RNA molecule. The 5000-fold difference in volume allows, like therapeutic antibodies, for easier tissue penetration than LNPs.

The project

A SmartCoat™ consists of modular peptidergic building blocks. SmartCoat™ structures were produced in high yield and quality (>95% purity) at the FHNW Muttenz. They allow to bind to double stranded siRNA, but not single stranded RNA. All SmartCoats™ design iterations undergo a structural validation at PSI in Villingen. We have shown that siRNA-loaded complexes readily form in the presence of the SmartCoat™ and naked siRNA. The physical protection provided by an optimized SmartCoat™ will allow the siRNA-loaded complexes to be stable in serum for an extended space of time, as opposed to a few minutes for naked siRNA. This feature is required to allow long circulation times in the patients. This foresightful design will reduce the risk of regulatory issues and clinical problems in the later development stages. SmartCoats™ have been designed as a platform to deliver siRNAs specifically to diseased cell types but not healthy cells. They can load any siRNA sequence for direct knockdown of the genetic root cause of a given disease. The revolution of genetic medicine will allow to target any dysregulated genetic mechanism. The SmartCoat™ approach aims to support treatment of many currently incurable diseases.

The outlook

The next optimization steps will be to achieve good knockdown of critical genes in tumor cell lines to stop cell proliferation and tumor growth. Tumor cell lines used in the project have been carefully selected to allow seamless progression into the respective mouse models for an in vivo proof of concept.

References

[1] B. Hu, L. Zhong, Y. Weng, L. Peng, Y. Huang, Y Zhao, XJ. Liang, Therapeutic siRNA: state of the art. Signal Transduct Target Ther. 5, 101 (2020)

[2] W. Tai, X. Gao. Functional peptides for siRNA delivery. Adv Drug Del Rev. 110-111, 157-68 (2017)

Publications

C. L. Alter, P. Detampel, R. B. Schefer, C. Lotter, P. Hauswirth et al., High efficiency preparation of monodisperse plasma membrane derived extracellular vesicles for therapeutic applications. Comm. Biol. 6, 478 (2023) https://doi.org/10.1038/s42003-023-04859-2

M. Amer, O. Leka, P. Jasko, D. Frey, X. Li, R. A. Kammerer, A coiled-coil-based design strategy for the thermostabilization of G-protein-coupled receptors, Sci. Rep. 13, 10159 (2023) https://doi.org/10.1038/s41598-023-36855-1

M. Carrillo, T. J. Mason, A. Karpik, I. Martiel, M. W. Kepa, et al., Micro-structured polymer fixed-target for serial crystallography at synchrotrons and XFELs, IUCrJ, 10(6), 2052-2525 (2023) https://doi.org/10.1107/S2052252523007595

C. Ciaccia, R. Haller, A. C. C. Drachmann, T. Lindemann, M. J. Manfra, et al. Gate Tunable Josephson Diode in Proximitized InAs Supercurrent Interferometers, Phys. Rev. Research 5(3), 33131 (2023) https://doi.org/10.1103/PhysRevResearch.5.033131

M. Degen, J. C. Santos, K. Pluhackova, G. Cebrero, S. Ramos et al. Structural basis of NINJ1-mediated plasma membrane rupture in cell death. Nature 618, 1065–1071 (2023) https://doi.org/10.1038/s41586-023-05991-z

V. Doffini, H. Liu, Z. Liu, M. A. Nash, Iterative Machine Learning for Classification and Discovery of Single-Molecule Unfolding Trajectories from Force Spectroscopy Data, Nano Letters, 23, 10406–10413 (2023) https://doi.org/10.1101/2023.08.08.552253

O. M. Eggenberger, P. Jaśko, S. Tarvirdipour, C.-A. Schoenenberger, C. G. Palivan, Advances in Biohybridized Planar Polymer Membranes and Membrane-Like Matrices, Helv. Chim. Acta 106(4) e202200164, (2023) https://doi.org/10.1002/hlca.202200164

M. Endres, A. Kononov, H. S. Arachchige, J. Yan, D. Mandrus, et al., Current-phase relation of WTe2 Josephson junctions, Nano Letters 23, 4654-4659 (2023) https://doi.org/10.1021/acs.nanolett.3c01416

M. Ernzer, M. Bosch Aguilera, M. Brunelli, G.-L. Schmid, T. M. Karg, et al., Optical coherent feedback control of a mechanical oscillator, Phys. Rev. X, 13, 021023 (2023) https://doi.org/10.1103/PhysRevX.13.021023

L. Forrer, A. Kamber, A. Knoll, M. Poggio, F. R. Braakman, Electron-beam lithography of nanostructures at the tips of scanning probe cantilevers, AIP Adv. 13, 035208 (2023) https://doi.org/10.1063/5.0127665

N. Forrer, A. Nigro, G. Gadea, I. Zardo, Influence of Different Carrier Gases, Temperature, and Partial Pressure on Growth Dynamics of Ge and Si Nanowires. Nanomaterials. 13(21), 2879 (2023) https://doi.org/10.3390/nano13212879

R. Haller, M. Osterwalder, G. Fülöp. J. Ridderbos, M. Jung, and C. Schönenberger, AC Josephson effect in a gate-tunable Cd3As2 nanowire superconducting weak link, Phys. Rev. B 108, 94514 (2023) https://doi.org/10.1103/PhysRevB.108.094514

L. Heuberger, D. Messmer, E. C. dos Santos, D. Scherrer, E. Lörtscher et al., Microfluidic giant polymer vesicles equipped with biopores for high-throughput screening of bacteria, Advanced science (2023) https://doi.org/10.1002/advs.202307103

P. Hiret, K. Soni, A. Cherukulappurath Mana, E. Faudot, L. Moser, et al. Plasma sputtering of biased electrodes in an oblique magnetic field. Plasma Sources Sci Technol 32, 9 (2023) https://doi.org/10.1088/1361-6595/acfc63

W. Huang, O. Braun, D. I. Indolese, G. B. Barin, G. Gandus, et al., Edge Contacts to Atomically Precise Graphene Nanoribbons, ACS Nano 17, 18706 (2023) https://doi.org/10.1021/acsnano.3c00782

D. Jaeger, F. Fogliano, T. Ruelle, A. Lafranca, F. Braakman, M. Poggio, Mechanical Mode Imaging of a High-Q Hybrid hBN/Si3N4 Resonator, Nano Lett. 23 (5), 2016-2022 (2023) https://doi.org/10.1021/acs.nanolett.3c00233

C. Jünger, S. Lehmann, K. A. Dick, C. Thelander, C. Schönenberger, A. Baumgartner, Intermediate states in Andreev bound state fusion. Commun Phys 6, 190 (2023) https://doi.org/10.1038/s42005-023-01273-2

P. Karnatak, Z. Mingazheva, K. Watanabe, T. Taniguchi, H. Berger, et al., Origin of subgap states in normal-insulator-superconductor van der Waals heterostructures, Nano Letters 23(7), 2454–2459 (2023) https://doi.org/10.1021/acs.nanolett.2c02777

C. Li, C. Kaspar, P. Zhou, J.-C. Liu, O. Chahib, et al. Strong signature of electron-vibration coupling in molecules on Ag(111) triggered by tip-gated discharging. Nat Commun 14, 1 (2023) https://doi.org/10.1038/s41467-023-41601-2

J.-C. Liu, R. Pawlak, X. Wang, H. Chen, P. D'Astolfo et al., Proximity-induced superconductivity in atomically precise nanographene on Ag/Nb(110), ACS Materials Lett. 5(4), 1083–1090 (2023) https://doi.org/10.1021/acsmaterialslett.2c00955

Z. Liu, J. G. Vilhena, E. Meyer, A. Hinaut, S. Scherb, et al., Moire-Tile Manipulation-Induced Friction Switch of Graphene on a Platinum Surface. Nano Letters 23, 10, 4693–97 (2023) https://doi.org/10.1021/acs.nanolett.2c03818

J. Lopez-Morales, R. Vanella, E. A. Appelt, S. Whillock, A. M. Paulk et al., Protein Engineering and High-Throughput Screening by Yeast Surface Display: Survey of Current Methods, small science 3(12), 2300095 (2023) https://doi.org/10.1002/smsc.202300095

J. Lopez-Morales, R. Vanella, G. Kovacevic, M. Sá Santos, M. A. Nash, Titrating Avidity of Yeast-Displayed Proteins Using a Transcriptional Regulator, ACS Synth. Biol. 12(2), 419–431 (2023) https://doi.org/10.1021/acssynbio.2c00351

V. Maffeis, L. Heuberger, A. Nikoletić, C.-A. Schoenenberger, C. G. Palivan, Synthetic Cells Revisited: Artificial Cells Construction Using Polymeric Building Blocks, Adv. Sci. 2305837 (2023) https://doi.org/10.1002/advs.202305837

K. Mukaddam, M. Astasov-Frauenhoffer, E. Fasler-Kan, S. Ruggiero, F. Alhawasli et al., Piranha-etched titanium nanostructure reduces biofilm formation in vitro. Clin. Oral Investig. (2023) https://doi.org/10.1007/s00784-023-05235-4

G. N. Nguyen, C. Spinnler, M. R. Hogg, L. Zhai, A. Javadi et al., Enhanced Electron-Spin Coherence in a GaAs Quantum Emitter, Phys. Rev. Lett. 131, 210805 (2023) https://doi.org/10.1103/PhysRevLett.131.210805

H. Nicolas, R. C. Sousa, A. Mora-Hernandez, I.-L. Prejbeanu, L. Hebrard et al., Conditioning Circuits for Nanoscale Perpendicular Spin Transfer Torque Magnetic Tunnel Junctions as Magnetic Sensors, IEEE Sensors Journal 23(6), 5670-5680 (2023) doi: 10.1109/JSEN.2023.3241967

A. Ollier, M. Kisiel, X. Lu, U. Gysin, M. Poggio et al., Energy dissipation on magic angle twisted bilayer graphene, Commun. Phys. 6, 344 (2023) https://doi.org/10.1038/s42005-023-01441-4

J. Oswald, D. Beretta, M. Stiefel, R. Furrer, D. Vuillaume et al., The Effect of C60 and Penta-cene Adsorbates on the Electrical Properties of CVD Graphene on SiO_2. Nanomaterials 13, 1134 (2023) https://doi.org/10.3390/nano13061134

J. Oswald, D. Beretta, M. Stiefel, R. Furrer, S. Lohde et al., Field and Thermal Emission Limited Charge Injection in Au–C60–Graphene van der Waals Vertical Heterostructures for Organic Electronics. ACS Appl. Nano Mater. 6(11), 9444–9452 (2023) https://doi.org/10.1021/acsanm.3c01090

K. Regos, R. Pawlak, X. Wang, E. Meyer, S. Decurtins et al., Polygonal tessellations as predictive models of molecular monolayers. PNAS 120(16) (2023) https://doi.org/10.1073/pnas.2300049120

G. Romagnoli, E. Marchiori, K. Bagani, M. Poggio, Fabrication of Nb and MoGe SQUID-on-tip probes by magnetron sputtering, Appl. Phys. Lett. 122, 192603 (2023) https://doi.org/10.1063/5.0150222

F. Sanchez, A. Dmitriev, R. Antunes, R. Steiner E. Meyer, WO3 work function enhancement induced by filamentous films deposited by resistive heating evaporation technique. J Alloys Compd 968 (2023) https://doi.org/10.1016/j.jallcom.2023.171888

F. Sanchez, L. Marot, R. Steiner, D. Mathys, P. Hiret et al., Surface modification of ITER-like mirrors after one hundred cleaning cycles using radio-frequency plasma. J. Nuclear Mater. 581 (2023) https://doi.org/10.1016/j.jnucmat.2023.154382

U. Sanli, G. Rodgers, M. Zdora, P. Qi, J. Garrevoet et al., Apochromatic X-ray focusing, Light Sci Appl. 12(1), 10107 (2023) https://doi.org/10.1038/s41377-023-01157-8

S. Scherb, A. Hinaut, X. Yao, A. Goetz, S. H. Al-Hilfi, et al. Solution-Synthesized Extended Graphene Nanoribbons Deposited by High-Vacuum Electrospray Deposition. ACS Nano 17(1), 597-605 (2023) https://doi.org/10.1021/acsnano.2c09748

A. K. Sivan, B. Abad, T. Albrigi, O. Arif, J. Trautvetter, et al., GaAs/GaP Superlattice Nanowires for Tailoring Phononic Properties at the Nanoscale: Implications for Thermal Engineering, ACS Appl Nano Mater 6(19), 18602-18613 (2023) https://doi.org/10.1021/acsanm.3c04245

Y. Song, E. Meyer, Atomic Friction Processes of Two-Dimensional Materials. Langmuir 39(44), 15409–16 (2023) https://doi.org/10.1021/acs.langmuir.3c01546

J. Svirelis, Z. Adali, G. Emilsson, J. Medin, J. Andersson et al., Stable trapping of multiple proteins at physiological conditions using nanoscale chambers with macromolecular gates, Nat. Comm., 14, 5131 (2023) https://doi.org/10.1038/s41467-023-40889-4

J. H. Ungerer, D. Sarmah, A. Kononov, J. Ridderbos, R. Haller et al., Performance of high impedance resonators in dirty dielectric environments, EPJ Quantum Technology 10, 41 (2023) https://doi.org/10.1140/epjqt/s40507-023-00199-6

J. H. Ungerer, C. P. Kwon, T. Patlatiuk, J. Ridderbos, A. Kononov et al., Charge-sensing of a Ge/Si core/shell nanowire double quantum dot using a high-impedance superconducting resonator, Mater. Quantum Technol. 3, 031001 (2023) https://doi.org/10.1088/2633-4356/ace2a6

X. Yao, H. Zhang, F. Kong, A. Hinaut, R. Pawlak et al., Armchair Graphene Nanoribbons: Solution Synthesis and High Charge Carrier Mobility. Angew. Chem., Int. Ed. 62 (2023) https://doi.org/10.1002/anie.202312610

Z-H. Zhang, J. A. Zuber, L. V. H. Rodgers, X. Gui, P. Stevenson et al., Neutral Silicon Vacancy Centers in Undoped Diamond via Surface Control, Phys. rev. letters, 130, 166902 (2023) https://doi.org/10.1103/PhysRevLett.130.166902

J. A. Zuber, M. Li, M. Grimau Puigibert, J. Happacher, P. Reiser et al., Shallow Silicon Vacancy Centers with Lifetime-Limited Optical Linewidths in Diamond Nanostructures, Nano letters 23, 23, 10901-10907 (2023) https://doi.org/10.1021/acs.nanolett.3c03145

F. Züger, N. Berner, M. R. Gullo, Towards a Novel Cost-Effective and Versatile Bioink for 3D-Bioprinting in Tissue Engineering, Biomimetics 8, 27 (2023) https://doi.org/10.3390/biomimetics8010027

Educating
Talents
since 1460.

University of Basel
Petersplatz 1
Postfach 2148
4001 Basel
Switzerland

www.unibas.ch

Swiss Nanoscience Institute
University of Basel
Klingelbergstrasse 82
4056 Basel
Switzerland

www.nanoscience.ch